University of Strathclyde

Department of Mechanical & Aerospace Engineering

Atmospheric Reentry Modelling Using an Open-Source DSMC Code

Rodrigo Cassineli Palharini

A thesis presented in fulfilment of the requirements

for the degree of Doctor of Philosophy

2014

Declaration of author's rights

This thesis is the result of the author's original research. It has been composed by the author and has not been previously submitted for examination which has led to the award of a degree.

Rodrigo C. Palharini

September 2014

Abstract

Aerothermodynamic investigations of hypersonic re-entry vehicles provides crucial information to other key disciplines as structures and materials, assisting the development of efficient and lightweight thermal protection systems (TPS). Under the transitional flow regime, where chemical and thermal nonequilibrium are predominant, the most successful numerical method for such studies has been the direct simulation Monte Carlo (DSMC) numerical technique.

In the present work, the solver *dsmcFoam* has been benchmarked against experimental, numerical, and theoretical data found in the open literature for inert and chemically reactive flows. The Quantum-Kinetic (QK) chemistry model with a full set of 19 chemical reactions has been implemented into the code and it proved to be essential in the correct prediction of the shock wave structure and heating flux to the vehicle's surface during the re-entry phase.

Having implemented the QK chemistry model, the *dsmcFoam* solver was employed to investigate thermal protection system discontinuities. These TPS discontinuities, representative of panel-to-panel joints or the impact of micro meteorites/ice droplets, were modelled as a family of cavities with different length-to-depth ratios. The results showed that the cavity length has a significant impact on the flowfield structure and aerodynamic surface quantities distribution inside and around the cavities. In addition, for L/D = 5, the flow separates at the cavity upstream lip and attaches to the cavity bottom surface, representing a potentially catastrophic feature under rarefied gas conditions. Furthermore, the same phenomena is only observed in the continuum regime when L/D > 14.

"Engineering is not a science. Science studies particular events to find general laws. Engineering design makes use of these laws to solve particular problems. In this it is more closely related to art or craft; as in art , its problems are under-defined, there are many solutions, good, bad or indifferent. The art is, by a synthesis of ends and means, to arrive at a good solution. This is a creative activity, involving imagination, intuition and deliberate choice",

- Sir Ove Nyquist Arup (Engineer and philosopher, 1895-1988)

Acknowledgements

First and foremost, I must thank my advisor Dr. Thomas Scanlon for continual guidance and encouragement over the last four year. Dr. Scanlon has always been there to listen me, offer keen insight into the significance of my investigations and pointing out the right directions to overcome the obstacles. I would like also to acknowledge Prof. Jason Reese and Prof. Richard Brown who's knowledge and guidance made an invaluable contribution to my work. I am grateful for the opportunity to have been part of the James Weir Fluids Laboratory and my colleagues were always willing to share their knowledge and contribute to the group dynamic.

I would like to thank Dr. Richard Martin and all the staff from the Department of Mechanical and Aerospace Engineering at University of Strathclyde. In short, thanks for providing all of the academic and technical support over the past four years. I truly believe that your efficient work made our academic life much easier.

Special thanks goes out to Konstantinos Ritos, Nishanth Dongari, and Craig White. We had a great time together during these years. Your friendship made my life in Scotland more enjoyable and much more interesting. Beyond the fellowship, Craig was my tutor during the PhD. Thank you very much for being so generous in sharing your vast knowledge of both DSMC method and OpenFOAM.

While the people I have mentioned above played an important role in my life recently, there are a few people who have been there consistently throughout my life who I must acknowledge. Without the support of my parents, Darli and Cleide and my brother Marcelo, I truly would not be where I am today. A very special thank you to my grandparents, Salvador and Nida, who never let me forget my humble roots. I would like also to thank Rayana, for your comfort and support during my time spent writing this thesis, and for the happiness you have brought even far away from me.

Lastly, I am grateful for the financial support I received during my PhD studies from the National Council for Scientific and Technological Development (CNPq Grant N^o. 200473/2010-7).

Contents

List of Figures

List of Tables

List of Publications

1. Palharini, R. C. and Santos, W. F. N., Length-to-Depth Ratio Effects on Flowfield Structure of Low-Density Hypersonic Cavity Flow. In: Proceedings of the 42nd AIAA Thermophysics Conference, AIAA 2011-3130, 2011, Honolulu, Hawaii, 27-30 Jun.

2. Palharini, R. C. and Scanlon, T. J., Aerothermodynamic Comparison of Two- and Three-dimensional Rarefied Hypersonic Cavity Flow. In: Proceedings of the 43rd AIAA Thermophysics Conference, AIAA-2012-2997, 2012, New Orleans, USA, 25-28 Jun.

3. Palharini, R. C., Scanlon, T. J., and Reese, J. M., Effects of Angle of Attack on the Behaviour of Imperfections in Thermal Protection Systems of Re-Entry Vehicles. In: Proceedings of the 29th International Symposium on Shock Waves, 2013, Madison, USA, 14-19 Jul.

4. Palharini, R. C., Scanlon, T. J., and Reese, J. M., An Aerothermodynamic Comparison of Two- and Three-dimensional Rarefied Hypersonic Cavity Flows. Journal of Spacecraft and Rockets, AIAA Early Edition, 2014.

Nomenclature

Latin symbols

a	Speed of sound, m/s
C_f	Skin friction coefficient, $\tau/0.5\rho U^2$
C_h	Heat transfer coefficient, $q/0.5\rho U^3$
C_p	Pressure coefficient, $p\text{-}p_\infty/0.5\rho U^2$
c	Molecular velocity, m/s
$\mathbf{c}$	Molecular velocity vector, m/s
D	Cavity depth, mm
d	Molecular diameter, m
F_N	Number of real atoms/molecules each DSMC particle represents
F_n	Intermolecular force, N
H	Domain height, mm
i	Vibrational quantum level, dimensionless
k_B	Boltzmann constant, m^2 kg s^{-2} K^{-1}
k_f	Forward reaction rate coefficient, dimensionless
k_r	Reverse reaction rate coefficient, dimensionless
Kn	Knudsen number, λ/L
L	Cavity length, mm
L_d	Downstream cavity length, mm
L_u	Upstream cavity length, mm
l	Characteristic length, m

Ma	Mach number, U/a
m	Molecular mass, kg
m_r	Reduced mass, dimensionless
N	Number of molecules/DSMC particles
$\dot{N}$	Flux, particles/m^2s
n	Number density, m^{-3}
P	Scalar pressure, N/m^2
$\mathbf{p}$	Pressure tensor, N/m^2
$\mathbf{q}$	Heat flux vector, W/m^2
R	Universal gas constant, J/K.mol
R_{coll}	Collision rate in equilibrium VHS gas, dimensionless
Re	Reynolds number, $\rho UL/\mu$
R_f	Random fraction, dimensionless
R_n	Re-entry capsule nose radius, mm
$\mathbf{r}$	Molecule position vector, m
r	Molecular radius, m
T	Temperature, K
t	time, s
U	Freestream velocity, m/s
V_{cell}	Cell volume, m^3
W	Cavity width, mm
W_p	Plate width, mm
X_L	Normalised cavity length, dimensionless
X_{L_d}	Normalised downstream cavity length, dimensionless
X_{L_u}	Normalised upstream cavity length, dimensionless
Y_D	Normalised cavity depth, dimensionless
Z	Relaxation number, dimensionless
u, v, w	Velocity vector components, m/s
x, y, z	Spatial Cartesian co-ordinates, m

Greek symbols

α	Angle of attack, degree
γ	Ratio of specific heats, dimensionless
δ	Molecular mean separation, m
θ_d	Dissociation temperature, K
ε	Energy
θ_v	Characteristic vibrational temperature, K
λ	Molecular mean free path, m
μ	Viscosity, $\mathrm{Ns/m^2}$
ξ	Collision cross-section, $\mathrm{m^2}$
ρ	Mass density, $\mathrm{kg/m^3}$
ϱ	Energy accommodation coefficient, dimensionless
σ	Collision cross section, $\mathrm{m^2}$
ς	Degree of freedom, dimensionless
τ	Shear stress tensor, $\mathrm{N/m^2}$
τ	Wall tangential shear stress, $\mathrm{N/m^2}$
ω	Dynamic viscosity index, dimensionless

Superscripts

$*$	Post-collision/surface interaction properties
$'$	Thermal velocity

Subscripts

act	Activation
coll	Collision
d	Downstream surface
in	Inlet
ref	Reference
rot	Rotational
tra	Translational

u	Upstream surface
vib	Vibrational
w	Wall conditions
∞	Freestream conditions

Acronyms

AIAA	American Institute of Aeronautics and Astronautics
AGARD	Advisory Group for Aerospace Research and Development
CFD	Computational Fluid Dynamics
CAIB	Columbia Accident Investigation Board
CLL	Cercignani-Lampis-Lord
CNRS	Centre National de la Recherche Scientifique
DSMC	Direct Simulation Monte Carlo
FRSI	Felt Reusable Surface Insulation
GHS	Generalised Hard Sphere
HPC	High Performance Computer
HRSI	High Temperature Reusable Surface Insulation
LaRC	Langley Research Cente
LAURA	Langley Aerothermodynamic Upwind Relaxation Algorithm
LB	Larsen-Borgnakke
LRSI	Low Temperature Reusable Surface Insulation
MD	Molecular Dynamics
NAIT	NASA Accident Investigation Team
NASA	National Aeronautics and Space Administration
NC	Null Collision Technique
NIST	National Institute of Standards and Technology
NSF	Navier-Stokes-Fourier
NTC	No-Time-Counter
ONERA	Office National d'Etudes et de Recherches Aérospatiales

OpenFOAM	Open Field Operation And Manipulation
QK	Quantum-Kinetic
RCC	Reinforced Carbon-Carbon
STS	Space Transportation System
TC	Time Counter
TCE	Total Collision Energy
TPS	Thermal Protection System
VHS	Variable Hard Sphere
VSS	Variable Soft Sphere

Chapter 1

Introduction

Space vehicles re-entering the Earth's atmosphere may achieve speeds of tens of km/s. In order to slow down and reach the landing speed, the spacecraft experiences atmospheric friction effects which produce external surface temperatures as high as 1700 K, well above the melting point of steel. Although the hypersonic vehicles are built with advanced materials and methods, its airframe is constructed using lightweight aluminium and can only withstand temperatures ranging from 750 to 900 K without annealing or softening. In this scenario, reliable heat shields are required to protect the vehicle's surface and its crew from the extremely hostile re-entry environment [1].

External insulation materials as Reinforced Carbon-Carbon (RCC), Low- and High-Temperature Reusable Surface Insulation tiles (LRSI and HRSI, respectively), and Felt Reusable Surface Insulation (FRSI) blankets have been developed for such application [2, 3]. These materials are bonded to a substract, either directly to the airframe or to a supporting structure. For the Space Shuttle's development flights, more than 32,000 individual thermal protections system (TPS) tiles were used to cover the lower and upper surfaces. The tiles are arranged in a staggered or aligned pattern in the spacecraft surface and this can create numerous panel-to-panel joints, as shown in Figure 1.1. As such, cavities, gaps, and steps are often present on the surface of the aerospace vehicle. The implications for engineering and design requirements include the ability to account for thermal expansion and contraction of non-similar materials. In addition, gaps may be introduced by sensor installations, retro-propulsion systems, parachute and landing gears bays, or may be caused by the impact of orbiting debris

or near field experiments [4–7].

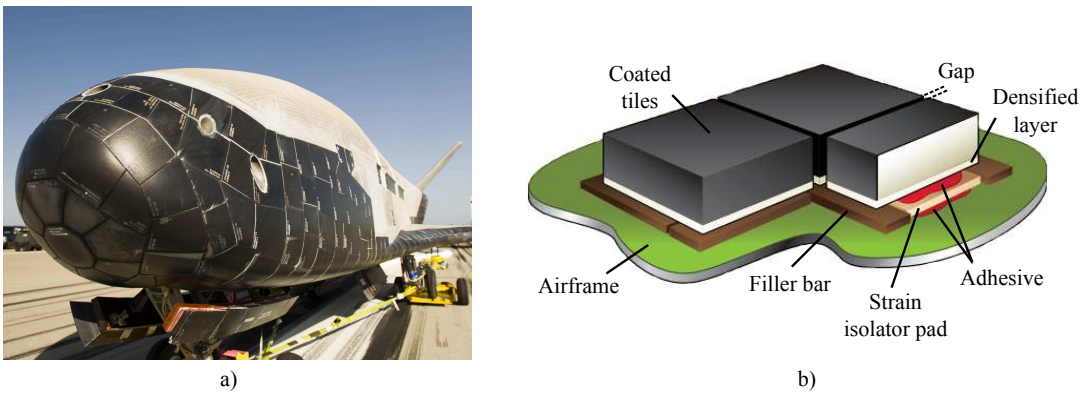

Figure 1.1: (a) X-37B space plane, (b) thermal protection system airframe (images credit: NASA).

During the atmospheric descent through the ever-thickening atmosphere, the hot gases can flow through the gaps leading to increased heating that could exceed the design limits of the vehicle's thermal protection system [8, 9]. Moreover, the flow configuration becomes more complex if the vehicle structure is deformed by thermal or mechanical loads. These loads may cause significant changes in the dimensions of the cavities, gaps or steps between the thermal protection tiles. Consequently, such modifications can lead to the appearance of stagnation points, hot spots, flow separation and attachment or it may induce an early boundary layer transition from a laminar to turbulent conditions [10, 11].

On 1st of February 2003, the Space Shuttle Columbia experienced a catastrophic failure during the atmospheric reentry at Mach 18 and an altitude of 61.3 km. Immediately after the accident, members of the Aerothermodynamics Branch of the NASA Langley Research Center (LaRC) started the investigations in order to clarify the aerothermodynamic environment of the STS-107 flight. At that time it was known from the telemetry data that off-nominal high temperatures had been measured by the backside resistance temperature detectors located on the side fuselage above the Orbiter wing. However, it was not known if this temperature rise was the origin of the aerodynamic heating that caused the Space Shuttle Columbia loss [12].

Many computer simulations were carried out to support ground based experimental investigations for different Shuttle damage scenarios [13–16]. The resulting accident in-

vestigations, led by the Columbia Accident Investigation Board (CAIB) and supported by the NASA Accident Investigation Team (NAIT) concluded that the most probable cause for the loss of the Space Shuttle Columbia was a breach in the thermal protection system of the leading edge of the left wing caused by a fragment of insulation foam released from external fuel tank during the ascent. The damage from the strike compromised the RCC panels on the leading edge exposing the wing structure to high energy air flow [17, 18].

This accident highlights the importance and the complexity of the study of thermal protection systems discontinuities under reentry conditions. In addition, it indicates that an accurate determination of aerothermodynamic loads is a necessary requirement for an optimal design of re-entry vehicles.

1.1 Re-entry flow regimes

Space vehicles reentering in the Earth's atmosphere undergo not only different velocity regimes, hypersonic, supersonic and subsonic, but also different flow regimes, free molecular flow, transition, and continuum. Each of these flow regimes must be considered during the vehicle aerothermodynamic design. As shown in Fig. 1.2 (a), important physical interactions arise between the vehicle and its surroundings during the reentry.

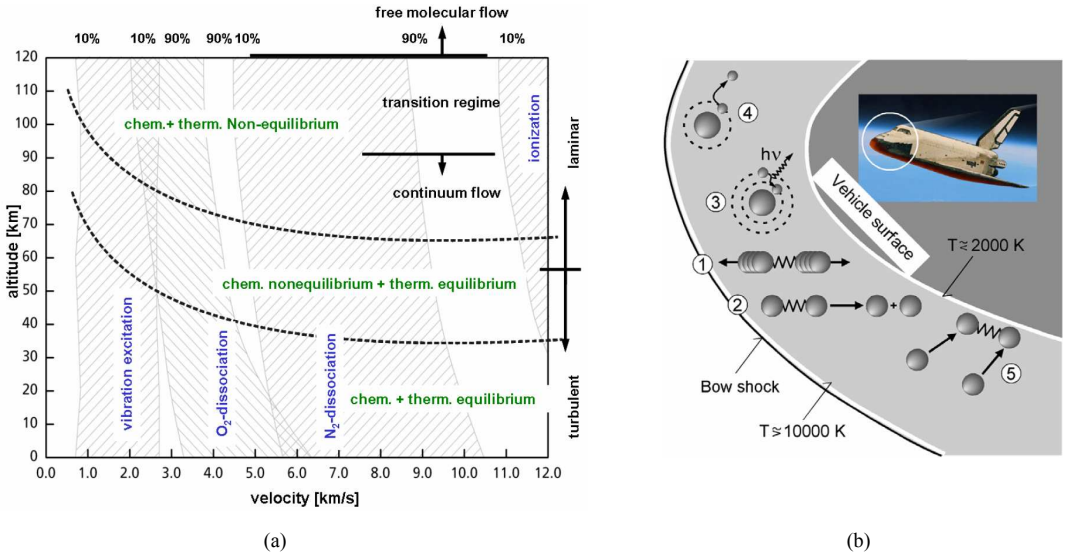

Figure 1.2: (a) High speed flow physical and chemical features, (b) High temperature effects behind a compression shock during the atmospheric reentry [19].

At the highest altitudes, the interaction of the vehicle with the atmospheric air is characterised by the free molecular flow. In this regime, the air molecules collide and interact with the vehicle's surface. However, collisions of reflected particles from the surface with freestream particles are not likely to occur.

As the vehicle enters deeper into the Earth's atmosphere, the mean free path decreases and collisions between particles reflected from the vehicle surface and the incoming freestream particles can no longer be ignored. As a result, the flow in this condition defines the transition flow regime, i.e., transition between the free molecular flow regime and the continuum flow regime. In the transition flow regime, the contribution of aerodynamic forces and heat flux to the vehicle surface start to increase rapidly with decreasing altitude, causing large changes in the aerodynamic characteristics of the vehicle when compared with those observed in the free molecular flow. At such altitudes, strong shock waves are formed in front of the vehicle and new flow features such as thermodynamic and chemical nonequilibrium become important for the correct prediction of heating rates and pressure loads acting on the vehicle's surface. As schematically shown in Figure 1.2 (b), the degrees of freedom of the gas at that particular altitude become excited (1), the molecular species may dissociate into atoms (2) with possible gas ionisation (3) and new species are formed (4). With reactions taking place during the reentry, the flow energy budget is reduced as well as the shock bow temperature due the energy exchange between the nascent gas molecules and atoms. Finally, these particles interact with the spacecraft surface which requires reliable models for accommodation coefficients, catalytic walls, and material ionisation (5) [19].

As the vehicle continues to enter into the atmosphere, it finally reaches a dense atmosphere characterised as the continuum flow regime. In this regime, the flow around the vehicle is treated by a macroscopic model that considers the air as a continuum and the description of the flow is made in terms of spatial and temporal variations of the macroscopic properties, such as velocity, pressure, density and temperature.

The basic criterion that determines the flow regime - collisionless, transition or continuum - is given by the Knudsen number as follows,

$$Kn = \frac{\lambda}{l}, \tag{1.1}$$

where λ is the mean free path travelled by particles between collisions and l is a characteristic length of the body.

The identification of a characteristic length l, defined in Equation 1.1, sometimes, is not immediate. In order to circumvent this problem, a local Knudsen number is used instead of the overall Knudsen number. The local Knudsen number is defined by the ratio of the local mean free path, λ, to a characteristic length defined by the gradient of any macroscopic property, hence,

$$l = \frac{\varphi}{\bigtriangledown\varphi} \tag{1.2}$$

Figure 1.3 presents the limits of typical mathematical formulations expressed in terms of the local Knudsen number. A flow is defined in the continuum regime when the Knudsen number tends to zero. On the other hand, a flow is defined in the free molecular flow as the Knudsen number approaches infinity.

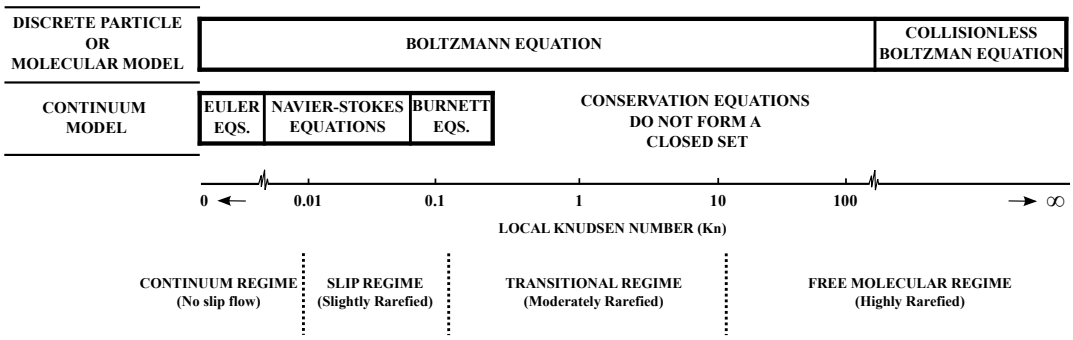

Figure 1.3: The Knudsen number limits and flow regime classification (adapted from Ref. [20]).

In the macroscopic model or continuum model, the general expressions of the fundamental conservation principles that govern the motion of gases are valid for all flow regimes. However, these expressions do not form a system of equations in a closed form when the Knudsen number increases. The application of conservation equations requires additional information concerning the shear stress tensor and the heat flux vector expressed in terms of macroscopic quantities. The Euler equations for inviscid

flow assume that the flow is in local thermodynamic equilibrium, with the velocity distribution function at any point equalling the Maxwellian distribution function. This is the limiting case as the Knudsen number tends to zero.

The continuum model, expressed by the Navier-Stokes-Fourier equations, is assumed to be valid when the Knudsen number is relatively small. In this case, the velocity distribution function can deviate from the Maxwellian distribution function. However, this deviation is still small enough such that the transport coefficients, obtained from the Chapman-Enskog theory, are valid [21]. Usually, the terms in the Navier-Stokes-Fourier expressions represent the conservation of linear momentum, mass, and energy in viscous fluids and they are usually applied to the study of Newtonian fluids, where the shear stress tensor is linearly proportional to the deformation rate tensor.

Boyd *et al.* [22, 23] have shown that the velocity distribution function differs significantly from the Maxwellian distribution function for a local Knudsen number Kn > 0.05, indicating that both the Chapman-Enskog theory and the Navier-Stokes equations are no longer valid. One alternative approach to this problem of the failure of the Navier-Stokes equations is to perform the Chapman-Enskog expansion to a high order to obtain the Burnett equations [24, 25]. Each level of approximation implies in a different distribution function that deviates from the Maxwellian. The interest in the Burnett equations, based on the second order expansion of the Chapman-Enskog for solving problems of rarefied hypersonic flows has increased [26–36]. However, the application of the Burnett equations has presented additional difficulties with the formulation of the boundary conditions and numerical instability [31]. In addition, the Burnett equations increase the order of the differential equations that govern the momentum and energy transport in the gas. These equations are harder to solve numerically, and fail when the degree of rarefaction is sufficiently high. The Burnett equations may not satisfy the second law of thermodynamics in certain situations, such as a negative dissipation function or the presence of a heat flux in an isothermal gas [35]. Finally, references [37] and [38] present a detailed description of the use of the Burnett equations to solve problems of rarefied hypersonic flow.

In the microscopic model or molecular model, the gas is treated as a collection of particles where the position and velocity of these particles are described individually.

Such a system requires the solution of the Boltzmann equation [39]. Analytical solutions of the Boltzmann equation are possible for collisonless flow, i.e., when the Knudsen number tends to infinity. However, analytical difficulties are found for finite Knudsen numbers. The Boltzmann equation is an integral-differential equation with the velocity distribution function as the only dependent variable. In contrast, the Navier-Stokes-Fourier equations have the flow velocity and thermodynamic properties as dependent variables. The reduction in the number of dependent variables in the Boltzmann equation is made at the expense of increasing the number of independent variables from the physical space to that of phase space. Thus, a one-dimensional monoatomic gas problem at steady state becomes a three-dimensional gas in phase space.

Analytical solutions of the Boltzmann equation usually involve simple molecular models, one independent macroscopic variable and flows with small disturbances. However, rarefied hypersonic flow problems are associated with complex physical effects, such as chemical reactions and thermal radiation, which have not yet been incorporated into the Boltzmann formulation. Consequently, the mathematical difficulties associated with the direct solution of the Boltzmann equation have stimulated the development of physically-based numerical methods. Nowadays, the most widely used technique to compute gas flows at the molecular level and to provide solutions to the Boltzmann equation are the molecular dynamics method (MD) [40, 41] and the direct simulation Monte Carlo (DSMC) method [20, 42]. For the purpose of this work, only the DSMC method will be presented and discussed herein.

1.2 Previous work

Flows over cavities are directly related to civil and military aircraft development in early 1940's and their studies extend to the present. It is a very challenging problem due to complex flow characteristics such as hypersonic flow separation and reattachment, increased drag and heating, noise and resonance. These physical phenomenas directly affect the aircraft aerodynamic performance under low or high speed flow conditions.

The first attempt to provide detailed experimental data on cavity flows was performed by Roshko [43]. Pressure and velocity was measured at side and bottom walls for cavities length-to-depth ratios (L/D) ranging from 0.016 to 2.5. It was observed

that pressure in the shallow cavities are considerably higher than those in the deeper ones. For L/D = 1 , i.e., a square cavity, the pressure at all measurements points was steady. Lower pressures were noticed near the centre of the walls and bottom and high pressures at the corners, characteristics of single stable vortex. According to this work, the formation of the vortex is caused by the deflection of part of the boundary layer into the cavity with a high pressure region at the downstream edge. Intermittent regions are also noticed for some values of length-to-depth ratios, which were the cause of strong pressure and velocity variations. This work presented the first insights into the cavity flowfield structure and physical explanation of stable and unstable vortex formation.

The most well known theoretical analysis on laminar separated flow and heat transfer was conducted by Chapman [44]. In his simple theory, the air pressure in pure laminar separations with negligible boundary layer thickness at separation was considered to include heat transfer. The flowfield consisted of a thin constant pressure viscous mixing layer separated from the solid surface by an enclosed region of low velocity. The heat transfer in the separated flow region was predicted to be 56% of the attached flow value. Later, Carlson [45] attempted to improve the Chapman's theory by including the effects of reverse flow along the floor of the separated region using arbitrary polynomial profiles for velocity and enthalpy.

Larson [46] conducted experiments to provide heat transfer data for equivalent separated and attached boundary layers, enabling a direct comparison with Chapman's predictions. Results were obtained for laminar and turbulent supersonic flow over a wide range of Mach numbers, M = 0.3 to 4.0. The experimental results for laminar flow agreed well with the Chapman's analysis; however, a considerable disagreement between experiment and theory was found for turbulent flow.

Charwat *et al.* [47, 48] have investigated the heat transfer and pressure distribution features for rectangular cavities for turbulent flow at M = 2 to 3.5. According to the authors, a critical length-to-depth ratio exists which defines the frontier between "open" and "closed" cavities. The results for turbulent boundary layer in open cavities indicated an increase of the heat transfer coefficients towards the reattachment point and good agreement was found when compared with Larson's results [46].

In the late 1960's the first Space Shuttle concept started to be explored and the program formally commenced in 1972. Projected to be a reusable space vehicle and last for a hundred or more missions with minimal refurbishment costs [49]; the accuracy on the thermal protection systems design would prove to be of extreme importance. Many experimental and numerical studies were carried out to define and develop new materials for reusable thermal protections system that could withstand the harsh reentry environment and to accurately predict the required spacing between the TPS tiles [50–60]. Only a few of these studies will be briefly discussed below.

Bertran and Wiggs [50] have investigated experimentally the effect of distortions, consisting of slots, small steps and local curvatures, on the wing of hypersonic vehicles. The effect of distortions in the distribution of pressure and heat flux to the surface was investigated for Mach numbers of 7 and 10, and angles of attack up to 20 degrees. According to the results, the surface distortions had a much smaller effect on local pressure than on the local heating. The study showed that all the distortions investigated caused at least a high local increase in aerodynamic heating.

Experiments on hypersonic turbulent flow over steps and cavities was conducted by Nestler *et al.* [51]. The experiments considered a flat plat with adjustable steps and cavities at two different angles of attack and local Mach numbers of 6.3 and 8.5. It was observed that the heat flux on the downstream step was higher than the heat flux to the upstream step, since the forward-facing step acts as a stagnation region for the reattaching shear layer. In addition, relatively low heating rates were noticed for open cavity flows; however, much higher heating rates were observed on the cavity floor for closed cavity flow.

A theoretical analysis of the cavity geometry effect on the boundary layer and heat transfer was performed by Hodgson [52]. In this study, the author showed that the cavity depth has no effect on the heat transfer rate to the downstream wall and as the cavity depth is increased, the floor is subjected lower convective heat loads. Furthermore, for small cavities exposed to thick boundary layers the streamline velocity is proportional to the width to the power of 1/3; and the heat transfer rate for a given depth-to-length ratio is proportional to the width to the power of 1/4.

Based on the available literature [61–63], high speed flows over cavities may be

classified in four types. These four types appear to be primarily a function of the cavity length-to-depth ratio (L/D), as shown in Fig. 1.4 and are briefly described below:

- Gap (L/D $<$ 1): The first flow type occurs for very short or deep cavities. The induced shearing provokes the main flow to develop a column of counter rotating vortices inside the gap and hot spots occur when the vortices directionally align and impinge on the sidewall.

- Open cavity (1 $<$ L/D $<$ 10): The mainstream flow does not enter the cavity directly and the high pressures ahead of the rear face and low pressure region downstream of the front face cause the shear layer to flow over or bridge the cavity. A weak shock wave may form near the downstream lip as a result of the flow being compressed by the shear layer and heat fluxes slowly increase at this region. The pressure coefficients over the cavity floor are slightly positive and relatively uniform with a small adverse gradient occurring ahead of the rear face due the shear layer reattachment on the outer edge of this face.

- Transitional cavity (10 $<$ L/D $<$ 14): Typically characterised by unsteady flow behaviour since it alternates between an open and closed cavity. In this case, the shear layer turns through an angle to exit from the cavity coincident with the impingement shock and the exit shock collapsing into a single wave. A pressure plateau is observed in the reattachment region and a uniform pressure increase from the low values in the region aft of the front face with peak values on the rear face.

- Close cavity (L/D $>$ 14): In this case, the shear layer separates from the upstream cavity lip, reattaches at some point on the cavity floor, and then separates again before reaching the cavity rear face. Two distinct separation regions are formed, one downstream of the forward face and one upstream of the rear face. The cavity floor pressure distribution consists of low pressures in the separation region followed by an increase in pressure and pressure plateau occurring in the reattachment region. The local flow over the cavity front and rear faces are very similar to the flows over reward-facing and forward-facing steps, respectively.

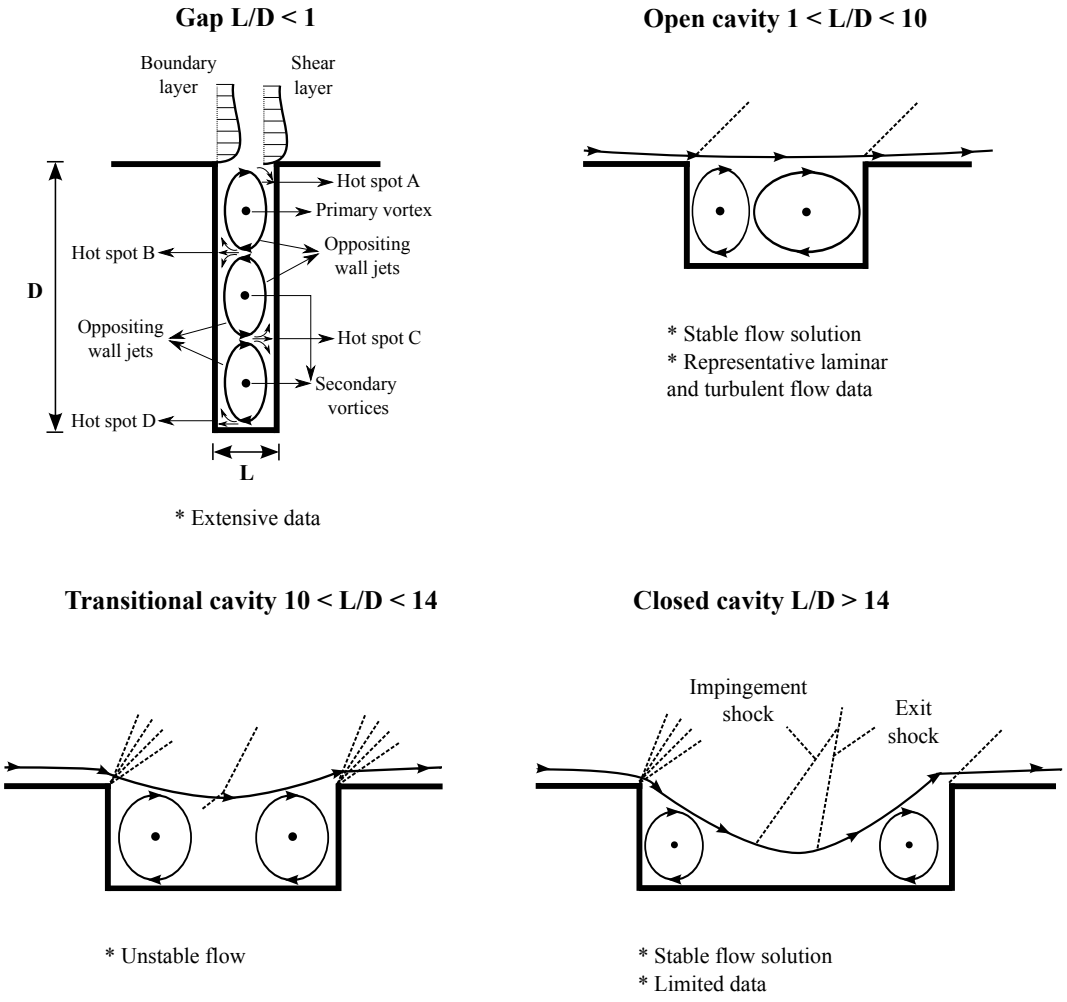

Figure 1.4: Cavity flowfield structure in the continuum regime [63].

In response to the Space Shuttle Columbia accident, a thermal protection system damage assessment, which involved the development and maintenance of physics-based computer models for TPS damages, was created following CAIB recommendations [7, 17]. The main idea was to detect possible surfaces damage, collect detailed images from the vehicle TPS when connected to the International Space Station and then perform fast simulations with simplified representations of the cavity damage site. As a result of their recommendations, a large number of research studies on cavity flows were performed [64–70].

Computational aerothermodynamic simulations of the space shuttle orbiter wind-side tile damage was performed by Pulsonetti and Woods [68]. The tile damage was simulated by a missing RCC panel and the results were compared with wind tunnel

data. According to the authors, the peak heating bump factors, defined as the local heating to a reference value upstream of the cavity, on the cavity floor for simulations were 67% larger than the peak wind tunnel values. On the downstream face of the cavity the flight simulation values were 60% larger than the wind tunnel values. The higher heating bump factors observed in the flight simulations were due to the larger driving potential in terms of energy entering the cavity.

Everhart *et al.* [70] conducted a combined computational and experimental study on open and closed cavity geometries to assess the Space Shuttle Columbia accident. For open cavities, no appreciable heat flux rise was observed at the cavity floor; however, significant heat augmentation was noticed when the cavity depth was increased. Closed cavities results were characterised by highly vortical regions promoting significant energy transfer not only to the cavity floor from the external stream, but also to the endwall and the surrounding side and downstream surfaces.

Cavity flow regimes are generally defined in terms of the length-to-depth (L/D) ratio. However, there are other parameters that can affect the exact value of L/D ratio. These parameters include Mach number, angle of attach, presence of chemical reactions, cavity width, and flow regimes which can vary from laminar to turbulent and from continuum to rarefied regimes. The complexity of cavity flows as well as the flowfield structure characterisation and pressure load and heating rates prediction are clearly highlighted in many areas of the previous research. In this way, further investigations are necessary for a better understanding of this problem under rarefied gas conditions.

1.3 Project objectives

The objective of this project is to investigate the impact of discontinuities or imperfections on the Orion Command Module surface during the atmospheric re-entry phase. A detailed study is performed in order to assess the impact of reacting and inert flows on the flowfield structure and on the aerodynamic surface quantities inside and around the TPS discontinuities. In this work, the flowfield structure is defined by the distribution of the primary properties, such as velocity, density, pressure, and the kinetic temperature, adjacent to the vehicle surfaces. Aerodynamic surface quantities are identified by

the heat flux, and the normal and tangential forces acting on the vehicle surface.

In the present study, discontinuities or imperfections are modelled by cavities situated in a hypersonic flow at a sufficiently high altitude where the appropriate mean free path becomes large for the use of the continuum hypothesis but not large enough for applying free molecular concept. In order to assess the overall performance of these cavities, a study related to the effects of the length-to-depth (L/D) ratios are explored. In pursuit of this goal, three-dimensional hypersonic cavity flows are be investigated by employing the direct simulation Monte Carlo (DSMC) method.

The application of the DSMC method has been aimed primarily at the transition flow regime, which is characterised by Knudsen numbers that are above the upper limit for the validity of the Navier-Stokes-Fourier equations but below the level at which the flow falls into the free molecular flow regime. In the transition flow regime, the aerodynamic heating and the forces acting on the vehicle surfaces are highly sensitive to the degree of rarefaction. Therefore, attempts are made to isolate the sensitivity of the thermal and pressure loads for different Knudsen numbers by changing the cavity L/D ratio.

The main objectives of this thesis are described below:

- Verification and validation of the *dsmcFoam* solver for rarefied hypersonic non-reacting flows over simple and complex geometries;
- Implementation of the Quantum-Kinetic (Q-K) chemistry model into the *dsmcFoam* code in order to improve the heating rates and pressure loads calculations during reentry phase;
- Verification and validation of the *dsmcFoam* solver for rarefied hypersonic reacting flows applied to real cases of atmospheric reentry;
- Study of thermal protection system discontinuities under the transitional regime. For the first time, multi-dimensional cavity flows have been investigated taking into account rarefied hypersonic reacting and non-reacting conditions flow;
- Categorisation of cavity length-to-depth (L/D) ratios for hypersonic flows in the transition-continuum regimes.

1.4 Thesis outline

In Chapter 2 the DSMC method used to perform all of the simulations in this thesis is discussed. The basic DSMC algorithm and the physical models implemented in the *dsmcFoam* code are described. The "Quantum Kinetic" chemistry model implementation in *dsmcFoam* is explained in detail.

Chapter 3 address the verification and validation of the *dsmcFoam* code for the intended research purpose. In the verification process, simulations are performed to certify that correct DSMC procedures are respected. For the validation procedure, *dsmcFoam* results for reacting and inert flows over simple and complex geometries are compared with experimental, analytic, and numerical results available in the current literature.

The flowfield structure and aerodynamic surface quantities for the Orion Command Module are studied in Chapter 4 using the assumption of a smooth surface heat shield. Next, surface discontinuities of different length-to-depth ratio are introduced at the Orion thermal protection system and their aerothermodynamic impact on the capsule are analysed.

The key findings of this research are presented in Chapter 5 together with a discussion of future work.

Chapter 2

Computational Method

2.1 The direct simulation Monte Carlo method

The direct simulation Monte Carlo method (DSMC) was almost exclusively developed by Bird [20] between 1960 and 1980 and has become one of the most important numerical techniques for solving rarefied gas flows in the transition regime. The DSMC method is based on physical concepts of rarefied gases and on the physical assumptions that form the basis for the derivation of the Boltzmann equation [39]. However, the DSMC method is not derived directly from the Boltzmann equation. As both, the DSMC method and the Boltzmann equation are based on classical kinetic theory, then the DSMC method is subject to the same restrictions of the Boltzmann equation, i.e., assumption of molecular chaos and restrictions related to dilute gases.

The DSMC method models the flow as a collection of particles or molecules. Each particle has a position, velocity and internal energy. The state of the particle is stored and modified with the time as the particles move, collide and interact with the surface in the simulated physical domain. The assumption of dilute gas (where the mean molecular diameter is much smaller than the mean molecular space in the gas) allows the molecular motion to be decoupled from the molecular collisions. The particles movement is modelled deterministically, while collisions are treated statistically. Since it is impossible to simulate the real number of particles in the computational domain, a small number of representative particles are used and each one represents a large number of real particles. Simulations can vary from thousands to millions of DSMC

simulators particles in rarefied flow problems.

A computational grid, representing the physical space to be investigated, is required for the method execution. Each cell provides a convenient reference for the sampling of the macroscopic gas properties and for the choice of the potential collision pairs.

The linear dimensions of the cells should be small in comparison with the length of the macroscopic flow gradients normal to the streamwise directions, which means that the cell dimensions should be the order of or smaller than the local mean free path [20, 71, 72]. An additional requirement of the DSMC method is related to the minimum number of simulated particles in the cells. As mentioned earlier, the DSMC method uses the a cell-based system for the sampling of the macroscopic properties and for the selection of collision partners. As the collision rate is a function of the number of particles in the cells, it is desirable that each cell has the largest possible number of particles. However, the possible number of collision partners is a function of the number of particles in each cell. In this scenario, the greater the number of particles, the greater is the number of possible collision pairs. As a result, it is necessary to determine the optimum number of particles in each cell; enough to promote statistical accuracy while maintaining realistic computational expenditure.

In order to solve this conflict, Bird [73] introduced the option of subdividing the cells into an arbitrary number of sub-cells for the selection of collision pairs. This procedure improves the accuracy of the method by ensuring that collisions occur only between near neighbour particles. Thus, it is desirable that each cell has a minimum number around 20 to 30 particles [20].

Another requirement of the DSMC method is the setting of an appropriate time step Δt. The trajectories of the particles in physical space are calculated under the assumption of the decoupling between the particle motion and the intermolecular collisions. The time step should be chosen to be sufficiently small in comparison with the local mean collision time [74, 75].

2.1.1 Basic algorithm of the DSMC method

The DSMC algorithm can be conveniently divided in four individual steps: (1) move particles over the time step Δt; (2) apply boundary conditions such as introducing new particles at inflow boundaries, removing particles at outflow boundaries, and processing reflections at solid boundaries; (3) sort particles into cells and calculate collisions; and (4) sample average particle information. Figure 2.1 show the basic algorithm followed by all DSMC solvers.

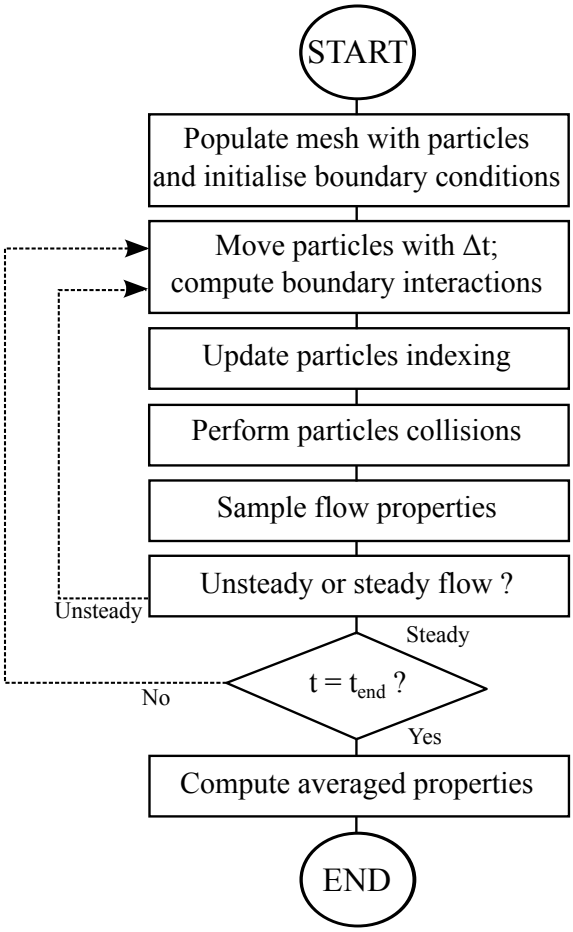

Figure 2.1: Flowchart of the standard DSMC algorithm.

The computational domain is initialised under the assumption of thermodynamic equilibrium based on the freestream conditions in the physical space. The density, temperature, velocity and internal energy of particles entering in the computational domain during each time step are specified according to a known boundary conditions.

The velocity of a simulated particle is assumed as a linear combination of the thermal velocity and the freestream velocity. The boundary conditions corresponding to the desired flow are imposed at the time zero. A steady flow is established after a sufficiently large time has elapsed, and the desired steady result is a time average of all values calculated after reaching steady state.

After defining the position and velocity, all particles are moved through distances appropriate to their velocity components and the size of the time step. After moving the particles, their location in the computational domain is determined. This can be obtained in different ways. For Cartesian grids, the new particle position is readily identified, and the destination cell is computed by using the indexing scheme defined by Bird [20]. For structured and unstructured grids, particle location schemes are outlined in Refs. [76–78] and for more complex computational grids, such as hexahedral or tetrahedral, different techniques can be used to determine the particle position [79–81]. Having defined the new location, appropriate actions are taken for particles crossing boundaries which represent solid surfaces, symmetry planes or inlets and outlets.

Particles leaving the computational domain are removed from the flow when the boundary is defined as vacuum and new particles are introduced into the computational domain for boundaries considered as flow patches. Collisions with surfaces can be treated as specular, diffuse or a combination of these two types. The treatment of particle-surface interaction requires the application of the conservation laws and the application of Maxwellian velocity distribution function. Such treatment allows the DSMC method to be extended to include physical effects such as chemical reactions, catalytic walls, radiation effects, and ionised flows without major changes in the basic algorithm.

After determining the new location of the particles, they should be indexed by cell location for the two subsequent steps: calculation of intermolecular collisions and sampling of the flowfield. For the selection and calculation of intermolecular collisions, each cell is defined in a index system such that all other particles in the cell can be assessed through a cross-reference list. An efficient indexing scheme was introduced by Bird [42] in the original DSMC algorithm.

In the next step, intermolecular collisions are considered in a probabilistic manner in

contrast to the deterministic treatment that characterised the ballistic motion. In doing so, several different collision modelling schemes have been formulated and applied in the DSMC method. Among them, the Time-Counter (TC) technique [42], Null-Collision (NC) technique [82, 83], No-Time-Counter (NTC) [84], and the generalised scheme [85] of the NTC technique. The NTC scheme proposed by Bird [84] is the dominant scheme in the DSMC approach and will be described in further detail in the following sections.

The collision procedure takes place in a cell-by-cell basis. Therefore, the time step, the cell volume and the number of particles on the cell, are parameters that determine the number of possible pairs of candidate particles in the collision process. The pairs of particles are chosen randomly with the restriction that the mean separation between them be a fraction of the mean free path. This restriction is imposed by selecting collision pairs from the list of particles in the subcell. The DSMC method evaluates individual collisions on a probabilistic basis, conserving mass, momentum and energy during the collisions.

Finally, the current description is completed by considering the sampling process of the macroscopic flow properties. These properties density, velocity, temperature and pressure are computed by appropriate average of the microscopic state of particles in each cell.

2.1.2 Physical models of the DSMC method

The most frequently used physical models implemented in DSMC calculations for hypersonic reentry flows are presented in this section. The main goal is to describe the basics ideas of the physical phenomena modelling including boundary conditions, molecular and collision models, rotational and vibrational energy exchange, and chemical reactions.

Boundary conditions

In gas dynamic problems there are basically two types of boundary conditions: those specified by the freestream macroscopic properties, and those defined by the physical behaviour of a solid surface that interacts with the particles.

In the molecular-discrete approach, the first boundary type deals with the inlet and

outlet of particles through a given boundary. The main idea of the inlet procedure is to define the flux and thermal state of the molecules that are moving into the simulated domain. Particles are inserted at the inlet boundaries based on the equilibrium Maxwellian number flux across a boundary $\dot{N}_{in}$:

$$\dot{N}_{in} = \frac{n_{in}}{\beta(2\pi^{1/2})}[exp(-s^2 cos^2\theta) + \pi^{1/2} s\ cos\theta(1 + erf(s\ cos\theta))], \tag{2.1}$$

with

$$\beta = \left(\frac{m}{2k_B T_{in}}\right)^{1/2}, \tag{2.2}$$

and

$$s = \mathbf{c}_{o_{in}}\beta \tag{2.3}$$

where the subscript in denotes properties at an inlet and θ is the angle between the velocity vector $\mathbf{c}_{o_{in}}$ and the inlet.

The outlet procedure simply consists in removing the particles that leave the domain. Obviously, both procedures must be consistent with the desired flow conditions.

The second boundary type treats the gas-surface interactions, which can modify the thermal state of the impinging particles. The influence of the gas-surface interaction model on the aerodynamic forces and heat transfer increases significantly as the gas rarefaction increases and plays an important role in hypersonic aerothermodynamics calculations [86].

The first gas-surface interaction model for kinetic theory was proposed by Maxwell in 1879 [87]. In this model, two types of interactions are considered: specular and diffuse. Specular reflection is perfectly elastic with the particle velocity component normal to the surface being reversed, while those parallel to the surface remain unchanged. Thus, the angle of reflection is the same as the angle of incidence. Usually, the specular boundary condition is considered to represent a perfectly smooth surface or symmetry plane.

A diffuse reflection represents a microscopically rough surface in which the particle's post-interaction velocity is not related to its pre-interaction velocity. The post-

interaction velocity is computed based on thermal equilibrium with the local surface temperature and the direction of the velocity vector is chosen with equal probability in all directions according to the Maxwellian distribution function. In the diffuse gas-surface interaction model just a single accommodation coefficient is required and the scattering angle is independent of the particle's incoming angle. A schematic view of the diffuse and specular gas-surface interactions is shown in Fig. 2.2 (a).

Accommodation coefficients depend upon the fluid, surface material and surface roughness. Theoretical and experimental works have shown [88–90] that when particles are reflected from a solid surface the show evidence of a preferential direction of reflection resulting in an offset elliptical scattering distribution as shown in Fig. 2.2 (b). This behaviour is poorly represented by the Maxwell model and in order circumvent this issue, a phenomenological model was proposed by Cercignani and Lampis in 1971 [91].

The Cercignani-Lampis (CL) model is based on the definition of the coefficients α_n and α_t that represent the accommodation coefficients for the kinetic energy associated with the normal and tangential components of velocity. In addition, the scattering angle is always a function of the incoming particle angle. This model is relatively simple and has been shown a good agreement when compared with experimental results [92]. A DSMC application of the CL model was proposed by Lord [93] in 1990 through a relatively simple algorithm. In addition, Lord later extended the CLL model to account for rotational and vibrational energy exchange at the surface along with the capability to have diffuse reflections with incomplete energy accommodation [94, 95]. The CLL model is currently implemented in the *dsmcFoam* code and the validation process is available in Ref. [96].

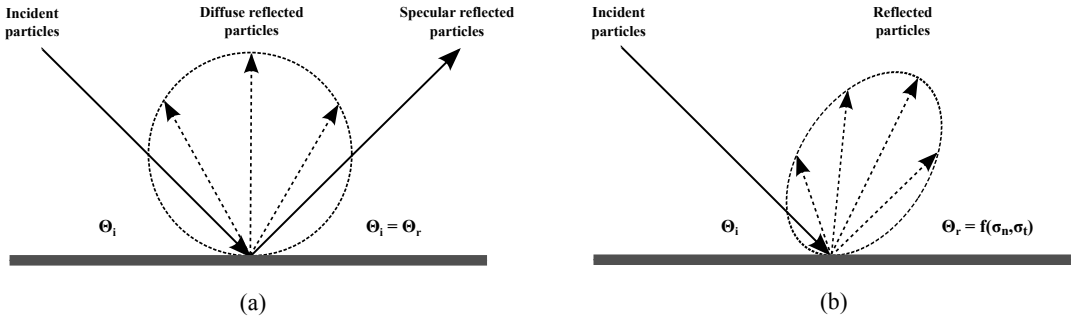

Figure 2.2: (a) Maxwell's diffuse and specular gas-surface interaction models, and (b) Cercignani-Lampis-Lord gas-surface interaction model.

Molecular model

The particle's behaviour during the collision process depends upon the choice of the intermolecular force field. A simple molecular model that is accurate enough for the majority of hypersonic calculations is the inverse power law. In this model, the intermolecular force is modelled as the inverse of the repulsive power force as follows,

$$F_n = \frac{C}{r^{\eta}}, \tag{2.4}$$

where r is the distance between the particles involved in the collision and C and η are constants. In addition, the model proposed in Eq. 2.4 corresponds to a Maxwellian gas for $\eta = 5$ and the Hard Sphere model (HS) is obtained by setting $\eta \to \infty$. In hypersonic flow simulations, millions or billions of particles/molecules are considered and a simple molecular model is required for engineering purposes. In this scenario, the HS model is the simplest and most computationally-efficient alternative.

In the HS molecular model, the collision cross section is invariant for a single gas specie. The scattering angle is isotropic and the post-collision relative velocity is sampled to form a uniform solid angle distribution. Nevertheless, the HS molecular model is not realistic, since the total collision cross-section σ_T does not depend on the relative velocity of the pair of particles involved in the collision process. When the intermolecular potential law is given by Eq. 2.4, the theory of Chapman-Enskog provides a direct relationship between the coefficient of viscosity and the gas temperature given by,

$$\mu \propto T^{\omega}, \tag{2.5}$$

where $\omega = 1/2(\eta+3)/(\eta\text{-}1)$ and η represents a free parameter.

According to Eq. 2.5, the coefficient of viscosity has a fixed temperature exponent. This exponent is 1 for the Maxwell model and 0.5 for the HS model. HS and Maxwell models are applied for theoretical gases that can be considered as the limiting cases for the behaviour of a real gas where the temperature exponent ranges from 0.6 to 0.9.

Alternative molecular models, based on the HS model, have been proposed. These models have proven very successful at computationally efficiently reproducing the correct viscosity of a gas. The first alternative model was the Variable Hard Sphere (VHS) model proposed by Bird [97]. The VHS model treats particles as "hard-spheres" with respect to the distribution of the scattering angle, i.e., all directions are equally possible for the post-collision velocity in a reference frame based on the centre of mass. Moreover, the total cross-section σ_T varies with the relative speed of colliding particles. The VHS model has been the most popular molecular model used in DSMC applications.

In the VHS model, the collision cross-section is defined as,

$$\sigma \equiv \pi d^2 \propto \left(\frac{1}{2} m_r c_r^2\right)^{-\omega}, \tag{2.6}$$

where m_r represents the reduced mass, c_r the relative speed of colliding particles and ω an exponent to be defined subsequently.

The collision cross section σ varies with temperature and the relative speed between the particles,

$$\sigma \propto c_r^{-4(\eta-1)} \propto T^{-2/(\eta-1)}. \tag{2.7}$$

A comparison of Eqs. 2.6 and 2.7 shows that ω is related to the exponent of the inverse power law molecular force as follows:

$$\omega = \frac{2}{\eta - 1}. \tag{2.8}$$

where ω is equal to zero for the HS model, 1/4 for the inverse power law model, and 1/2 for the Maxwell model.

For a gas in thermodynamic equilibrium, the collision cross section is inversely proportional to the temperature to the power ω,

$$\sigma = \sigma_{ref}\left(\frac{T}{T_{ref}}\right)^{-\omega}. \tag{2.9}$$

The reference value for the cross-section is based on a reference temperature T_{ref}. For a non-equilibrium gas the collision energy should be used, and Eq. 2.6 may be written as:

$$\sigma = \sigma_{ref}\left(\frac{c_r^2}{c_{r_{ref}}^2}\right)^{-\omega}. \tag{2.10}$$

The mean collision energy in an equilibrium gas at temperature T is:

$$\frac{1}{2}\overline{m_r c_r^2} = 2\left(\frac{\eta-2}{\eta-1}\right)k_B T = (2-\omega)\kappa T, \tag{2.11}$$

where where k_B is the Boltzmann constant. The Eqs. 2.10 and 2.11 can then be combined as follows

$$\sigma = \sigma_{ref}\left(\frac{m_r c_r^2}{2(2-\omega)\kappa T_{ref}}\right)^{-\omega}. \tag{2.12}$$

Koura and Matsumoto [98, 99] further improved the VHS model and introduced the Variable Soft Sphere (VSS) molecular model. The VSS model considers anisotropic post-collision scattering. The second parameter introduced by the post-collision scattering dynamic in the VSS model is chosen in order to reproduce correctly the real viscosity and diffusion coefficients of the gases. Hassan and Hash [100] introduced the Generalized Hard Sphere (GHS) molecular model. The GHS molecular model takes into account both attractive and repulsive parts of the particle-particle interaction. Since the GHS model can reproduce the effects of the attractive portion of an interaction potential, then the model is suitable to simulate low temperature flows that are dominated by attractive collisions [101, 102] and are diffusion-driven.

Collision model

There are a number of techniques for simulating collisions in the DSMC method. Among them, the Time Counter (TC) [42], Null Collision (NC) [82, 83], NTC method [84], and the Generalised Scheme [85]. Bird's NTC technique is the most widely used collision scheme and it will be discussed here.

The establishment of the correct collision rate is essential in the DSMC approach. From the kinetic theory, it can be shown that the number of collisions (N_{coll}) pairs to be simulated in a cell over the time step $\triangle$t is as follows:

$$N_{coll} = \frac{1}{2}\frac{Nn(\overline{\sigma_T c_r}) \triangle t}{V_c}, \tag{2.13}$$

where n is the number density, N is the number of particles in the cell, σ_T is the collision cross section, and c_r is the relative velocity.

In order to determine the total number of collisions during the time step $\triangle$t, the average product of the mean relative velocity c_r and the collision cross section σ_T must be calculated for all possible collision pairs. For such calculations, the numerical code that employs this procedure would have a computational time proportional to N^2. In order to overcome this issue, Bird [42] introduced the parameter $(\sigma_T c_r)_{max}$ where the subscript max denotes the largest value for the product in the cell and it should be updated during a binary collision if the real product $\sigma_T c_r$ were greater than $(\sigma_T c_r)_{max}$. In addition, the parameter $(\sigma_T c_r)_{max}$ is used to determine a real collision according to the following operations:

1. A pair of particles is randomly chosen within a cell volume;
2. The product of the mean relative velocity c_r and the collision cross σ_T for the colliding pair is calculated;
3. If the product $\sigma_T c_r$ is greater than $(\sigma_T c_r)_{max}$, the maximum value is updated;
4. The probability of a collision occuring is given by:

$$P_{coll} = \frac{\sigma_T c_r}{(\sigma_T c_r)_{max}} \tag{2.14}$$

if the probability P_{coll} is greater than R_f, then the pair of particles is accepted for collision, where R_f is a uniform random number ranging from 0 to 1. Otherwise, a new pair is randomly chosen and the procedure is repeated. This acceptance-rejection method to select the collision pair of particles is described in detail by Bird [20].

5. If the pair of particles is accepted for the collision process, then cell time is advanced by an increment δt by setting $N_{coll} = 1$,

$$\delta t = \frac{2}{N n \sigma_T c_r}; \tag{2.15}$$

6. The number of collisions are calculated in the cell until the sum of δt is slightly larger than the time step $\triangle$t. The procedure describe above is called Time Counter (TC) and it was proposed by Bird in 1976 [42].

Despite reproducing the correct non-equilibrium collision rate with an optimal computational performance, the TC technique can lead to some problems under extreme nonequilibrium conditions, such as in strong shock waves. The acceptance of low probability collisions, i.e., pairs with a small value of $\sigma_T c_r$, results in large δt values. Consequently, the time increment sum can exceed $\triangle$t by unacceptable amounts. From a computational aspect, as reported by Baganoff and McDonald [103], the total number of simulated collisions may be very different from one cell to another. Besides, this number is unknown until time step $\triangle$t is determined. Such an implementation makes the numerical vectorisation of the collision procedure a difficult task.

In order to overcome this problem, Bird [84] proposed the collision model named No Timer Counter (NTC). NTC and TC techniques have the same selection rule for the collision pair, which is based on the acceptance-rejection method; however, in the NTC technique the maximum number N_{coll} of collisions to be selected over $\triangle$t in a cell is set before the selection of the colliding pairs. In this new collision method, the time count is replaced by an explicit dependence of N_{coll} on the time step, i.e., the number of collisions does not dependent on the choice of pairs or particular values of $\sigma_T c_r$. In this new approach, this number of collisions is given by:

$$N_{coll} = \frac{1}{2}\frac{N\overline{N}F_N(\sigma_T c_r)_{max} \triangle t}{V_c}, \tag{2.16}$$

where F_N is the number of real molecules represented by each simulated molecule, N is the number of particles within a cell, and $\overline{N}$ is a mean value of N. The collision probability for each chosen pair is given by Eq. 2.14. Additional information about the NTC method are available in Ref. [20].

Usually, in the dilute gases, the intermolecular collisions are considered as a binary process. In addition, an elastic collision is defined as one in which there is no exchange of energy between the translational and internal modes. The pre-collision velocities of two colliding particles may be denoted by $\mathbf{c}_1$ and $\mathbf{c}_2$ as shown in Fig. 2.3. If the physical properties and trajectories of these particles are known, the post-collision velocities $\mathbf{c}_1^*$ and $\mathbf{c}_2^*$ can be determined. In order to determine the post-collision velocities, the linear momentum and energy must be conserved in the during collision,

$$m_1\mathbf{c}_1 + m_2\mathbf{c}_2 = m_1\mathbf{c}_1^* + m_2\mathbf{c}_2^* = (m_1 + m_2)\mathbf{c}_m, \tag{2.17}$$

$$m_1 c_1^2 + m_2 c_2^2 = m_1 c_1^{*2} + m_2 c_2^{*2}, \tag{2.18}$$

where m_1 and m_2 are the mass of the two particles selected for the collision process, and $\mathbf{c}_m$ is the velocity of the centre of mass of the two particles as follows,

$$\mathbf{c}_m = \frac{m_1\mathbf{c}_1 + m_2\mathbf{c}_2}{m_1 + m_2} = \frac{m_1\mathbf{c}_1^* + m_2\mathbf{c}_2^*}{m_1 + m_1}. \tag{2.19}$$

Equation 2.17 shows that the velocity of the centre of mass does not change with the collision process. In this way, the pre- and post-collision values of the relative velocity between the particles can be defined by:

$$\mathbf{c}_r = \mathbf{c}_1 - \mathbf{c}_2 \qquad \mathbf{c}_r^* = \mathbf{c}_1^* - \mathbf{c}_2^*, \tag{2.20}$$

Equations 2.17 and 2.20 may be combined to provide the following expressions:

$$\mathbf{c}_1 = \mathbf{c}_m + \frac{m_2}{m_1 + m_2}\mathbf{c}_r \qquad \mathbf{c}_2 = \mathbf{c}_m - \frac{m_2}{m_1 + m_2}\mathbf{c}_r. \tag{2.21}$$

Similarly, the post-collision components are defined by:

$$\mathbf{c}_1^* = \mathbf{c}_m + \frac{m_2}{m_1 + m_2}\mathbf{c}_r^* \qquad \mathbf{c}_2^* = \mathbf{c}_m - \frac{m_2}{m_1 + m_2}\mathbf{c}_r^*. \tag{2.22}$$

It is assumed that particles are centres of force, i.e., the force between them acts only between their centres. As a result, throughout the collision, the intermolecular force and trajectories remain in the same plane that was previously determined by the pre-collision velocities.

The energy conservation equation, Eq. 2.18 can be rewritten by using Eqs. 2.21 and 2.22 as follows,

$$m_1 c_1^2 + m_2 c_2^2 = (m_1 + m_2)c_m^2 + m_r c_r^2, \tag{2.23}$$

$$m_1 c_1^{*2} + m_2 c_2^{*2} = (m_1 + m_2)c_m^2 + m_r c_r^{*2}, \tag{2.24}$$

where m_r , called the reduced mass, is given by,

$$m_r = \frac{m_1 m_2}{m_1 + m_2}. \tag{2.25}$$

A comparison between the Eqs. 2.23 and 2.24 with Eq. 2.18 shows that the magnitude of the relative velocity does not change in the collision process, i.e.,

$$\mathbf{c}_r^* = \mathbf{c}_r. \tag{2.26}$$

Since $\mathbf{c}_m$ and $\mathbf{c}_r$ can be calculated from the pre-collision velocities, the determination of post-collision velocities reduces the calculation to a determination of the post-collision relative velocity vector.. If $\mathbf{F}$ is the force between two spherically symmetric point centres of force of between the particles, and $\mathbf{r}_1$ and $\mathbf{r}_2$ are their position vectors, then the equations of motion of the particles are as follows,

$$m_1 \ddot{\mathbf{r}}_1 = \mathbf{F}, \tag{2.27}$$

$$m_2 \ddot{\mathbf{r}}_2 = -\mathbf{F}, \tag{2.28}$$

Combining last two equations,

$$m_1 m_2(\ddot{\mathbf{r}}_1 - \ddot{\mathbf{r}}_2) = (m_1 + m_2)\mathbf{F} \tag{2.29}$$

Considering relative velocity as $\mathbf{c}_r = \dot{\mathbf{r}}_1$ - $\dot{\mathbf{r}}_2 = \dot{\mathbf{r}}$, then

$$m_r \dot{\mathbf{r}} = \mathbf{F} \tag{2.30}$$

The motion of the particle of mass m_1 relative to the particle of mass m_2 is equivalent to the motion of the particle of mass m_r relative to the fixed centre of force. For completeness, the results discussed above are summarised in Fig. 2.3. Based on this figure, the transformation from the centre of mass coordinate system changes the three-dimensional trajectories into two-dimensional trajectories, which are symmetrical about the apse line AA'.

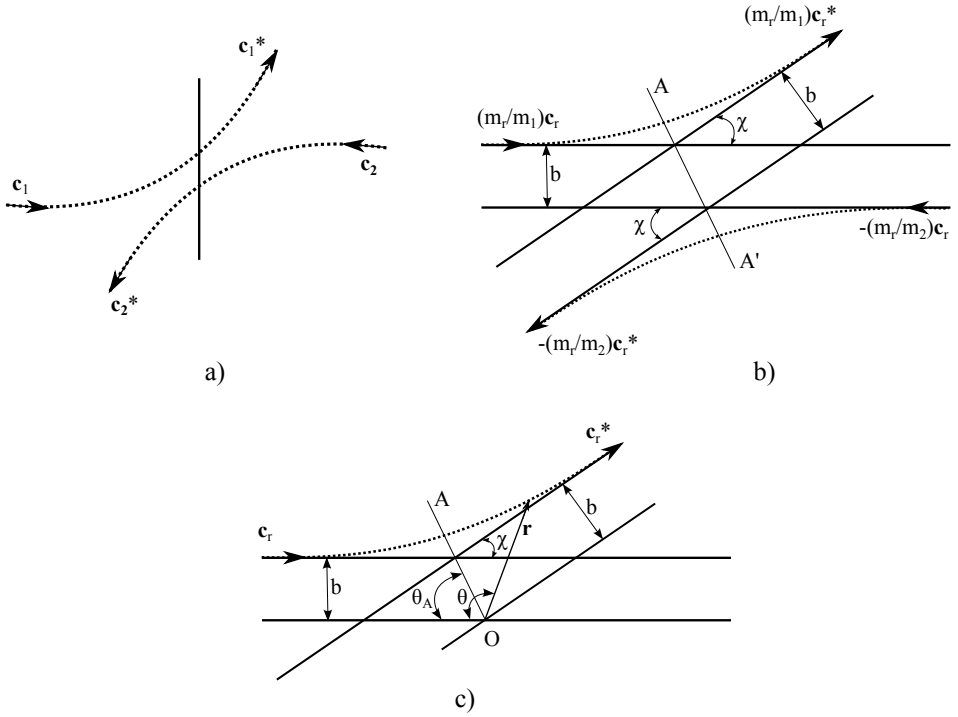

Figure 2.3: Schematic of the binary collisions. a) Representation of a planar collision. b) Binary collision in the center of mass frame of reference, and c) Interaction of reduced mass particle with a fixed scattering centre. [20].

The trajectories of the two particles are reduced to one in the further transformation to the reduced mass frame of reference and this trajectory remains symmetrical about

the transformed apse line which passes through the scattering centre O. This symmetry reflects the equation symmetry with respect to the pre-collision and post-collision velocities.

Rotational and vibrational energy exchange

The thermal nonequilibrium may have a significant influence on the amount of chemical reactions produced during atmospheric entry. In this scenario, it is of great importance that the model used in the energy exchange between kinetic and internal modes be physically realistic. For polyatomic gases, the energy exchange can not be computed accurately using a simple collision model.

The internal energy transfer between the various modes is usually implemented into the DSMC method by the phenomenological model introduced by Borgnakke and Larsen [104]. In this model, the probability of an inelastic collision determines the rate at which energy is transferred between translational and rotational mode after an inelastic collision. A fraction φ of the translational collisions are assumed to be inelastic, and the rest of collisions (1 - φ) are considered as elastic. The fraction φ can be interpreted as the average probability of the energy exchange between rotational or vibrational modes for translational collisions.

This average probability can be determined from measurements of relaxation times. The relaxation time is a function of local flow properties and may be related to the relaxation number (or collision number) Z. The relaxation or collision number Z is usually defined by:

$$Z = \frac{\tau}{\tau_c}, \tag{2.31}$$

where τ is the relaxation time τ and τ_c is the mean collision time. The collision number is the average number of molecular collisions that are required for a particular mode to attain equilibrium energy. Therefore, given this number, the average probability φ for each mode in a given collision is conveniently defined as,

$$\varphi = \frac{1}{Z}. \tag{2.32}$$

Usually, DSMC calculations employ the rotational collision number $Z_{rot} = 5$. In other words, it means that, on average, the rotational energy relaxation occurs once every five collisions. In general, this is a good approximation for engineering problems; however, more realistic models for rotational collision number as a function of the translational temperature or translational energy have been proposed [105–107].

Lumpkin *etal.* [108] have noted that the mechanisms of energy transfer used in DSMC calculations affect the energy transfer rate. According to them, the value of the collision number used in the DSMC should be approximately half of that determined experimentally and employed in a continuum computations. In this scenario, the following equation should be applied:

$$Z_{rot}^{DSMC} = \frac{Z_{rot}^{cont}}{\left(1 + \frac{\zeta_{rot}}{\zeta_{tra}}\right)}, \tag{2.33}$$

where ζ_{rot} and ζ_{tra} are the degrees of freedom for rotational and translational energy, respectively.

The vibrational modes of a gas are activated when the particles that compose the fluid are sufficiently excited. This situation may occurs in the presence of strong compressibility effects and high temperatures regions provoked by shock waves. In DSMC calculations, it is commonly accepted that the vibrational energy can only assume discrete quantum levels, as proposed by Haas *etal.* [109] and Bergemann and Boyd [110]. In the present account, the vibrational energy redistribution occurs before rotational and translational energy exchange and a serial application of the quantum Larsen-Borgnakke method is considered here. In addition, as two particles p and q selected for collisions have no knowledge of the surrounding temperature; avoiding in this way the use of the macroscopic temperature, a "quantised collision temperature", T_c, based on the collision energy of the particle pair is defined as:

$$T_c = \frac{i_{max}\ \Theta_v}{\frac{7}{2} - \omega}, \tag{2.34}$$

where

$$i_{max} = \left\lfloor \frac{E_c}{k_B \Theta_v} \right\rfloor, \tag{2.35}$$

and $\lfloor ... \rfloor$ denotes truncation, i_{max} is the maximum quantum level available to the particle, Θ_v represents characteristic vibrational temperature of the species in question, k_B is the Boltzmann constant, ω is the temperature exponent of viscosity, E_c is the sum of the relative translational energy of the colliding pair and the pre-collision vibrational energy of the particle under consideration, i.e.

$$E_c = \varepsilon_{tra,pq} + \varepsilon_{v,p}. \tag{2.36}$$

The vibrational collision number Z_v can then be calculated [111] as:

$$Z_{vib} = \left(\frac{\Theta_d}{T_c}\right)^{\omega} \left[Z_{ref} \left(\frac{\Theta_d}{T_{Z_{ref}}} \right)^{-\omega} \right] exp\left[\left(\frac{\Theta_d}{T_c} \right)^{\frac{1}{3}} - 1 \right] / \left[\left(\frac{\Theta_d}{T_{Z_{ref}}} \right)^{\frac{1}{3}} - 1 \right], \tag{2.37}$$

where Θ_d represents the characteristic dissociation temperature, and Z_{ref} is the vibrational collision number at a reference temperature $\mathrm{T}_{Z_{ref}}$, which is usually taken to be the characteristic vibrational temperature, Θ_v, as cited in Ref. [112],

$$E_c = \left(\frac{C_1}{T_{Zref}^{\omega}} \right) exp\Big(C_2 T_{Zref}^{-1/3} \Big), \tag{2.38}$$

where C_1 and C_2 are constants which can be found in Appendix A of Ref. [20], and $\mathrm{T}_{Z_{ref}}$ is set as Θ_v.

Once the vibrational collision number has been calculated, the particle is tested for vibrational energy exchange and is accepted if

$$\frac{1}{Z_{vib}} > R_f, \tag{2.39}$$

where R_f is a random number between 0 and 1. An integer post-collision vibrational quantum level i^* is chosen uniformly between 0 and the maximum possible level i^*_{max} and the acceptance-rejection method is used to select a value of i^* using a quantised version of the Larsen-Borgnakke probability ratio [110]:

$$\frac{P}{P_{max}} = \left(1 - \frac{i^* k_B \Theta_v}{E_c} \right)^{3/2-\omega_{pq}}, \tag{2.40}$$

where ω_{pq} is the average viscosity exponent of the collision pair p and q. The total energy of the colliding pair is reduced accordingly and particle p is then considered for

relaxation into rotational and translational modes using the standard Larsen-Borgnakke method.

When particles are initialised using dsmcInitialise, introduced at a freestream boundary, or reflected at a diffuse surface, they must be assigned a vibrational energy. First, a quantum level is chosen by analogy to how rotational energy is chosen for a diatomic molecule, i.e.

$$i = \left\lfloor \frac{-ln(R_f)T_{vib}}{\Theta_v} \right\rfloor, \tag{2.41}$$

where T_{vib} is the vibrational temperature, and then the vibrational energy of the particle is assigned from the relation

$$\varepsilon_{vib} = ik_B\Theta_v. \tag{2.42}$$

In order to verify the current implementation of the vibrational energy exchange in the *dsmcFoam* code, a test case involving relaxation to equilibrium is considered. In this test case, similar to that used by Bird [113], an adiabatic box is filled with 1.2 million DSMC nitrogen particles with translational and rotational temperatures at 20,000 K and no energy in the vibrational mode. The particles were allowed to collide and transfer energy to the vibrational mode which the equipartition was achieved at a temperature of 14,720 K. The *dsmcFoam* results were compared with those obtained in the DS2V code [113] and very good agreement between both codes was achieved. Further information about this test case is available in Ref. [114].

Chemical reactions

Considerable number of chemistry models relevant for hypersonic aerothermodynamics have been developed as Rebick and Levine [115] model, vibrational bias model [116], threshold line model [117], maximum entropy model [118], and the total collision energy model (TCE) model [20, 119, 120].

Introduced by Bird [119], the TCE model became the most commonly used chemistry model for DSMC simulations of rarefied hypersonic reacting flows. This model is based on a modified Arrhenius rate coefficient of the form:

$$C = aT^b exp\left(\frac{\varepsilon_{act}}{k_B T}\right), \tag{2.43}$$

where a and b are constants, and ε_{act} is the activation energy of the reaction.

The probability of a reaction, P, is obtained by integrating the equilibrium distribution function for the total collision energy and equating it to the chemical rate coefficient,

$$C = \langle \sigma c_r \rangle \int_{\varepsilon_{act}}^{\infty} P(\varepsilon_c)\ f_B(\varepsilon_c)\ d\varepsilon_c, \tag{2.44}$$

where σ is the elastic cross section, c_r is the relative velocity, and $\mathrm{f}_B(\varepsilon_c)$ is the equilibrium Boltzmann distribution function for the total collision energy, ε_c. The total collision energy consists of the translational collision energy, and the sum of the rotational and vibrational energies of the two colliding particles considered for a reaction. In this case, the reaction probability for the TCE model is given by:

$$P_{TCE} = A\frac{(\varepsilon_c - \varepsilon_{act})^{\psi}}{(\varepsilon_c)^{\chi}}, \tag{2.45}$$

where,

$$A = \frac{a\epsilon\sqrt{\frac{1}{2}m_r\pi}}{\sigma_{ref}[(2-\omega)k_B T_{ref}]^{\omega} k_B^b} \frac{\Gamma(\zeta + 2 - \omega)}{\Gamma(2-\omega)\Gamma(\zeta + b + \frac{3}{2})}$$

$$= B\frac{\Gamma(\zeta + 2 - \omega)}{\Gamma(2-\omega)\Gamma\left(\zeta + b + \frac{3}{2}\right)}, \tag{2.46}$$

the parameters ω, σ_{ref}, and T_{ref} are employed in the Variable Hard Sphere collision model [20], ζ the average number of rotational and vibrational degrees of freedom, and m_r is the reduce mass of two colliding particles. In addition, $\epsilon = 1$ for collisions of two particles of the same species, and $\epsilon = 1/2$ for different species.

The exponents in Eq. 2.46 is given by:

$$\psi = b + \frac{1}{2} + \zeta, \tag{2.47}$$

and,

$$\chi = 1 + \zeta - \omega. \tag{2.48}$$

The TCE model was extended [121, 122] to take into account the coupling between vibrational energy and the collision-induced dissociation. This model extension, called Vibrationally Favored Dissociation (VFD), includes an additional dependence of the reaction probability on the vibrational energy of the reactant particle. In addition, the results using the TCE and VFD model when compared with experimental data for reacting shock waves of nitrogen [121] and oxygen dissociation [122] showed a very good agreement.

The Total Collision Energy model is highly phenomenological and employs equilibrium kinetic theory to convert the conventional Arrhenius rate coefficients, defined in terms of macroscopic gas temperature, to collision probabilities which are a function of the collision energy at microscopic level. In addition, this model is dependent on the availability of experimental data to fit the Arrhenius rate coefficient equation.

DSMC being a particle-based method, it is of fundamental importance to develop a molecular level chemistry model that predicts equilibrium and non-equilibrium reaction rates using only kinetic theory and fundamental molecular properties. In doing so, Bird recently proposed a chemical reactions model based solely on the fundamental properties of the two colliding particles, i.e., total collision energy, the quantised vibrational levels, and the molecular dissociation energies. These models link chemical reaction and cross sections to the energy exchange process and the probability of transition between vibrational energy states. The Larsen-Borgnakke [104] procedures and the principle of microscopic reversibility are used to derive a simple model for recombination and reverse reactions. Called "quantum-kinetic", this DSMC chemistry model has been developed over the past 5 years [111, 123–127] and its implementation in the *dsmcFoam* code is presented as follows.

The "Quantum-Kinetic chemistry model (Q-K)

The vibrational energy plays a key role in the Q-K chemistry model and can only assume discrete quantum values [109, 110]. Having implemented the quantised vibrational energy into the *dsmcFoam* code (Section 2.1.2), the next step is the implementation of a 5-species reacting air model. In this model, the molecular species nitrogen (N_2) and oxygen (O_2), nitric oxide (NO), and nitrogen (N) and oxygen (O) atoms are considered and four different reactions types can be defined, as follow:

- Dissociation type I: $AB + CD \rightarrow A + B + CD$
- Dissociation type II: $AB + C \rightarrow A + B + C$
- Molecular recombination: $A + B + C \rightarrow AB + C$
- Exchange reactions: $AB + C \rightarrow AC + B$

where A, B, C, and D are atomic species (O and N), AB, CD, and AC are molecules (O_2, N_2, and NO).

In the simulation of high temperature, low density air, the chemical processes are described by 19 reactions given in Table 2.1, where molecular recombination is neglected. According to Bird [126], the condition for recombination in a collision between two molecules (or atoms) is that there is another molecule (or atom) within a ternary collision volume. Since the mean free path (λ_∞) at high altitudes is comparable to the re-entry capsule size, the probability of a ternary collision is very low. Because recombination is only an important mechanism at relatively high density, these reactions are omitted from hypersonic *dsmcFoam* analyses.

Table 2.1: Chemical reaction list and equivalent Arrhenius rate variables for the 5-species air model in *dsmcFoam*.

N^o	Reaction	Heat of formation $\times 10^{-19}$ J	C_1	C_2	Activation energy $\times 10^{-19}$ J
1	$O_2 + N \rightarrow O + O + N$	8.197	1.1×10^{-10}	-1	8.197
2	$O_2 + NO \rightarrow O + O + NO$	8.197	1.1×10^{-10}	-1	8.197
3	$O_2 + N_2 \rightarrow O + O + N_2$	8.197	1.3×10^{-10}	-1	8.197
4	$O_2 + O_2 \rightarrow O + O + O_2$	8.197	5.33×10^{-11}	-1	8.197
5	$O_2 + O \rightarrow O + O + O$	8.197	1.5×10^{-10}	-1.05	8.197
6	$N_2 + O \rightarrow N + N + O$	15.67	4.0×10^{-12}	-0.54	15.67
7	$N_2 + O_2 \rightarrow N + N + O_2$	15.67	1.5×10^{-11}	-0.68	15.67
8	$N_2 + NO \rightarrow N + N + NO$	15.67	1.5×10^{-11}	-0.68	15.67
9	$N_2 + N_2 \rightarrow N + N + N_2$	15.67	4.1×10^{-12}	-0.62	15.67
10	$N_2 + N \rightarrow N + N + N$	15.67	1.0×10^{-11}	-0.68	15.67
11	$NO + N_2 \rightarrow N + O + N_2$	10.43	2.1×10^{-10}	-1	10.43
12	$NO + O_2 \rightarrow N + O + O_2$	10.43	2.0×10^{-10}	-1	10.43
13	$NO + NO \rightarrow N + O + NO$	10.43	1.0×10^{-10}	-1	10.43
14	$NO + O \rightarrow N + O + O$	10.43	4.0×10^{-10}	-1.1	10.43
15	$NO + N \rightarrow N + O + N$	10.43	4.0×10^{-10}	-1.1	10.43
16	$NO + O \rightarrow O_2 + N$	2.719	1.1×10^{-18}	0.34	2.719
17	$N_2 + O \rightarrow NO + N$	5.175	1.0×10^{-16}	0	5.175
18	$O_2 + N \rightarrow NO + O$	-2.719	6.310×10^{-17}	0	0
19	$NO + N \rightarrow N_2 + O$	-5.175	2.512×10^{-17}	0	0

- **Dissociation reactions**

The condition for a dissociation reaction in the Q-K model is as follows: if the energy in a collision is high enough to allow a dissociation event, it will always occur. The reaction being considered is AB + C → A + B + C, where AB is the molecule considered for dissociation, C is the reactant (either a molecule or an atom) and A and B are the atomic products of the dissociation. Considering the serial application of the quantum Larsen-Borgnakke model [20], the collision energy E_c of a particle pair (AB + C) is the sum of the relative translational energy and the pre-collision vibrational energy of the particle currently being considered, as described by Eq. 2.36. Assuming a harmonic oscillator model, the maximum vibrational level that can be reached is that given in Eq. 2.35, then the dissociation occurs if this level is higher than the dissociation level, i.e.

$$i_{max} > \frac{\Theta_d}{\Theta_v}, \tag{2.49}$$

in which the molecule AB must be dissociated before any vibrational or rotational relaxation can be considered. Applying the serial application of the quantum Larsen-Borgnakke model [20], the potential post-collision states i^* are chosen uniformly from the states equal or below i_{max} and are selected through and acceptance-rejection routine with probability given in Eq. 2.40.

A distinct feature of the Q-K model is that although the DSMC implementation does not necessitate that the gas be in equilibrium, if it is assumed that it is, then analytical solutions for the reaction rates can be derived. For a VHS gas in equilibrium, the rate coefficient $k_f(T)$ for the dissociation of a molecules AB with a molecule or atom C is

$$k_f(T) = R_{coll}^{AB,C} \Upsilon(i_{max})^{AB,C}, \tag{2.50}$$

where $R_{coll}^{AB,C}$ is the collision rate between species AB and C divided by the number density product. For a equilibrium VHS gas,

$$R_{coll}^{AB,C} = \frac{2\pi^{1/2}}{\alpha}\left(r_{ref}^{AB} + r_{ref}^{C}\right)^2 \left(\frac{T}{T_{ref}}\right)^{1-\omega^{AB,C}} \left(\frac{2k_B T_{ref}}{m_r^{AB,C}}\right)^{1/2}, \tag{2.51}$$

where r_{ref}, T_{ref}, and ω are the standard VHS properties of the relevant gas species. m_r is the reduced mass of the collision pair, and T is the macroscopic temperature of the gas. The symmetry factor α is set to 2 if the molecules in the collision are identical or 1 for dissimilar molecules. The $\Upsilon(i_{max})^{AB,C}$ parameter defines the fraction of the collision that will have sufficient energy to dissociate. Taking i as the pre-collision vibrational state of the dissociating molecule, the result is

$$\Upsilon(i_{max})^{AB,C} = \sum_{i=0}^{i_{max}-1} \frac{1}{z_v(T)^{AB}} \left[Q\left(\frac{5}{2} - \omega^{AB,C}, \left(\frac{(i_{max}-1)\Theta_v^{AB}}{T}\right)\right) exp\left(\frac{-i\Theta_v^{AB}}{T}\right)\right], \tag{2.52}$$

where Q(a,x) = Γ(a,x)/Γ(a) is a form of the incomplete Gamma function and $z_v(T)^{AB}$=1/[1-exp(-Θ_v/T)] is the vibrational partition function [126].

The Q-K dissociation model has been implemented in the *dsmcFoam* code for nine molecule-molecule dissociations (Table 2.1 reactions 2, 3, 4, 7, 8, 9, 11, 12, and 13), which were termed "Type I" dissociations. In addition, six molecule-atom dissociation, or "Type II" dissociations (Table 2.1 reactions 1, 5, 6, 10, 14, and 15).

In order to assess the accuracy of the Q-K model, two dissociation test cases involving thermochemical equilibrium and non-equilibrium were considered. In these test cases, an adiabatic box of side length 1×10^{-5} , with six specularly reflective surfaces, were used for this purpose. Following the work of Haas [128], a total of 50,000 DSMC particles were used in each simulation, at time step size 1.52×10^{-9} s, and the rotational and vibrational collision numbers were set to 1. The particles were allowed to move and exchange energy and if the particle met the criterion for dissociation to occurs (Eq. 2.49) then the counter was updated within the DSMC simulation and no particle splitting was allowed occur. This procedure enables reactions rates to be calculated at a constant temperature for a gas in equilibrium and then be compared to the analytical Q-K solutions of Eq. 2.50. Only the forward reaction was considered during the reaction, and recombination was discounted.

For the non-equilibrium calculations, particle splitting was allowed to occur and nascent species were introduced with the associated conservation of mass, momentum, and energy. The fate of each species was measured in a transient manner as the reaction proceeded from the equilibrium initial conditions, through a non-equilibrium reaction

process to a final state approaching equilibrium. Once again, the backward recombination reaction has been deactivated and only the forward chemistry is considered. The *dsmcFoam-QK* results are compared with analytical solutions. The analytical solutions are generated for the simultaneous solution of rate kinetic equations describing the time evolution of the concentration of each chemical species as well as the equilibrium temperature of the reacting gas mixture [129]. The overall rate of change of the concentration of species s is given by the summation over all individual rate processes of the form:

$$\frac{d[X_s]}{dt} = -k_f[X_s][X_r] + k_b[X_{p1}][X_{p2}], \tag{2.53}$$

where k_f and k_b are the forward and backward rate coefficients, X_r is a reactant species, and X_{p1} and X_{p2} are the species products. Only the forward reaction is considered and the backward reaction is deactivated. The k_f is determined from the equilibrium Q-K rate (Eq. 2.50) and is set in Arrhenius form as shown in Table 2.1. A system of five equations is solved simultaneously for species N_2, O_2, NO, N, and O for high-temperature air. The overall energy balance is also analysed accounting for the internal energy modes (translational, rotational, and vibrational) and chemical reactions in order to determine the equilibrium temperature.

Figure 2.4 shows the Type I and II equilibrium dissociation reactions rates for reactions 4 and 5 (Table 2.1), respectively. Good agreement is found between the *dsmcFoam*-QK calculation and analytical Q-K rates (Eq. 2.50). Comparison is also made with the DSMC results of Gallis *etal*. [123] for which excellent agreement is found, validating the *dsmcFoam* implementation of the Q-K approach for dissociation. Finally, comparison with the TCE solution of Boyd [130] is made and reasonable concurrence is found, with Q-K predicting slightly higher rate coefficients for Type I and slightly lower for Type II dissociation.

The non-equilibrium dissociation results are shown in Fig. 2.5. The species concentrations at any instant in time (n_s^t) have been non-dimensionalised with respect to the initial number density of the species (n^0). The analytical and numerical Q-K solutions seems to be in good agreement, with species constancy being approached after 10^{-5} s. In addition, the transient temperature variation for the gas mixture showed an

excellent concurrence with the analytical solution. Dissociation, being an endothermic reaction process, results in a decrease of the gas temperature to approximately 6000 K after 10^{-5} s.

The results described above reinforce the importance of the dissociation reactions for hypersonic aerothermodynamics. The dissociation reactions require the absorption of energy from the freestream to take place and act as an energy sink in hypersonic reacting flows. Furthermore, the energy redistribution during the chemical reaction manifests itself as a reduction in the enthalpy of the flow, with consequent reduction in the surface heat transfer to the hypersonic body.

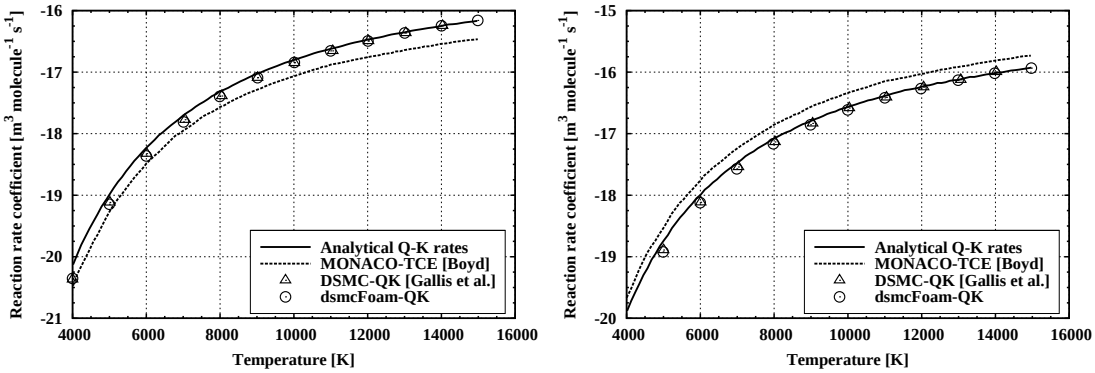

Figure 2.4: Equilibrium dissociation rate coefficient for type I dissociation: $O_2 + O_2 \rightarrow O + O + O_2$ (left), and equilibrium dissociation rate coefficient for type II dissociation: $O_2 + O \rightarrow O + O + O$ (right).

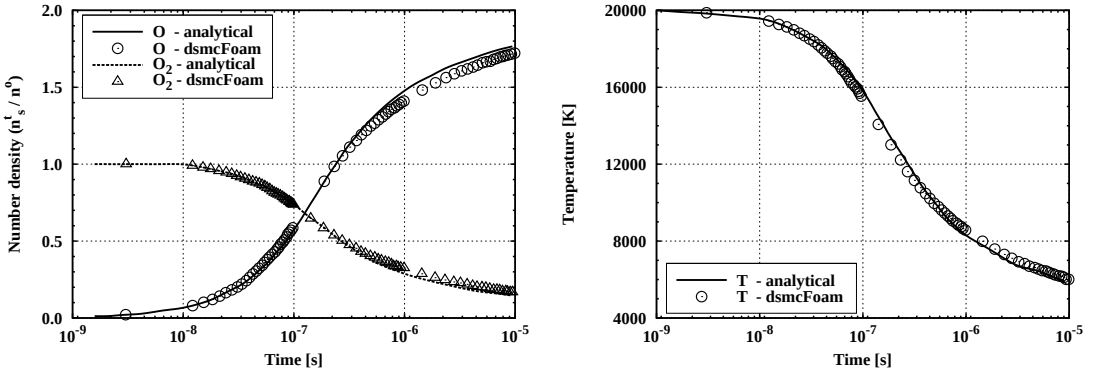

Figure 2.5: Species concentration (left) and overal temperature (right) during the non-equilibrium dissociation of an O_2 reservoir from an initial temperature of 20,000 K and a pressure of 0.063 atm.

Although not presented in the present work for reason of conciseness, the remaining Type I and Type II dissociation reactions have been implemented in the *dsmcFoam* code and demonstrated similar levels of agreement when compared with the Q-K analytical rate, Gallis *etal*. [123] DSMC results and Boyd's [130] DSMC-TCE rates. All further details of the current implementation of the Q-K reaction model into the *dsmcFoam* code can be found at Ref. [114] and the full set of Q-K-derived Arrhenius rate coefficients are presented in Table 2.1.

- **Exchange reactions**

Exchange reactions are binary reactions in which one stable molecule and one radical may occurs before and after the reaction process. The DSMC procedure for exchange reactions is similar to that for dissociation. For both the forward and reverse reactions, the reaction probability is equal to that of Eq. 2.40 with i* set to the vibrational level corresponding to the activation energy of the reaction, E_a

$$i^* = \left\lfloor \frac{E_a}{k_B \Theta_v} \right\rfloor . \tag{2.54}$$

In the 5-species air reacting model, the exchange reactions take the form A+B↔C+D, where A and C are molecules, and B and D are atoms (reactions 16 to 19 from Table 2.1). These reactions exist either as a forward (endothermic) reaction or a backward (exothermic) one, resulting in a total of four exchange reactions. The current Q-K model implementation of exchange chemistry leads to reactions being possible if the collision energy E_c is greater than the activation energy E_a, with a probability of

$$P_{exchange} = \frac{\left(1 - \frac{E_a}{E_c}\right)^{3/2-\omega}}{\sum_{i=0}^{i_{max}} \left(1 - \frac{i k_B \Theta_v}{E_c}\right)^{3/2-\omega}}. \tag{2.55}$$

The summation in the denominator can be taken as unity when $E_a/k < \Theta_v$ and the analytical Q-K rates given by Bird [126] are

$$k_f(T) = \frac{R_{coll}^{A,B} exp\left(\frac{E_a^{A,B}}{k_B T}\right)}{z_v(T)^A}, \tag{2.56}$$

and

$$k_r(T) = \frac{R_{coll}^{C,D} exp\left(\frac{E_a^{C,D}}{k_B T}\right)}{z_v(T)^C}, \tag{2.57}$$

where k_f and k_r are the forward and reverse reactions rates, respectively, $z_v(T)$ is the vibrational partition function, R_{coll} is the collision rate between the species indicated in the superscript and is given by Eq. 2.51.

The default activation energy for the forward exchange reactions is the heat of reaction, E_r, and for the reverse reaction it is zero. The activation energies and heats of formation for the four exchange reactions are shown in Table 2.1.

In order to ensure that the ratio of the number of forward to reverse exchange reactions is consistent with that predicted by statistical mechanics it is necessary to adjust the activation energies in a phenomenological manner. For forward to exchange reactions, the adjusted activation energy $E'_{a,f}$ is

$$E'_{a,f} = |E_h| \left[1 + a\left(\frac{T}{273}\right)^b\right], \tag{2.58}$$

and for the reverse exchange reaction it is

$$E'_{a,r} = |E_h| \left[a\left(\frac{T}{273}\right)^b\right], \tag{2.59}$$

where $|E_h|$ represents the modulus of the heat of formation (Table 2.1) and a and b are adjustable parameters [114].

In the Q-K chemistry model implementation, the values of a and b for the four exchange reactions were chosen to enable the DSMC results to agree satisfactorily with both the analytical equilibrium Q-K rates of Eqs. 2.56 and 2.57, the analytical equilibrium rates predicted by Eq. 2.53, and, finally, to ensure that the ratio of the forward to reverse reactions is consistent with that predicted by statistical mechanics [126]. The parameters a and b were determined using Bird's QK rates program [131].

Similarly to the equilibrium dissociation reactions previously presented, an adiabatic box was used to perform exchange reaction simulations in order to measure the equilibrium rate coefficients for each of the four exchange reactions. Furthermore, a 50% split of each species was used as the initial condition.

Figure 2.6 shows the equilibrium reaction rates for the forward (endothermic) and reverse (exothermic) reaction NO+O $\leftrightarrow$ O_2+N. The TCE rates were obtained from Ref. [130], the DSMC data from Gallis *etal*. [123], and the rate representative of the National Institute of Standards and Technology (NIST) database [132] are also included. In addition, the *dsmcFoam* implementation for exchange has been calculated using two different definitions for temperature in Eqs. 2.58 and 2.59, these being the macroscopic and the collision temperature. The collision temperature has been used for all *dsmcFoam* calculations in the present work and it's definition is [126]:

$$T_{coll} = \frac{\left(m_r^{A,B} c_r^2\right)/(2k_B)}{\left(\frac{5}{2} - \omega^{A,B}\right)}. \tag{2.60}$$

In his 2011 paper, Bird [126] recommends that if the collision temperature is used then the exchange factor a in Eqs. 2.58 and 2.59 needs to be replaced by:

$$a' = \left[\frac{\left(5/2 - \omega^{A,B}\right)^b \Gamma\left(5/2 - \omega^{A,B}\right)}{\Gamma\left(5/2 - \omega^{A,B} + b\right)}\right] a \tag{2.61}$$

This step was considered necessary due to the inequality of macroscopic and collision temperatures when the parameter b is not equal to zero or unity. However, the *dsmcFoam*-QK calculations for exchange reactions showed no apparent difference whether T_{coll} was used in tandem with Eq. 2.61 or not. It is desirable that the collision temperature be used in the DSMC procedure rather than the macroscopic value as information should be passed upwards from molecular level. However, it is evident from all the figures for exchange reactions that the use of macroscopic temperature in the *dsmcFoam*-QK code produces equilibrium rates that match the Q-K analytical rates.

The simulated Q-K rates using T_{coll} are seen in Fig. 2.6 (left) to fall the range covered by th TCE and the NIST rates for temperatures in excess of around 7000 K. It is interesting to note that the Gallis *etal*. [123] data, based on a DSMC implementation which did not consider the adjustment of the activation energies, shows consistently higher reaction rates across the range of the temperatures considered.

The corresponding reverse exothermic equilibrium rate for the NO+O $\leftrightarrow$ O_2+N exchange reaction is shown in Fig. 2.6, on the right hand side. Additional experimental data from Gupta *etal*. [133] and Bortner [134] have been included. Close agreement

is observed between the Q-K rates using the collision and macroscopic temperatures because the coefficient b is small (0.1) for this reaction. The trend of decreasing reaction rate with temperature is similar for both Q-K and TCE, however the Q-K rates are higher across the range of temperatures studied and are closer of the results of Gupta *etal*. and Bortner. In comparison with the activation energy-adjusted Q-K approach presented in this work, the previous incarnation of Q-K considered by Gallis *etal*. predicts lower rates for this reaction with their results being closer to the TCE rates.

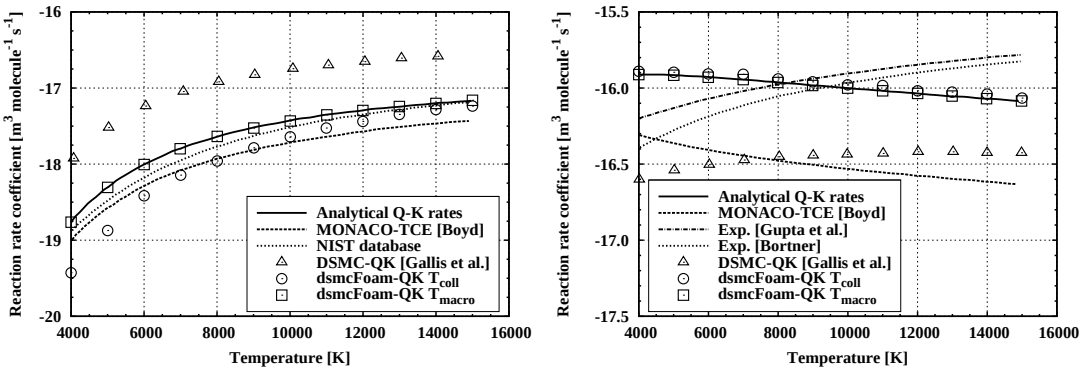

Figure 2.6: Forward endothermic equilibrium exchange rate coefficient for NO + O → O_2 + N (left), and reverse exothermic equilibrium exchange rate coefficient for O_2 + N → NO + O (right).

Figure 2.7 shows the molar concentration and temperature fields respectively for exothermic reverse exchange reaction NO + N → N_2 + O. Once again, very reasonable agreement is obtained between the analytical Eq. 2.53 and the *dsmcFoam*-QK predictions. The overall temperature field is seen to achieve equilibrium after a time of approximately 1.0×10^{-5} s, with a temperature of around 27,700 K being reached after 1.0×10^{-4} s. The NO overall temperature scatter, evident towards the end of the reaction, may be put down to statistical fluctuations as the NO becomes rapidly depleted.

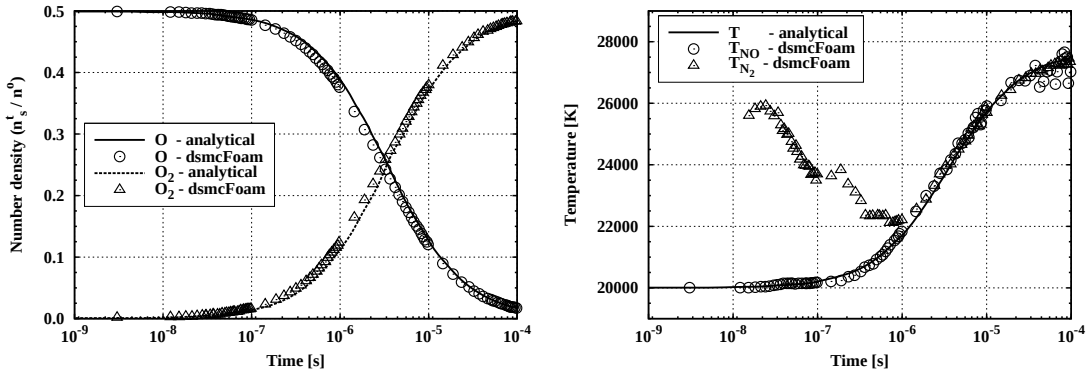

Figure 2.7: Species concentration (left) and overall temperature (right) during the non-equilibrium reverse exchange reaction NO + N $\rightarrow$ N_2 + O from an initial temperature of 20,000 K and pressure of 0.063 atm.

- **Air reactions**

Having implemented the full set of 19 reactions in the *dsmcFoam* code, a case involving all 19 reaction was considered. For this purpose, the reactions showed in Table 2.1 are considered in a adiabatic box filled with air at an initial composition of 79% N_2 and 21% O_2 and pressure of 0.063 atm. Three cases are considered for initial temperatures of 30,000 K, 20,000 K, and 10,000 K.

Figure 2.8 shows the evolution of the species and overall temperature for the heat bath from 30,000 K. In general, the *dsmcFoam*-QK predictions of the constituent evolution agree well with the analytical results although there is an under-prediction of NO towards the end of the reactions. Oxygen scatter towards the tail of the reaction is due to its rapid depletion as the reactions progresses. Considering the overall temperature field for the gas mixture, very good agreement between the current implementation of the Q-K chemistry model and the analytical solutions is evident, with any scatter being explained by the extinction of the O_2 and NO molecules towards the end of the reaction process.

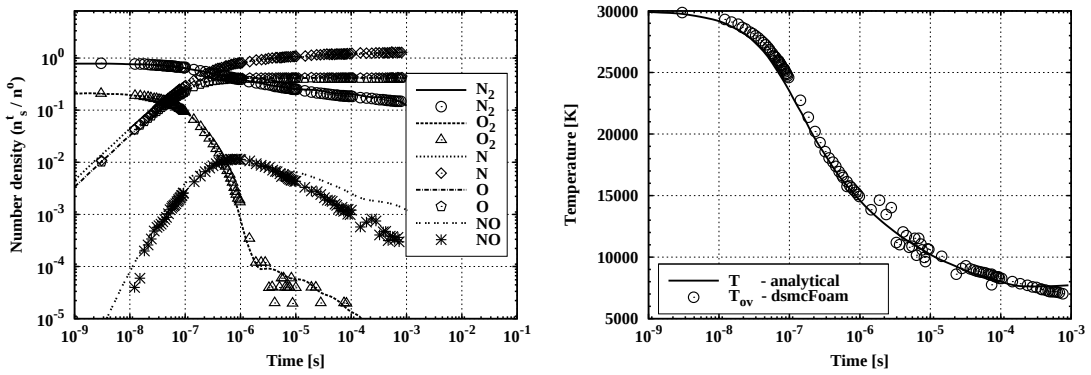

Figure 2.8: Species concentration (left) and overall temperature (right) during the decomposition of air from an initial temperature of 30,000 K and pressure of 0.063 atm. Solid lines represent the analytical rates and symbols the Q-K rates, respectively.

In his 2011 Q-K paper [126], Bird does not present any DSMC simulations data: it is solely analytical work with a description of the DSMC procedure for each reaction. Gallis *etal*. [123] and Wysong *etal*. [127] have presented some DSMC simulations data, however these works were performed using a DSMC implementation for exchange reactions that has since been superseded. In this way, the present work aimed to generate the first database set for the "Quantum-Kinetic chemistry model for which further details are available in Ref. [114]. In addition, the application of Q-K model for real cases of atmospheric reentry are presented in Chapter 3, validating in this way the chemistry model for its intended purpose.

2.2 The *dsmcFoam* code

The *dsmcFoam* code is employed in the current work to solve rarefied reacting and non-reacting hypersonic flows over simple and complex geometries. Based on Bird's algorithm, this new freeware has been developed to solve complex engineering problems [135]. The *dsmcFoam* solver has been developed within the framework of the open-source computational fluid dynamics toolbox OpenFOAM [136] and it is freely available for download under the GNU general public licence. The main features of the *dsmcFoam* code include particle initialisation in arbitrary geometries, particle tracking in unstructured meshes, the capability to perform both steady state and transient DSMC simulations, and unlimited parallel processing.

Powerful meshing tools, such as the *snappyHexMesh*, are also provided by OpenFOAM, allowing to the user build complex structured and unstructured meshes for use in DSMC simulations. In addition, force measurements tools provide a very useful way to calculate the external forces acting on a body during the re-entry phase. Post-processing is carried out using the Paraview software provided by the OpenFOAM, or with a variety of other post-processing softwares, such as Tecplot. The main features of the *dsmcFoam* solver are summarised in the list below:

- Arbitrary 2D/3D geometries;
- Mesh generation, walls/freestream properties extraction, and force measurements tools;
- Steady state and transient simulations;
- Automatic 8 sub-cells generation;
- Arbitrary number of gas species;
- Availability of different boundaries conditions, such as freestream, vacuum, cyclic, and specular/diffuse/CLL models for gas-surface interactions;
- Possibility to perform non-reacting and reacting flow simulations ("Quantum-kinetic" chemistry model).

When using the *dsmcFoam* solver, six main step may are employed: 1) build the computational mesh; 2) set up the freestream properties, boundary conditions, and time step size; 3) fill the mesh with DSMC particles with dsmcInitialise; 4) Start the simulation using the command *dsmcFoam*; 5) Enable the time averaging process once the steady state solution has been archived; 6) Using the Paraview software, perform the post-processing.

2.2.1 Macroscopic properties measurements in the *dsmcFoam* code

The DSMC technique is a particle-based method in which the macroscopic gas properties, such as mass density, velocity, pressure, and temperature are recovered from the particle movements and collisions at the microscopic level. The DSMC method uses

the cell system for sampling these macroscopic properties and then they are used for engineering purposes. One of the most simple basic property is the number density n; defined as the number of particles N within a volume V,

$$n = \frac{N}{V}, \tag{2.62}$$

and the mass density ρ is defined as the product of the molecular mass m and the number density,

$$\rho = nm. \tag{2.63}$$

Some other macroscopic gas properties are related to the transport of mass, momentum, and energy through the molecular motion during the simulations. The macroscopic, or stream, velocity $\mathbf{c}_0$ is defined as the mean instantaneous molecular velocities $\mathbf{c}$ as follow,

$$\boldsymbol{c}_0 = \frac{\sum_{i=1}^{N} \mathbf{c}}{N}. \tag{2.64}$$

The instantaneous velocity of a molecule relative to the stream velocity is called peculiar, or thermal, velocity **c'**,

$$\boldsymbol{c'} = \boldsymbol{c} - \boldsymbol{c}_0, \tag{2.65}$$

The pressure tensor $\mathbf{p}$ is composed by nine tensor components and can be written as,

$$\boldsymbol{p}_{ij} = \rho \overline{c'_i c'_j}, \tag{2.66}$$

in which the subscripts i and j contain three values each representing a single component of the velocity vector, i.e.,

$$c'_1 = u', \quad c'_2 = v', \quad c'_3 = w', \tag{2.67}$$

where, u, v, and w being the velocity components in the x, y, and z directions, respectively.

The scalar pressure P is defined as the average value of the three components in the normal component of the pressure tensor ($\mathbf{p}_{xx}$, $\mathbf{p}_{yy}$, $\mathbf{p}_{zz}$),

$$P = \frac{1}{3}\rho\big(\overline{u'^2} + \overline{v'^2} + \overline{w'^2}\big). \tag{2.68}$$

Considering an equilibrium gas all the three normal components of the pressure tensor are equal; however, they are different for a non-equilibrium gas.

The viscous stress tensor $\boldsymbol{\tau}$ is the negative of the pressure tensor with the scalar pressure subtracted from the normal components as follow,

$$\boldsymbol{\tau} \equiv \tau_{ij} = -\Big(\rho\overline{c_i' c_j'} - \delta_{ij}p\Big), \tag{2.69}$$

where $\delta_{ij}p$ is the Kronecker delta and may assume value equal one if $i = j$, or zero if $i \neq j$.

The average specific kinetic energy associated with the thermal velocity of a molecule can be given as

$$e_{tra} = \frac{1}{2}\big(\overline{u'^2} + \overline{v'^2} + \overline{w'^2}\big). \tag{2.70}$$

Combining Eq. 2.68 and Eq. 2.70,

$$P = \frac{2}{3}\rho e_{tra}. \tag{2.71}$$

The definition for translational temperature T_{tra} is given by comparing the Eq. 2.70 and the equation of state for a ideal gas as follow,

$$T_{tra} = \frac{1}{3k_B}m\big(\overline{u'^2} + \overline{v'^2} + \overline{w'^2}\big). \tag{2.72}$$

Eq. 2.72 shows that the equation of state is valid for a dilute gas, even in a state of non-equilibrium, as long as the pressure is based only on the translational temperature. The measurement of the translational non-equilibrium is also possible just defining a translational temperature for each of the temperature components ($[\mathbf{T}_{tra}]_x$, $[\mathbf{T}_{tra}]_y$, $[\mathbf{T}_{tra}]_z$).

In a system which contains only monoatomic gas just the translational temperature of the molecules is considered and it represents the actual temperature of the system.

Nonetheless, simulations that take into account diatomic and polyatomic gases are very often used in hypersonic aerothermodynamics. In this scenario, rotational and vibrational energy should be incorporated in the computational code. The rotational temperature T_{rot} is similarly obtained from Eq. 2.72,

$$T_{rot} = \frac{2m\varepsilon_{rot}}{k_B \zeta_{rot}}, \tag{2.73}$$

where ε_{rot} represents the specific rotational energy and ζ_{rot} is the number of rotational degrees of freedom.

The measurement of vibrational temperature T_{vib} includes a summation over all species that composes the gas:

$$T_{vib} = \frac{\sum_{m=1}^{n} \left(\zeta_{vib,m} T_{vib,m}\right)}{\sum_{m=1}^{n} \left(\zeta_{vib,m}\right)}, \tag{2.74}$$

in which n is the number of gas species, and $T_{vib,m}$ is the vibrational temperature of the specie m calculated as follow,

$$T_{vib,m} = \frac{\Theta_{vib,m}}{ln\left(1 + \frac{1}{\bar{i}_m}\right)}, \tag{2.75}$$

where $\bar{i}_m$ is the average quantum level of particles of gas species m. The number of degrees of freedom for a given species m,$\zeta_{vib,m}$ is calculated as

$$\zeta_{vib,m} = \frac{2\Theta_{vib,m}/T_{vib,m}}{exp\left(\Theta_{vib,m}/T_{vib,m}\right) - 1}, \tag{2.76}$$

and the average vibrational degrees of freedom $\overline{\zeta_{vib}}$, calculated over all the species is given by

$$\overline{\zeta}_{vib} = \frac{\sum_{m=1}^{n} \zeta_{vib,m}}{n}, \tag{2.77}$$

The overall temperature T_{ov} consider all of the internal energy modes and can be defined as the weighted average of the translational, rotational, and vibrational modes with respect to the degrees of freedom,

$$T_{ov} = \frac{3T_{tra} + \overline{\zeta}_{rot}T_{rot} + \overline{\zeta}_{vib}T_{vib}}{3 + \overline{\zeta}_{rot} + \overline{\zeta}_{vib}}. \tag{2.78}$$

In a thermal nonequilibrium flow the temperatures associated with the translational, rotational and vibrational internal modes of energy are unequal, i.e., these modes do not share a common distribution of energies.

Finally, the heat flux measurement is given in vector form as follows,

$$\boldsymbol{q} \equiv q_i = \frac{1}{2}\rho\overline{c'^2 c'_i} + n\overline{\varepsilon_{rot}c'_i}, \tag{2.79}$$

where ε_{rot} represents the rotational energy of a single particle.

As mentioned earlier in this section, the macroscopic properties of the gas are recovered after all the particle movement and collisions have been processed. However, in the DSMC methodology a single particle can represent a large number of real particles. In this way, the sampling process of the gas properties should take into account the number of real particles F_N that a single DSMC particle represents. For example, the number density is sampled as

$$n = \frac{F_N\overline{N}}{V_{cell}}, \tag{2.80}$$

where $\overline{N}$ is the average number of DSMC particles within a cell volume V_c during the measurement interval.

The *dsmcFoam* solver possesses the capability to perform both transient and steady state simulations. For steady state calculations, all of the gas properties are measured over a large time period and consequently a large enough sample size that will effectively reduce the statistical scattering. This statistical error can be estimated using the equations provided in Ref. [137]. In transient cases, the simulation must be repeated enough times to provide a large enough sample and the results can be represented as an ensemble average.

Chapter 3

Verification and validation

Computer predictions of physical events play an increasingly important role in making critical decisions that affect our daily lives. As the computational power continues to grow, they have been used for a wide range of different applications in order to obtain vital information on events that influence the economy, health, security, Earth sciences, and so on [138].

Because of the impact that modelling and simulation can have, the accuracy and reliability of the computer predictions has been the focus of much study and debate for many years in the fluid dynamics community. Computational codes can only be considered reliable if they pass through rigorous process of verification and validation (V&V). In an effort to standardise the V&V process, a relatively large literature has been produced on the subject [139–146]. Among the noteworthy studies on this endeavour, the American Institute of Aeronautics and Astronautics (AIAA) [143] has created the following definitions of V&V which will be adopted in this work:

Verification: the process of determining that a model implementation accurately represents the developer's conceptual description of the model and the solution to the model.

Validation: the process of determining the degree to which a model is an accurate representation of the real world from the perspective of the intended use of the model.

In another words, verification deals with mathematics and the conceptual model that relates to the real word is not an issue; validation deals with physics and address the accuracy of the conceptual model comparing with the real world, i.e., experimental

measurements [142, 144].

In the DSMC context, the code accuracy relies mainly on four main constraints: (i) the cell size must be proportional to the local mean free path; (ii) the simulation time step must be chosen so that particles only cross a fraction of the average cell length per time step; (iii) the number of particles per cell must be roughly constant in order to preserve collisions statistics; and (iv) the statistical scatter is determined by the number of samples. In addition, the validation strategy consists in comparing the results obtained by the *dsmcFoam* code with other numerical, analytical, or experimental results available in the literature. Since the *dsmcFoam* is a new DSMC code, it is of extreme importance that the computational code should be verified and validated for its intended purpose. In the following sections, the V&V process for the *dsmcFoam* code is discussed in detail.

3.1 *dsmcFoam* code verification

The main idea of a verification process is to examine if the original DSMC requirements were rigorously respected. For this purpose, a flow over zero thickness flat plate was chosen as a test case. The flat-plate geometry provides a simple and effective verification test case for numerical methods.

In the present study, the freestream conditions are similar to those investigated by Lengrand *et al.* [147]. In this experimental study, a sharp flat plate of 0.1 m length and 0.1 m width was positioned at a distance from a nozzle producing a flow with a freestream Mach number of 20.2, freestream temperature of 13.32 K, and pressure of 6.831×10^{-2} N/m^2.

In the computational solution, the geometry was constructed as a 3D flat plate, 0.1 m long and 0.1 m wide, positioned 0.005 m downstream of a uniform nitrogen stream, parallel to the plate itself. More details concerning the freestream conditions are shown in Table 3.2 at Section 3.2.1. Based on these properties, the freestream Knudsen number Kn_∞ is 0.0235 and the Reynolds number Re_∞ is 2790, using the flat-plate length as the characteristic length.

The computational domain used for the calculation is made large enough so that flat plate disturbances do not reach the upstream and side boundaries, where freestream

conditions are specified. A schematic view of the computational mesh and boundary conditions are illustrated in Fig. 3.1. Side I-A represents the flat-plate surface. Diffuse reflection with complete thermal accommodation is the boundary condition applied to this side. Side I-B represents a surface where all flow gradients normal to the surface is zero. This boundary condition is equivalent to a specular reflecting boundary, where the normal component of the incident velocity is reversed, while the parallel component is left unchanged. Sides II and III are boundaries with a specified freestream condition. Particles crossing the boundary into computational domain are generated at these sides. Finally, the side IV is defined as vacuum in which particles are removed from computational domain. The option for vacuum is suitable for an outflowing gas since there are no particles moving upstream with Mach number greater than three [20].

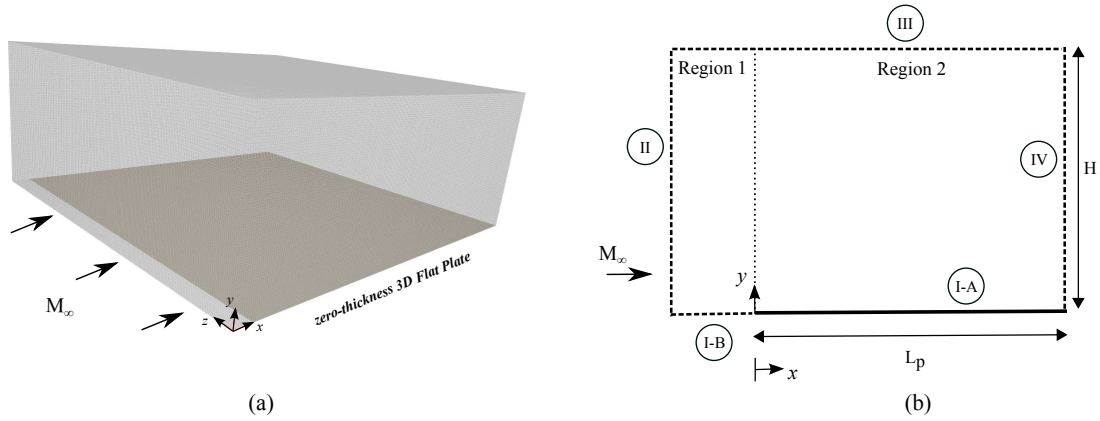

Figure 3.1: (a) 3D flat plate computational mesh, and (b) side view of the computational domain with specified boundary conditions.

3.1.1 Spatial discretisation effects

In order to accurately model collisions by using a statistical approach, the cell size should be of the order of one third or smaller than the local mean free path in the direction of primary gradients [20]. Near to the body surface, the cell size in the normal direction to the surface should be of the same order. This is because in certain regions, such as in the vicinity of the surfaces, the cell size must be small enough to adequately capture flowfield physics near the wall. Near-wall cells need to be small enough to adequately capture the steep macroscopic gradients close to the body surface.

In order to examine the effect of the grid resolution on the heat transfer, pressure and skin friction coefficients, a set of simulations using standard, fine, and coarse meshes are used. Grid independence is investigated by performing calculations for different numbers of cells in x- and y-directions and then compared with the standard grid. Figure 3.1 shows the standard computational domain which is divided into two regions. Region 1 consists of 10 cells along side I-B and 80 cells along side II and region 2 consists of 200 cells distributed along side I-A and 80 cells normal to the plate surface, i.e., along side IV. In this way, the effect of altering the cell size in the x-direction may be analysed for coarse and fine grids by halving or doubling the number of cells with respect to the standard grid, while the number of cells in the y-direction is kept the same. The same procedure is adopted for y-direction, i.e., the cell size is altered keeping the number of cells in x-direction constant. Table 3.1 shows the number of cells used in the coarse, standard and fine meshes.

Table 3.1: Number of cells in the x-, y- and z-direction for the flat-plate verification case.

	Coarse (x)	**Coarse** (y)	**Standard**	**Fine** (x)	**Fine** (y)
Region 1	5×80×200	10×40×200	10×80×200	20×80×200	10×160×200
Region 2	100×80×200	200×40×200	200×80×200	400×80×200	200×160×200
N^o cells	1.68×10^6	1.68×10^6	3.36×10^6	6.72×10^6	6.72×10^6

The influence of the cell size on the heat transfer, pressure, and skin friction coefficients is shown in the Fig. 3.2. According to these figures, the results for the three independent meshes are approximately the same, indicating that the results for the standard mesh is essentially grid independent.

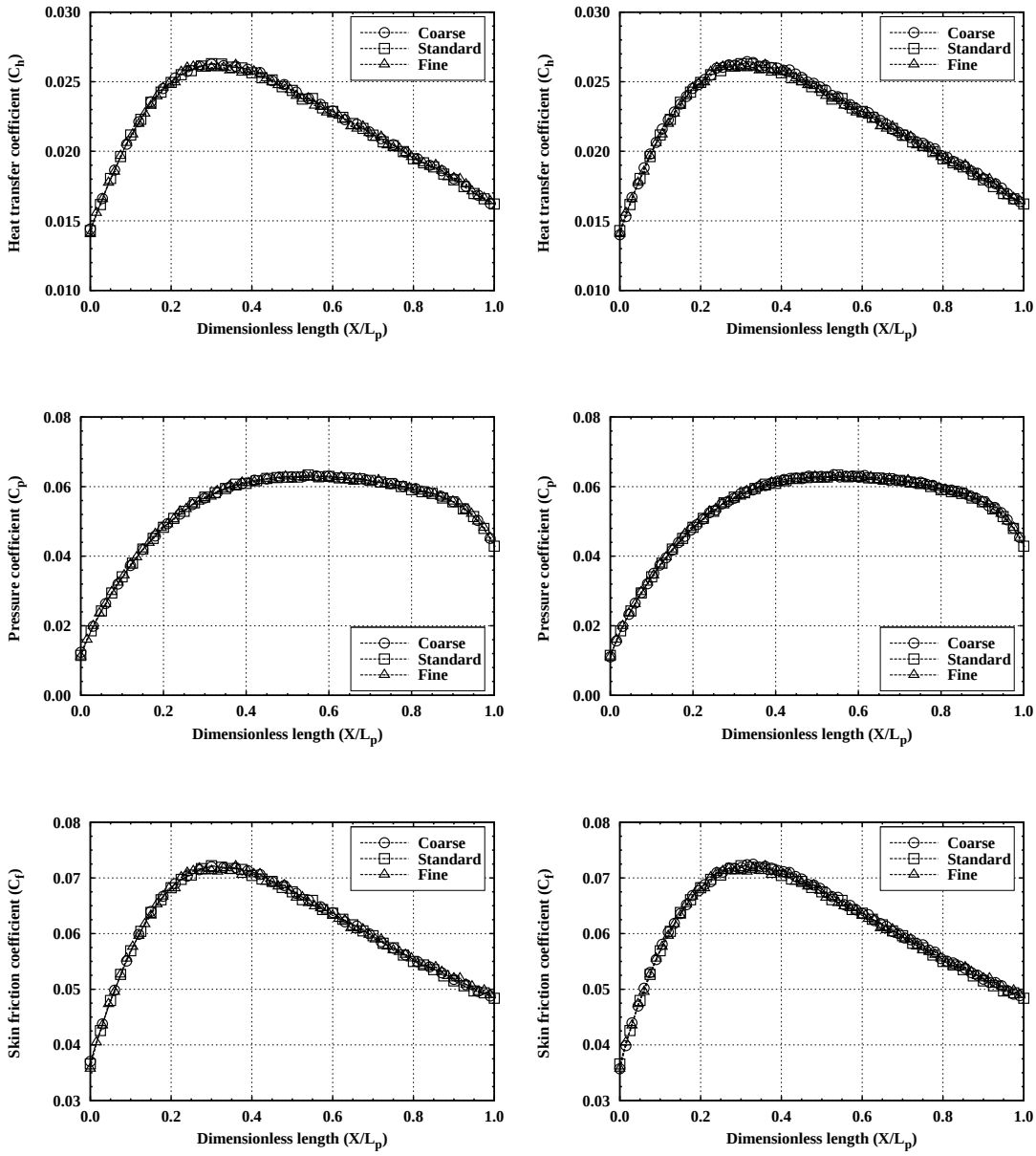

Figure 3.2: Influence of varying the number of cells in the x- (left) and y- (right) directions on the flat plate aerothermodynamic properties.

3.1.2 Time discretisation effects

As the DSMC method is unconditionally transient, a time-step sensitivity analysis must be performed. The selection of a time step must be smaller than the local mean collision time to allow the uncoupling between the movement and collisions a set particles. In addition, if the time step is too large, particles can cross many cells in one time step and consequently the results may be inaccurate. On the other hand, too small a time step will result in inefficient computation [74, 75, 148].

In a similar manner to the grid independence study, the influence of the time step size on the aerodynamic properties is examined here. The time step is calculated based on the typical cell dimensions, which is one third of the freestream mean free path [149], and on the residence time (Δt_{res}) of a particle inside the cell. In this context, two variations of the reference time step (Δt_{ref}), used in the standard grid calculations, are considered, with the time step is set equal to (Δt_{ref})/4 and (Δt_{ref})×4. According to Fig. 3.3, the resulting simulations are essentially independent of the time step as long as the time step and cell size requirements are respected.

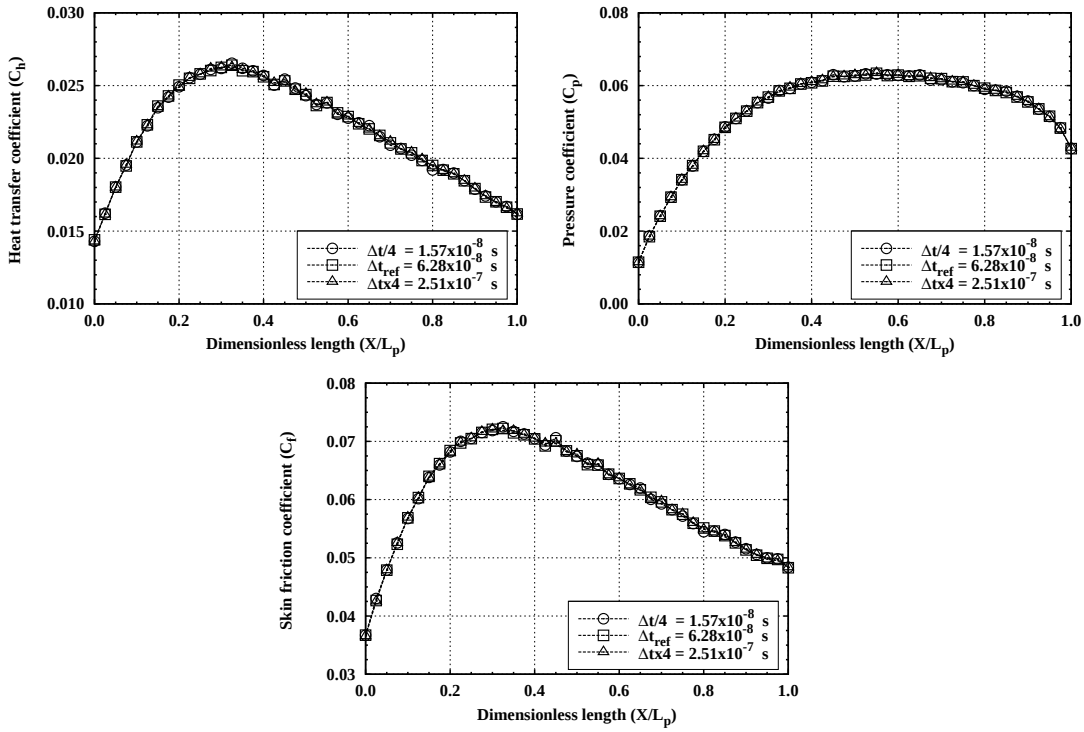

Figure 3.3: Influence of varying the time step size on the flat plate aerodynamic properties.

3.1.3 Particle number assessment

In DSMC simulations the intermolecular collisions are the principal driver in the flow-field development. These intermolecular collisions occur in each macroscopic cell and sufficient particles should be employed in in order to reduce the statistical error during the sampling process. However, the use of a large number of particles greatly increases the computational effort. A balance between computational effort and accuracy has been studied by many authors [150–153] with a value of 30-40 particles per cell being commonly found [154–158]. However, there are some DSMC simulations [159, 160] in which employed as few as 10 particles in each cell, and some computations [161] as large as 50 to 120 particles per cell. It appears evident that there is no certain solution to the optimal number of particles necessary for a given simulation.

In order to clarify this question, an additional study has been carried out to estimate the influence of the number of simulated particles on the *dsmcFoam* solution of a hypersonic flow over a flat plate. Considering that the standard mesh corresponds to a total of 4.37×10^7 particles, two new cases were investigated using the same mesh. These cases correspond, on average, to 2.18×10^7 and 8.74×10^7 particles in the entire computational domain. The effects of such variations on heat transfer, pressure and skin friction are shown in Fig. 3.4. Hence, the standard grid with a total of 4.37×10^7 particles is considered sufficient for the present computations.

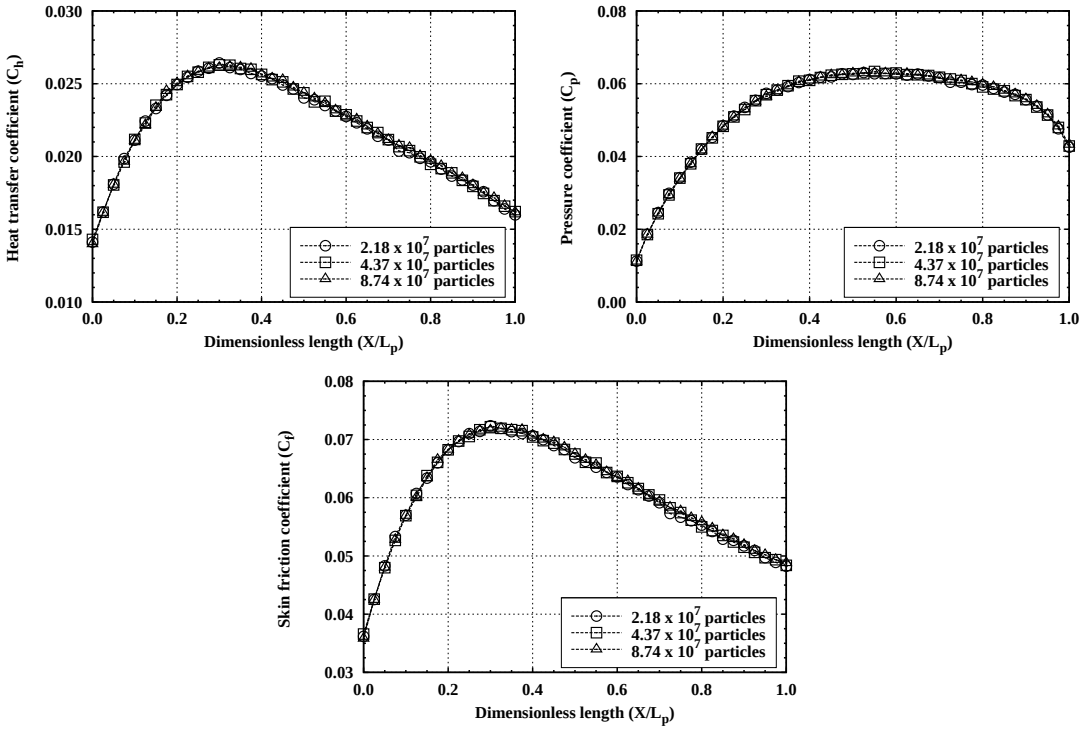

Figure 3.4: Influence of particle number on the flat plate aerothermodynamic properties.

3.1.4 Sampling effects

The accuracy of the DSMC method is also affected by the number of samples (N_s) [154–160]. Since all of the macroscopic properties of the flow are obtained by sampling the total number of particles within a cell, the number of samples must be sufficient to minimise the statistical error. The magnitude of the statistical error declines as the square root of the sample size and it is importance to determine the value of N_s that provides tolerable data scattering. For this purpose, the standard mesh with approximately 3.36×10^6 particles was run for 50,000, 100,00 200,000, and 300,000 sampling time steps.

Figure 3.5 shows a very good agreement for the number of samples considered. Based on these plots, N_s equal to 300,000 is considered as a value that provides acceptable fluctuation level for the case investigated.

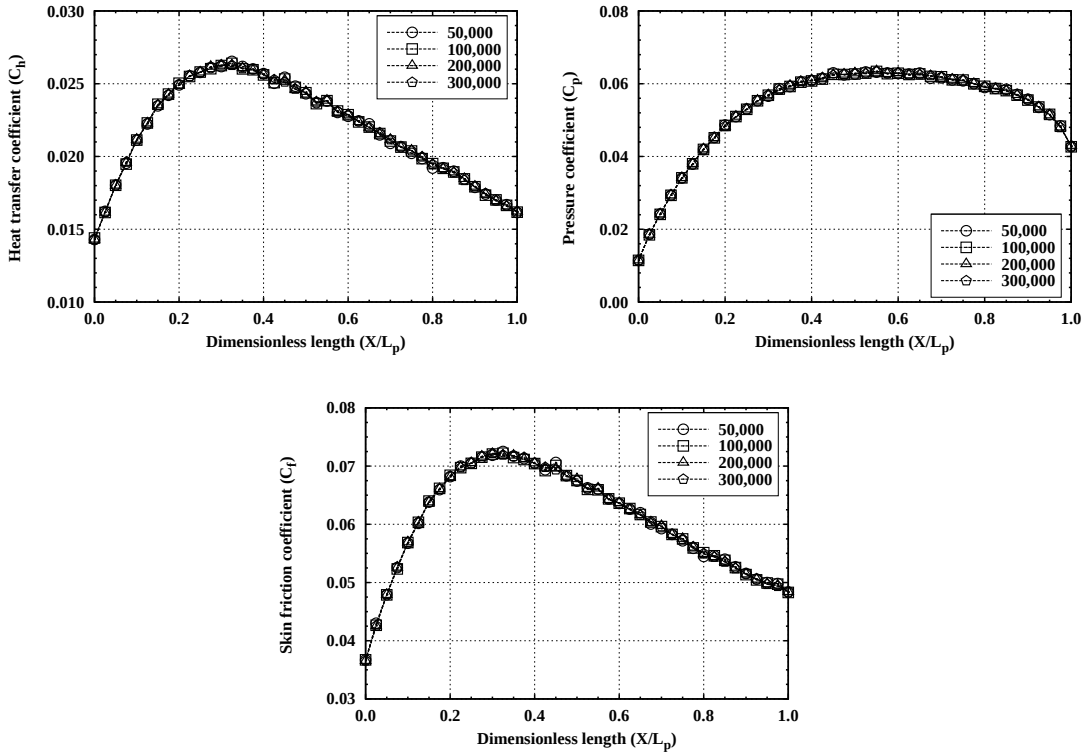

Figure 3.5: Influence of number of samples on the flat plate aerothermodynamic properties.

3.2 *dsmcFoam* validation for hypersonic non-reacting flows

The lack of experimental and computational data to demonstrate the rarefaction effects acting on spacecraft during the reentry has been an issue for many years. In an effort to address these problems, the Advisory Group for Aerospace Research and Development (AGARD, working group 18) [162] conducted a series of experiments and simulations to enhance the understanding of the physical phenomena and to assess the capability of numerical techniques in predicting nonequilibrium aerothermodynamics.

In this section, the *dsmcFoam* code is used to solve rarefied non-reacting flows over flat plates and the Mars Pathfinder probe[163, 164]. The main idea is to validate the computational code for simple and complex geometries in order to build up confidence in hypersonic flows analysis. For this purpose, the results obtained are compared with numerical and experimental data available in the current open literature.

3.2.1 Rarefied hypersonic flow over sharp and truncated flat plates

Rarefied hypersonic flow past a flat plate has been studied theoretically, experimentally, and numerically extensively by many authors, since it demonstrates the development of the highly nonequilibrium kinectic flow at the leading edge through the transition-merged regions and into the weak-strong interactions regime [163–169]. Moreover, the extremely simple geometry makes the flat plate one of the most useful test cases for numerical validation.

The test cases chosen to validate the *dsmcFoam* code for non-reacting flows are based on the experimental-numerical study conducted by Lengrand *et al.* [147] and Allegre *et al.* [163]. In their experimental work, sharp and truncated flat plates of 0.1 m of length, 0.1 m width and 0.005 m thick were positioned in a flow of nitrogen at two angles of incidence, 0^o and 10^o. The physical model was supplied with an internal water cooling system which maintained the wall temperature at 290 K. Wall pressure and heat flux measurements were made by placing pressure transducers and chromel alumel (Ch/Al) thermocouples along the longitudinal symmetry axis of the flat plates. In addition, density flowfield measurements employing an electron beam fluorescent technique were carried out surrounding the truncated flat plate. For the uncertainty in the referred experiment, pressure, heat flux and density are estimated to be 15%, 10%, and 10%, respectively. Figure 3.6 and Table 3.2 presents in detail the *dsmcFoam* computational domains and the experimental freestream conditions considered.

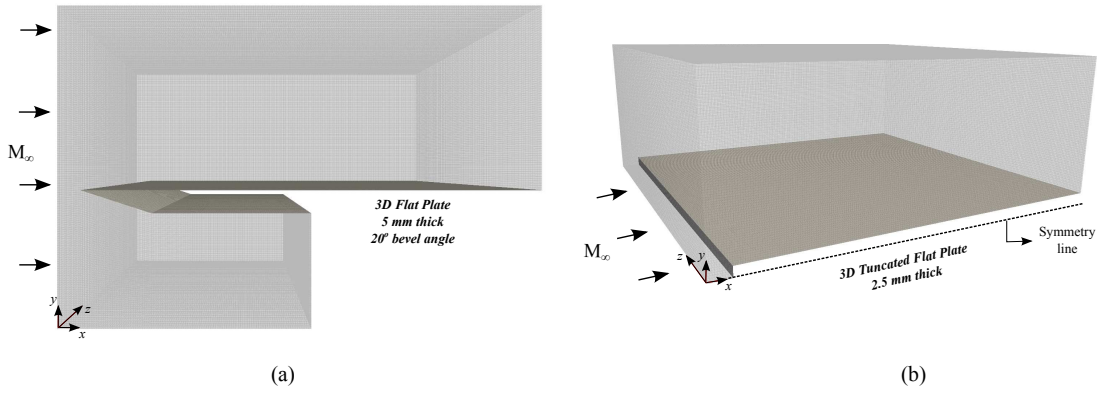

Figure 3.6: Schematic of the 3D computational domain, (a) sharp and (b) truncated flat plates.

In addition to the experimental work, numerical simulations were performed using Navier-Stokes (N-S) [147, 163] and direct simulation Monte Carlo (DSMC) [147, 163, 164] techniques. The N-S results were obtained at ONERA using an implicit finite-volume method taking into account the slip velocity and temperature jump at the wall. DSMC *in house* codes presented in the results were developed by the Laboratoire d'Aérothermique of Centre National de la Recherche Scientifique (CNRS) [147] and Institute of Space and Aeronautical Science (ISAS) [164]. Since the data and assumptions employed in each method are available in the literature, the subsequent discussions are limited only to details considered as necessary.

Table 3.2: Freestream conditions for flat-plate simulations.

Parameter	**Value**	**Unit**
Velocity (V_∞)	1503	m/s
Temperature (T_∞)	13.32	K
Number density (n_∞)	3.719×10^{20}	m^{-3}
Density (ρ_∞)	1.729×10^{-5}	kg/m^3
Pressure (p_∞)	6.831×10^{-2}	Pa
Dynamic viscosity (μ_∞)	9.314×10^{-7}	$N.s/m^2$
Mean free path (λ_∞)	2.350×10^{-3}	m
Overall Knudsen (Kn_L)	0.0235	
Overall Reynolds (Re_L)	2790	

In order to validate the *dsmcFoam* code, 3D sharp and truncated flat plates with the same dimensions and freestream conditions used by Lengrand *et al.* [147] and Allegre *et al.* [163] are assumed here. In the present computational solution, the two models are immersed in nitrogen gas where the inlet is imposed at 0.005 m upstream of the flat plate. The computational domains, showed in Fig. 3.6, are similar to those presented as a verification test case (Section 3.1) in which diffuse reflection with complete thermal accommodation is applied as wall boundary condition.

Normalised density (ρ/ρ_∞) contours for zero-thickness, sharp, and truncated flat plates are shown en Fig. 3.7 and compared with numerical and experimental results. On examining this set of density contours plots, very good agreement is evident between the *dsmcFoam* results and the numerical and experimental studies [163, 164].

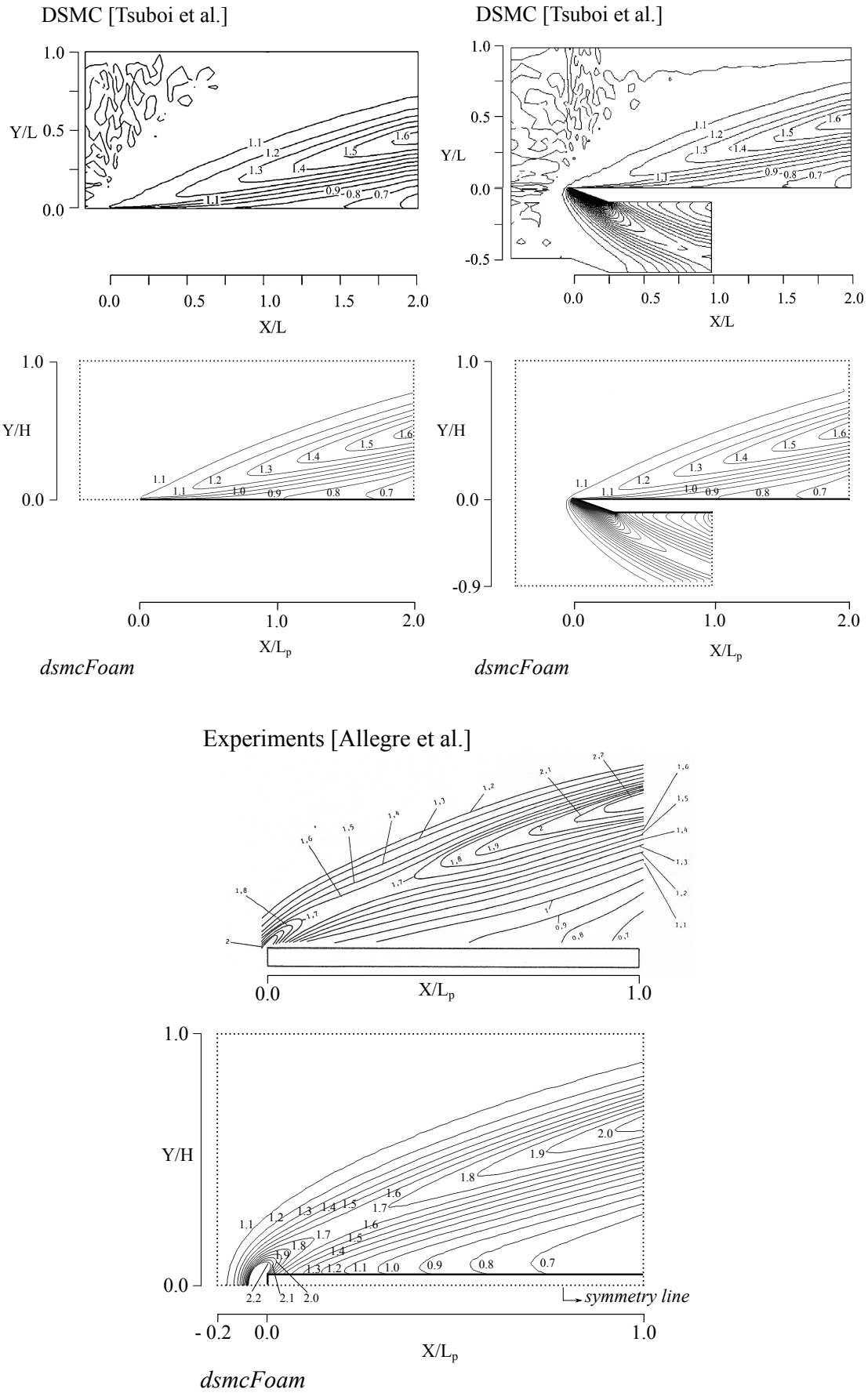

Figure 3.7: Density ratio (ρ/ρ_∞) contours around zero thickness, sharp, and truncated flat-plates.

The density (ρ/ρ_∞) and temperature (T/T_∞) distributions normal to the flat-plate surface for a location X/L = 1.5 are shown in Fig. 3.8 (a). Good agreement is found for the density distribution close to the flat-plate surface. The density ratio peak is well captured by the present simulation and it follows the same trend of the numerical and experimental results performed by Tsuboi *et al.* [164] and Lengrand *et al.* [147]; however, as the upper boundary condition is approached the *dsmcFoam* simulation predicts higher density ratios.

Analysing the temperature distribution plot, Fig. 3.8 (b), it is observed a difference between the rotational and translational temperatures, demonstrating thermal nonequilibrium conditions. Close agreement is observed in the translational temperature for the *dsmcFoam* simulations when compared with CNRS-DSMC results.

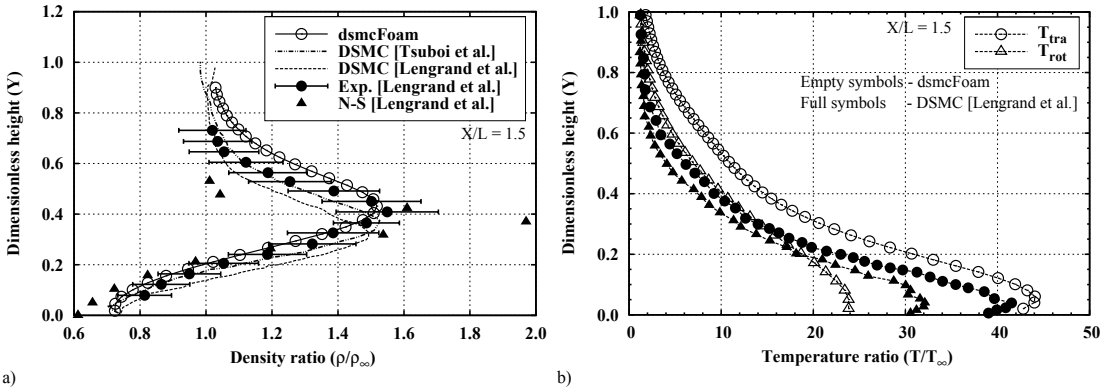

Figure 3.8: Density (ρ/ρ_∞) and temperature (T/T_∞) profiles normal to the flat plate at X/L = 1.5.

Figure 3.9 presents the heat transfer (C_h), pressure (C_p) and skin friction (C_f) coefficients along the flat plates. For the sharp flat plate case (left column) the comparison of the computed results with the experimental data in the vicinity of the leading edge shows a very good concurrence. As the flow approaches the trailing edge, a significant disagreement is observed between experimental results and DSMC simulations. However, a similar level of discrepancy was observed in both the N-S and DSMC-CNRS simulations.

According to Lengrand *et al.* [147], the possible sources of experimental error are related with uncertainties in the freestream conditions, measurements procedures, and the influence of the leading edge bluntness or bevel angle. In order to investigate the

impact of the leading edge bluntness, Fig. 3.9 (right column) shows the comparisons of the *dsmcFoam* results with experimental, DSMC, and N-S data for the truncated flat plate. It is clear that the heat transfer and pressure coefficients are affected by the flat plate bluntness from a location of $X/L_p = 0$ to $X/L_p \cong 0.2$. As the flow approaches the trailing edge, good agreement is found between the numerical and experimental data.

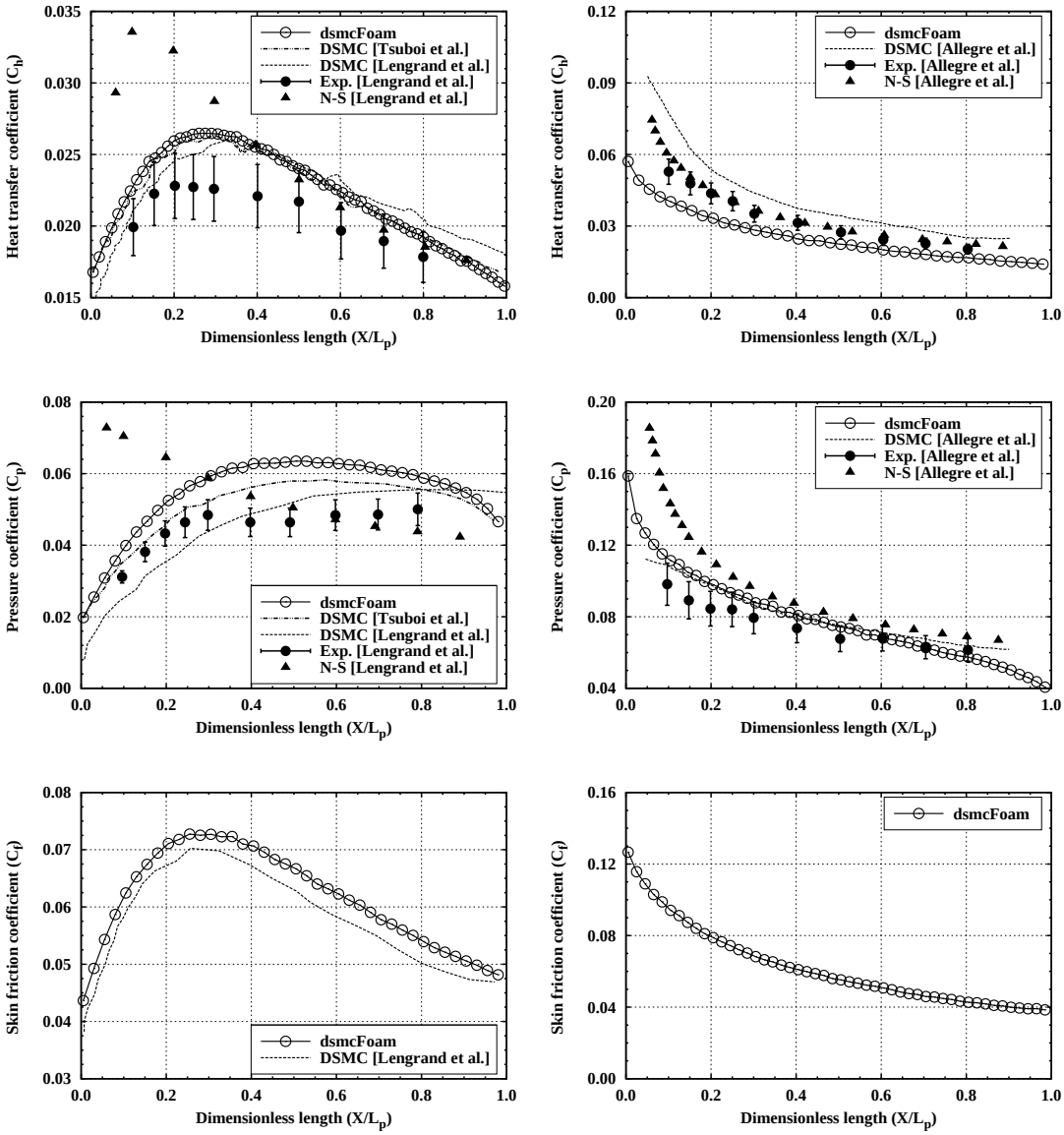

Figure 3.9: Comparison of heat transfer (C_h), pressure (C_p), and skin friction coefficients (C_f) for *dsmcFoam* simulations and numerical-experimental data for sharp (left) and truncated (right) flat plates.

To summarise this section, three-dimensional simulations of zero-thickness, sharp, and truncated leading edges were performed using *dsmcFoam* for hypersonic non-reacting flows. An excellent agreement was found for the density contour plots when compared with numerical and experimental data. The results also demonstrate how the leading edge affects the flow and shock structure over different flat plates. In addition, for the sharp flat plate a good concurrence was found for the aerodynamic properties at the leading edge until a location of $X/L_p = 0.2$; however, certain discrepancies were observed as the trailing is approached. In contrast with the sharp flat plate, the truncated case exhibited differences between the numerical and experimental data in the flat-plate leading edge and a good agreement towards the trailing edge. Furthermore, the comparisons between the DSMC and N-S results presented in this section demonstrated that the continuum approach, even when using slip velocity and temperature jump as boundary conditions, cannot be used with confidence to predict hypersonic aerothermodynamics under high nonequilibrium conditions.

3.2.2 Rarefied hypersonic flow over a 70° blunted cone

The flow over blunt bodies at high speeds and high altitudes is associated with complex flow interactions and the precise determination of the heating rate, aerodynamic forces, the flowfield surrounding the spacecraft, as well as the characterisation of the wake region is a key factor for the success of a re-entry mission.

In the the following experimental set-up, a 70° blunted cone, identical to that of the Mars Pathfinder probe, was chosen by the AGARD Working Group 18. The rarefied experiments were performed in five different facilities: the SR3 wind tunnel at Centre National de la Recherche Scientifique (CNRS-Meudom), the V2G, V3G and HEG wind tunnels at the Germany Aerospace Center (DRL-Göttigen), and the LENS wind tunnel at the Buffalo Research Center (Calspan University of Buffalo, USA). The experimental test conditions used in each of these experimental facilities are available in Ref. [162], however, only the experiments performed by the CNRS will be used in the present work aiming the *dsmcFoam* code validation for complex geometries.

Allegre *et al.* [170–172] provided detailed information regarding the rarefied experiments conducted at the CNRS facilities in Meudon, France. The CNRS group employed

three freestream flow conditions, representative of different levels of rarefaction, and three probe models, each one having a base and afterbody sting diameter of 0.05 and 0.0125 m, respectively.

The model utilised for the density flowfield measurements was made of brass, water cooled, and consequently the wall temperature remained close to 290 K during the all measurements. A electron beam fluorescent technique was used to measure the density field around the blunted cone [170]. For the aerodynamic force measurements, the model was made of aluminium, uncooled with the wall temperature estimated to be close to 350 K. The model was directly attached to an external balance which provided direct measurements of drag, lift, and pitching moment and indirect determinations of the centre of pressure at different angles of attack [171]. For heat transfer measurements, a steel model was used in which the wall temperature was kept close to 300 K [172]. Chrome alumel (Ch/Al) thermocouples were embedded through the wall thickness at nine locations along the forebody, base plane, and sting and the thin-wall technique was applied for measuring the heat fluxes on the steel probe. The freestream conditions for a chemically frozen flows used in the SR3 wind tunnel experiments are presented in Table 3.3.

Table 3.3: Freestream conditions for the 70° blunted cone simulations.

Parameter	**Value**	**Unit**
Velocity (V_∞)	1503.1	m/s
Temperature (T_∞)	13.316	K
Number density (n_∞)	3.717×10^{20}	m^{-3}
Density (ρ_∞)	1.730×10^{-5}	kg/m^3
Pressure (p_∞)	6.833×10^{-2}	Pa
Dynamic viscosity (μ_∞)	7.279×10^{-6}	$N.s/m^2$
Mean free path (λ_∞)	1.691×10^{-3}	m
Overall Knudsen (Kn_d)	0.034	
Overall Reynolds (Re_d)	178.6	

An extensive set of simulations at these experimental test conditions were made using both DSMC [173–182] and Navier-Stokes [183–186] methods prior to the release of the experimental data. In this way, it was possible to perform a blind validation

process of the computational codes.

In the present work, the simulated freestream conditions are similar to those used in the SR3 low-density wind tunnel (case 1) [170–172]. The Mars pathfinder probe was assumed to be immersed in a nonreacting nitrogen uniform flow with energy exchange allowed between the translational, rotational and vibrational modes. The energy exchange between the kinetic and internal modes was controlled by the Larsen-Borgnakke statistical model [104]. The molecular collision kinetics were modelled by the variable hard sphere (VHS) model [97] and the no time counter (NTC) collision sampling technique [187].

Figure 3.10 (a) presents information concerning the experimental model configurations and Fig 3.10 (b) shows an amplified view of the *dsmcFoam* mesh. The computational mesh was composed of 7,125,852 hexahedral cells with 10.5 simulated molecules per cell. Each simulation was performed using 240 processors on the HPC machine University of Strathclyde.

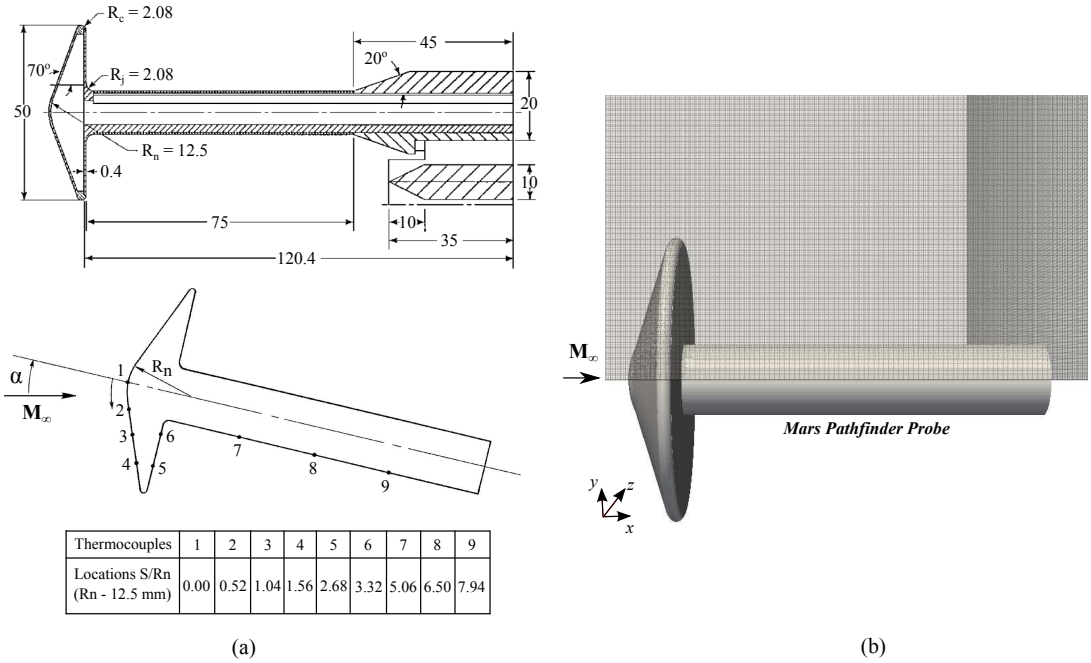

Thermocouples	1	2	3	4	5	6	7	8	9
Locations S/Rn (Rn - 12.5 mm)	0.00	0.52	1.04	1.56	2.68	3.32	5.06	6.50	7.94

(a) (b)

Figure 3.10: (a) Experimental model for heat transfer measurements and thermocouple locations [172], and (b) Magnified view of the *dsmcFoam* three-dimensional computational mesh.

The computational domain adopted was large enough such that the upstream, downstream, and top boundaries conditions could be specified as freestream conditions. In order to minimise the computational effort, the numerical simulation utilized the symmetry of the problem and half of the actual geometry was modelled. The undisturbed freestream conditions were imposed 0.02 m upstream of the probe, and the computational domain normal to the probe extended to a distance of 0.08 m in the y- and z-directions. The wall temperature was set at 290, 300, and 350 K for density, heat transfer and aerodynamic force measurements, respectively. The surface boundary condition assumed the gas-surface interaction to be diffuse with full thermal accommodation at the specified surface temperature.

In Fig. 3.11 experimental density flowfields at different angles of attack [170] are compared with the results from the *dsmcFoam* calculations. The experimental results are normalised using the free-stream values without the model in the test section and the calculated results are divided by the freestream conditions shown in Table 3.3. Qualitatively, the results show a good level of concurrence between the experimental and *dsmcFoam* results. According to Ref. [170] the flowfield density measurement accuracy is estimated to be 10% except for the region encompassing the shock wave located in the forebody region, which is characterised by high-density gradients.

Comparisons is also made with the DAC (DSMC Analysis Code) simulations, developed at the NASA Johnson Space Flight Center [188], and available in Ref. [173]. According to Fig. 3.12, an excellent agreement of density ratio (ρ/ρ_∞), overall temperature (T_{ov}), and Mach number (M) contours at zero degree angle of attack was achieved between the codes.

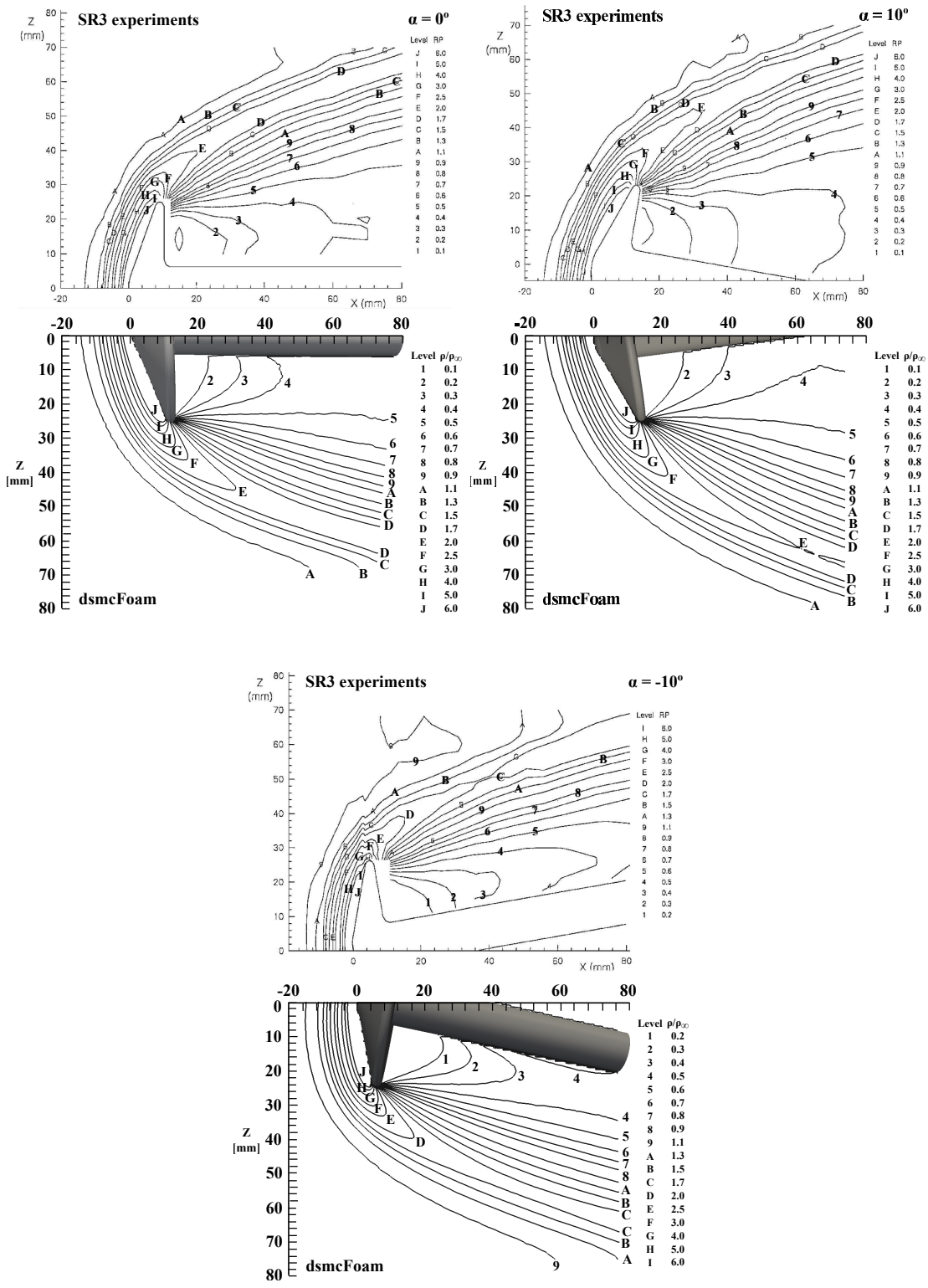

Figure 3.11: Density ratio (ρ/ρ_∞) distribution for *dsmcFoam* and SR3 [170] experiments at different angles of attack.

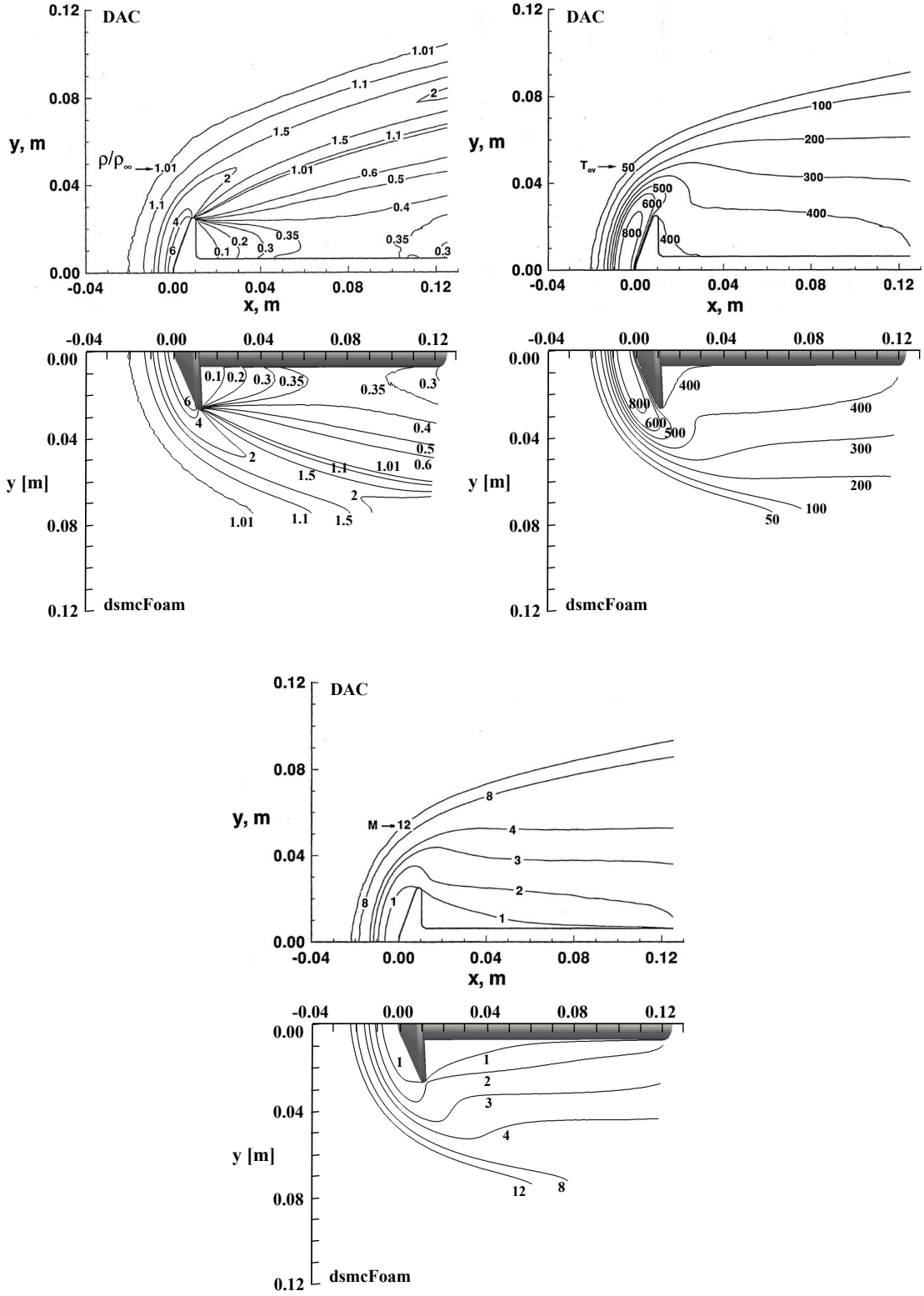

Figure 3.12: Density ratio (ρ/ρ_∞), overall temperature (T_{ov}) and Mach number (M) distribution for *dsmcFoam* and DAC simulations [173] at zero angle of attack.

The aerodynamic forces and moments were also experimentally and numerically studied [171, 175, 177] at different angles of attack. According to Figs. 3.13 and 3.14 a satisfactory concurrence is found between the experimental data and *dsmcFoam* simulations. According to Ref. [171], the global uncertainty on the aerodynamic coefficients and forces not exceeded ±3% and the maximum difference between measured and simulated results was 8.6% on the normal force at 20^o angle of attack. Table 3.4 shows the drag and lift coefficients, axial and formal forces for experimental measurements and numerical predictions using the *dsmcFoam* code.

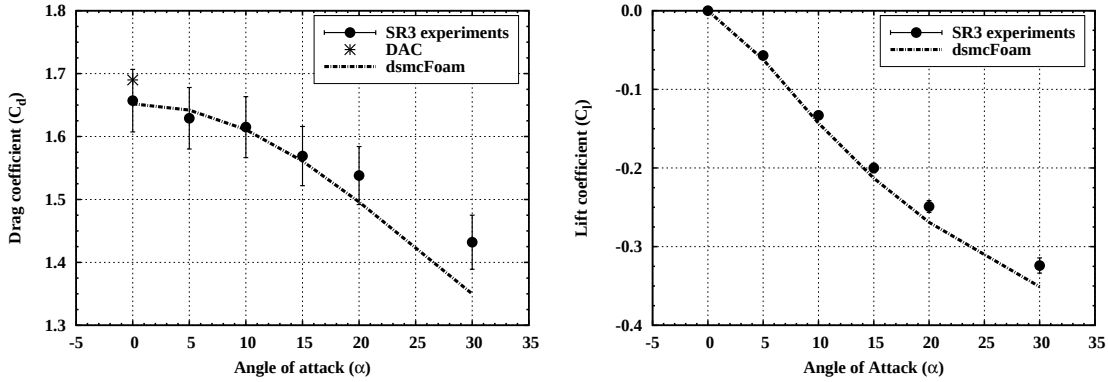

Figure 3.13: Drag (C_d) and lift (C_l) coefficient at different angles of attack.

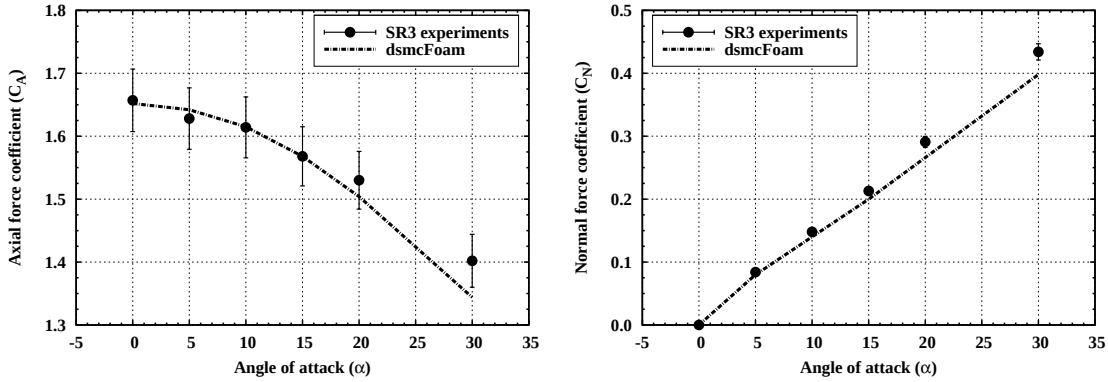

Figure 3.14: Axial (C_A) and normal (C_N) force at different angles of attack.

The impact of the angle of attack on the heat transfer (C_h) and pressure (C_p) coefficients are shown in Figs. 3.15 and 3.16. In this set of plots, the data are presented as a function of the arc distance (s/R_n) measured from the forebody stagnation point to the end of the sting. Furthermore, dotted lines represent the *dsmcFoam* simulations,

Table 3.4: Experimental and *dsmcFoam*-calculated aerodynamic coefficients and forces.

Angle	**Drag**		**Lift**		**Axial force**		**Normal force**	
	exp.	**calc.**	**exp.**	**calc.**	**exp.**	**calc.**	**exp.**	**calc.**
0^o	1.657	1.652	0.000	0.000	1.657	1.652	0.000	0.000
5^o	1.629	1.642	-0.057	-0.062	1.628	1.642	0.084	0.080
10^o	1.615	1.611	-0.133	-0.143	1.614	1.615	0.148	0.140
15^o	1.569	1.561	-0.200	-0.213	1.568	1.568	0.213	0.200
20^o	1.538	1.496	-0.249	-0.269	1.530	1.504	0.291	0.266
30^o	1.432	1.350	-0.324	-0.351	1.402	1.344	0.434	0.398

and the full line and points show the DAC simulations and CNRS experimental results, respectively [172, 174].

When the *dsmcFoam* results for (C_h) and (C_p) are compared with the DAC and SR3 low-density wind tunnel results at zero angle of attack, the agreement is very good in the region of the forebody, base plane and sting. However, the same level of agreement is not observed between the present simulated data and the experimental results when the angle of attack is increased. In addition, it is observed from Fig. 3.17, that the peak of the transfer at 30^o occurs just before the flow expansion on the probe shoulder, where there are no thermocouples located. According to Fig. 3.10 (a), the last thermocouple on the forebody region is located at $S_{Rn} = 1.56$ and the simulated heat transfer peak occurs at $S_{Rn} = 2.0$.

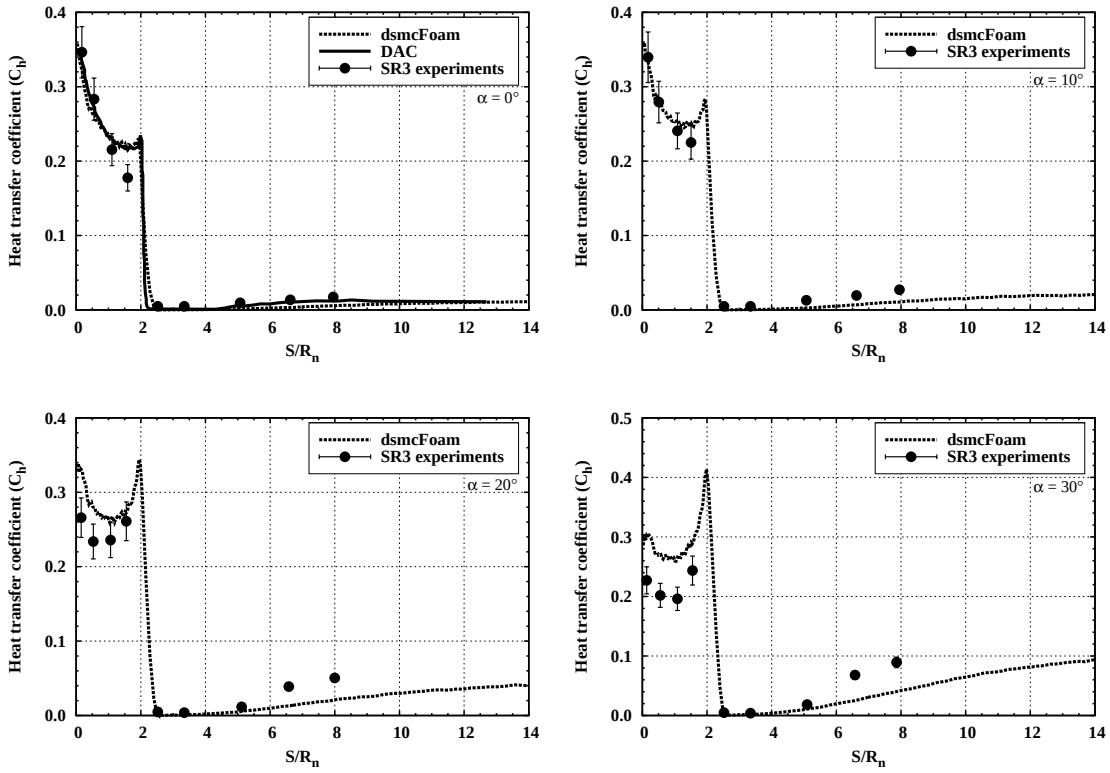

Figure 3.15: Heat transfer (C_h) coefficient for *dsmcFoam*, DAC, and CNRS experiments at different angles of attack.

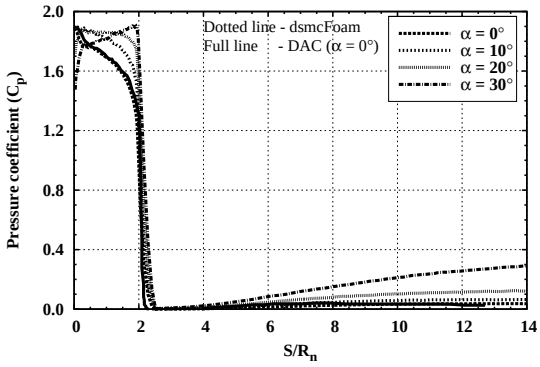

Figure 3.16: Pressure (C_p) coefficient for *dsmcFoam* and DAC simulation at different angles of attack.

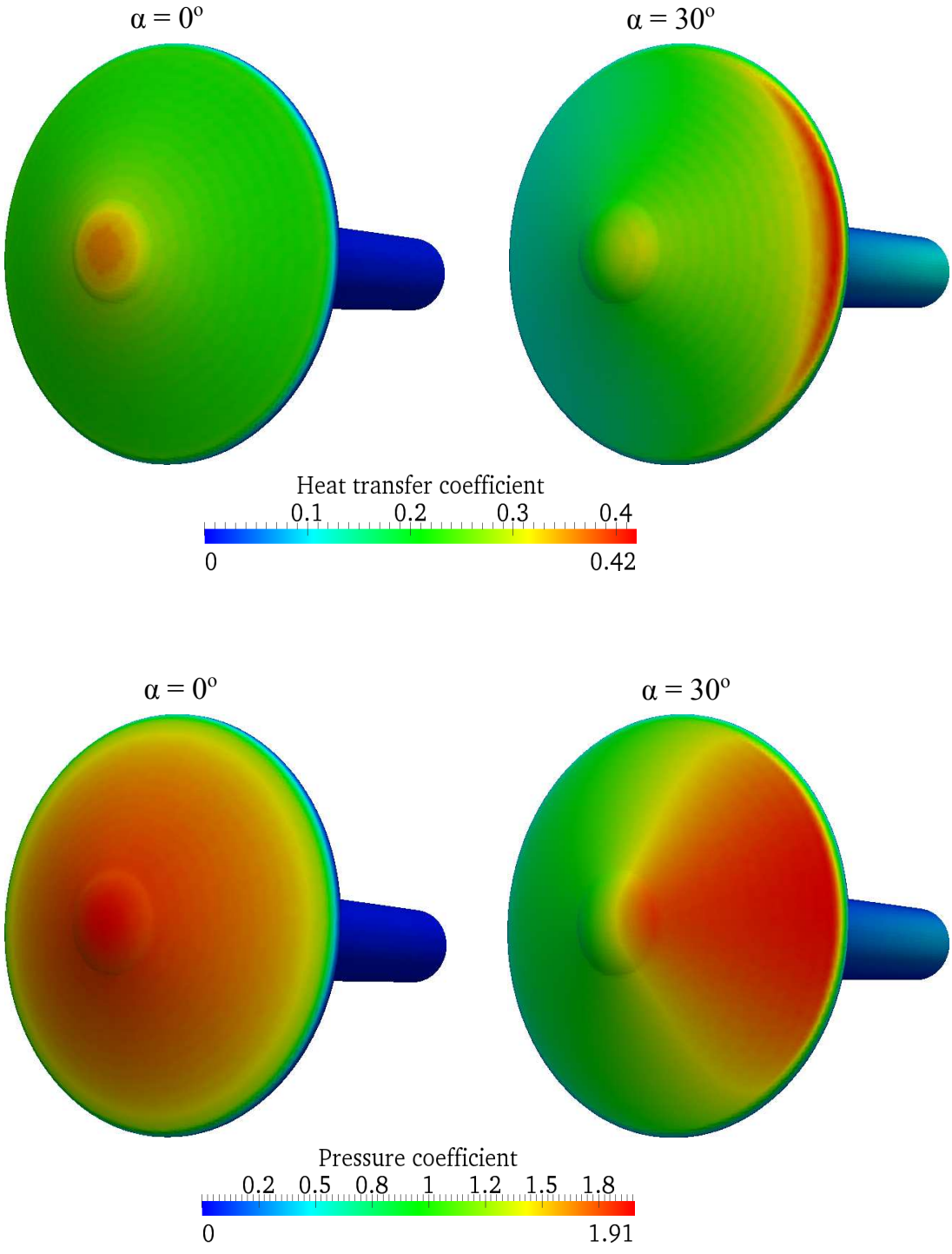

Figure 3.17: Heat transfer (C_h) and pressure (C_p) coefficient contours at 0^o (left) and 30^o (right) angle of attack.

When a probe enters a planetary atmosphere at high velocities the forebody flowfield is dominated by a strong shock wave which causes the excitation, dissociation and possibly ionisation of the gas surrounding the vehicle. Moreover, this highly thermochemical nonequilibrium flow rapidly expands around the probe shoulder into the near wake region with a significant increase in the degree of rarefaction and flow complexity in the afterbody region as shown in Fig. 3.18 (a) [173, 189, 190]. Due the flowfield complexity, the aerothermodynamics of a wake may not be accurately predicted. According to Wright and Milos [191] the uncertainty related to the aeroheating predictions on this region are typically assumed to be in the range of 50-300%. This level of uncertainty plays a significant role on the vehicle design and in the correct selection of a thermal protection system (TPS).

In order to compare the results obtained using the *dsmcFoam* code and those provided by Moss *et al.* [173], normalised density, velocity, and temperature are determined for four different locations in the probe afterbody region as depicted in Fig. 3.18 (b).

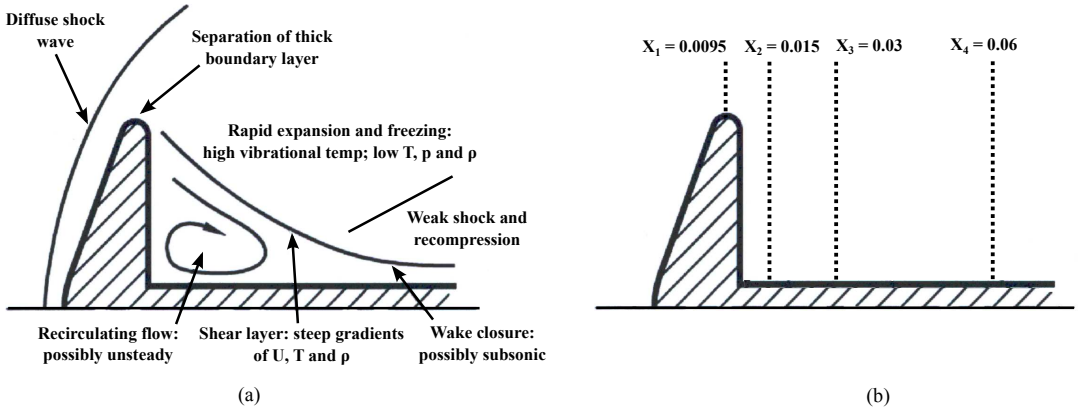

Figure 3.18: (a) Schematic of the planetary probe flow structure [190], and (b) Freestream properties measurement locations.

According to Fig. 3.19, 3.21 and 3.20, it is clear that a very good agreement exist for both DSMC simulations. However, a small disagreement is observed in the expansion region for density and temperature profiles at $X_1 = 0.0095$, probe shoulder. In this region a very strong flow expansion occurs and different meshing procedures between the codes may have some influence on the flowfield structure.

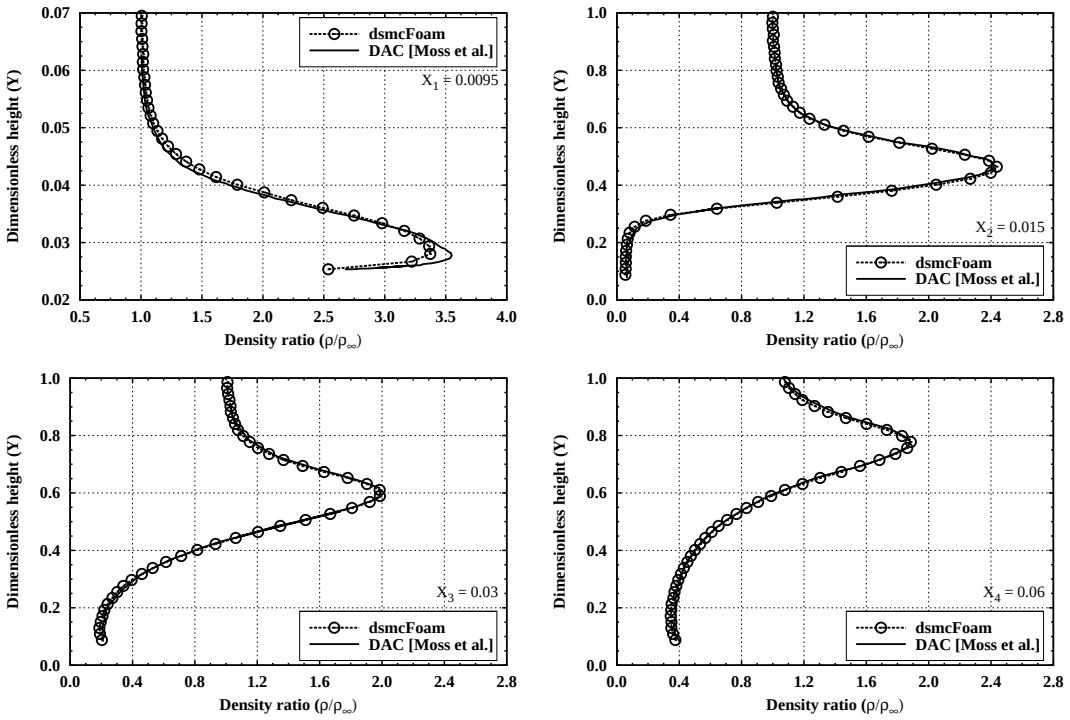

Figure 3.19: Density profiles (ρ/ρ_∞) for *dsmcFoam* and DAC.

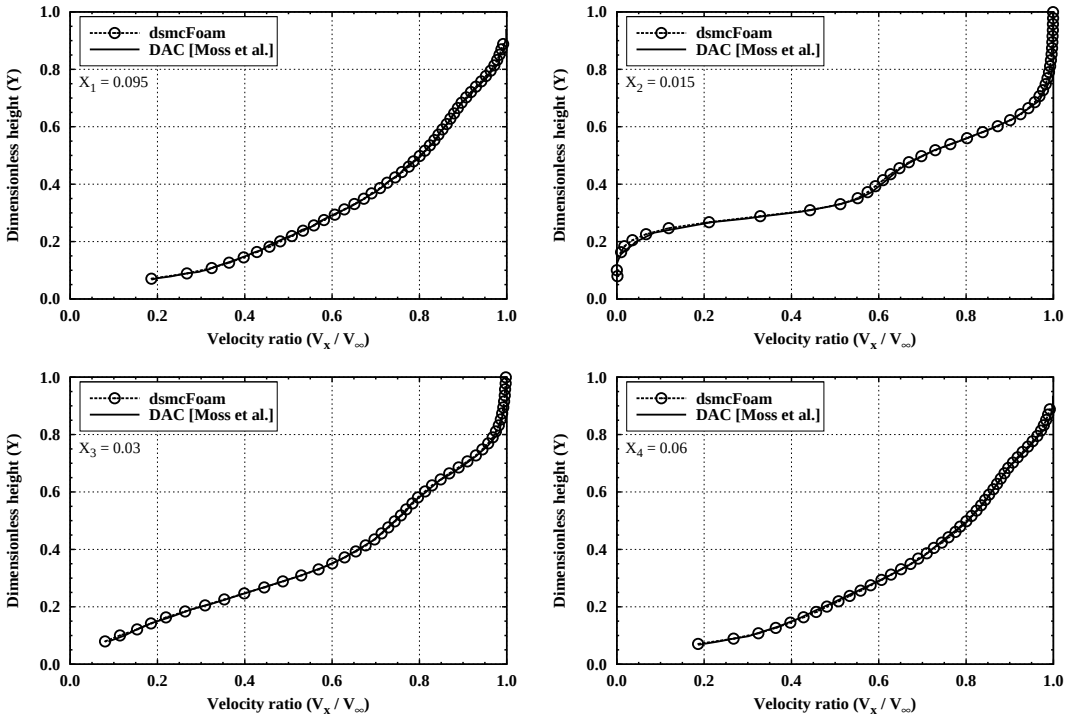

Figure 3.20: Velocity profiles (V_x/V_∞) for *dsmcFoam* and DAC.

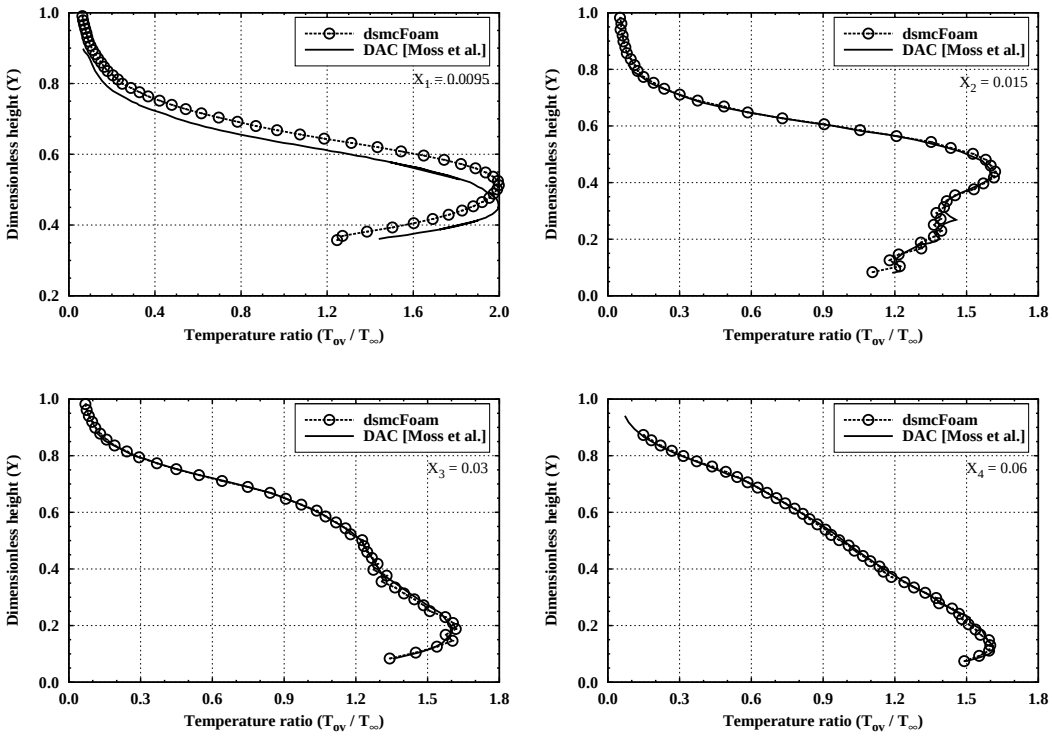

Figure 3.21: Temperature profiles (T_{ov}/T_{∞}) for *dsmcFoam* and DAC.

To summarise this section, simulations were performed using the *dsmcFoam* code for non-reacting flows over flat plates and the Mars Pathfinder probe. The present data were compared with experimental and numerical solutions available in the current open literature. Assuming the uncertainty of the experimental data to be approximately 10% [147, 163, 170–172] a satisfactory level of agreement between the the measurements and computations has been achieved. It is concluded that the *dsmcFoam* code has been validated for non-reacting flows with sufficient accuracy for simple and complex 3D geometries.

3.3 *dsmcFoam* validation for hypersonic reacting flows

During reentry into the Earth's upper atmosphere, a strong bow-shock is formed upstream of the reentry vehicle leading to a increase of the surrounding air temperature. This temperature may exceed 10,000 K causing the vibrational excitation of the gas with chemical reactions such as dissociation, exchange and possible ionisation occur-

ring. Chemical reactions can have a significant influence on the heating rates and pressure loads acting on the vehicle surface during the reentry phase and the ability to accurately model the nonequilibrium and chemically reacting flows becomes a key feature in hypersonic aerothermodynamics.

As mentioned earlier in Section 2.1.2, a chemistry model called the "Quantum-Kinetic" (QK) approach, which rely on the vibrational states of colliding molecules, has been implemented in the *dsmcFoam* code. In order to validate this chemistry model, it is suitable to test the implementation for real cases of atmospheric reentry. In pursuit of this goal, rarefied hypersonic reacting and non-reacting flows over a cylinder and the Orion Crew Module are presented in the following subsections.

3.3.1 Rarefied hypersonic flow over a 2D cylinder

In order to validate the QK model implementation, a hypersonic reacting flow over a 2D cylinder of 2 m diameter is considered. The atmospheric freestream conditions are described in Table 3.5.

Table 3.5: Freestream conditions for the 2D cylinder.

Parameter	**Value**	**Unit**
Velocity (V_∞)	6813	m/s
Temperature (T_∞)	187	K
Number density (n_∞)	1.433×10^{20}	m^{-3}
Density (ρ_∞)	6.865×10^{-6}	kg/m^3
Pressure (p_∞)	3.698×10^{-1}	Pa
Dynamic viscosity (μ_∞)	1.339×10^{-5}	$N.s/m^2$
Mean free path (λ_∞)	8.241×10^{-3}	m
Overall Knudsen (Kn_d)	0.004	
Overall Reynolds (Re_d)	6985.6	

These conditions correspond to the Earth's atmosphere at 86 km altitude composed by 78.85% N_2 and 21.15% O_2 with reentry Mach number equal to 24.85. The cylinder walls are modelled as fully diffuse, and two cases are considered; one with no reactions, and one with all 19 reactions described in Table 2.1. Comparison are made with the equivalent solutions using the established DSMC code MONACO [130] which employs

the TCE chemistry model [119]. In all cases all the rotational and vibrational collision numbers are set to 5 and 50, respectively, and the TCE Arrhenius rates for dissociation and exchange are provided by the QK analytical equilibrium values. The mesh size for the *dsmcFoam* study is composed by 240,000 cells with a time-step fixed at 1.0×10^{-7} s and, following the particle sensitivity trials, there were 23.4 million DSMC particles in the system at the steady-state. For the MONACO study the domain contains 175,000 with automatic sub-cell generation and the total number of DSMC particles at steady-state was 37.5 million. In addition, cell-based, variable time-step are used such that ratio of the time step to mean collision time in each cell is approximately 0.2. In this scenario, the reacting flow over the 2D cylinder is considered as a benchmark trial for future chemistry model implementations.

Figure 3.22 show the reacting and non-reacting comparisons between the DSMC codes for number density, temperature, and velocity along the stagnation streamline. For the non-reacting case, it is clear that the number density profiles are almost equivalent, while the translational, rotational, and vibrational temperatures profiles show very close concurrence. The velocity profiles predicted by both codes along the stagnation streamline are in close agreement, and the shock region covers a distance between 26 and 40 cm from the cylinder stagnation point.

With all 19 reactions activated, number density, temperature, and velocity profiles along the stagnation line are again compared. As the chemical reaction occur are mainly characterised by endothermicity, the local enthalpy is reduced and the maximum shock stand-off distance moves to a position close to the cylinder (approximately 36 cm) in comparison with the non-reacting case (40 cm).

Turning to Fig. 3.22, right-hand column, the N_2 and NO levels calculated by each code are in relatively close agreement. Although trends are similar, the values for atomic species predicted by *dsmcFoam* (QK) are in excess to those determined by MONACO (TCE). However, the opposite is true for O_2, with the MONACO producing producing values exceeding those of *dsmcFoam* (QK). The increase number of dissociation events using the QK may be qualitatively explained with reference to Wysong *et al.* [127]: the magnitude of the lower level vibrational cross-section for the QK method would mean that more dissociation events are likely, compared with the TCE approach, in

non-equilibrium flows with relatively low vibrational excitation, such as high-altitude reentry.

Significant reduction in the values of all three temperature modes under reacting flows are evident. Both codes predicted a peak of translational temperature along the stagnation line of approximately 20,000 K. This is in contrast with the non-reacting case, which has a peak of approximately 25,000 K. The peaks of rotational and vibrational temperatures are also in close agreement, however, the general *dsmcFoam* QK temperatures values shows a small but consistent shift to the left in comparison with MONACO-based ones. This effect is consistent with the differences in the shock structure indicated by the left-ward shift in the velocity plots.

The surface properties are shown in Figs. 3.23 and 3.24. The surface pressure values are in very close agreement between the codes for both reacting and inert conditions. A reduction of almost 100% for the heat flux on the cylinder is evident when comparing the reacting and non-reacting cases. It is clear that the process of dissociation has lead to reduced flow energy and a consequential reduction of energy transfer to the body. For reacting condition, the peak-value of the heat flux is 67 W/m^2 for QK. This difference is 4.6% compared with TCE and represents a similar margin to the range of the peak-heat fluxes found in a separate case study of non-reacting flow over a 2D cylinder using a variety of DSMC codes [192].

Figures 3.24 shows the surface temperature jump and slip-velocity predictions for inert and reacting conditions. The general trends are similar for MONACO and *dsmcFoam*, however, there appears to be a greater level of disparity at some location on the cylinder surface compared with the results for pressure and heat flux, with *dsmcFoam*-QK predicting generally higher values jump and slip.

Finally, Figs. 3.25 and 3.26 show the Mach number and NO density, and temperatures contours for each code, respectively. It is clear that the diffuse nature of the rarefied shock has been captured by both codes. Although, differences exists between the results for the predicted velocity and temperature fields, it is evident that the local Mach numbers are in close agreement. For the NO field, small differences are observed between the solutions in this qualitative comparison, with the *dsmcFoam* (QK) approach appearing to predict a thinner species layer in the range approaching to the

peak of NO values. Nonetheless, the general flow features appear to be similar for both chemistry approaches. In addition, the temperature fields, in general, shows a similar qualitative concurrence in all areas of the flowfield, with only subtle differences apparent in certain regions.

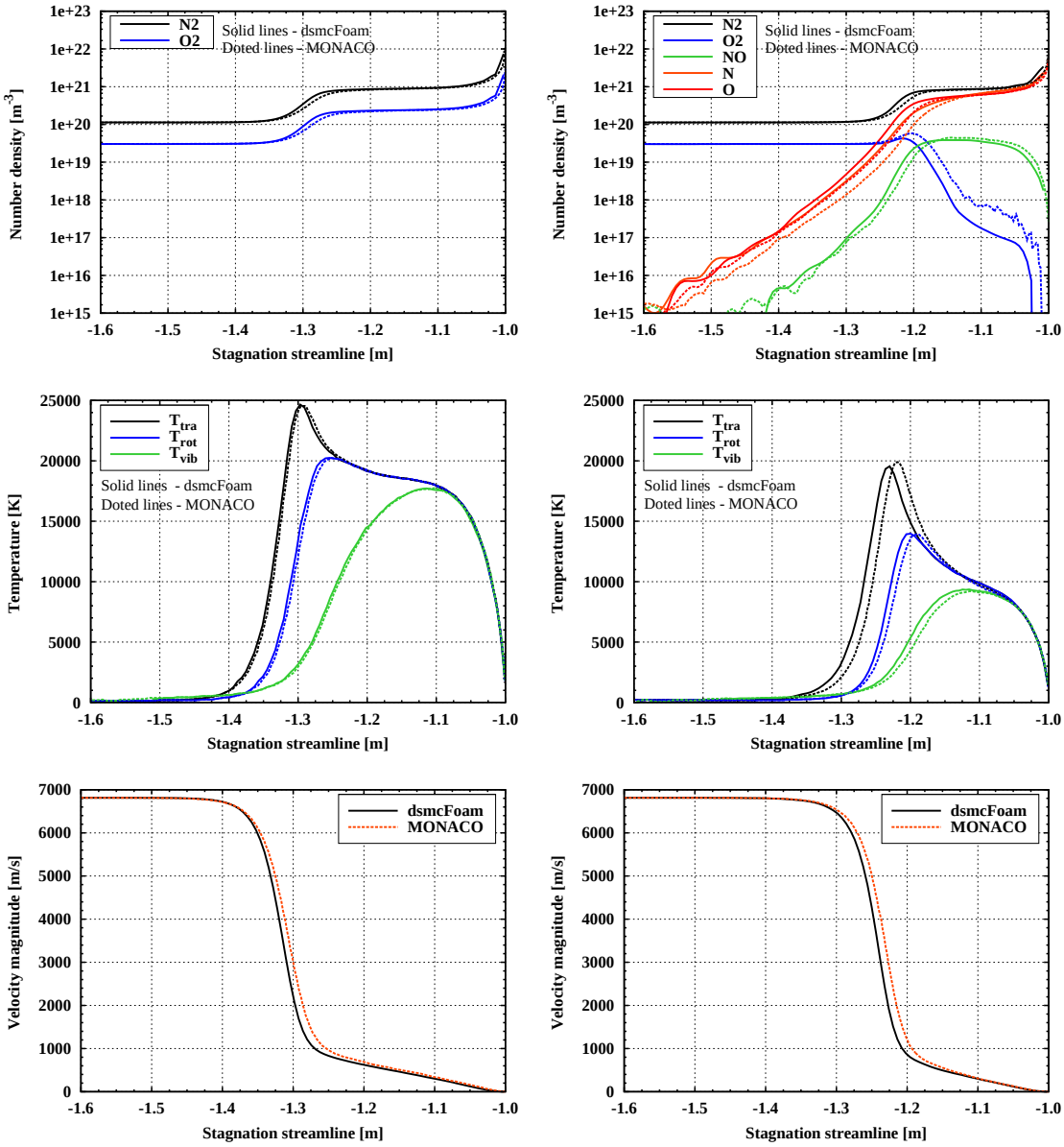

Figure 3.22: Number density, temperature and velocity profiles along the stagnation streamline for non-reacting (left) and reacting (right) air flow over a 2D cylinder.

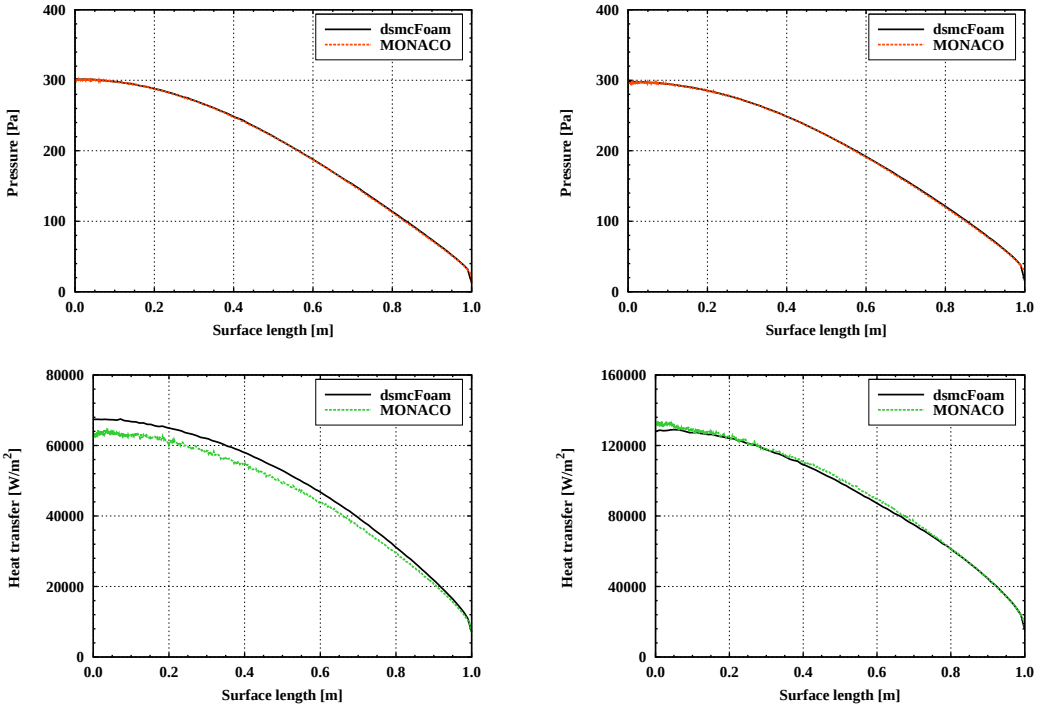

Figure 3.23: Surface heat transfer and pressure along the 2D cylinder for reacting (left) and non-reacting (right) air flow.

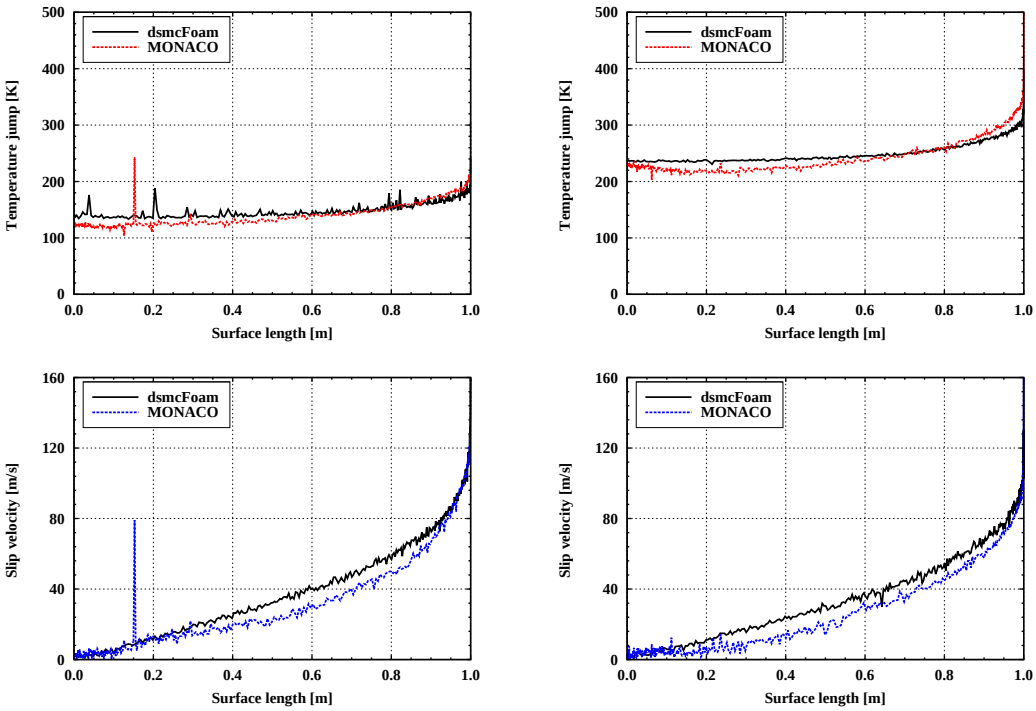

Figure 3.24: Slip velocity and temperature jump along the 2D cylinder for reacting (left) and non-reacting (right) air flow.

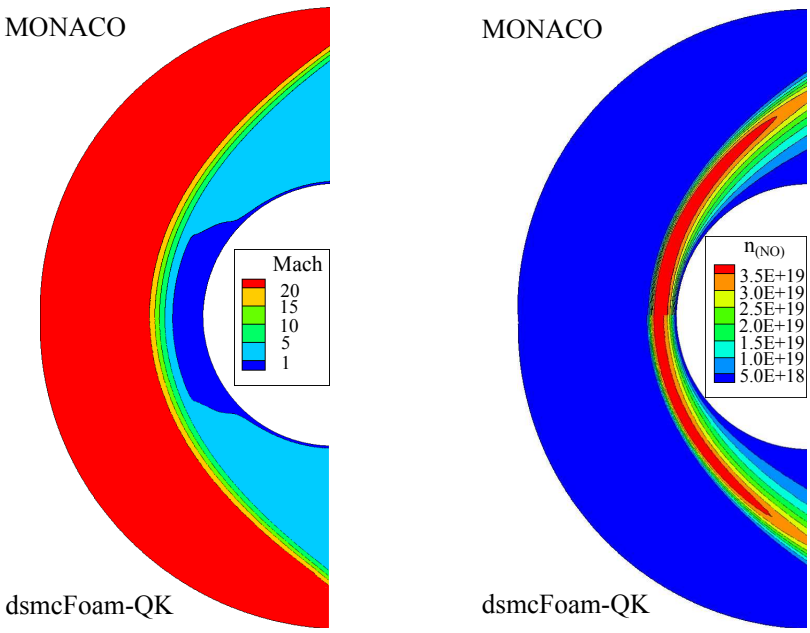

(a) (b)

Figure 3.25: Mach number and NO contours predicted by *dsmcFoam* (QK) and MONACO (TCE) for reacting air flow over a 2D cylinder.

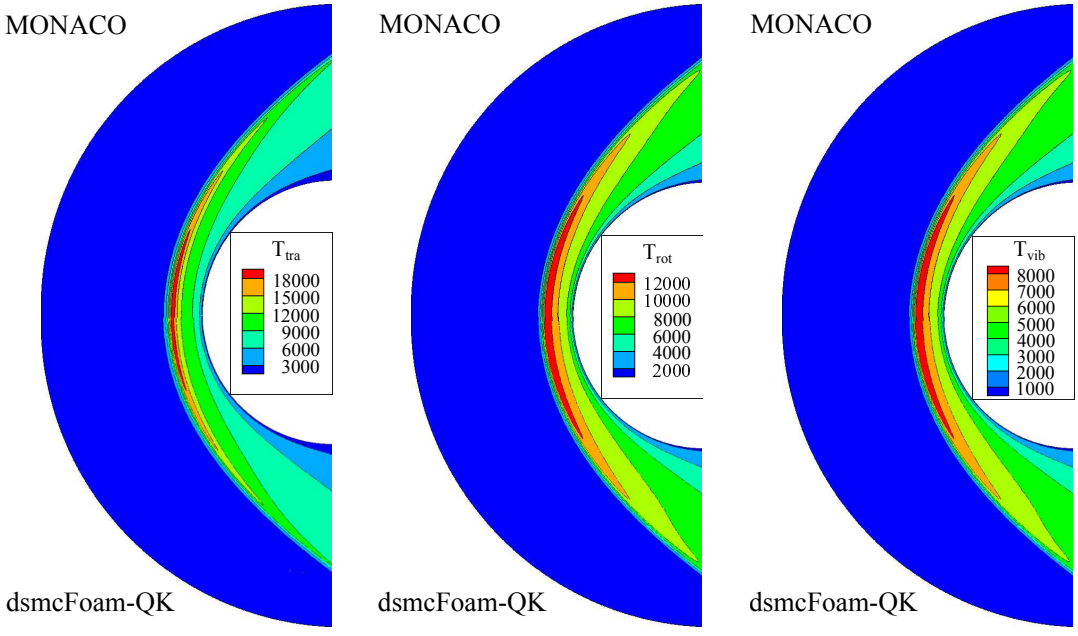

(a) (b) (c)

Figure 3.26: Translational, rotational, and vibrational temperature contours predicted by *dsmcFoam* (QK) and MONACO (TCE) for reacting air flow over a 2D cylinder.

3.3.2 Rarefied hypersonic flow over the Orion Crew Module

Rarefied hypersonic reacting flow is used here to study the Orion Crew Module (CM) during the reentry at altitudes of 95 and 105 km, respectively. In this validation test case, results obtained using the *dsmcFoam*-QK (19 species reaction model) and *dsmcFoam*-NR (no reactions) are compared with numerical solutions provide by Wilmoth *et al.* [193] and Moss *et al.* [194].

DSMC simuation was performed by Wilmoth *et al.* [193] using the DS2V code [20] with both traditional rate-based chemistry models (TCE) and a mixture of TCE-QK model, and labeled as "new chemistry" [193]. In this mixed chemistry model, exchange and recombination reactions were not available at the time of the simulations and they were treated with the traditional rate-based methods. However, dissociation reactions were performed using the new QK collision-based methodology.

Moss *et al.* [194] conducted a series of numerical simulations in order to characterise the Orion CM aerodynamics from free molecular to continuum hypersonic conditions. For the rarefied portion of the Earth's atmosphere, two DSMC mature codes was employed, DS3V and DAC, both using a five-species reacting air gas model.

In the present work, advantage was taken from Orion's symmetry in order to reduce the computational costs. In this way, the computational mesh was prepared using a quarter-section model with symmetry boundary condition, as depicted in Fig 3.27 For the 105 km altitude case, a numerical mesh of $130\times100\times100$ was employed covering a domain size of 13 m in the flow direction and 10 in the y- and z-directions. The OpenFOAM mesh utility called $snappyHexMesh$ was used to 'snap' the mesh on to the Orion CAD geometry creating hexahedral cells onto the surface. After this process, a total of 15.06×10^6 and 1.293×10^6 cells were employed by the *dsmcFoam* calculation for 95 and 105 km altitude, respectively.

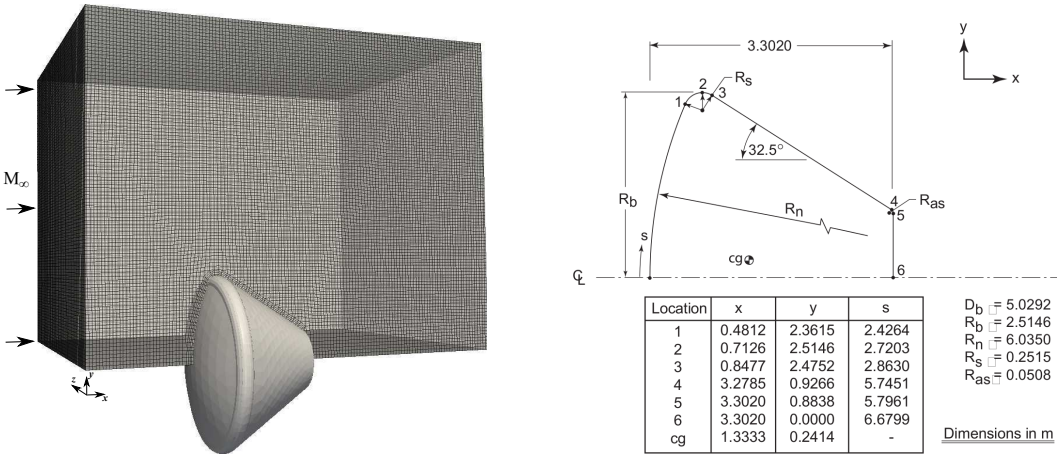

Figure 3.27: Orion computational mesh for 105 km of altitude (left), and capsule main geometric parameters (right) [194].

The freestream conditions are similar to those previously analysed by Moss *et al.* [194] for the Orion CM in real re-entry conditions. At both altitudes considered here, a freestream velocity of 7600 m/s was adopted with the capsule surface being modelled as diffusive with full thermal and momentum accommodation. Details of the entry conditions used in the present work as well as the gas properties are shown in Tables 3.6 and 3.7.

Table 3.6: Re-entry freestream conditions for the Orion Crew Module.

Altitude (km)	**Density (kg/m^3)**	**Temperature (K)**	**Pressure (Pa)**	**Kn_∞**
95	1.38×10^{-6}	189	0.076	0.0108
105	2.30×10^{-7}	211	0.014	0.0629

Table 3.7: Representative gas properties.

Parameter	Nitrogen (N_2)	Oxygen (O_2)	Atomic Oxygen (O)
Molecular mass (kg)	46.5×10^{-27}	53.12×10^{-27}	26.56×10^{-27}
Molecular diameter (m)	4.17×10^{-10}	4.07×10^{-10}	3.00×10^{-10}
Composition (95 km)	0.78685	0.19719	0.0108
Composition (105 km)	0.78187	0.15280	0.0629
Viscosity index	0.74	0.77	0.80

Figure 3.28 shows a comparison of the molecular and atomic mole fractions extracted along the stagnation line for the two altitudes considered. Excellent agreement is observed between the *dsmcFoam*-QK and the DS2V (new chemistry). Nevertheless, the production of the molecular species NO through exchange in the *dsmcFoam* calculations seems to be slightly underpredicted when compared with DS2V computations. Considering that Wilmoth's simulations were performed using a mixed TCE-QK chemistry model, very good concurrence was achieved with the *dsmcFoam*-QK code.

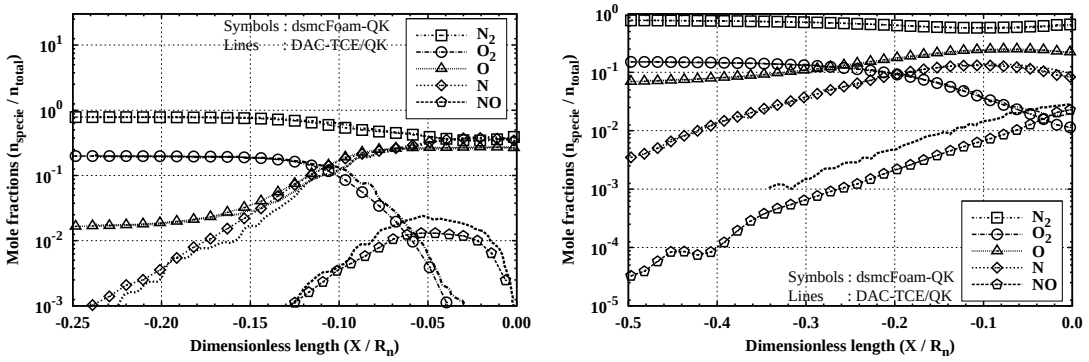

Figure 3.28: Mole fractions for molecular and atomic species predicted using *dsmcFoam* (QK) and DS2V (new chemistry), 95 (left) and 105 (right) km.

One of the most important features for atmospheric reentry is the heat flux measurements acting on the body which have a direct influence on the thermal protection system design and material selection. In order to investigate the influence of reacting and non-reacting flows over the the Orion capsule surface at 95 and 105 km of altitude,

comparisons of surface heat flux measurements using the *dsmcFoam*, DS2V, and DAC codes are presented in Fig. 3.29. According to the left-hand side plot, at 95 km altitude, the heat transfer coefficients (C_h) calculated by both codes are in relatively close agreement. Although the trends are similar, it is evident that the heat flux predicted using the *dsmcFoam*-QK is in excess when compared with the DS2V calculations. Comparing the *dsmcFoam* computations at 95 km altitude for reacting and non-reacting flows, a reduction of 36.8% in the C_h is observed.

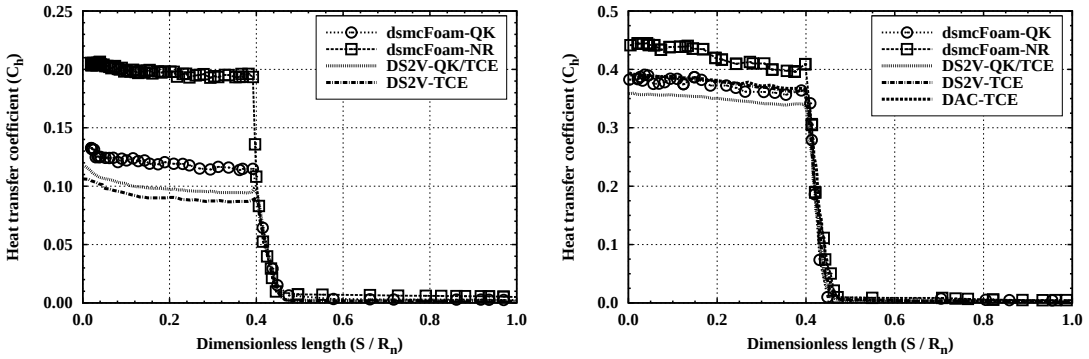

Figure 3.29: Orion surface heat transfer coefficient (C_h) predicted using *dsmcFoam* (QK), DS2V (new and old chemistry), and DAC for 95 (left) and 105 (right) km..

According to the right-hand plot of Fig. 3.29, it is evident that the heat transfer coefficient predicted by *dsmcFoam*-QK is in very close agreement with DS2V (old chemistry). Furthermore, in spite of following a similar pattern to the QK approach, the DS2V (new chemistry) appears to underpredict C_h.

The sensitivity of the aerodynamic forces and moments to chemical reactions is presented in Table 3.8 for an altitude of 95 km. According to the simulated data, the DSMC solutions show that the Orion aerodynamics are insensitive to the inclusion of chemical reactions where the maximum difference was of the order of 1.28%. In spite of the chemical insensitivity, reactive flows do play a very important role on the shock wave temperature and heat flux reduction to the vehicle surface, as previously discussed.

Finally, Tables 3.9 and 3.10 shows the *dsmcFoam* aerodynamic calculations for the Orion capsule at 105 km altitude and two angles of attack, 0^o and -26^o, respectively. Included in these tables are the results from DAC and DS3V codes, which both use the DSMC technique, and LAURA which provide solutions to the Navier-Stokes-Fourier equations [194]. For both angles of attack investigated, good agreement is shown between the *dsmcFoam*, DAC, and DS3V. However, due the rarefaction effects, the results obtained using the LAURA code show significant differences compared with the DSMC solutions. In general, the results show a good level of agreement and consistency between the different computational tools.

Table 3.8: *dsmcFoam* aerodynamic calculations of a rarefied hypersonic nonreacting (NR) and reacting (QK) flow over the Orion CM at 95 km altitude and 0^o angle of attack.

Parameter	***dsmcFoam*** **(NR)**	***dsmcFoam*** **(QK)**	**Difference** **(%)**
Drag (C_D)	1.566	1.587	1.28
Lift (C_L)	0.000	0.000	0.00
Axial force (C_D)	1.566	1.587	1.28
Normal force (C_N)	0.000	0.000	0.00
Pitching moment ($C_{m,cg}$)	-0.07518	-0.07616	1.30
Pitching moment ($C_{m,0}$)	0.00000	0.00000	0.00

Table 3.9: *dsmcFoam* and DAC [194] aerodynamic calculations of a rarefied hypersonic over the Orion CM at 105 km altitude and 0^o angle of attack.

Parameter	***dsmcFoam*** **(NR)**	***dsmcFoam*** **(QK)**	**DAC**
Drag (C_D)	1.7007	1.7092	1.709
Lift (C_L)	0.0000	0.000	0.000
Axial force (C_D)	1.7007	1.7092	1.709
Normal force (C_N)	0.000	0.000	0.000
Pitching moment ($C_{m,cg}$)	-0.08163	-0.08204	-0.0820
Pitching moment ($C_{m,0}$)	0.0000	0.0000	0.0000

Table 3.10: *dsmcFoam*, DAC, DS3V, and LAURA aerodynamic calculations of a rarefied hypersonic over the Orion CM at 105 km altitude and -26^o angle of attack.

Parameter	***dsmcFoam*** **(NR)**	***dsmcFoam*** **(QK)**	**DAC**	**DS3V**	**LAURA**
Drag (C_D)	1.479	1.480	1.449	1.460	1.753
Lift (C_L)	0.390	0.393	0.347	0.349	0.342
Axial force (C_D)	1.500	1.503	1.455	1.465	1.726
Normal force (C_N)	-0.298	-0.296	-0.323	-0.327	-0.461
Pitching moment ($C_{m,cg}$)	-0.04830	-0.04841	-0.0412	-0.0431	-0.0356
Pitching moment ($C_{m,0}$)	0.103	0.102	0.114	0.114	0.069
Centre of pressure ($x_{xp,m}$)	1.733	1.737	1.779	1.752	1.849

Chapter 4

Modelling thermal protection system discontinuities

Efforts to operate hypersonic re-entry vehicles are constrained by many factors. One of the most significant aspects that can affect the entry trajectory is the shaping and design of the thermal protection system (TPS). Excessive temperatures may result in an increased structural and TPS weight to avoid high stress levels and heat loads for the materials that compose the spacecraft. Hence, to achieve the structural efficiency required for feasible hypersonic flight, and to decrease the production and launch costs, the designer must be able to predict the surface heating rates and pressure loads with a reasonable degree of accuracy.

In this Chapter, the backbone of the Orion Command Module re-entry environment is considered under the assumption of a smooth body surface. Usually, this assumption is considered as a starting point for the understanding of the aerodynamic characteristics and flowfield structure surrounding the re-entry vehicle [193, 194]. In this scenario, DSMC simulations of a rarefied hypersonic reacting and non-reacting flow were performed at two points of the Orion re-entry trajectory, 95 and 105 km altitude, respectively. With a framework already in place for providing a smooth baseline, heat shield surface discontinuities, representative of TPS panel-to-panel joints or damage, this study would provide a comprehensive analysis of the flowfield structure and aerodynamic surface quantities in the interior and around of a family of cavities.

4.1 Impact of chemical reactions on the Orion CM

In order to accurately determine the Orion capsule aerodynamic characteristics two reentry points were considered at 95 km and 105 km altitude. Simulations were performed using the new Q-K chemistry model [126] implemented into the *dsmcFoam* solver and the results are compared with those generated by inert gas computations. The geometry and freestream conditions are identical to those discussed earlier in Section 3.3.2 and presented by Moss *et al.* [194]. The *dsmcFoam* simulations were performed using the VHS model collision model, with the model parameters shown in Table 3.7.

The computational mesh was filled with 94 million and 17.5 million DSMC particles for 95 and 105 km altitude, respectively. Freestream boundaries conditions were applied at the inlet, top, and sides of the computational domain. The flow at the downstream outflow boundary is supersonic and vacuum conditions were specified. For all computations, the outflow boundary was located 2.0 body diameters (10 m) downstream of the forebody stagnation point. In addition, for the two cases considered, the wall temperature was constant at 951 K and 760 K, respectively, with the surface being modelled as a diffusive wall with full thermal and momentum accommodation.

The effect of chemical reactions on the computed results is of particular interest in the present Section. The flowfield structure for the Orion Command Module is shown in Fig. 4.1, where translational temperature ratio (T_{tra}/T_{∞}) is presented for non-reacting (*dsmcFoam*-NR) and reacting (*dsmcFoam*-QK) conditions. Being the chemical reaction mainly characterised by endothermicity (dissociation), a significant decrease on the shock wave temperature is clearly visible. A temperature reduction of 25.3% and 18.5% at altitudes of 95 and 105 km, respectively, demonstrates that the presence of chemical reactions have a significant impact on the shock wave stand-off distance, shock thickness, and temperature distribution at the wake region.

Having shown a general picture of the flow surrounding the Orion capsule, it is worth to take a closer look at the shock wave in order to better characterise its structure. In this way, temperature, number density, pressure, and velocity profiles along the stagnation streamline are presented in Fig. 4.2. According to this set of plots, the peak values of translational, rotational, and vibrational temperatures reach a maximum

inside the shock; and the chemical reactions demonstrated to a have a significant impaction in the temperature profiles. At 95 km altitude the chemical reactions promoted a reduction of 7000 K in the translational temperature and it is quite evident a shift in the T_{trat} profile from X = -0.61 m to X = -0.52 m, caused by the endothermic reactions. For both altitudes considered, the chemical reactions promoted a significant decrease in temperature behind the shock wave and all three temperatures relax to almost the same values farther downstream, close to the Orion surface.

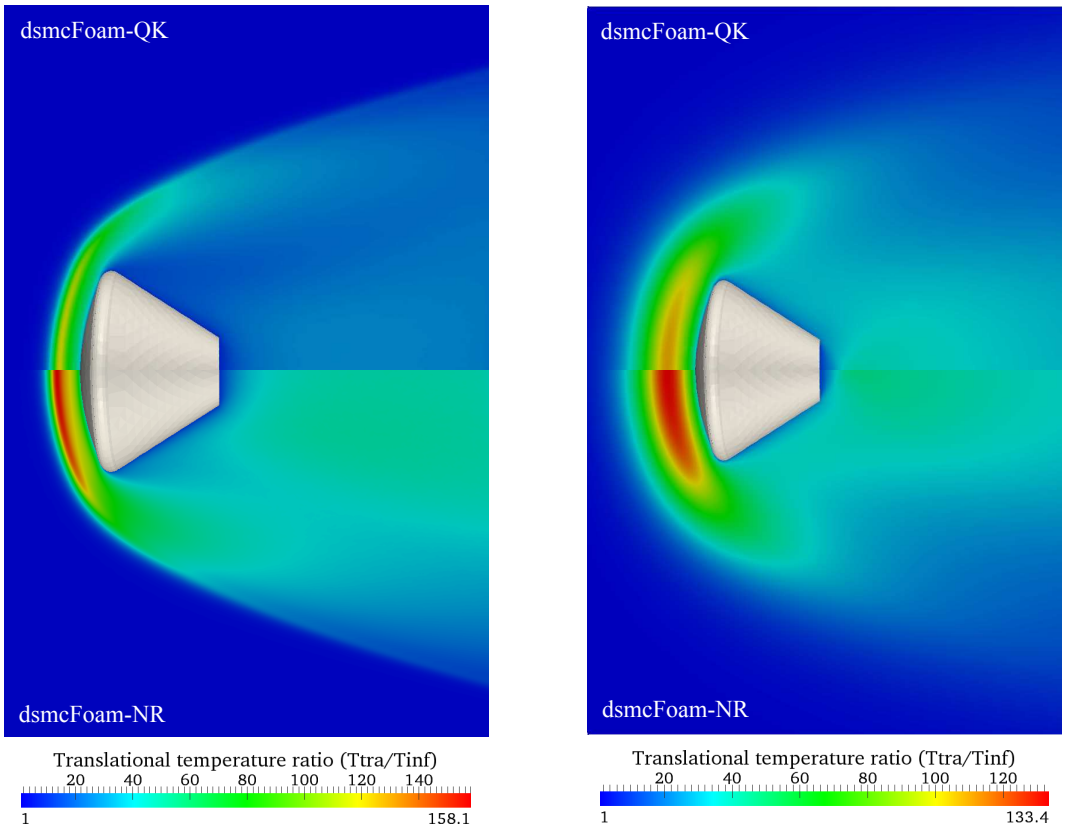

Figure 4.1: Translational temperature ratio (T_{tra}/T_{∞}) for reacting and non-reacting flows over the Orion Command Module at 95 (left) and 105 (right) km altitude.

Of note is the large degree of thermal nonequilibrium on the temperature plots, where the overall kinetic temperature, translational, rotational, and vibrational temperature are presented. Furthermore, as the altitude changes, it is possible to observe an alteration on the curve shape, i.e., from steep gradient at 95 km altitude to shallower gradients at 105 km altitude. This behaviour demonstrates the diffuse nature of the shock wave when the degree of gas rarefaction increases.

The the density profile for the initial species along the stagnation streamline is also shown in Fig. 4.2. At 95 km altitude, the number density profiles are identical for reacting and non-reaction flows at location X < -0.65 m. However, for X ≈ -0.60 m significant changes are evident for the number density ratio as flow moves towards the Orion's surface. Due to its low dissociation threshold, the molecular oxygen is the first species to dissociate leading a decrease in the O_2 concentration and in an increase of atomic oxygen across the shock layer. In contrast, a slightly decrease in the molecular nitrogen number density is observed when reacting and inert gas flows results are compared. Since molecular nitrogen dissociation temperature is approximately double that of O_2, just a more severe re-entry condition with higher enthalpy is able to fully dissociate the N_2. At 105 km altitude, the dissociation process is much less intense than that for the case of 95 km altitude. Consequently, a slight decrease of O_2 and increase of atomic oxygen concentration is evident close to the Orion surface and no appreciable changes in the temperature, pressure, and velocity are noticed for reaching flow at this altitude.

Many methodologies have been employed in order to characterise the shock wave structure under rarefied conditions. The most well know techniques for this purpose are described by Ivanov [195] and Santos [196]. According to Ivanov [195], the shock wave structure may be characterised by taking into account the temperature distribution along the stagnation streamline, i.e., the flow along the stagnation line can be divided into three zones: shock-wave front (up to the point of equilibration of the translational and rotational temperatures), the viscous shock layer (the location where thermal equilibrium is achieved), and surface boundary layer. In another approach, a particle-based method for the shock wave description has been used by Santos [196]. In this technique, the flow is assumed to consist of three distinct classes of molecules: those molecules from the freestream that have not been affected by the presence of the body, denoted as class I molecules; those molecules that, at some time in their past history, have struck and been reflected from the body surface, denoted as class II molecules; and those molecules that have been indirectly affected by the presence of the vehicle are defined as class III molecules. This molecule classification has been implemented into the *dsmcFoam* solver and successfully validated for non-reacting flows [96], however,

more studies are necessary to incorporate both reactions and particle classification.

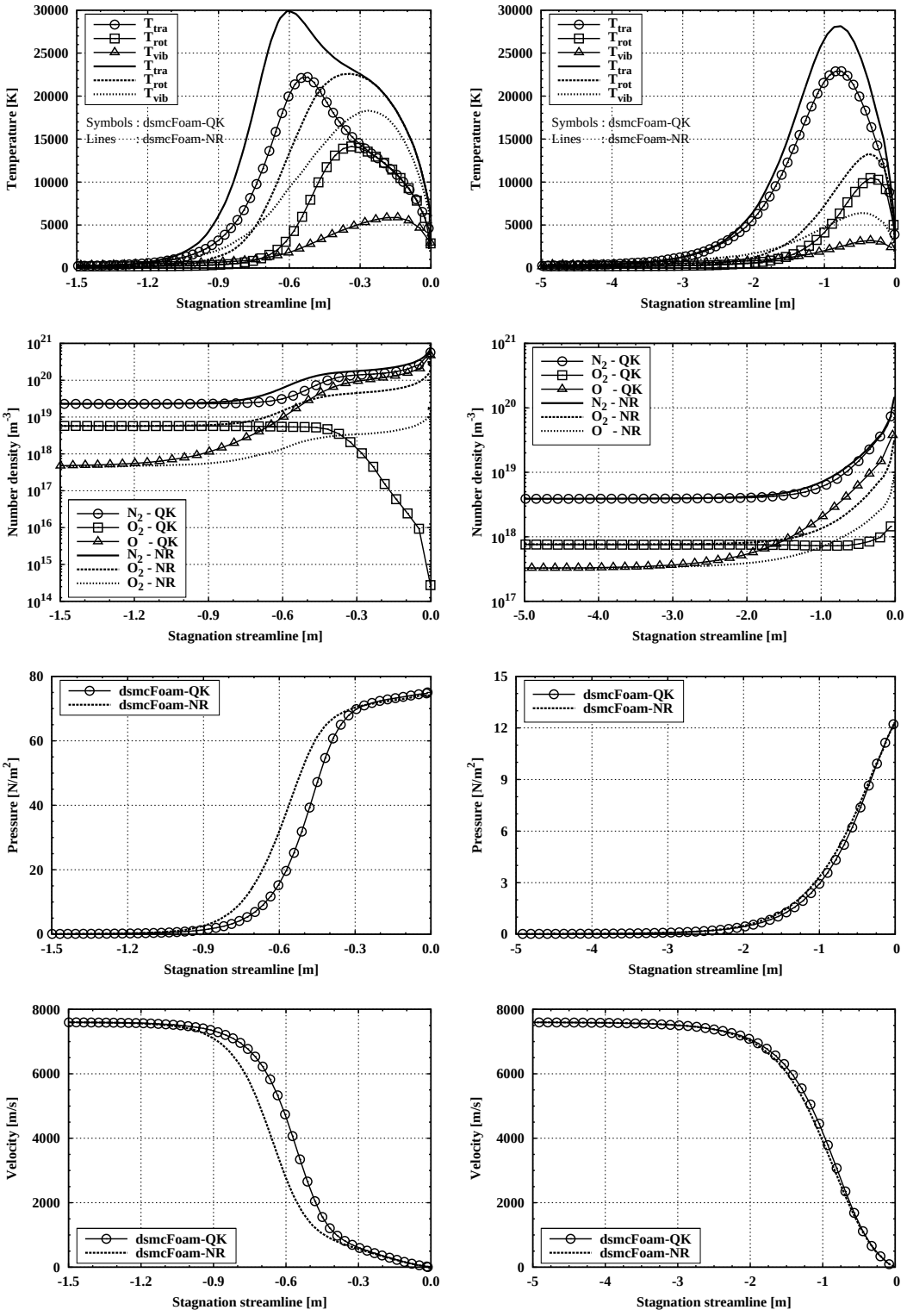

Figure 4.2: Freestream properties along the stagnation streamline for reacting and non-reacting flows over the Orion Command Module at 95 (left) and 105 (right) km altitude.

Mach number, number density, and translational temperature ratio contours are depicted in Fig. 4.3 for the hypersonic reacting flow over the Orion capsule at 95 and 105 km altitude, respectively. In this set of contours plots, total number density and translational temperature are normalised by the freestream conditions. According to the Mach number contours, the diffuse shock effect is evident over all of the computational domain and particularly in the wake region. While the sonic line at the forebody is located at the almost the same position for both altitudes studied, the same phenomena is not observed in the wake region. At 95 km altitude, low Mach number values are observed at the wake region and the position of the sonic line extends far downstream of the Orion capsule. However, for the 105 km altitude case, the sonic line is located closer to the vehicle afterbody.

On examining the number density and translational temperature ratio the extremely diffuse nature of the shock wave is evident at 105 km altitude and the shock structure extends well upstream of the Orion body. On the other hand, at 95 km altitude, the shock is confined to a region much closer to to the vehicle heat shield. The number density in the near wake is relatively low for both altitudes with magnitudes as low as 10% of the freestream value. Along the forebody, as the flow is compressed against the thermal protection system a significant temperature increased is observed. In the wake region, the temperature decreases during the expansion process and the highest value, which is 35 times the freestream temperature, can be found for the 105 km altitude case.

At the initial phase of the simulations, the atmospheric gas that surrounds the Orion capsule is mainly composed of molecular nitrogen and oxygen and atomic oxygen. If the spacecraft reentry is of sufficiently high speed, dissociation and exchange reactions may take place and new molecular and atomic species are introduced into the simulations. To demonstrate this, normalised number density contours for each individual species are shown in Fig. 4.4. According to this group of contours plots, the highest nitric oxide (NO) and atomic oxygen concentration occurs in the forebody region of the Orion Command Module as a consequence high temperature inside the shock wave promoting chemical reactions. Reactant species are also found at the afterbody region, however, their concentration are at least one order of magnitude lower than on the forebody.

The study conducted above proves that an accurate aeroheating environment definition and the presence of chemical reactions plays a critical role in capturing the correct physics during spacecraft reentry simulations.

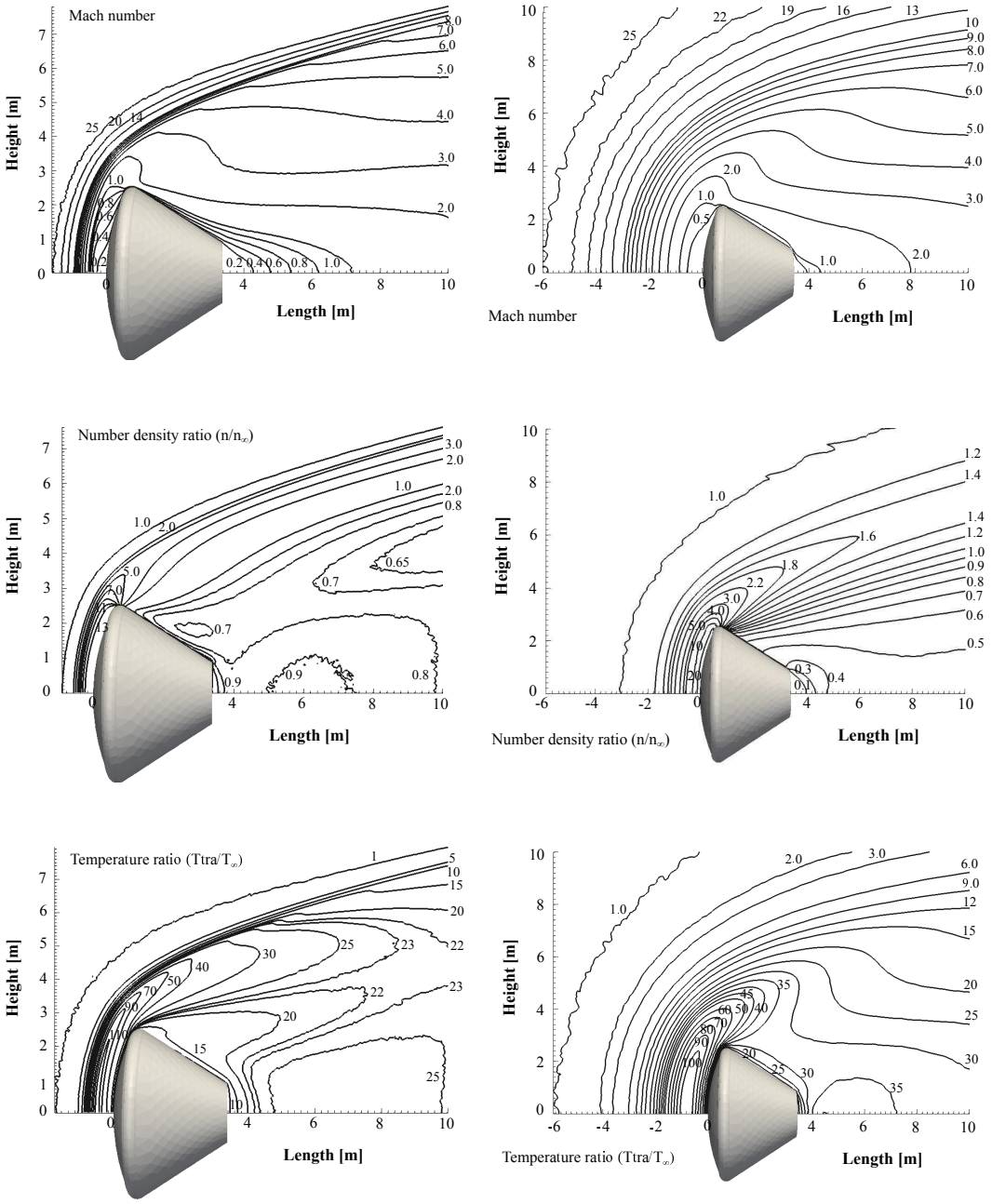

Figure 4.3: Mach number, number density, and translational temperature contours for reacting flow over the Orion Command Module at 95 (left) and 105 (right) km altitude.

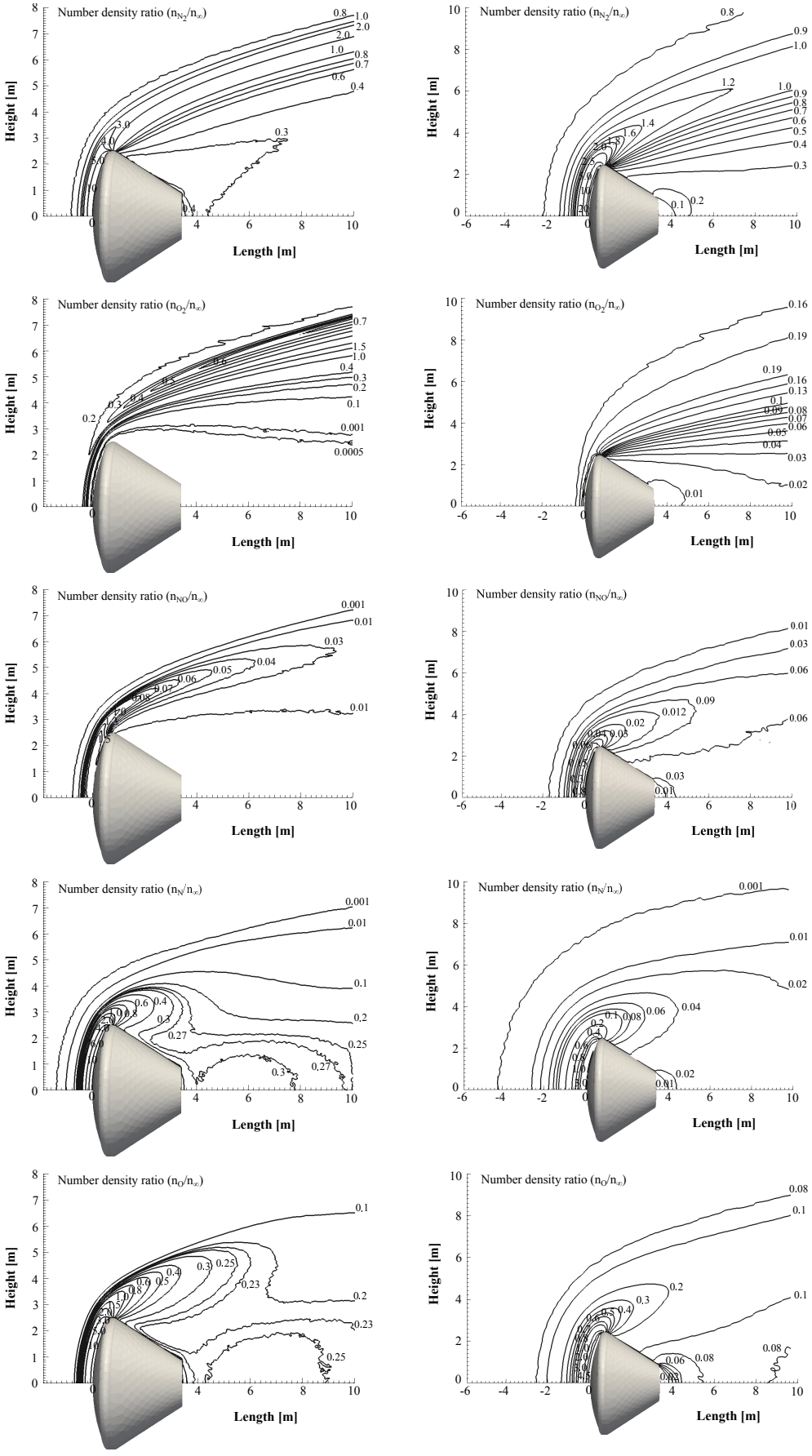

Figure 4.4: Normalised species number density for reacting flow over the Orion Command Module at 95 (left) and 105 (right) km altitude.

4.2 Modelling thermal protection system discontinuities

In the previous section, the impact of rarefied hypersonic reacting and non-reacting flows on the flow structure and aerodynamic surface properties on the Orion Command Module was presented. The Orion re-entry calculations were performed at two points of the reentry trajectory while considering the heat shield to exist as a smooth surface. However, in a real spacecraft design, thermal protection system panel-to-panel joints or even TPS damage should require a rigorous assessment in order to ensure a safe return.

In this thesis, panel-to-panel joints or TPS damage are modelled as three-dimensional cavities of different lengths. By considering that the cavity length L is much smaller than the spacecraft's nose radius R, i.e., $L/R \ll 1$, then the environmental conditions may be represented by hypersonic flow over a flat plate with a cavity [10, 63] positioned sufficiently far enough from the stagnation point.

Figure 4.5 as show a schematic of the 3D cavity and its main parameters. For the family of cavities investigated in this work, the cavity depth D is fixed at 3 mm, while L assumed values ranging from 3 to 15 mm. The upstream and downstream plate length and width was kept constant with 50 mm and 4.5 mm, respectively. The cavity length-to-depth ratio (L/D) considered in this study was 1, 2, 3, 4, and 5.

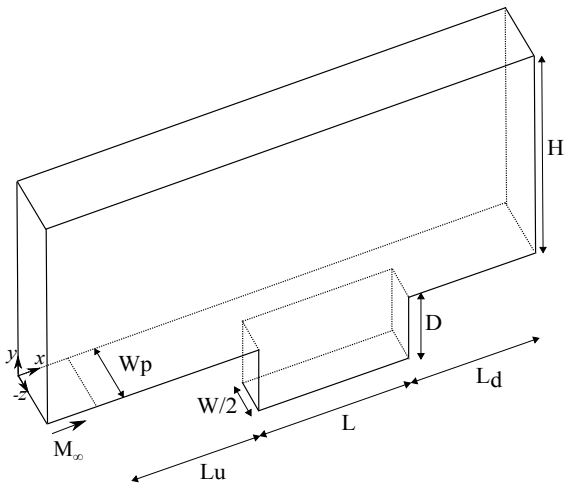

Parameter	Values (mm)
Length (L)	3, 6, 9, 12, 15
Depth (D)	3
Width (W/2)	1.5
Height (H)	40
Plate width (W_p)	4.5
Upstream length (L_u)	50
Downsteam length (L_d)	50

Figure 4.5: Schematic of the cavity configuration and its main geometrical parameters.

In order to implement the DSMC procedure, the flowfield around the cavities is divided into a number of regions, which are subdivided into computational cells. The computational cells are further subdivided into subcells with two subcells per cell in each coordinate direction. The cell provides a convenient reference for the sampling of the macroscopic gas properties, while the collision partners are selected from the same subcell for the establishment of the collision rate; subcells promote nearest-neighbor collisions and therefore a more realistic transport of mass, momentum, and energy. The computational domain used for the calculation is made large enough such that cavity disturbances do not reach the upstream and side boundaries, where freestream conditions are specified. A schematic view of the computational domain and mesh is depicted in Fig. 4.6. The computational domain is divided into four regions, with side I-A defining the cavity surface, with diffuse reflection and complete momentum/thermal accommodation applied as a boundary condition. Side I-B is a symmetry plane, where all flow gradients normal to the plane are zero; at the molecular level, this plane is equivalent to a specular reflecting boundary. This boundary condition is also applied on the half-symmetry plane which bisects the 3D cavity. Sides II, III, and IV are defined as freestream, and simulated particles enter and exit the domain at these locations.

In the DSMC algorithm, the dimensions of the cells should be small in comparison with the length scale of the macroscopic flow gradients, which means that the cell dimensions should be of the order of (or even smaller than) the local mean free path [71, 72]. The cell size also needs to be small enough to restrict collisions to nearby particles, but should, at the same time, contain a sufficient number of particles to maintain the statistical accuracy of the method. The time step should also be chosen to be sufficiently small in comparison with the local mean collision time [74, 75, 197]. In the present work, the time step and the mean collision time are 3.8×10^{-9} s and 9.2×10^{-6} s, respectively. Following the good DSMC practice details described above, a structured computational mesh consisting of $430\times134\times21$ ($x\times y\times z$) cells was employed all the cases. The total number of cells was 1.2 million and the number of DSMC particles in the system at steady-state reached 13 million.

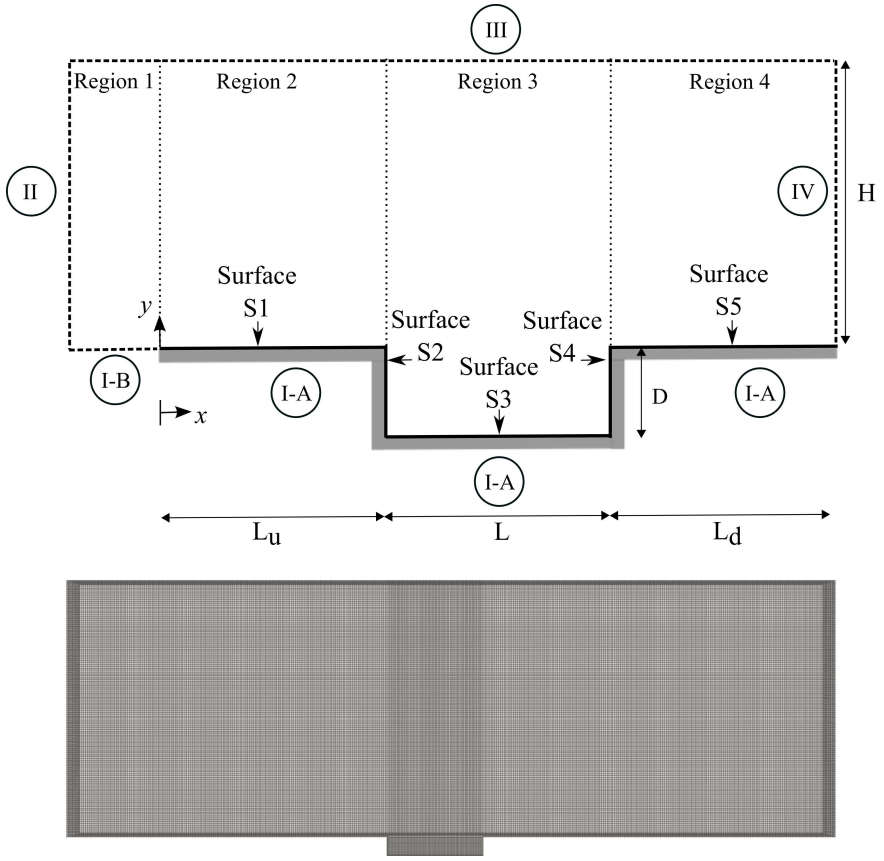

Figure 4.6: Schematic of the cavity boundary conditions and computational mesh.

The freestream conditions employed in the present calculations are shown in Table 4.1. These flow conditions represent those typically experienced by a reentry vehicle at an altitude of 80 km in the Earth's atmosphere [198]. At this altitude, the atmosphere is composed by 78.8% nitrogen and 21.2% oxygen and the inflow boundary condition is imposed 5 mm upstream of the cavities' leading edge plate (L_u). The freestream velocity U_∞ is assumed to be constant at 7600 m/s, which corresponds to a freestream Mach number M_∞ of 22.4. The surface temperature T_w is assumed constant at 1000 K, which is chosen to be representative of the surface temperature near the stagnation point of a re-entry vehicle, and is assumed to be uniform over all surfaces including the cavity. It is important to highlight that the surface temperature is low compared to the stagnation temperature of the air. This assumption is reasonable since practical surface materials would be likely to disintegrate if the surface temperature approached the flow stagnation temperature.

Table 4.1: Freestream flow conditions at 80 km altitude.

Parameter	**Value**	**Unit**
Velocity (U_∞)	7600	m/s
Temperature (T_∞)	198.62	K
Pressure (p_∞)	1.04	N/m^2
Number density (n_∞)	3.793×10^{20}	m^{-3}
Density (ρ_∞)	1.764×10^{-5}	kg/m^3
Dynamic viscosity (μ_∞)	1.321×10^{-5}	Ns/m^2
Mean free path (λ_∞)	3.160×10^{-3}	m

Assuming the cavity length L as the characteristic length, the global Knudsen numbers Kn_L are 1.053, 0.526, 0.351, 0.263, and 0.211 for cavity lengths of 3, 6, 9, 12, and 15 mm, respectively. The global Reynolds numbers Re_L are 31.45, 60.89, 91.34, 121.78, and 152.23 for cavity lengths of 3, 6, 9, 12, and 15 mm, respectively, based on the undisturbed freestream conditions.

It may be noted that parameters such as Mach number, Knudsen number, angle of attack, gas-surface interaction, and surface temperature may play an important role on cavity flow structure and consequently on the aerodynamic surface properties. However, the focus of the present work is to investigate the impact of reacting and inert rarefied hypersonic gas flows at zero angle of attack for a family of cavity characterised by length-to-depth ratio of 1 to 5.

4.3 Computational results and discussion

In this section, the impact of the cavity length-to-depth ratio on the flowfield structure and aerodynamic surface properties is discussed. Since it was demonstrated in the previous sections that chemical reactions play a significant role on the heating rates and pressure loads acting on a spacecraft during reentry, cavity simulations were performed for both reacting and inert rarefied gas conditions.

4.3.1 Flowfield structure

In this section, the primary macroscopic properties such as velocity, density, pressure, and kinetic temperature are presented for hypersonic reacting flow over the cavities. In order to better understand the impact of increasing the cavity length on the flow structure inside and around the cavities, the macroscopic properties are measured for a series of vertical and horizontal profiles as shown in Fig. 4.7.

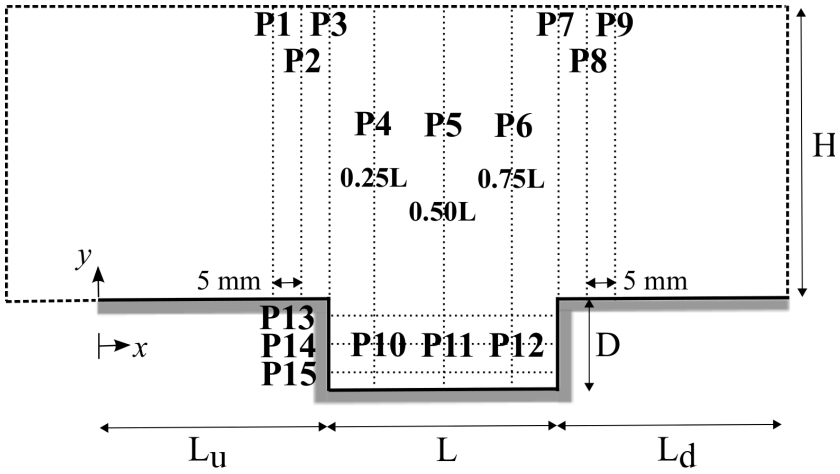

Figure 4.7: Schematic of the macroscopic property measurement profiles.

As shown in Fig. 4.7 the macroscopic property measurement profiles ranging from P1 to P9 are localised upstream, above, and downstream of the cavities. Inside the cavities, the vertical profiles (P10 to P12) are taken at three different length positions, 0.25L, 0.50L, and 0.75L, respectively. Similarly, the horizontal profile measurements (P13 to P15) are located at three different cavity depths, 0.25D, 0.50D, and 0.75D, respectively.

The velocity flowfield

With the DSMC technique being a statistical method, the macroscopic properties are computed from local averages of the microscopic properties. Thus, the local macroscopic velocity vector is given by the following equation,

$$\mathbf{c}_0 = \frac{\overline{m\boldsymbol{c}}}{\overline{m}} = \frac{\sum_{j=1}^{N} m_j \boldsymbol{c}_j}{\sum_{j=1}^{N} m_j}, \tag{4.1}$$

where m and $\mathbf{c}$ represents the mass and the velocity vector of each individual particle, and N is the total number of simulated particles within a cell.

It should be noted that the mean molecular velocity $\mathbf{c}$ ($\equiv \mathbf{c}_0 \equiv \mathrm{u}\mathbf{i} + \mathrm{v}\mathbf{j} + \mathrm{w}\mathbf{k}$) defines the macroscopic mean velocity. In addition, the velocity of the molecules relative to the macroscopic mean velocity, defined as thermal or peculiar velocity, is denoted by $\mathbf{c'} = \mathbf{c} - \mathbf{c}_0$. Since the velocity is composed by a linear combination of the macroscopic and peculiar velocities, the mean molecular velocity $\mathbf{c}$ is equal to $\mathbf{c}_0$ as the mean of the random molecular motion gives $\overline{\mathbf{c'}} = 0$.

The velocity profiles ($\mathrm{U/U_\infty}$) for nine locations above the cavities are shown in Figs. 4.8, 4.9, and 4.10. In this set of plots, the velocity profiles are measured at three different regions, i.e., close to the trailing edge of the upstream plate (L_u), above the cavity, and at the leading edge of the downstream plate (L_d) and normalised by the freestream velocity U_∞. In addition, Y_H and Y_D refer to the y-coordinate direction normalised by either the domain height H or the cavity depth D, and X_L stands for the x-coordinate direction normalised by the cavity length L.

As shown in Figs. 4.8 to 4.10 no appreciable changes in the velocity profiles are observed at these nine locations when the cavity lengths is increased. It is worth noting from Figs. 4.8 and 4.10 that the velocity ratio is non-zero close to the cavity wall ($\mathrm{Y}_H = 0$), indicating the presence of velocity slip. Such a phenomenon is a classical feature in rarefied flows and it has been well-captured by the *dsmcFoam* code.

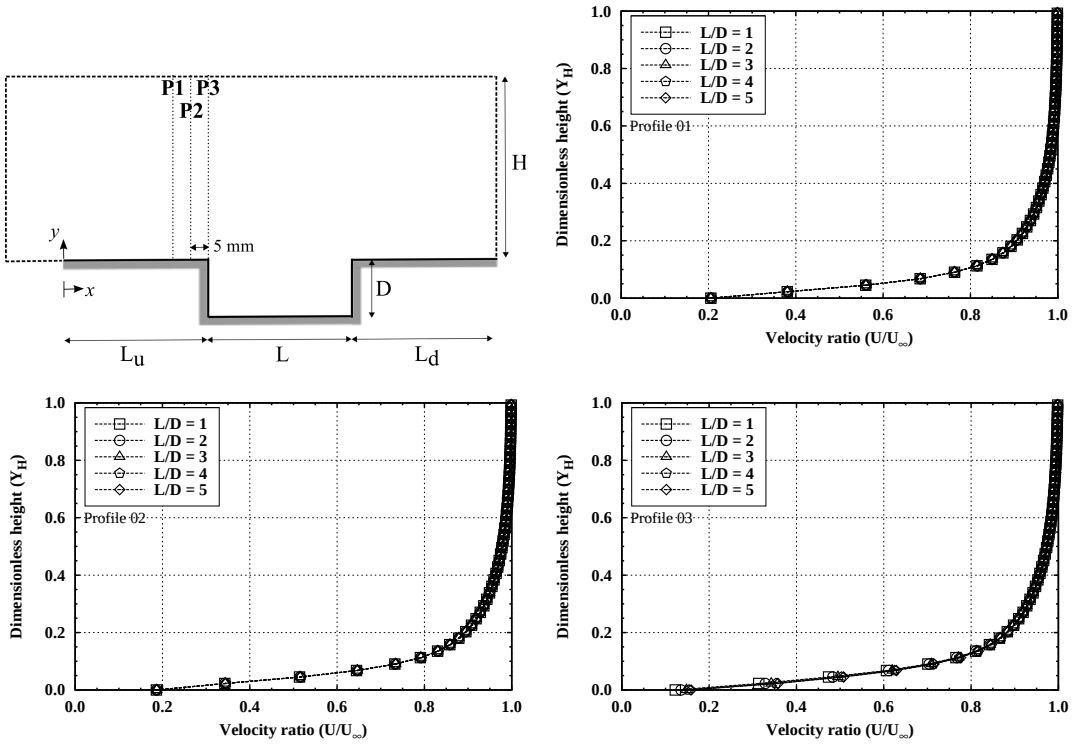

Figure 4.8: Velocity ratio (U/U_∞) profiles for three locations at surface S_1.

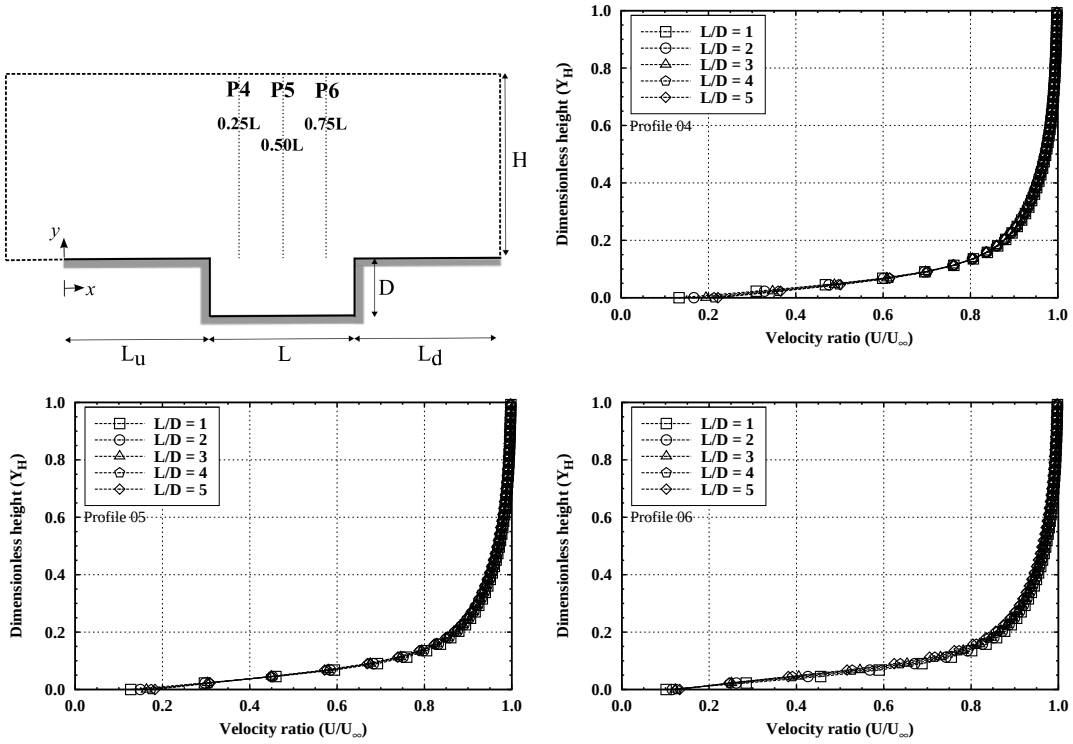

Figure 4.9: Velocity ratio (U/U_∞) profiles for three locations above the cavity.

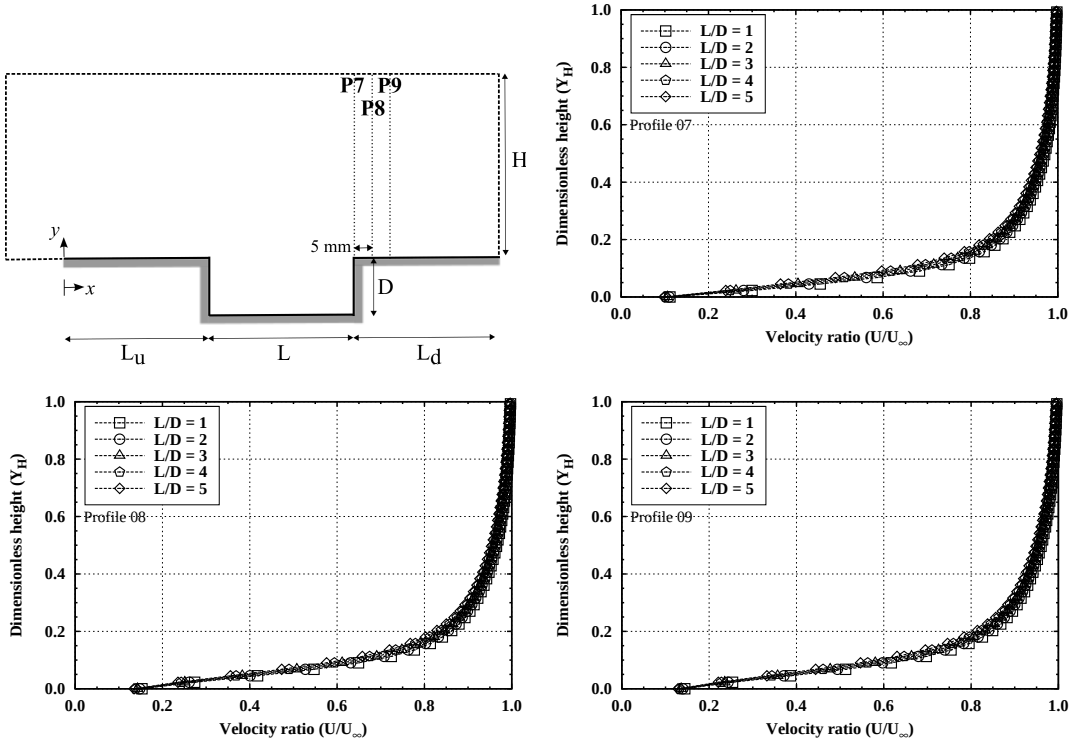

Figure 4.10: Velocity ratio (U/U_∞) profiles for three locations at surface S_5.

The impact of the cavity length-to-depth ratio on the velocity profiles inside the cavity is shown in Fig. 4.11. The velocity ratio profiles are measured for three vertical locations as a function of the cavity length L, i.e, P10 = 0.25L is located close to the upstream vertical face of the cavity, P11 = 0.50L corresponds to the centre of the cavity, and P12 = 0.75L is positioned near to the downstream vertical cavity face. In a similar manner, three horizontal velocity profiles are plotted as a function of the cavity depth D, i.e, P13 = 0.25D which is positioned close to the cavities' lip, P14 = 0.50D corresponds to the half-cavity depth, and P13 = 0.75D, located adjacent to the cavities' bottom surface.

On examining Fig. 4.11 for the vertical velocity profiles on the left hand side, it is clear that the normalised velocity profiles are negative at the bottom of the cavities ($Y_D \approx$ -1). Moving upward, the velocity profiles becomes positive and reach a maximum value close to the cavities opening. At this location, it is interesting to notice that an increase in the length-to-depth ratio, from L/D = 1 to L/D = 5 leads to a velocity augmentation of 41% in the profile P10. In contrast, for the profile P12, the increment

in the velocity was 21.2%. These results suggest that that an expansion region and a compression zone have been formed around the upstream and downstream cavity lips. In order have a deeper understanding of the flowfield structure inside around the cavities, the density, pressure, and temperature fields will be explored in the next sections.

Still referring to Fig. 4.11, the horizontal velocity profiles are shown on the right hand side. According to this group of plots, it is clear that the velocity is reduced as the flow penetrates deeper into the cavity, from $Y_D = 0$ to Y_D = -1. Furthermore, at location P15, close to the cavity bottom surface, a change in the flow topology inside the cavity is evident. For cavities of length-to-depth of 1 to 3, the velocity profiles are negative meaning that the flow is reversed along cavity base. Nonetheless, for L/D = 5, the velocity achieves a minimum at location $X_L = 0.15$, increasing towards a positive value at $X_L = 0.275$ and reaching a maximum value at position $X_L = 0.55$. Also, the normalised velocity decreases towards negative values at location $X_L = 0.92$ and increases again close to the downstream face of the cavity. For the cavity depth of L/D = 4, a similar trend is observed, however, the maximum positive velocity is not as prominent as in the L/D = 5 ratio case.

In order to have a clearer picture of the flow structure around and inside the cavities, it is instructive to present graphically the computed flow topologies. The velocity ratio (U/U_∞) contours with streamline traces over the computational domain and inside of the 3D cavities are shown in Figs. 4.12 and Figs. 4.12 for L/D ratios of 1, 2, 3, 4, and 5. It is evident that the flow inside cavities is characterised by recirculation structures. The streamline patterns for L/D ratios of 1 and 2 shows that the flow has a primary vortex system, and the recirculating structure fills the entire cavity. A transition stage is evident for the case where the length-to-depth ratio is equal 3. In this case, the main flow is able to slightly penetrate into the cavity and an elongated recirculation region with two vortex cores is formed.

For the $L/D = 4$ and 5 cases, a different flow structure is observed: two vortices are formed, one of them close to the upstream face and the other in the vicinity of the downstream face of the cavity. The separated shear layer from the external stream does not reattach to the cavity floor, and the flow is reversed along the bottom cavity

surface for the $L/D = 4$. However, for the $L/D = 5$ case the recirculation regions are well-defined and the separated shear layer is able to penetrate deeper into the cavity and attach itself to the cavity base wall, enhancing momentum and energy transfer to the bottom surface.

It is important to highlight that in the continuum regime [63], the two recirculation regions and flow attachment to the cavity bottom surface occurs when the length-to-depth ratio is equal or greater than to 14 (Fig. 1.4). However, the same phenomena is observed in the transitional regime when the cavity $L/D = 5$. In this case, even a small cavity under rarefied gas conditions could promote serious damage to the heat shield during reentry, as the flow attaches to the cavity bottom surface when the L/D ratio is much lower to those observed in the continuum regime.

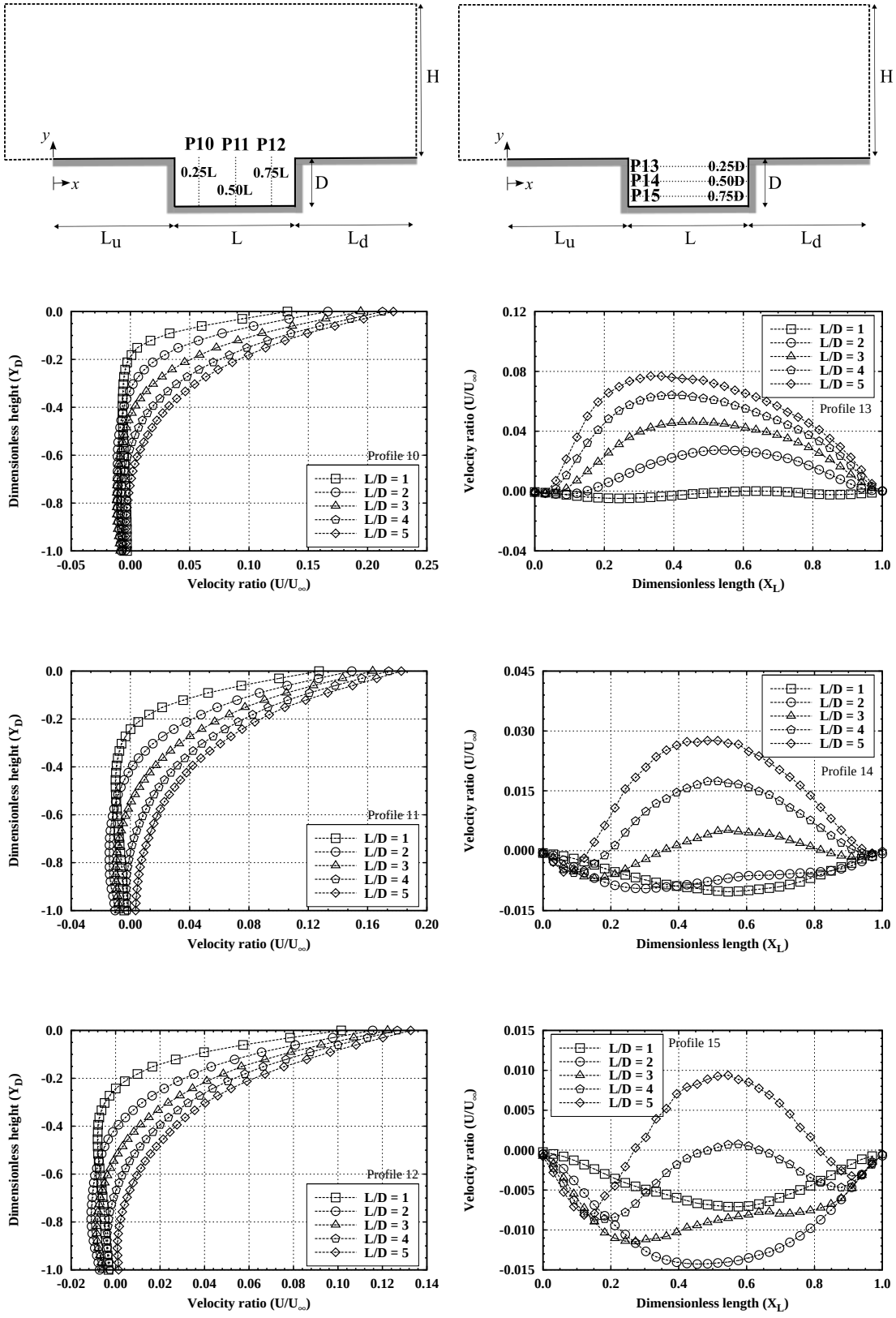

Figure 4.11: Velocity ratio (U/U_∞) profiles for six locations inside the cavity.

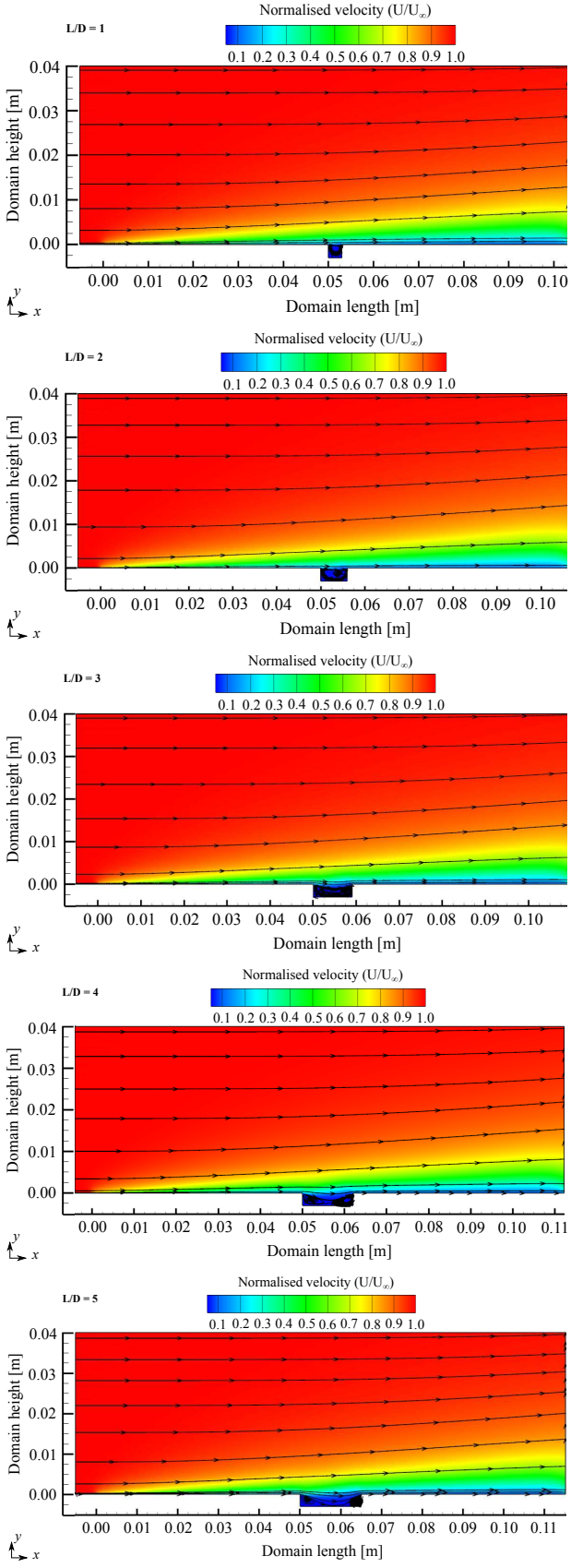

Figure 4.12: Velocity ratio (U/U_∞) distribution over the computational domain as a function of L/D ratio.

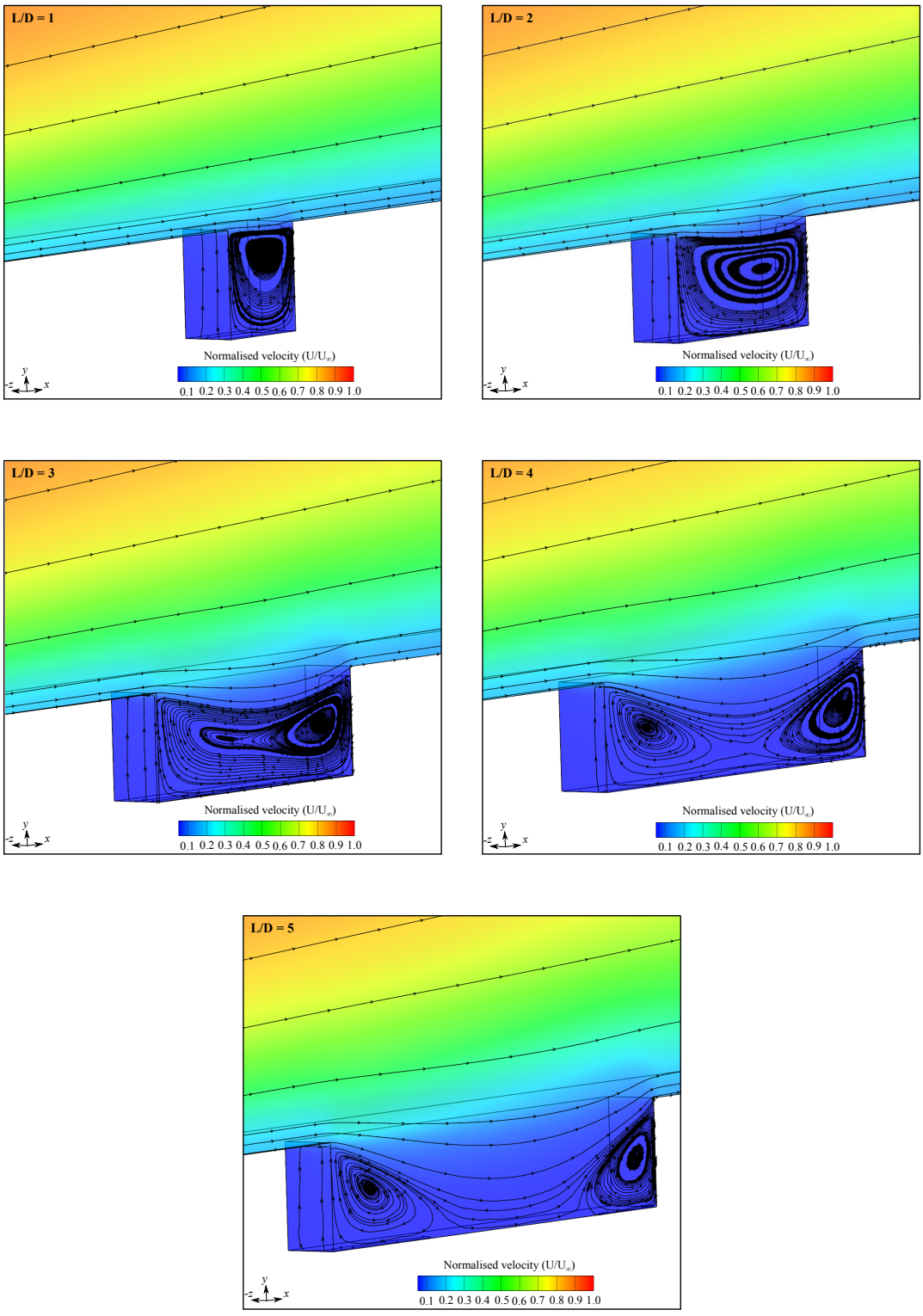

Figure 4.13: Velocity ratio (U/U_∞) distribution inside the cavities as a function of L/D ratio.

The density flowfield

The density within the computational cells on the *dsmcFoam* code is obtained using the following expression,

$$\rho = n\overline{m} = \frac{\overline{N}F_N}{V_c} = \frac{\sum_{j=1}^{N} m_j}{N}, \tag{4.2}$$

where n is the local number density, m is the molecular mass, and $\overline{N}$ and N are, respectively, the average and total number of simulated particles within a given cell. Furthermore, F_N represents any number of real particles and V_c is the computational cell volume.

The impact of the cavity length-to-depth ratio on the density profiles is investigated in this sub-section. In a similar manner to the velocity profiles, the density ρ is normalised by the freestream density ρ_∞ and measured at different location above and inside the cavities.

Normalised density profiles for the region above the cavity are show in Figs. 4.14, 4.15, and 4.16. According to these figures, it is observed that the density ratio experiences significant changes in the vicinity of the upstream (L_u) and downstream (L_d) plates. For the region confined between $Y_H \approx 0$ and $Y_H = 0.035$, the density ratio is high adjacent to the walls and then rapidly decreases towards a minimum value. This characteristic is observed when the body surface is colder than the stagnation temperature of the incoming gas. Consequently, the density close to the surface tends to be higher than of the rest of the wall surface boundary layer.

Still referring to this group of plots, it is noticed that increasing the L/D ratio promotes a significant change in the density distribution close to the upstream cavity lip and above the downstream plate (L_d). As the flow expands around the lip, a wake region is formed with a significant impact on the density ratio reduction. This phenomenon is clearly observed in the magnified view of the profile P3 in Fig. 4.14. In addition, as the flow penetrates deeper into the cavities, when the L/D ratio is increased, a compression region arises in the vicinity of the downstream vertical surface, having a significant influence on the density profile disturbance at L_d, where the density ratio increases significantly and reaches a maximum value of 1.3 inside the shock structure

at profile P9. Close to the upper boundary condition ($Y_H = 1$) the freestream density values are recovered.

Figure 4.17 shows the normalised density profiles for six locations inside the cavity. From this group of plots, it is quite clear that the cavity length-to-depth ratio plays a very important role in the density distribution inside the cavities. For profile 10 (P10), it is observed a slight decrease in the density up to location Y_D = -0.1 and an increase downwards to the cavity bottom surface. Furthermore, it worth noticing that the density ρ is smaller than the freestream density ρ_∞ ($\rho/\rho_\infty < 1$) for the cavities of L/D = 4 and 5. This is a important indication that a increased cavity length promotes a wake region close to the upstream vertical surface, with the characteristics of a flow expansion. On the other hand, at location P12, a pressure ratio augmentation of 41.3% is observed at the bottom surface for L/D = 5.

Three horizontal density profiles are shown on the right hand side of Fig. 4.17 as a function of the cavity depth. According to these plots, the density ratio for cavity L/D = 1 to 3 is smaller than 1.0 up to a location $X_L = 0.35$, then increases to a maximum value close to the downstream vertical surface.

In order to obtain a better insight into the density distribution, Figs. 4.18 and 4.19 show the density contour maps over the computational domain and inside the cavities.

According to Fig. 4.18, no significant changes in the density contours is observed above the cavities when the length-to-depth ratio is increased. However, it is possible to notice a thin layer of high density in the vicinity of the upstream (L_u) and downstream (L_d) plates, as already demonstrated in the density profile studies at Figs. 4.14 and 4.16. Furthermore, the high density region formed above the cavity due to the attached shock wave at the L_u leading edge remains unchanged for the range of L/D = 1 to L/D = 5.

Finally, the normalised density contour maps inside the cavities are shown in Fig. 4.19. From this group of plots, it is quite evident that the cavity length-to-depth ratio plays a significant role in the density distribution inside the cavities. As the cavity length is enlarged, the expansion into the cavity is characterised by a low density region, reaching a minimum of 0.5 close to the upstream vertical wall. In contrast, as the flow penetrates deeper into the cavity when the L/D ratio is increased, the DSMC particles are compressed against the downstream vertical surface and consequently a maximum

of $5.0\rho_\infty$ is observed.

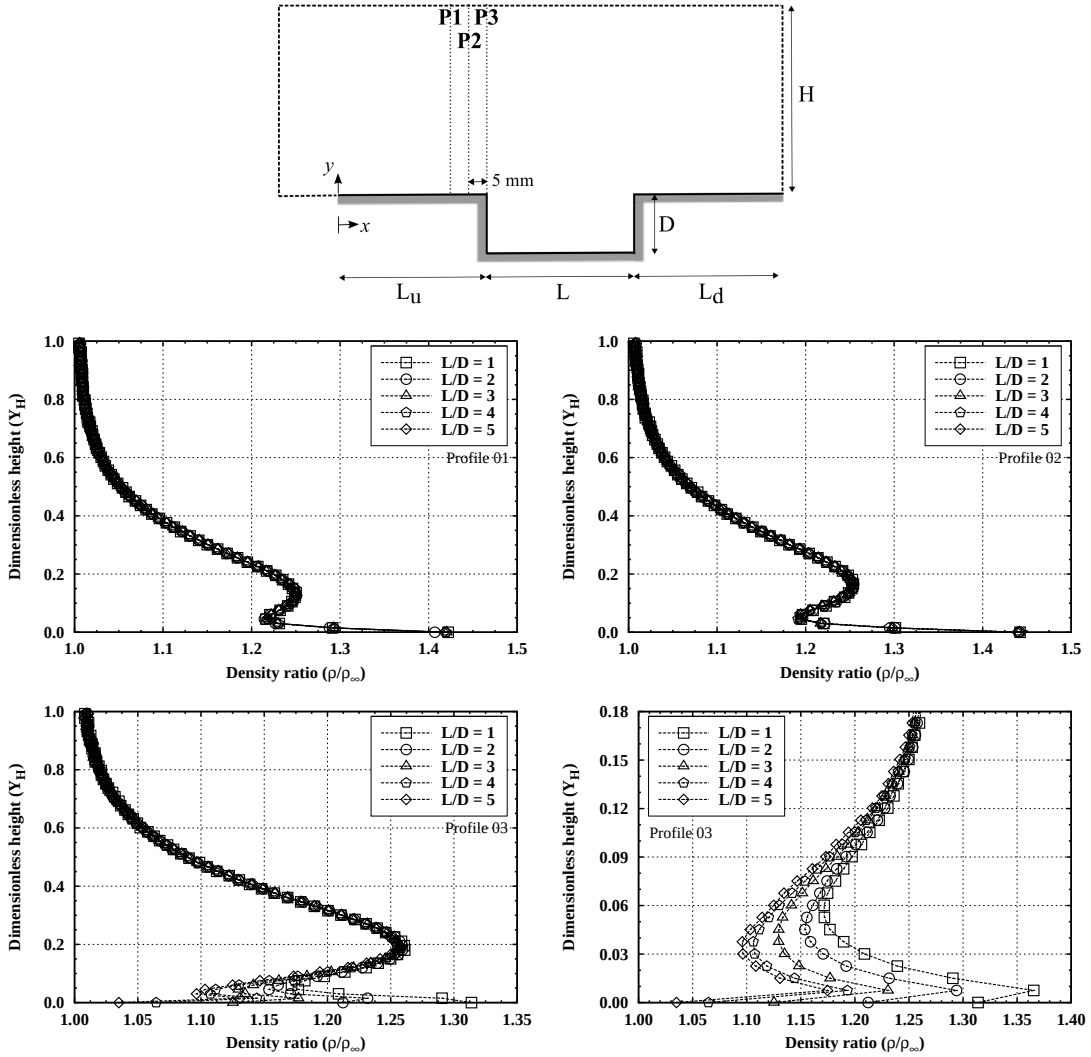

Figure 4.14: Density ratio (ρ/ρ_∞) profiles for three locations at surface S_1.

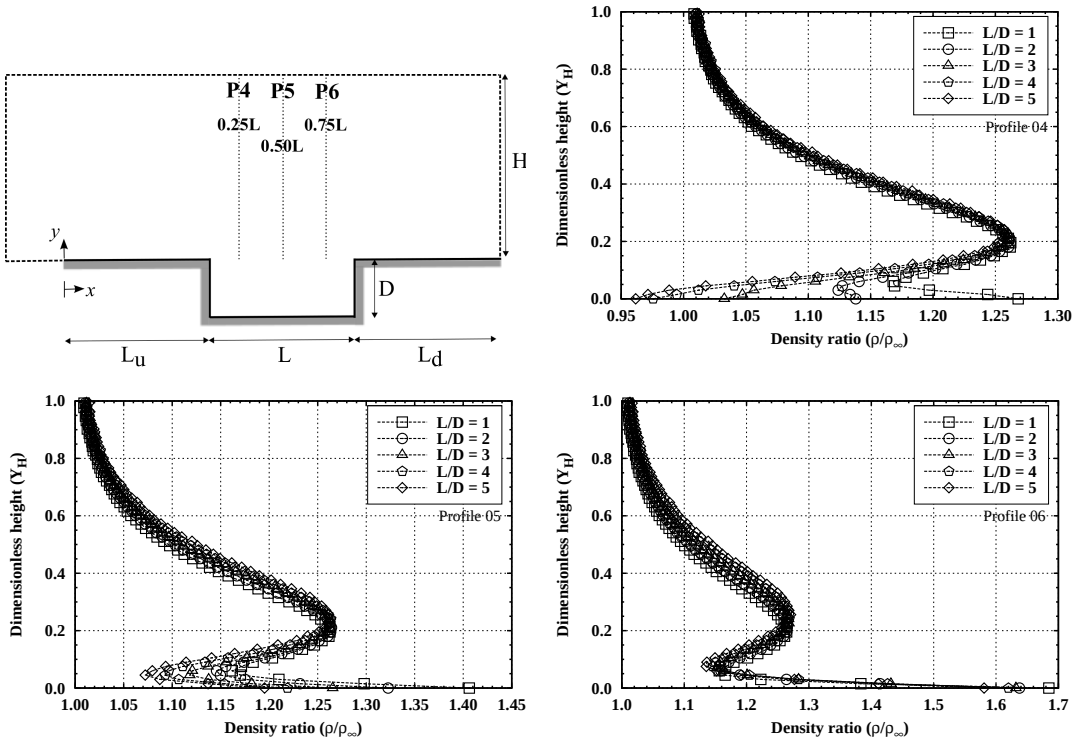

Figure 4.15: Density ratio (ρ/ρ_∞) profiles for three locations above the cavity.

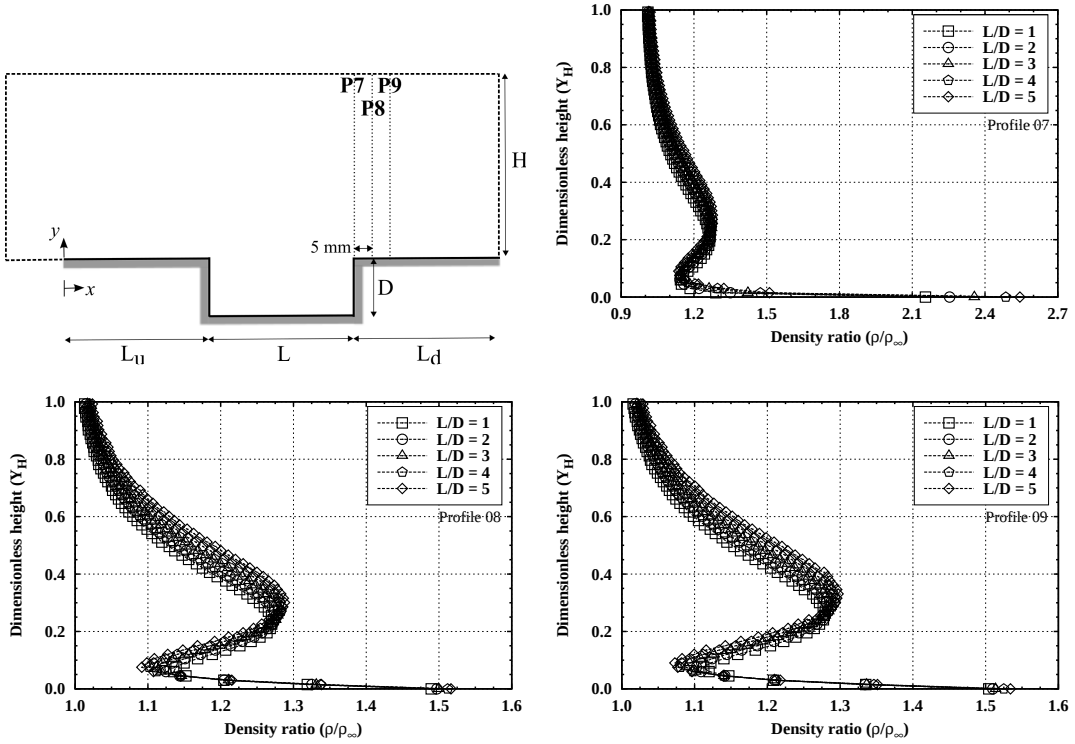

Figure 4.16: Density ratio (ρ/ρ_∞) profiles for three locations at surface S_5.

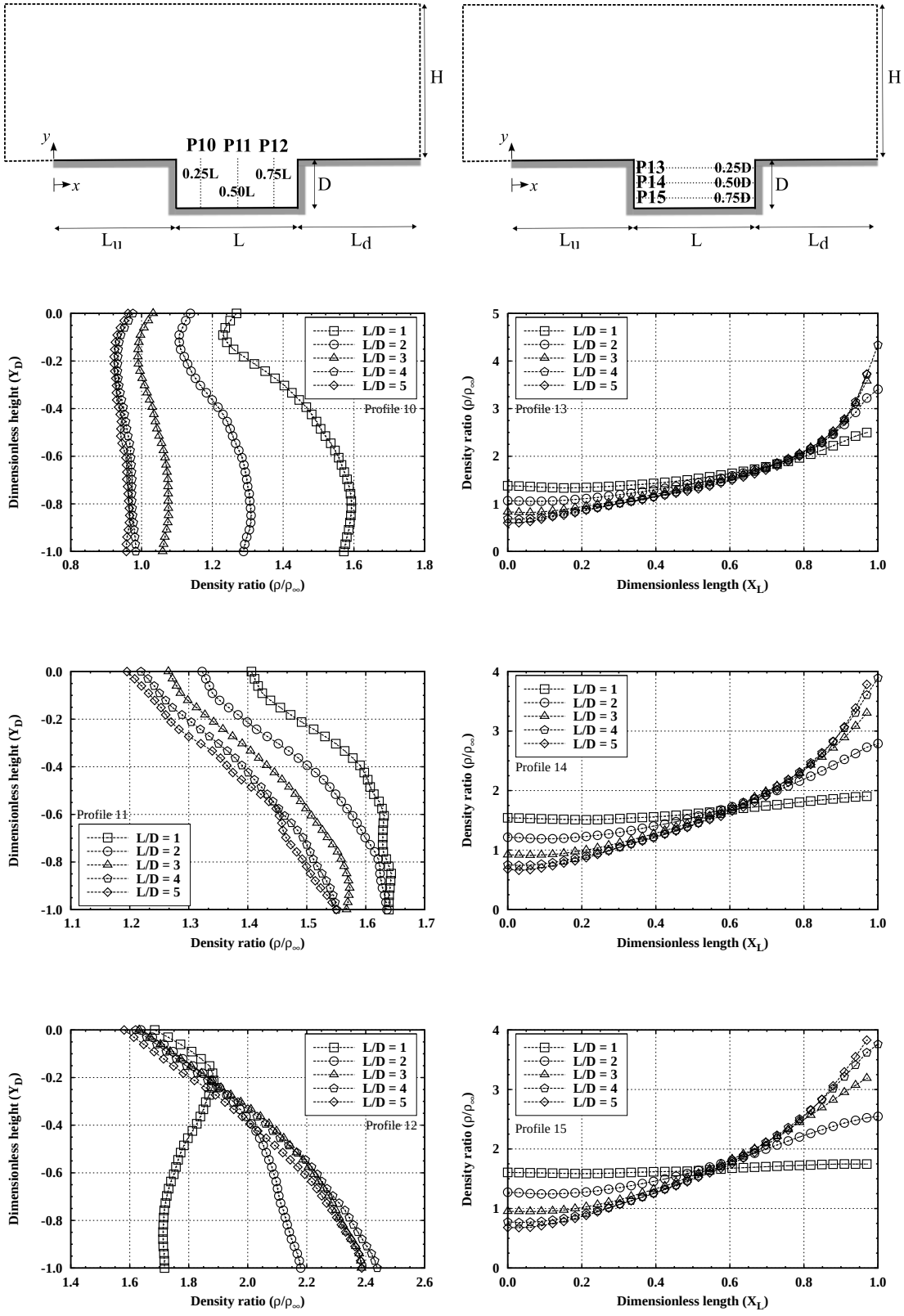

Figure 4.17: Density ratio (ρ/ρ_∞) profiles for six locations inside the cavity.

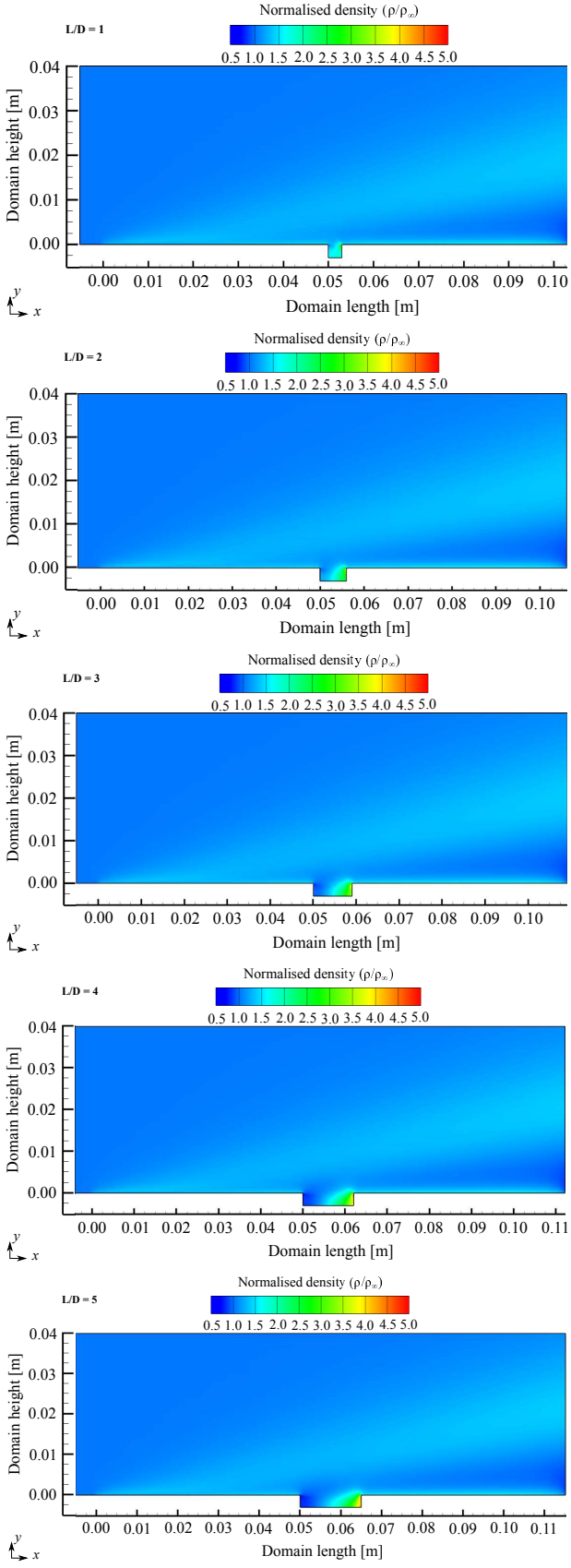

Figure 4.18: Density ratio (ρ/ρ_∞) distribution over the computational domain as a function of L/D ratio.

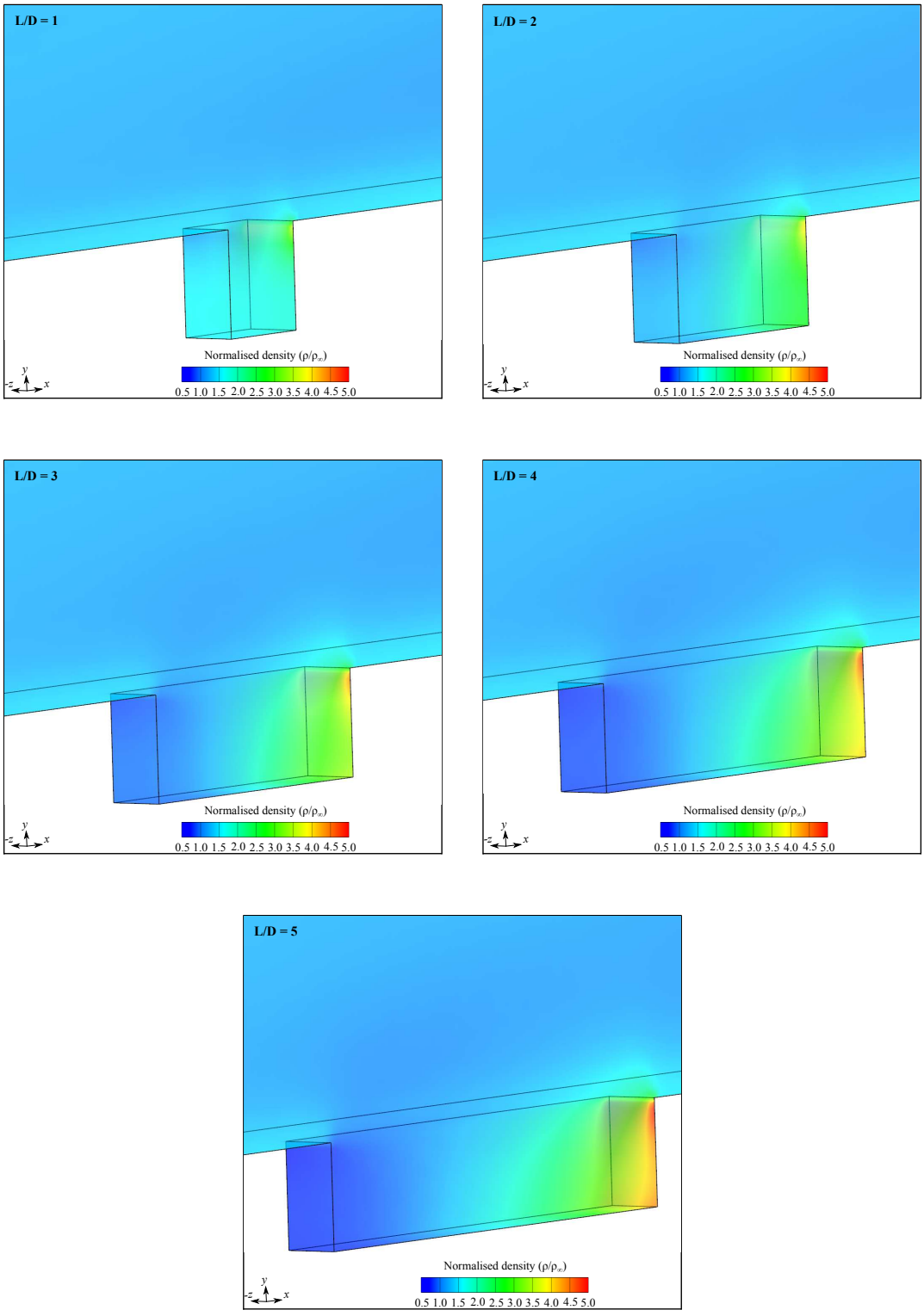

Figure 4.19: Density ratio (ρ/ρ_∞) distribution inside the cavities as a function of L/D ratio.

The pressure flowfield

The pressure determined by the *dsmcFoam* code is obtained using the following expression,

$$p = \frac{1}{3} n m \overline{\boldsymbol{c'}^2} = \frac{1}{3} \frac{\overline{N} F_N}{V_c} \frac{\sum_{j=1}^{N} m_j \boldsymbol{c'}^2}{N}, \tag{4.3}$$

where n is the local number density, m is the molecular mass, **c'** is the thermal velocity, $\overline{N}$ and N are, respectively, the average and total number of simulated particles within a given cell, and V_c is the computational cell volume.

In a similar approach, to the velocity and density profiles studied in the previous sub-sections, Figs. 4.20, 4.21, and 4.22 show the influence of the cavity length-to-depth ratio on the pressure profiles for nine vertical locations above the cavity. In addition, all of the profiles are normalised by the freestream pressure p_∞.

According to these set of plot, no apparent changes on the pressure profiles above the cavity is observed, However, it is encouraging to note a decrease of pressure for profile 3 at the region close to the upstream cavity lip. This situation reinforce that stronger expansion occurs when the cavity length is increased. In addition, as the L/D ratio is increase from 1 to 5 it is observed a convergence on the pressure values at this region, meaning that no significant changes will occurs if the L/D ratio is increased beyond L/D = 5.

The effects of the L/D ratio on the pressure profiles located inside the cavities are shown in Fig. 4.23. In this set of plots, the left- and right columns correspond to the horizontal and vertical profiles, respectively. Firstly, on the left hand side, it is evident that the pressure ratio inside the cavities decreases from the top to the bottom of the cavities for the range of L/H ratio investigated. Furthermore, when the pressure ratios are compared for L/D = 1 and L/D = 5 at the top and bottom of the cavity, an increase in the pressure of 19.2% and 50% is evident. This increase in pressure at the bottom surface for L/D = 5 and profile 12 demonstrates that the length of the cavity plays an essential role on the pressure augmentation. In contrast to the continuum regime where the flow attaches to the cavity bottom surface when L/D > 14, in the rarefied regime, this behaviour is observed for cavity length-to-depth greater than 5.

In this way, thermal protection system cavities, caused by the fabrication process (i.e. panel-to-panel joints) or damage promoted by external impacts (micro meteorites, ice droplets, etc) represent a potentially catastrophic feature under rarefied gas conditions.

In to have a better insight into the pressure ratio distribution over the computational domain and inside the 3D cavities, pressure-contour maps have been created. According to Fig. 4.24, in the vicinity of the upstream plate leading edge (L_u), the pressure is 100 times larger than the freestream pressure. Due the large amount of kinetic energy present in a hypersonic flow, this energy is converted by particle collisions into an augmented thermal energy surrounding the body and an increase in the local pressure.

Still referring to Fig. 4.24, no appreciable changes in the pressure values are observed for a small cavity, i.e, L/D = 1. On the other hand, as the cavity length is increased, a high pressure region is formed in the vicinity of the downstream cavity lip (downstream plate leading edge (L_d)), which may reach almost 90 times the freestream pressure at profile 06. Such a pressure increase may result in catastrophic consequences for spacecraft with a damaged heat shield.

Finally, the normalised pressure contour maps inside the cavities are presented in Fig. 4.25. As mentioned previously in the description of the velocity and density profiles, an expansion region is formed close upstream to the vertical surface when the cavity L/D ratio is increased. The flow separation occurs at the cavity lip and the flow attachment point depends on the cavity length. For the maximum L/D ratio studied, the flow is able to penetrate deeper in to the cavity promoting a decrease in the pressure and density ratio in the expansion region. In addition, as the flow proceeds inside the cavity, the freestream particles strike directly on the downstream vertical cavity surface and consequently pressure and density augmentation is detected in this area.

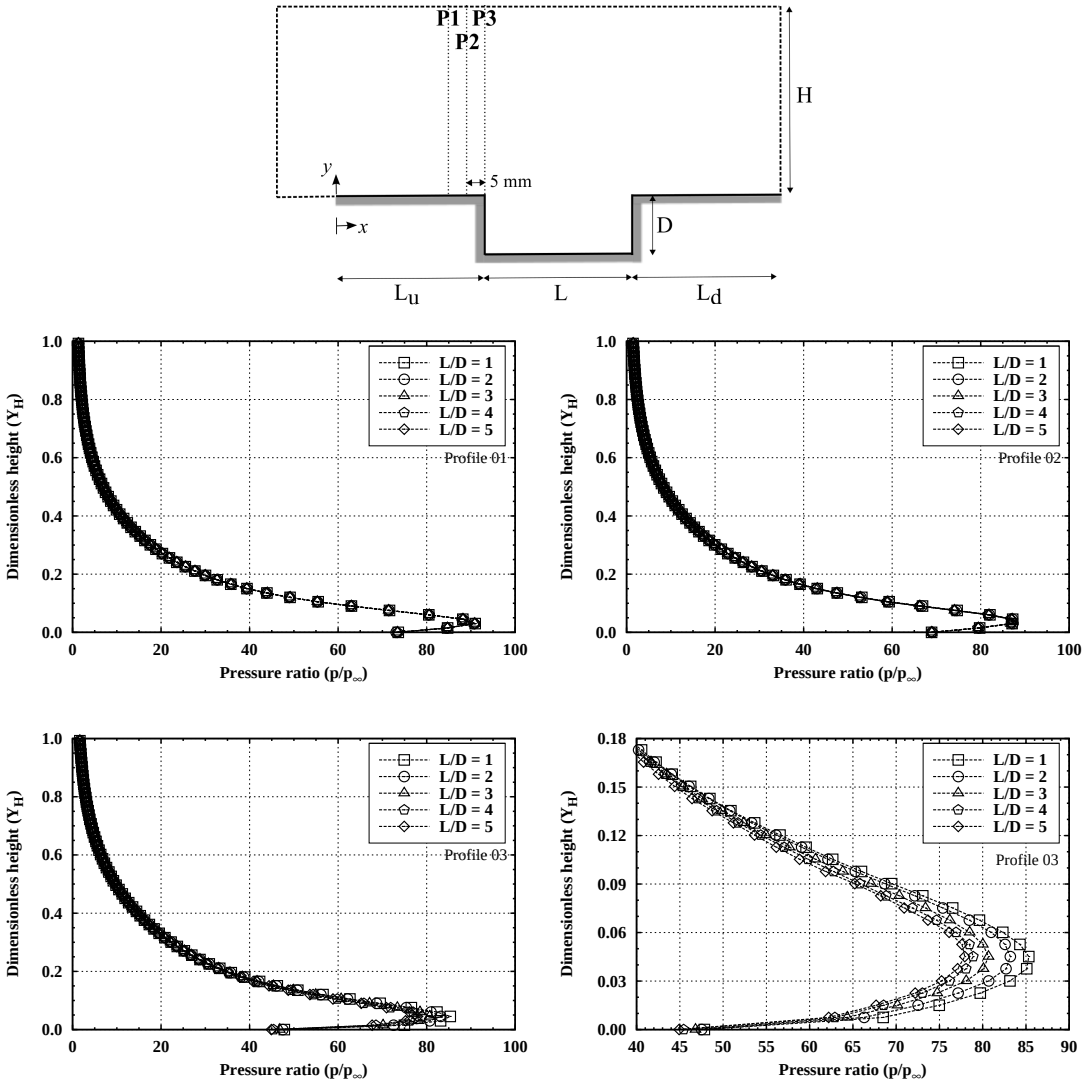

Figure 4.20: Pressure ratio (p/p_∞) profiles for three locations at surface S_1.

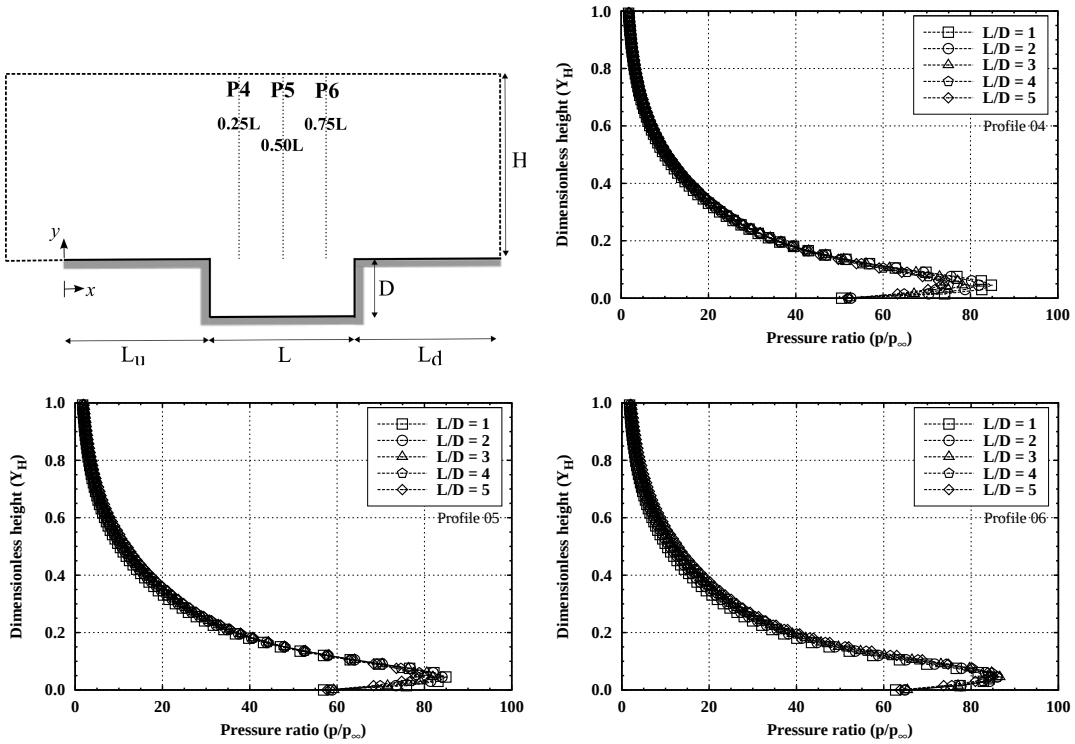

Figure 4.21: Pressure ratio (p/p_∞) profiles for three locations above the cavity.

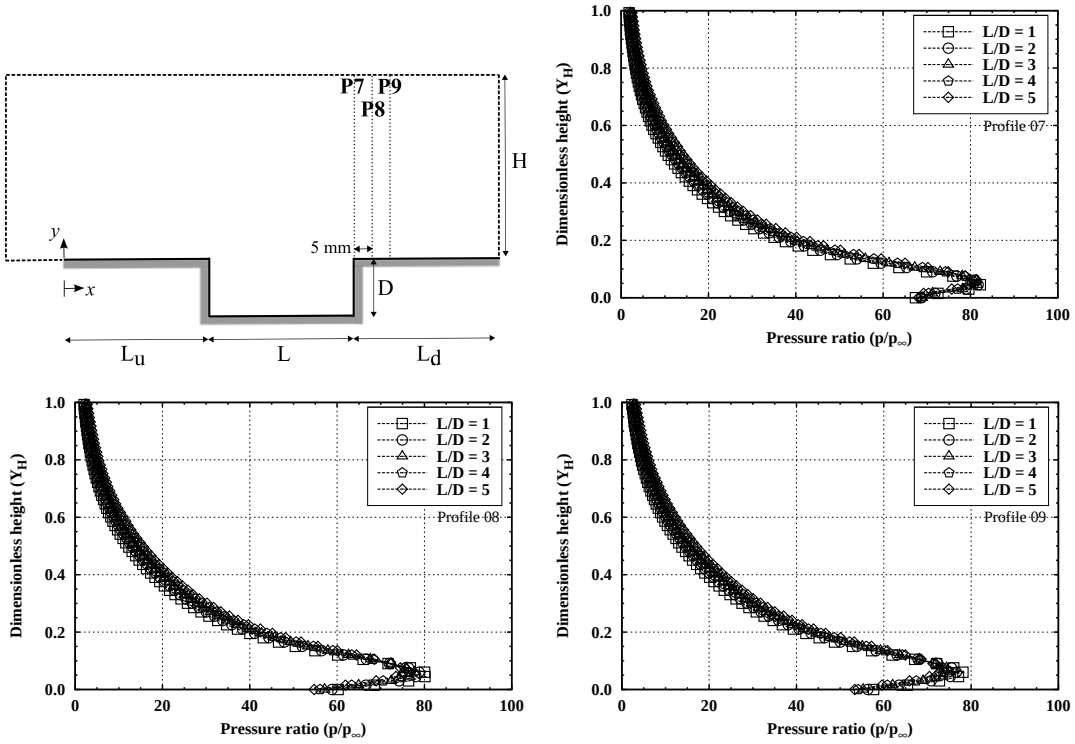

Figure 4.22: Pressure ratio (p/p_∞) profiles for three locations at surface S_5.

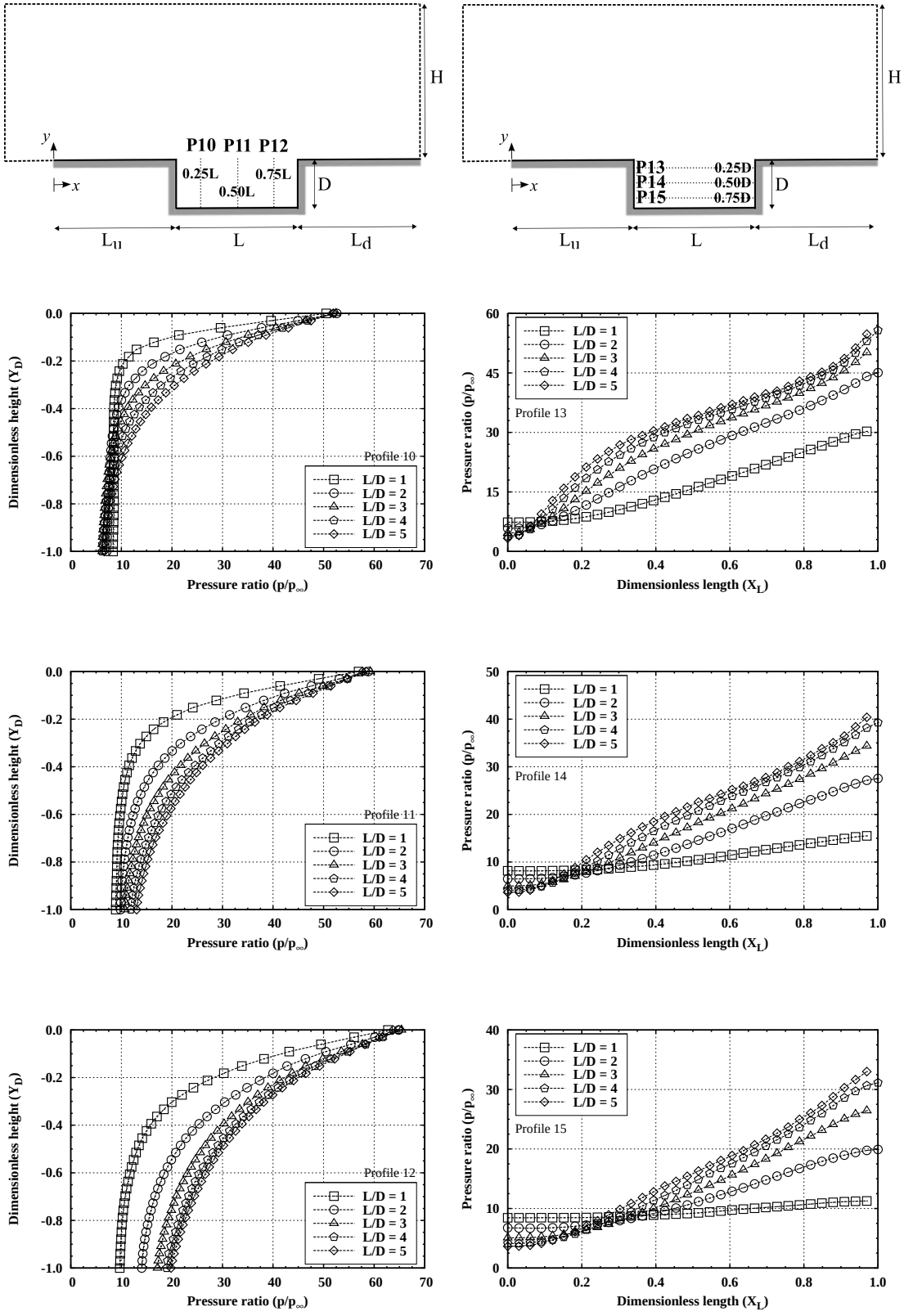

Figure 4.23: Pressure ratio (p/p_∞) profiles for six locations inside the cavity.

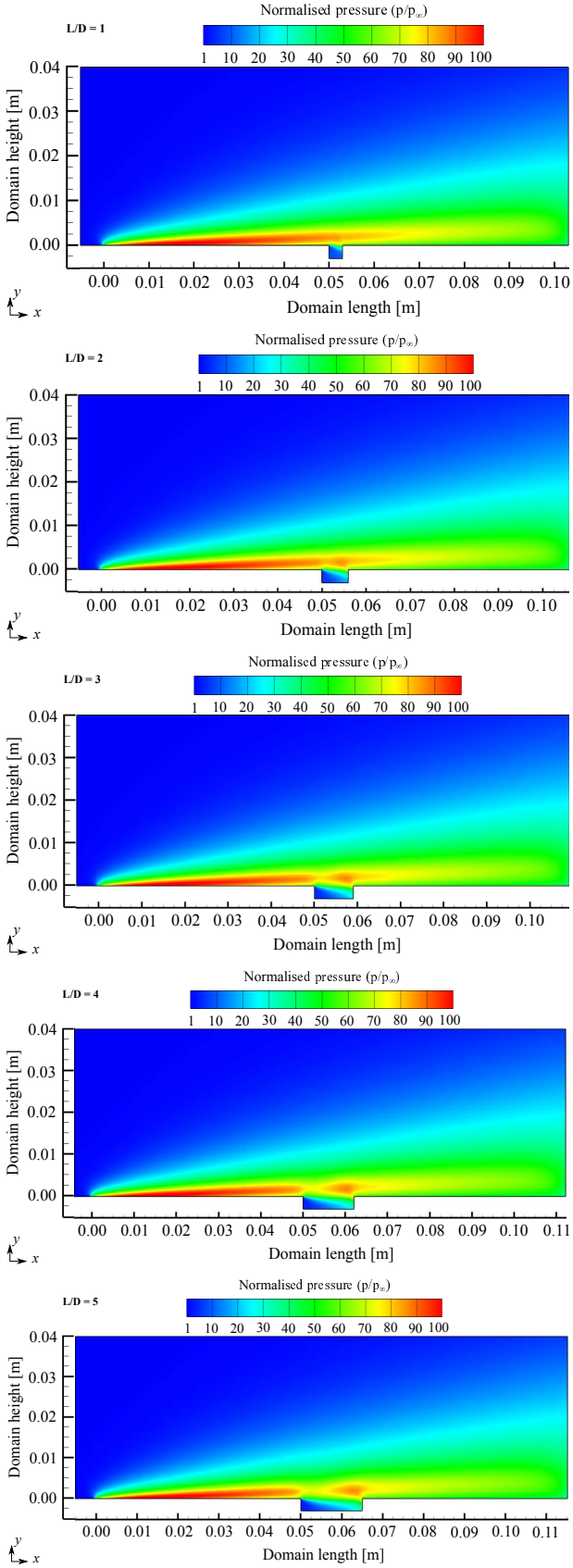

Figure 4.24: Pressure ratio (p/p_∞) distribution over the computational domain as a function of L/D ratio.

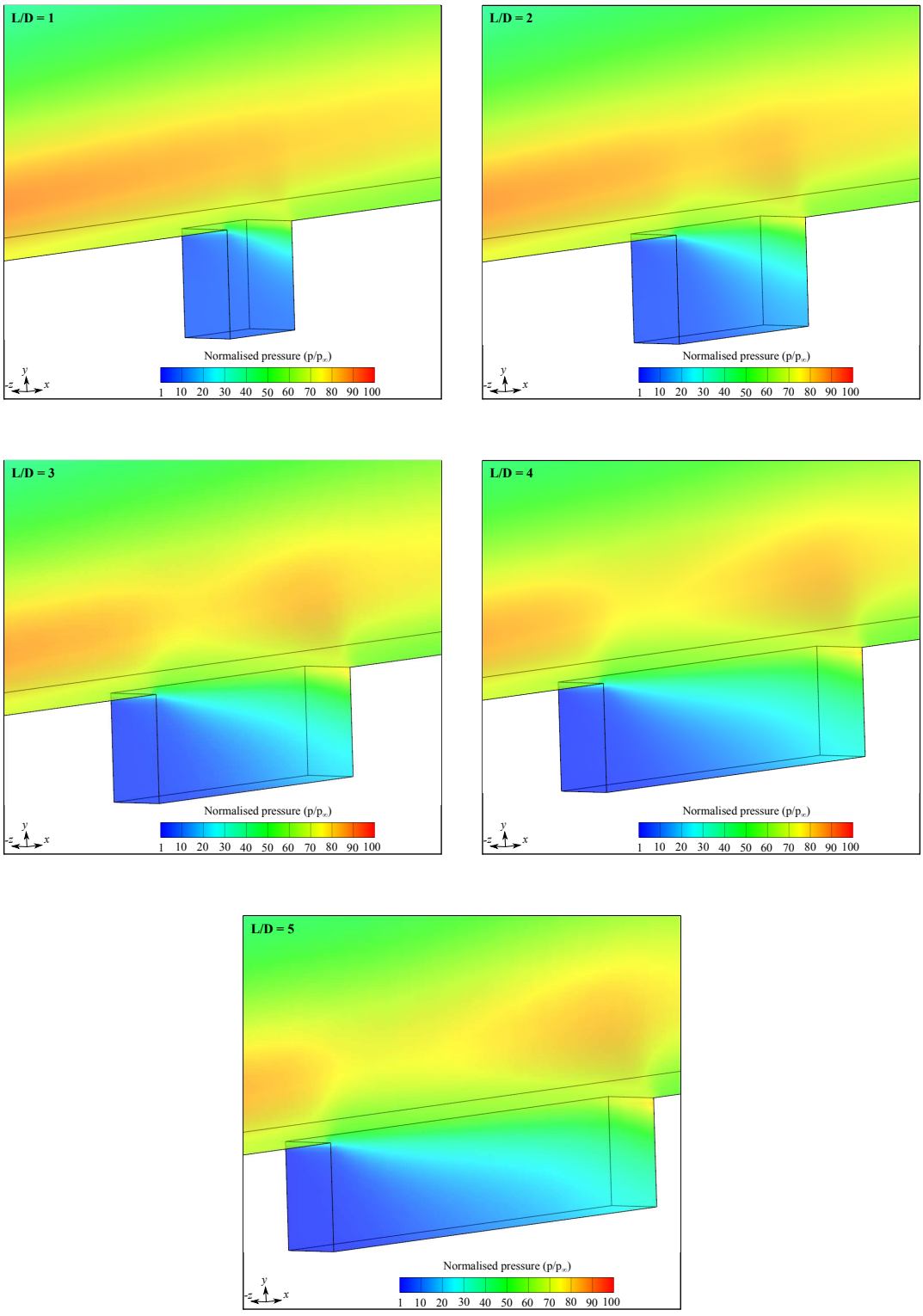

Figure 4.25: Pressure ratio (p/p_∞) distribution inside the cavities as a function of L/D ratio.

The temperature flowfield

During atmospheric reentry, a bow shock formation is one of the main characteristics of a supersonic/hypersonic flight. Across shock waves, part of the high kinetic energy present in the flow is rapidly converted to thermal energy having significant increase on the temperature and pressure in the shock wave region. As a consequence of the temperature augmentation, the molecules which surrounds the re-entry vehicle become excited and thermal-kinetic energy exchange is performed by successive intermolecular interactions. Following this, a relaxation process between translational and internal modes takes place in order to force each mode towards the equilibrium state. Thermodynamic equilibrium occurs when there is, statistically, complete energy equipartition between translational and internal modes. In this sense, the thermodynamic temperature is defined when the temperatures based on each energy mode, i.e., translational, rotational, vibrational and electronic temperatures, are equal to each other. However, the relaxation time, commonly expressed in terms of the relaxation collision number, differs from one mode to another. Therefore, thermal nonequilibrium arises if the local collision frequency is not sufficient to return the molecules to the total statistical equilibrium. In this scenario, for a gas in chemical and thermodynamic nonequilibrium, the overall temperature (T_{ov}) is defined in as the weighted average of the translational (T_{tra}), rotational (T_{rot}), and vibrational (T_{vib}) modes with respect to the degrees of freedom ($\overline{\zeta}$) [20], as follow:

$$T_{ov} = \frac{3T_{tra} + \overline{\zeta}_{rot}T_{rot} + \overline{\zeta}_{vib}T_{vib}}{3 + \overline{\zeta}_{rot} + \overline{\zeta}_{vib}}. \tag{4.4}$$

Translational, rotational and vibrational temperatures are obtained for each cell in the computational domain through the following equations,

$$T_{tra} = \frac{1}{3k_B}\overline{m\boldsymbol{c'}^2} = \frac{1}{3k_B}\frac{\sum_{j=1}^{N} m_j \boldsymbol{c'}^2}{N}, \tag{4.5}$$

$$T_{rot} = \frac{2m\varepsilon_{rot}}{k_B\zeta_{rot}} = \frac{2}{k_B\zeta_{rot}}\frac{\sum_{j=1}^{N} (\varepsilon_{rot})_j}{N}, \tag{4.6}$$

$$T_{vib} = \frac{\Theta_{vib}}{ln\left(1 + \frac{k_B \Theta_{vib}}{\overline{\varepsilon}_{vib}}\right)} = \frac{\Theta_{vib}}{ln\left(1 + \frac{k_B \Theta_{vib}}{\sum_{j=1}^{N} (\varepsilon_{vib})_j}\right)}. \tag{4.7}$$

where k_B represents the Boltzmann constant, $\overline{\varepsilon}_{rot}$ and $\overline{\varepsilon}_{vib}$ are average rotational and vibrational energies per particle computed within the respective cell, and Θ_{vib} the characteristic vibrational temperature.

In a different manner from the previous sub-Sections, the temperature profiles are presented here for cavity length-to-depth ratios equal to 1 and 5, i.e, for smallest and biggest cavities considered in this study. From L/D = 2 to 4, the results are intermediate and will not be presented.

The influence of the cavity length-to-depth ratio on the temperature profiles above the cavities are shown in Figs. 4.26, 4.27, and 4.28. In these plots, overall, translational, rotational, and vibrational temperatures are normalised by the freestream temperature (T_∞). In addition, empty and full symbols refer to profiles for L/D of 1 and 5, respectively.

In analysing this group of plots, it is clear that thermodynamic non-equilibrium occurs outside the cavities. Thermodynamic equilibrium is achieved in the undisturbed freestream, i.e, far from the cavities surface and close to the top boundary condition (at location $Y_H = 0.8$). It worth noting that the overall temperature, defined by Eq. 4.4, is equivalent to the thermodynamic temperature only under thermal equilibrium conditions and the ideal gas equation of state does not apply to this temperature in a non-equilibrium situation.

Close to the upstream (L_u) and downstream (L_d) flat plate surfaces, at location $Y_H \approx 0.075$, the translational kinetic temperature rises to well above the rotational and vibrational temperatures and reaches a maximum value of 72.5 times the freestream temperature. Since a large number of collisions are required to excite the vibrational mode of the particles from their ground state to the upper state, the vibrational temperature is seen to increase much more slowly than the rotational temperature. At location $Y_H \approx 0$, the translational, rotational, vibrational, and overall kinetic temperatures decrease, and reach a wall surface value that is in excess of the wall temperature

(T_w = 1000 K = 5.03T_∞), resulting in a temperature jump [199] and also indicating that the thermodynamic equilibrium is not achieved in the wall surface boundary layer.

Still referring to Figs. 4.26, 4.27, and 4.28, the major aspects of the temperature profiles of L/D = 1 and 5 are: (1) thermodynamic equilibrium is not achieved in the boundary layer, (2) the presence of a temperature jump, and (3) the cavity length-to-depth ratio has no significant effect on the temperature ratio profiles above the cavity for the cases investigated.

Figure 4.29 presents the temperature ratio profiles inside the cavities. The vertical and horizontal temperature profiles are shown as a function of the cavity length and depth, respectively. Again, only the results for L/D = 1 and 5 is demonstrated in this set of plots.

According to Fig. 4.29, on the left hand side, a high temperature ratio is observed at the top of the cavity and then it decreases to reach minimum values at the cavity bottom surface. In addition, it is worth highlighting a high degree of thermodynamic nonequilibrium at the cavity opening, however, as the flow moves downwards towards the cavity bottom surface, the conditions are driven towards thermodynamics equilibrium.

It is important to remark that the translational temperature at the top of the cavity for L/D = 5 at location P10 is 23.8% higher than P12. As P10 is characterised by a expansion region, a temperature decrease was anticipated in this region; however, the increase observed at P10 is associated with the high temperature generated by the attached shock wave on the upstream plate (L_u). This effect is clearly observed from the translational temperature contours maps in Fig. 4.30.

Figure 4.29, on the right hand side, presents the temperature ratio for 3 horizontal profiles inside the cavities. For L/D = 1, the temperature ratio is low in the vicinity of the upstream vertical surface and increases to a maximum value, at the cavity opening. The difference in the overall, translational, rotational, and vibrational temperatures is very small when compared to the cavity length-to-depth ratio equal to 5. Considering the biggest cavity (L/D = 5), it is observed that the temperature is low in the expansion region, increasing to a maximum value which depends on the cavity depth, and then decreases again towards the downstream vertical surface. Furthermore, at the cavity

bottom surface (P15), an increase of 38 times on the temperature ratio is observed when the cavity length-to-depth ratio is increased from 1 to 5, representing a highly dangerous situation in case of heat shield damage.

Finally, it is instructive to present the translational temperature contours maps inside the cavity. As depicted in Fig. 4.31, the development of a high temperature region above the cavity is due to the shock wave at the cavity leading edge. No appreciable changes in the translational temperature contour are observed for L/D = 1, however, as the cavity length is increased, it is evident that hotter gas coming from the shock is able to penetrate deeper into the cavities and contribute to the temperature rise.

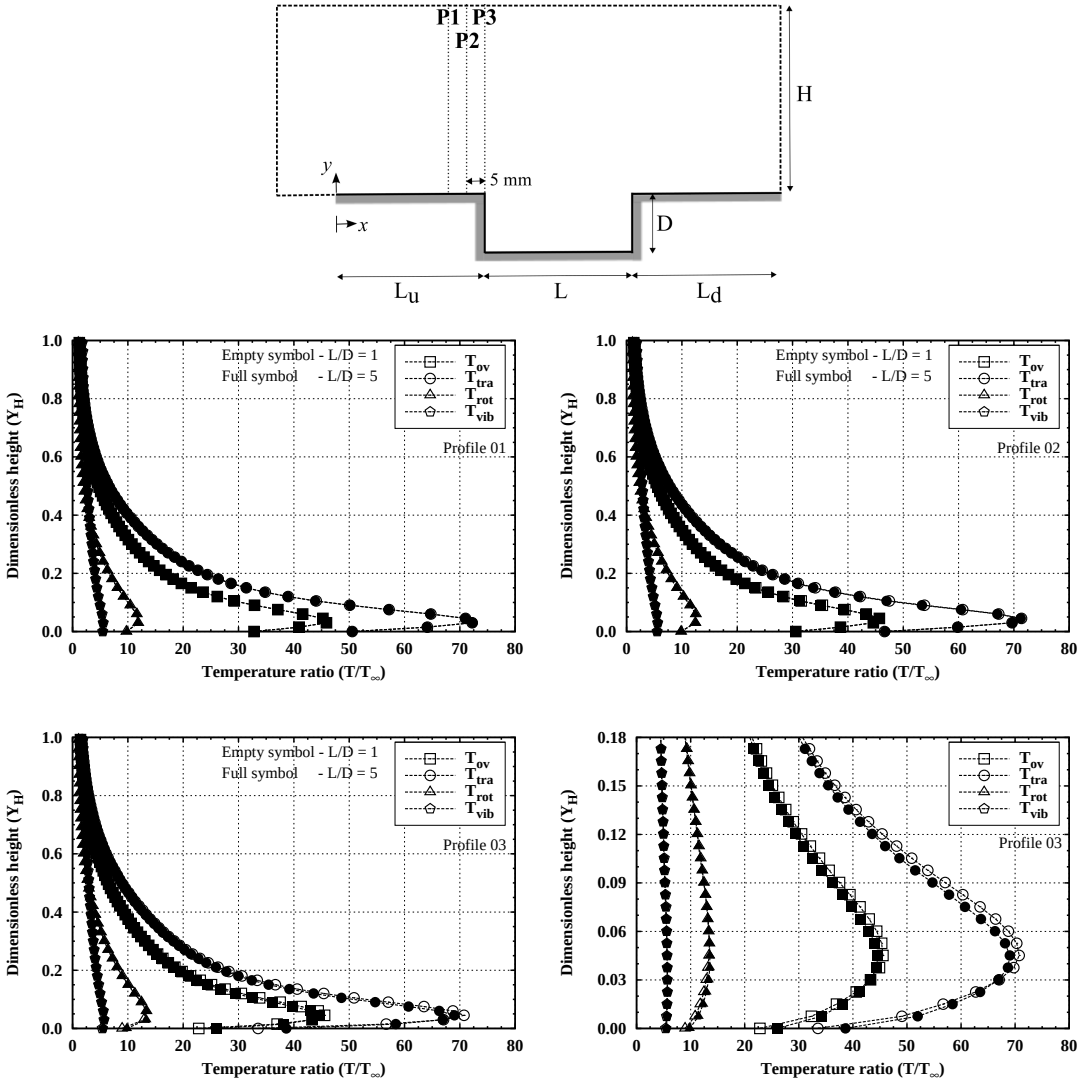

Figure 4.26: Temperature ratio (T/T_∞) profiles for three locations at surface S_1.

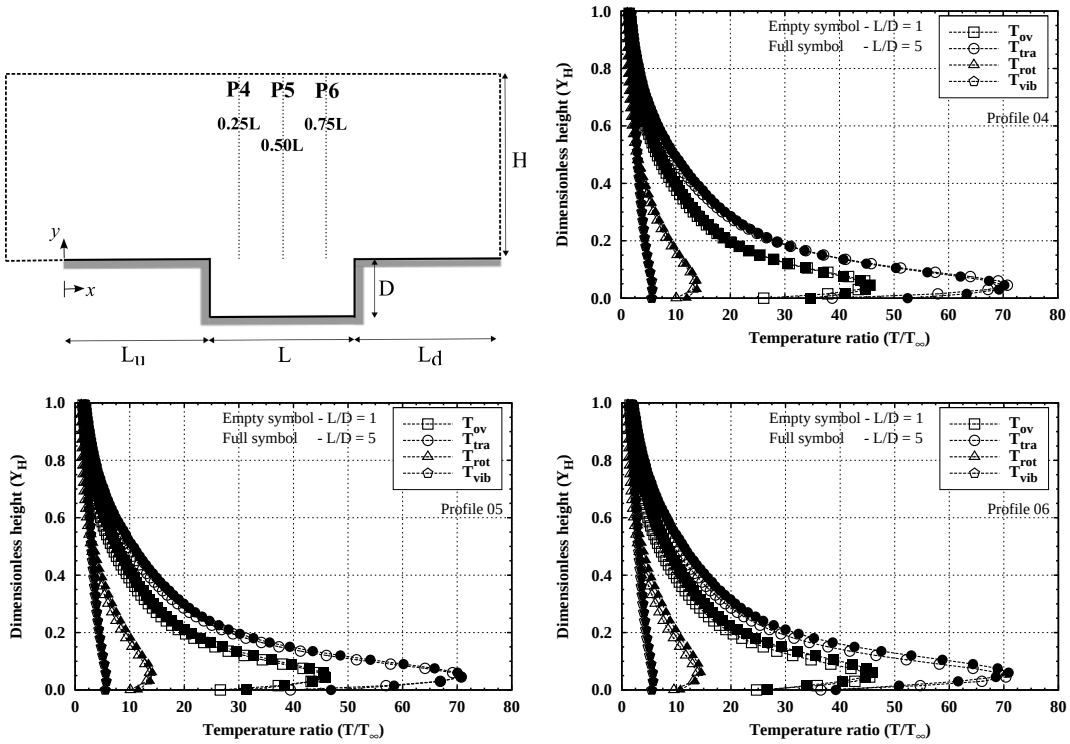

Figure 4.27: Temperature ratio (T/T_∞) profiles for three locations above the cavity.

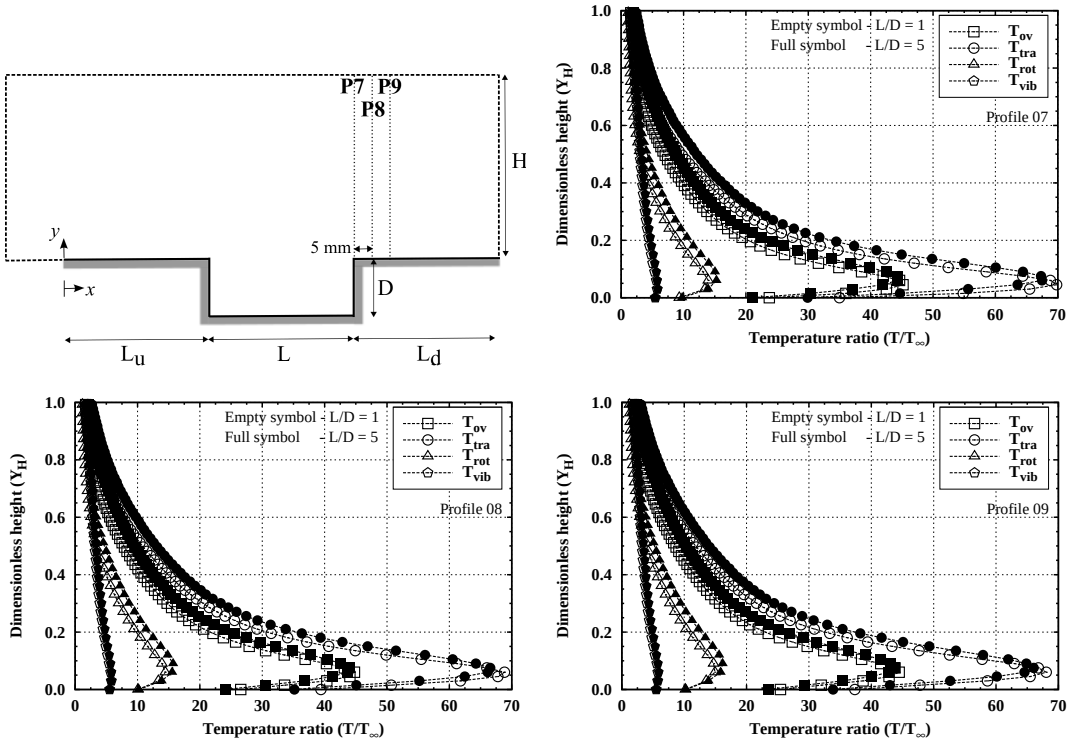

Figure 4.28: Temperature ratio (T/T_∞) profiles for three locations at surface S_5.

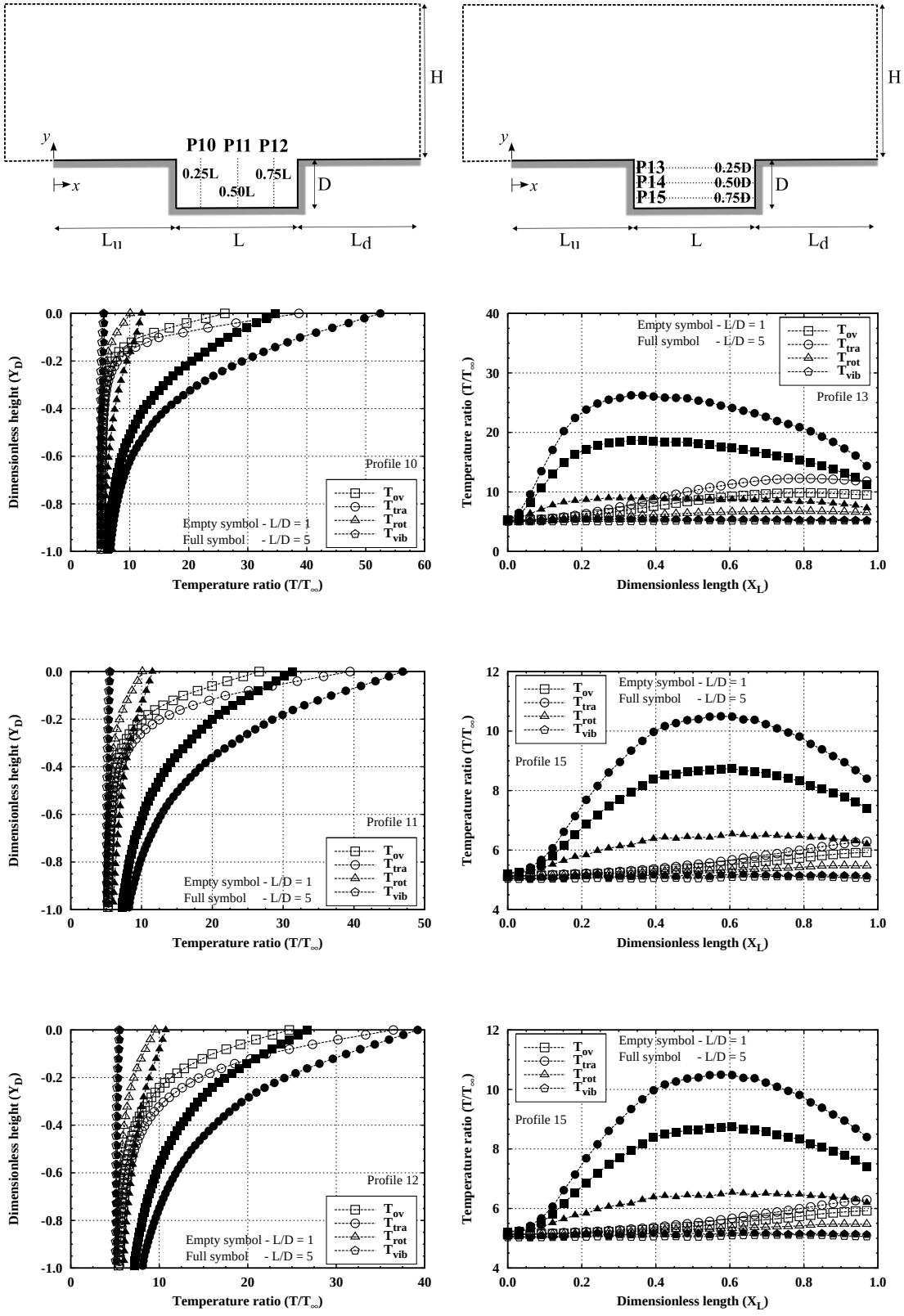

Figure 4.29: Temperature ratio (T/T_∞) profiles for six locations inside the cavity.

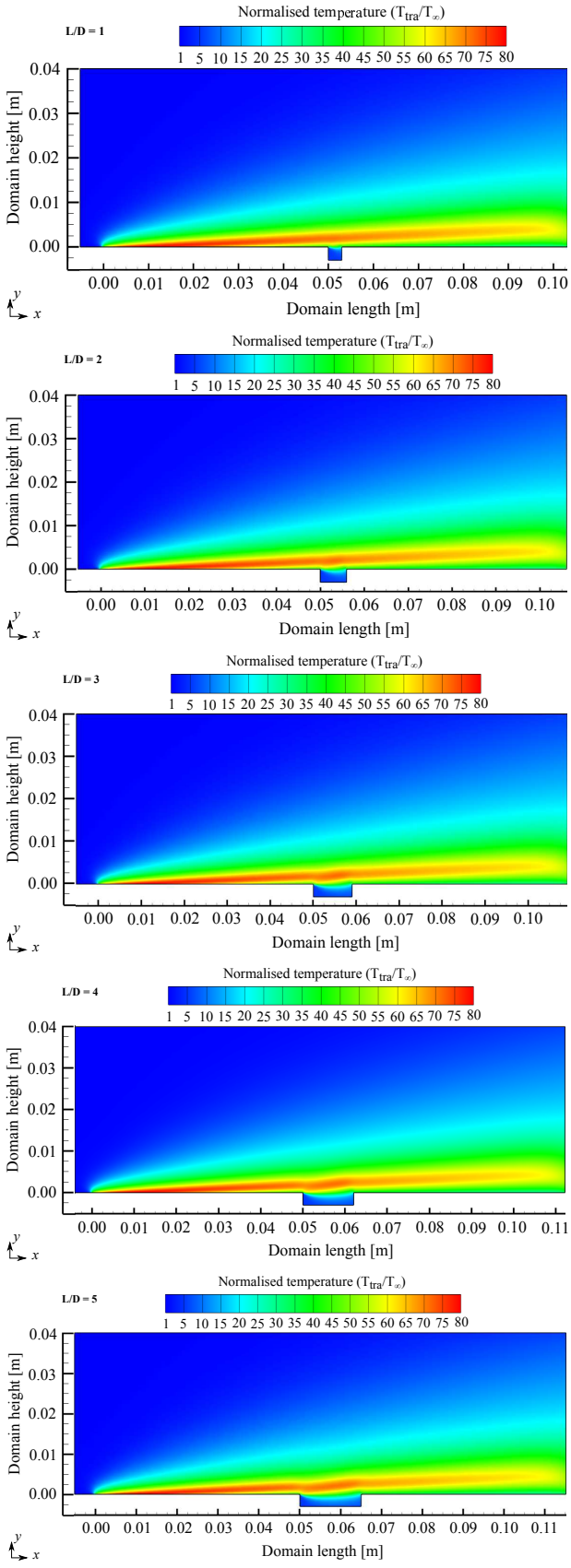

Figure 4.30: Temperature ratio (T_{tra}/T_∞) distribution over the computational domain as a function of L/D ratio.

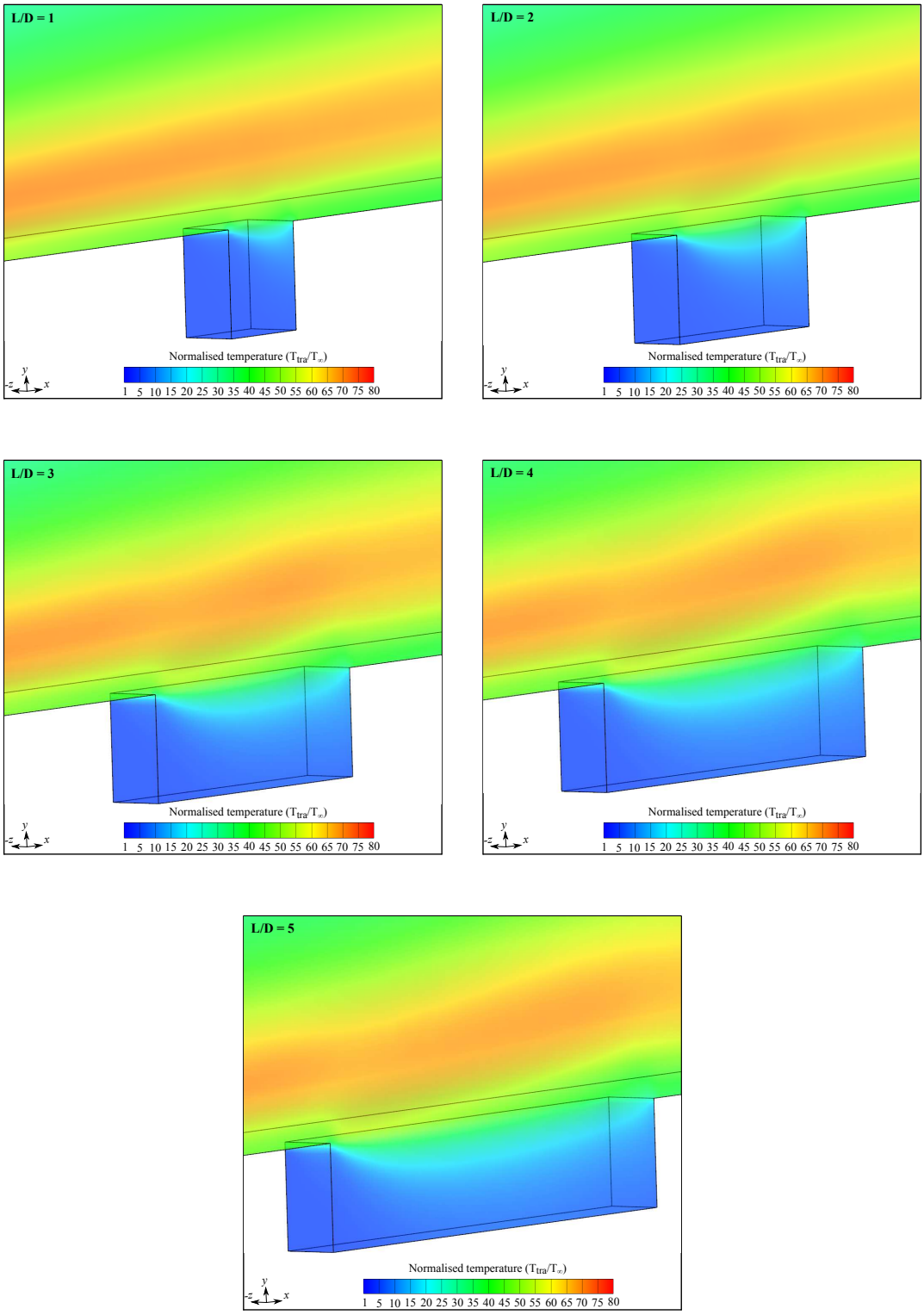

Figure 4.31: Temperature ratio (T/T_∞) distribution inside the cavities as a function of L/D ratio.

4.3.2 Aerodynamic surface quantities

The aerodynamic surface quantities of particular interest in this study are the heat transfer, pressure, and skin friction coefficients. The influence of the cavity length-to-depth ratio as well as the impact of hypersonic reacting and non-reacting flows on these quantities are discussed below.

Heat transfer coefficient

The heat transfer coefficient C_h is defined as:

$$C_h = \frac{q_w}{\frac{1}{2}\rho_\infty U_\infty^3} \tag{4.8}$$

where the heat flux q_w to the body surface is calculated as the net energy flux of molecules impinging on the surface. A flux is regarded as positive if it is directed toward the body surface. The net heat flux q_w is related to the sum of the translational, rotational and vibrational energies of both incident and reflected particles as defined by,

$$q_w = q_i - q_r = \frac{F_N}{A\Delta t}\sum_{j=1}^{N}\left\{\left[\frac{1}{2}m_j c_j^2 + e_{Rj} + e_{Vj}\right]_i - \sum_{j=1}^{N}\left[\frac{1}{2}m_j c_j^2 + e_{Rj} + e_{Vj}\right]_r\right\} \tag{4.9}$$

where F_N is the number of real molecules represented by a single simulated particle, Δt is the time step, A the cell surface area, N is the number of particles colliding with the surface per unit time and unit area, m is the mass of the particles, c is the particle velocity, and e_R and e_V are the rotational and vibrational energies, respectively. Subscripts i and r refer to incident and reflected particles.

The effects on the heat transfer coefficient C_h due to variations in the cavity L/D ratio is shown in Fig. 4.32. In this set of plots, the heat flux was measured along the cavity centre line for surfaces S_1 to S_5. In addition, X_{L_u}, X'_L, and X_{L_d} represent the horizontal surface dimensions normalised by their respective lengths, and Y_D refers to the depth y normalised by the cavity depth D.

According to Fig. 4.32, there are no apparent differences on C_h along the surface S_1 when the cavity length is increased. For the range of L/D ratios investigated, the

heat transfer coefficient is low at the leading edge, increases to a peak value of $C_h = 0.028$ at location $X_{Lu} = 8.0$, and then slightly decreases downstream towards the cavity upstream corner, i.e., at the junction of surfaces S_1 and S_2. Due the compression region formed around the downstream cavity shoulder, it is observed that C_h along the surface S_5 is largest at surface junction S_4-S_5 and decreases downstream to a minimum value at the trailing edge. It pointing out that the downstream disturbances caused by the presence of the cavity where the C_h along the surface S_5 for L/D = 5 shows slightly lower values of C_h when compared with L/D = 1.

For the backward facing, surface S_2, the heat transfer coefficient C_h is high at the cavity entrance $Y_D = 0$, and decreases to a minimum value close to the cavity corner. Along the cavity floor, surface S_3, C_h depends upon the L/D ratio and consequently on the flow structure inside the cavity. In general, C_h increases from near zero at location $X_L = 0$ to reach a maximum at location $X_L = 0.9$, close to the surface junction S_3-S_4. In addition, the larger the L/D ratio the larger the maximum value attained by C_h. For the forward facing surface S_4, C_h is highest at the top of the cavity, and it is observed to decrease along the surface, reaching lower values at the cavity corner. It important to observe that the C_h values along the surface S_4 are two order of magnitude larger than those found for the the surface S_2. As the cavity length is increased, a strong expansion region is produced in the vicinity of the surface S_2 leading to a significant reduction in the heat transfer coefficient. In contrast, due the deeper particle penetration into the cavity, the flow is compressed against the surface S_4 contributing to heat flux augmentation at this region.

Figure 4.33 shows the influence of chemical reactions on the heat transfer coefficient for a cavity of length-to-depth ratio equal to 5. In these plots, full symbols and empty represents the inert gas flow the reacting flows, respectively. With the chemical reactions being dominated by endothermic processes (dissociation), part of the freestream energy is used to excite and break the air molecules. During the simulation, an attached shock wave occurred at the leading edge of the upstream flat plate (L_u), however, it was not strong enough to activated the full set of 19 chemical reactions. Consequently, a reduction in the heat transfer coefficient C_h is only observed along surfaces S_2 and S_5.

From this group of plots, it is evident that the cavity length-to-depth as well as the chemical reactions play a key role in the heat flux distribution. By increasing the L/D ratios the molecules from the freestream may penetrate deeper into the cavity enhancing the momentum and energy transfer to the internal walls of joint-to-joint panels or thermal protection system damage.

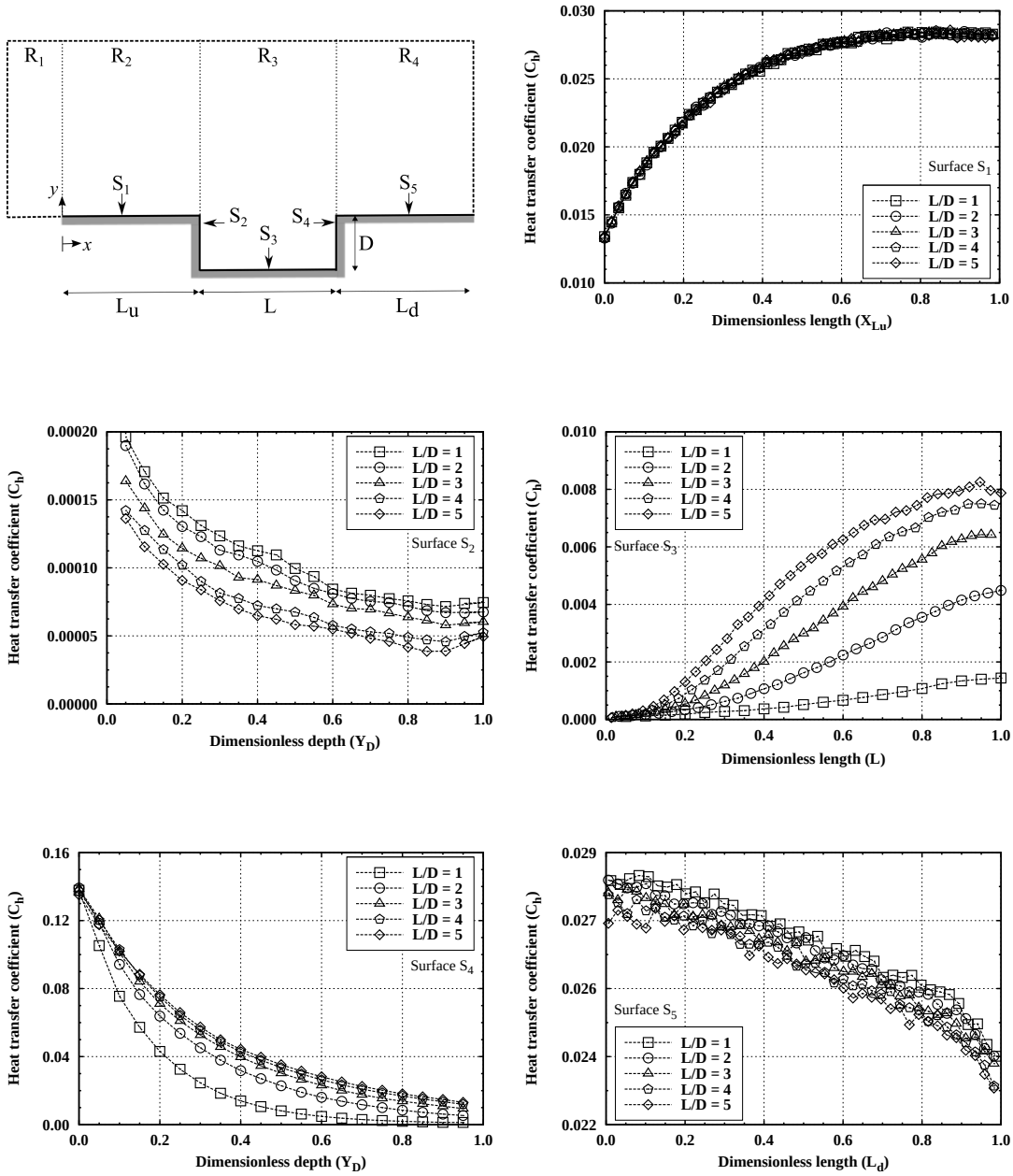

Figure 4.32: Heat transfer coefficient (C_h) distribution along the cavity surfaces as a function of the L/D ratio for reacting gas flow.

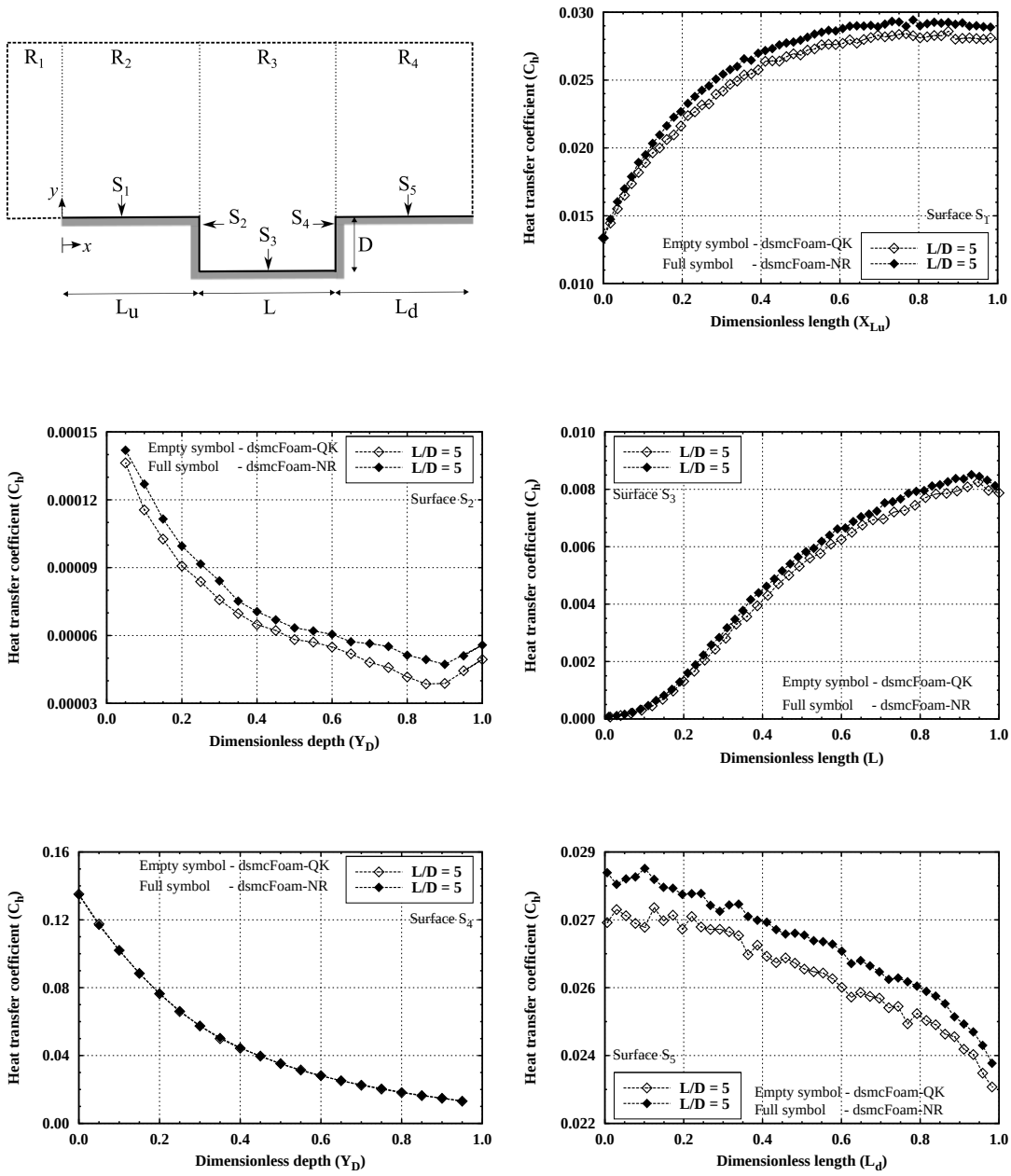

Figure 4.33: Heat transfer coefficient (C_h) distribution along the cavity surfaces as a function of the L/D ratio for non-reacting (*dsmcFoam*-NR) and reacting (*dsmcFoam*-QK) gas flow.

Pressure coefficient

The pressure coefficient C_p is defined as:

$$C_p = \frac{p_w - p_\infty}{\frac{1}{2}\rho_\infty U_\infty^2} \tag{4.10}$$

where the pressure p_w on the body surface is calculated as the sum of the normal momentum fluxes of both incident and reflected molecules at each time step, i.e.:

$$p_w = p_i - p_r = \frac{F_N}{A\Delta t}\sum_{j=1}^{N}\{[(mc_n)_j]_i - [(mc_n)_j]_r\} \tag{4.11}$$

where c_n is the normal component of the velocity of the DSMC particle j.

The variation in the pressure coefficient C_p along the cavity surfaces S_1 to S_5 is plotted in Fig. 4.34 for various L/D ratios. Along surface S_1 it is clear that C_p shows a similar behavior for all of the 3D cavities investigated. However, along the surface S_5 it is observed that the L/D ratio plays an important role in the pressure augmentation at the leading edge of this surface. The presence of small discontinuities in the thermal protection system is almost imperceptible for the incoming freestream particles. However, by increasing the cavity length-to-depth ratio, the freestream is effectively disturbed by the presence of the cavity.

The pressure coefficient on surface S_2 is small at the cavity entrance, $Y_D = 0$, due the expansion around the surface junction S_1-S_2, but increases along the surface reaching a maximum value at location $Y_D = 0.6$ and then decreases towards the cavity corner. Along the cavity floor, surface S_3, C_p increases and reaches its maximum value near the junction of the surfaces S_3 and S_4. According to Fig. 4.25, a high density region is observed at this junction, which contributes to high pressure augmentation in this region.

Along the forward facing surface S_4, the pressure coefficient behaviour contrasts with that observed along S_2, in the sense that C_p has its lowest value at the location $Y_D = 1.0$, and increases steadily along the surface, reaching a peak value at the surface junction S_4-S_5. This phenomenon is expected since the flow develops into a high compression region along this surface, mainly towards the cavity lip represented by

the junction of the surfaces S_4 and S_5. It is important to highlight that the pressure coefficient at surface S_4 is an order of magnitude greater than at surfaces S_2 and S_3.

Finally, the impact of reacting and non-reacting flows over a 3D cavity of L/D = 5 is shown in Fig. 4.35. In a similar manner to the heat transfer coefficient, it is seen that the chemical reactions have no apparent effect on C_p along the surfaces S_1, S_3, and S_4. However, a significant effect of chemical reactions is observed at surfaces S_2 and S_5.

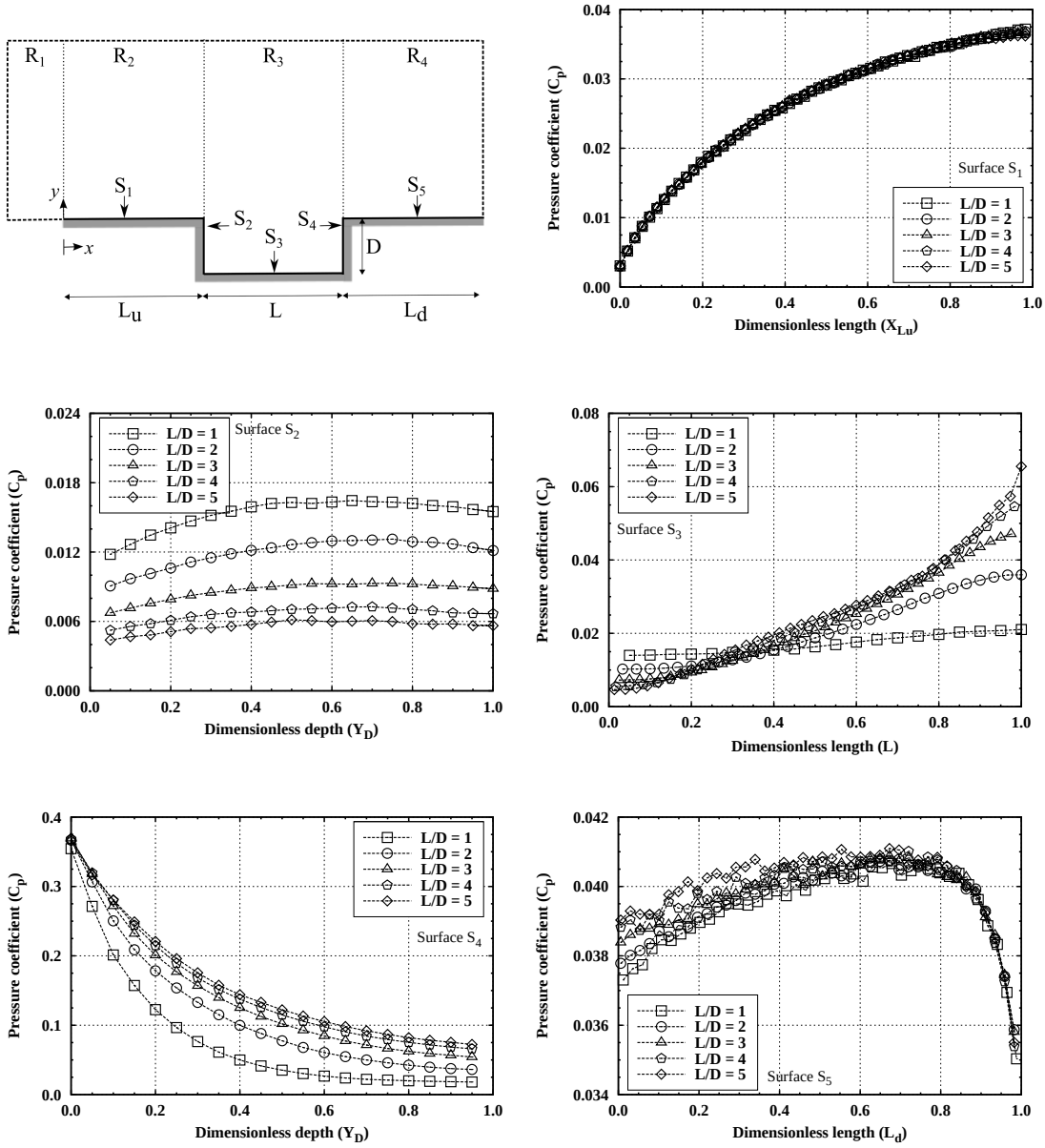

Figure 4.34: Pressure coefficient (C_p) distribution along the cavity surfaces as a function of the L/D ratio for reacting gas flow.

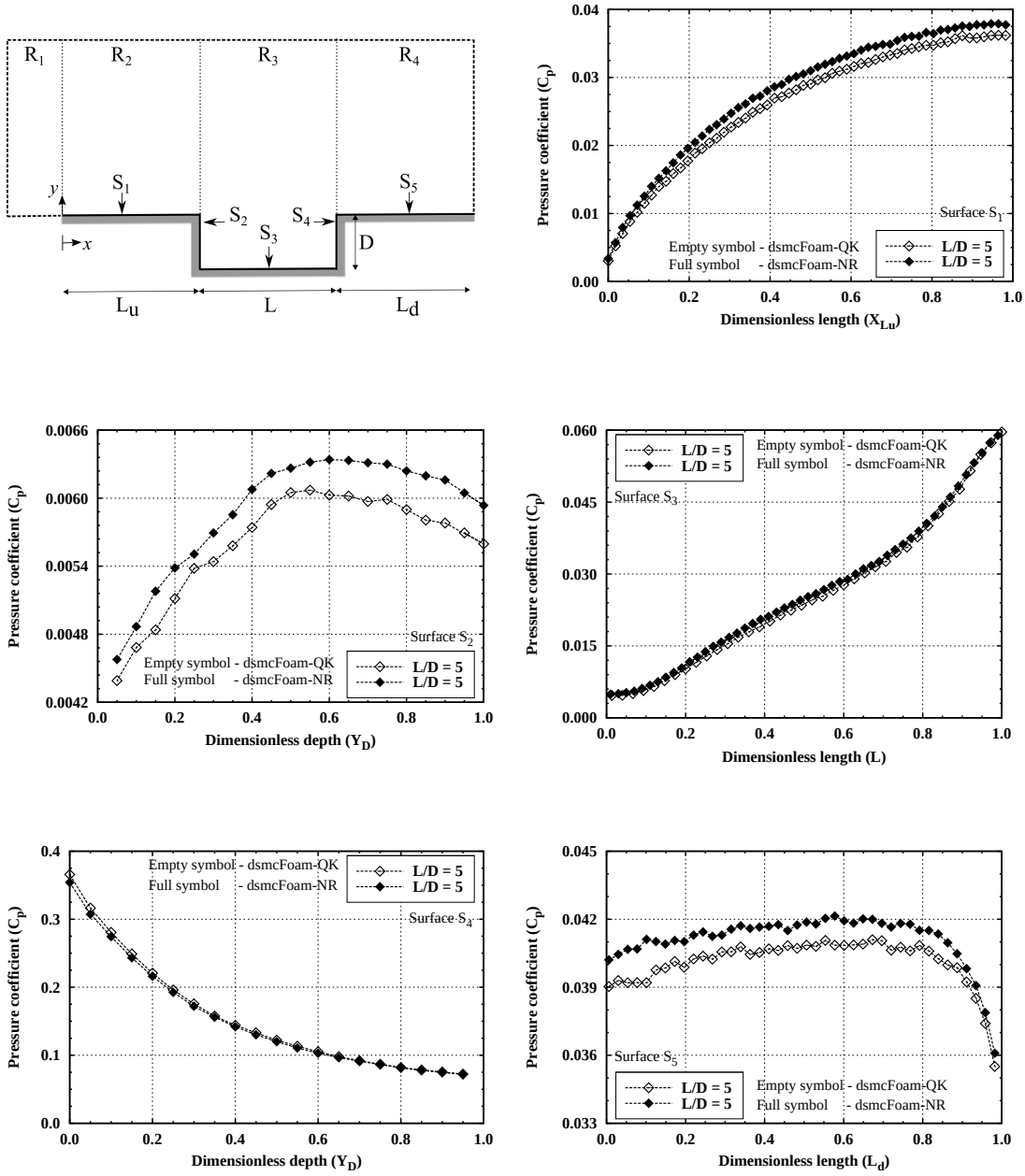

Figure 4.35: Pressure coefficient (C_p) distribution along the cavity surfaces as a function of the L/D ratio for non-reacting (*dsmcFoam*-NR) and reacting (*dsmcFoam*-QK) gas flow.

Skin friction coefficient

The skin friction coefficient C_f is defined as:

$$C_f = \frac{\tau_w}{\frac{1}{2}\rho_\infty U_\infty^2} \tag{4.12}$$

where the shear stress τ_w on the body surface is calculated as the sum of the tangential momentum fluxes of both incident and reflected molecules impinging on the surface at each time step,

$$\tau_w = \tau_i - \tau_r = \frac{F_N}{A\Delta t}\sum_{j=1}^{N}\{[(mc_t)_j]_i - [(mc_t)_j]_r\} \tag{4.13}$$

where c_t is the tangential velocity component of the velocity of the DSMC particle j.

For the particular case of completely diffuse reflection, which is the gas-surface interaction model adopted in the present work, the reflected particles have a mean tangential momentum of zero, since the particles lose, on average, their tangential velocity components. The net tangential momentum flux can therefore be simplified to:

$$\tau_w = \tau_i = \frac{1}{A\Delta t}\sum_{j=1}^{N}[(mc_t)_j]_i \tag{4.14}$$

The impact on the skin friction coefficient C_f due to changes in the 3D cavity L/D ratio is shown in Fig. 4.36, for surfaces S_1 to S_5. The skin friction coefficient for surfaces S_1 and S_5 follows a similar trend to that described for the heat transfer coefficient C_h in Fig. 4.32. However, it is observed that the peak values for C_f along surfaces S_1 and S_5 are 61.7% and 71.5% larger, respectively, than those observed for the pressure coefficient. As a result, the tangential forces, associated with the shear stress, are larger than the normal forces, which are related to the wall pressure, in this region.

The skin friction coefficient along surface S_2 is highest at the cavity entrance, $Y_D = 0$, and decreases along this surface reaching a smaller value at the cavity corner. For the cavity floor, surface S_3, the C_f behavior is influenced by the value of L/D. It is negative in the vicinity of the S_2/S_3 junction, then it becomes positive and reaches a

maximum value that depends on the L/D ratio. In contrast with surface S_2, on the forward facing surface S_4 the skin friction coefficient is always negative.

Normally, when C_f changes from positive to negative, the condition $C_f = 0$ may indicate the presence of a backflow, an attachment or a reattachment point. Here, these are directly related to the clockwise recirculation structure, defined by a primary vortex system observed for the $L/D = 1$ and 2 cases, and two recirculating structures observed for the $L/D = 3$ and 4 cases.

Skin friction measurements along the cavities' centre-line for inert and reacting gas flows are depicted in Fig. 4.37. According to this set of plots, there are no appreciate changes in the C_f value at the surfaces S_1, S_3, S_4, and S_5. Contrary, to the heat transfer and pressure coefficient, the skin friction distribution along the surface S_2 demonstrates a significant increase when chemically reactive flows are employed in the calculations.

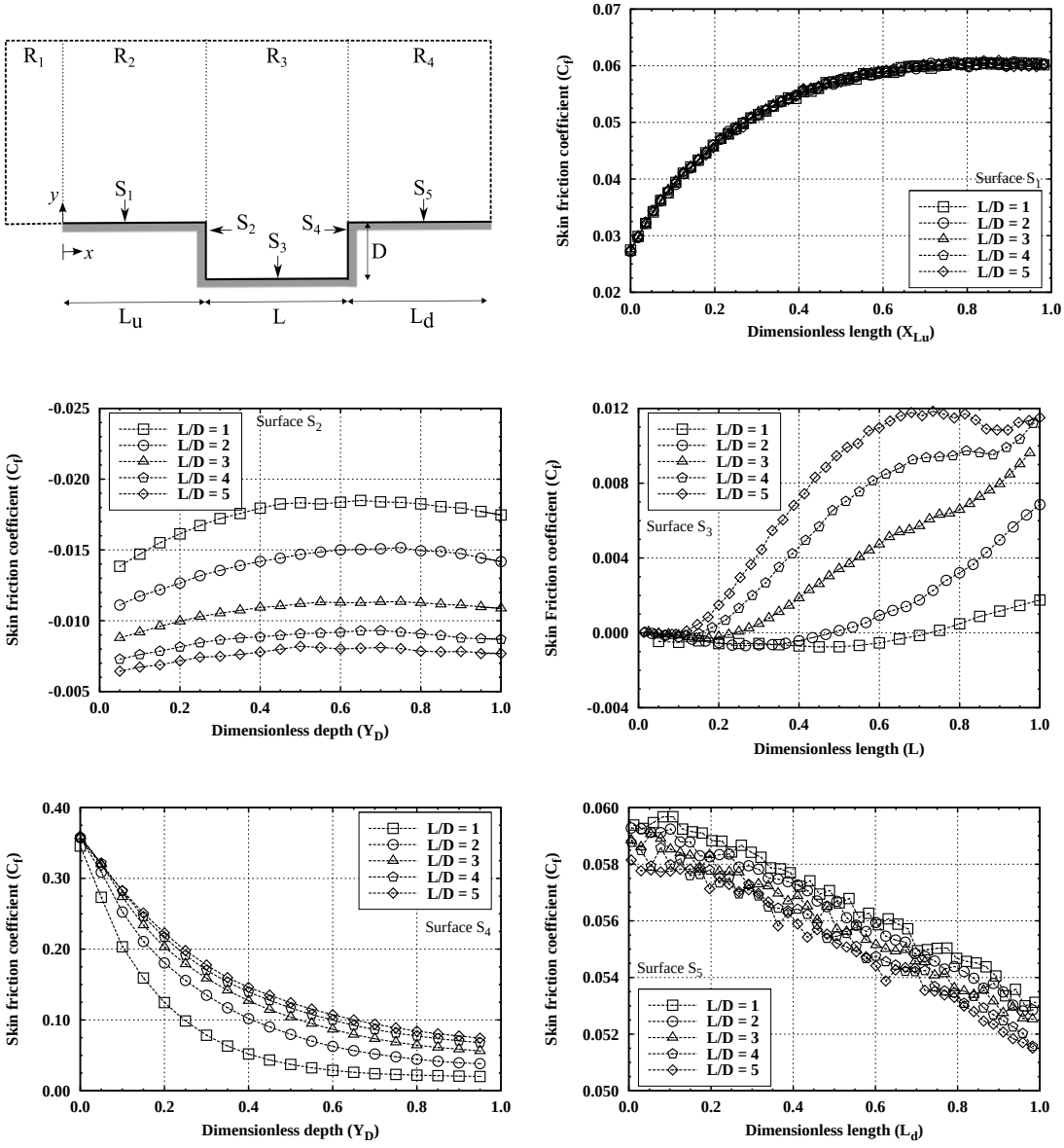

Figure 4.36: Skin friction coefficient (C_f) distribution along the cavity surfaces as a function of the L/D ratio for reacting gas flow.

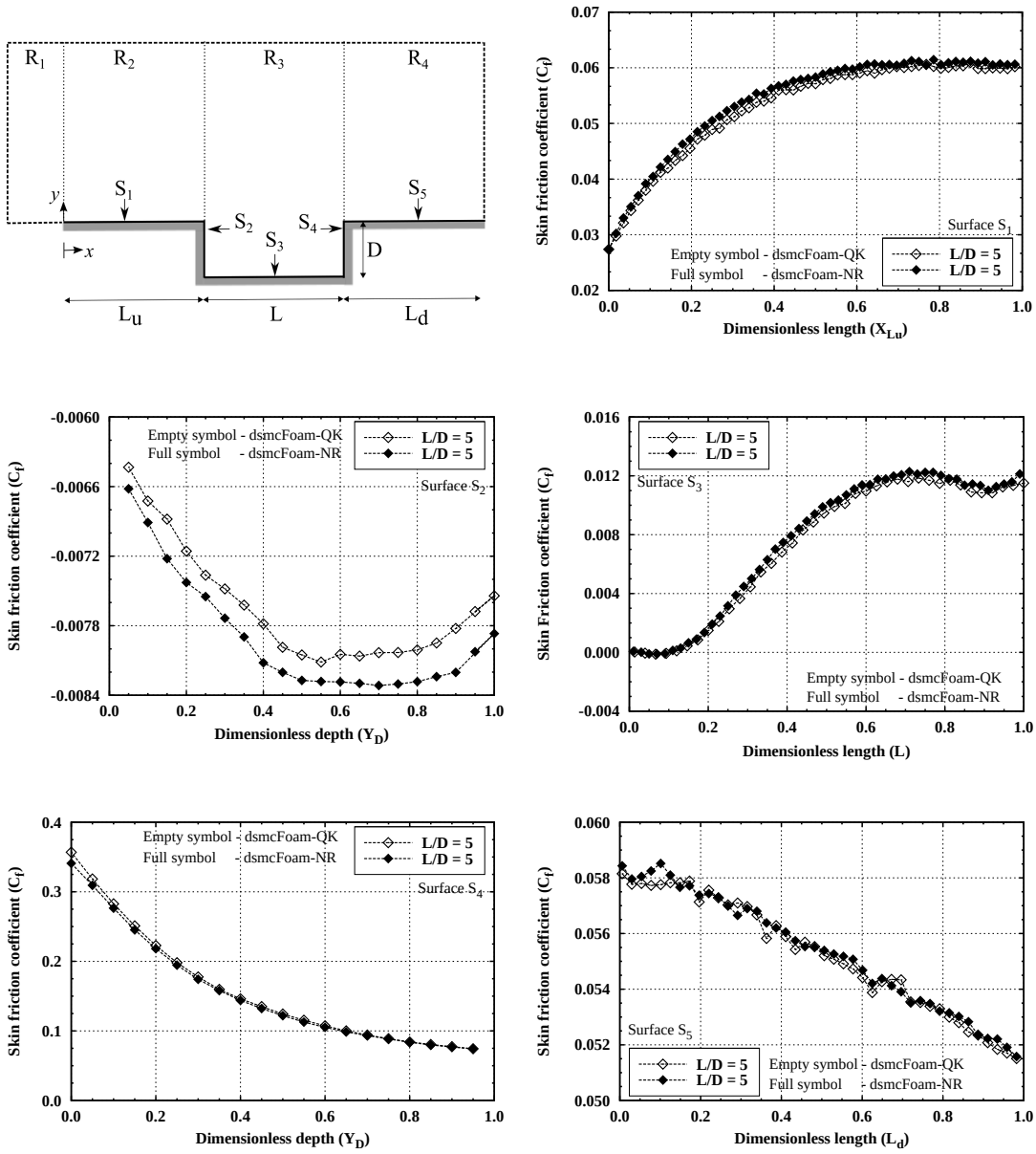

Figure 4.37: Skin friction coefficient (C_f) distribution along the cavity surfaces as a function of the L/D ratio for non-reacting (*dsmcFoam*-NR) and reacting (*dsmcFoam*-QK) gas flow.

Chapter 5

Conclusions

Validation and verification studies of the new open source DSMC code *dsmcFoam* have been undertaken for both inert and chemically-reacting, hypersonic rarefied flows. The novel chemistry approach called the Quantum-Kinetic (QK) model, recently implemented in *dsmcFoam*, has been explained in detail and assessed against experimental measurements and analytical solutions for both equilibrium and nonequilibrium conditions. The QK results showed close agreement for dissociation reaction rates with their experimental and analytical counterparts. However, for certain exchange reactions, modifications to the adjustable parameters in these reactions were found to be necessary in order to correctly match with the measured and analytical results. Further verification trials were executed on a variety of simple and complex test cases. Firstly, high-speed, rarefied flow of an inert gas over a sharp and truncated flat plates were considered with the results showing highly satisfactory agreement in comparison with experimental data and DSMC results from an alternative code. In addition, *dsmcFoam* predictions over the Mars Pathfinder probe showed good levels of concurrence in comparison with published physical data and other numerical solutions. Chemically-reacting flows over a 2D cylinder demonstrated excellent agreement compared with a solution using the established DSMC code MONACO. 3D studies of high-enthalpy, rarefied flow over the Orion Command Module were executed at two altitudes on the re-entry trajectory, 95 km and 105 km. The inclusion of chemical reactions in the *dsmcFoam* calculations resulted in an alteration of the flow structure with a reduced shock stand-off distance, a significant reduction in the translational,

rotational and vibrational temperatures in the shock layer, and a large decrease in the predicted convective heat flux to the vehicle surface when compared with the inert gas case. The activation of endothermic dissociation reactions in the calculations led to temperature reductions of 25.3% and 18.5% compared with inert flow for the lower and higher altitudes, respectively. Comparisons with NASAs DAC DSMC code showed highly satisfactory concurrence for the predicted flow field, including chemical composition.

Surface discontinuities on the Orion thermal protection system were considered and modelled as a family of cavities with varying length-to-depth (L/D) ratios. The magnitude of the L/D ratio was shown to have a significant effect on the flow structure inside and outside the cavities and heavily influenced the aerothermodynamic quantities acting on the thermal protection system and entire body geometry. It was concluded that even the smallest of cavities could provoke a significant increase in heat transfer and surface forces. Under rarefied conditions, twin recirculating vortices were found to exist inside the cavity when L/D = 5; however, the same phenomena is observed in the continuum regime for L/D $>$ 14. As the ratio of L/D was increased, flow penetration into the cavities resulted in an augmentation of the aerothermodynamic surface properties acting on the body.

For the first time multidimensional cavity flows was investigated under thermal and chemical nonequilibrium conditions. It was possible to categorise the flow structure and aerodynamic surface quantities for a wide range of cavities in which demonstrated significant differences when compared to those studied in the continuum regime.

In addition, the results presented in the present thesis clearly shown that a knowledge of the chemically reactive flows play crucial role for the precise characterisation of the vehicle aerothermodynamics and thermal protection system design.

5.1 Future work

Normally, discontinuities in the thermal protection systems are modelled by considering flow over a flat plate with a cavity. This does not represent an ideal approach for solving such problems, since the shock wave is attached to the leading edge of the flat plate and the flow conditions behind the shock do not accurately represent real reentry conditions.

An attached shock wave may be also highly dangerous during the reentry and for this reason blunt bodies have been used for decades. Such vehicles generate detached shocks resulting in a significant reduction in the heat transfer to the vehicles surface. In other cases available in the literature, simulations have been performed taking into account TPS discontinuities embedded in the vehicles surface [66, 68, 200]. However, since the damage (or TPS joint-to-joint junctions) can be an order of magnitude smaller than the spacecraft characteristic length, a precise analysis of aerodynamic surface properties and flow structure inside and around these discontinuities becomes difficult due to the large differences in scale.

Bearing this length scale separation in mind, a new technique is proposed by the author for future work considerations. This methodology consist of 3 main steps:

1. Perform simulations of a full 3D undamaged vehicle.

2. Extract flowfield values (velocity, number density for each species, and translational, rotational, and vibrational temperatures) for a specific region close to the full undamaged vehicle (smooth surface).

3. Perform TPS discontinuity simulations using the extracted flowfield values as the new boundary condition. A schematic view of this new technique is shown in Fig. 5.1.

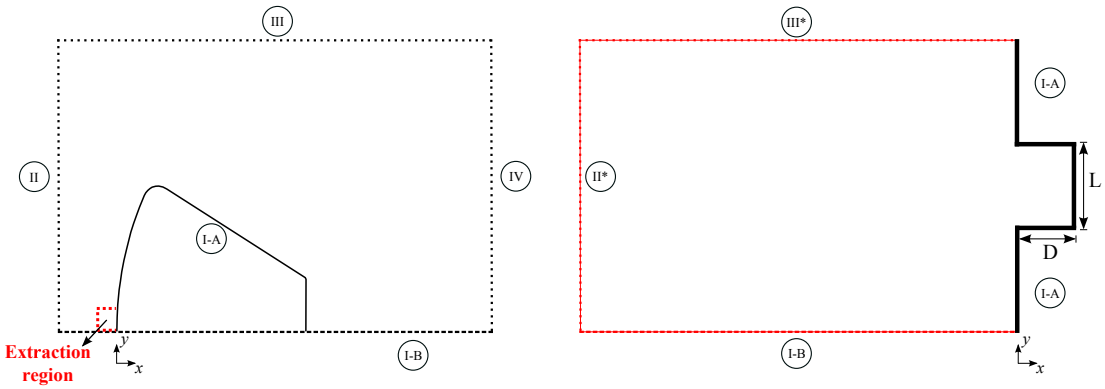

Figure 5.1: Orion computational domain (left) and amplified view of the flowfield properties extraction region for Orion smooth surface heat shield (right).

Initial numerical trials of this methodology have shown promise and the general research contained in this thesis opens a number of avenues for future investigations:

- Precise investigation of thermal protecting systems discontinuities through the flow extraction technique;
- Extension of the *dsmcFoam* code to include charged particles in order to investigate plasma formation around re-entry vehicles;
- Since the spacecrafts TPS are made of different materials, gas-surface interaction assessment becomes necessary;
- Surface ablation, outgassing and surface chemistry analysis;
- Study the influence of the cavity shape and depth on the flowfield structure and aerodynamic surface properties;
- Effect of angle of attack and surface temperature on hypersonic rarefied cavity flows;
- Investigation of transient effects and wall catalicity.

References

[1] F. W. Martin. Legacy of the space shuttle from an aerodynamic and aerothermodynamic perspective. In *AIAA Space 2011 Conference and Exposition*, number AIAA Paper 2011-7122. Long Beach, California, 2011.

[2] D. E. Myers, C. J. Martin, and M. L. Blosser. Parametric weight comparison of advanced metallic, ceramic tile, and ceramic blanket thermal protection systems. Technical Report NASA TM-2000-210289.

[3] S. J. Scotti, C. Clay, and M. Rezin. Structures and materials technologies for extreme environments applied to reusable launch vehicles. In *AIAA/ICAS International Symposium and Exposition*, number AIAA Paper 2003-2697. Dayton, OH, 2003.

[4] J. C. Dunavant and D. A. Throckmorton. Aerodynamic heat transfer to RSI tile surfaces and gap intersections. *Journal of Spacecraft and Rockets*, 6(6):437–440, 1974.

[5] C. A. Belk, J. H. Robinson, M. B. Alexander, W. J. Cooke, and Pavelitz. Meteoroids and orbital debris: effects on spacecraft. Technical Report NASA-1408, 1997.

[6] S. Evans and J. Williamsen. Orbital debris shape and orientation effects on impact damage to shuttle tiles. In *47th Structures, Structural Dynamics, and Materials Conference*, number AIAA Paper 2006-2221. Newport, RI, 2006.

[7] G. E. Palmer and C. Tang. Computational assessment of the thermal protection system damage experienced during STS-118. *Journal of Spacecraft and Rockets*, 46(6):1110–1116, 2009.

[8] V. E. Zoby, R. A. Thompson, and K. E. Wurster. Aeroheating design issues for reusable launch vehicles - a perspective. In *34th AIAA Fluid Dynamics Conference*, number AIAA Paper 2004-2535. Portland, Oregon, 2004.

[9] D. E. Glass. Ceramic matrix composite (CMC) thermal protection systems (TPS) and hot structures for hypersonic vehicles. In *15th AIAA Space Planes and Hypersonic Systems and Technologies Conference*, number AIAA Paper 2008-2682. Dayton, Ohio, 2008.

[10] J. L. Everhart and F. A. Greene. Turbulent supersonic/hypersonic heating correlations for open and closed cavities. *Journal of Spacecraft and Rockets*, 47(4):545–553, 2010.

[11] C. H. Campbell, R. A. King, S. A. Berry, M. A. Kegerise, and T. J. Horvath. Roles of engineering correlations in hypersonic entry boundary layer transition prediction. In *48th AIAA Aerospace Sciences Meeting Including the New Horizons Forum and Aerospace Exposition*. Orlando, Florida, 2010.

[12] M. A. Pulsonetti, R. A. Thompson, and S. J. Alter. Prediction of STS-107 hypervelocity flow fields about the shuttle orbiter with various wing leading edge damage. In *JANNAF 27th Airbreathing Propulsion Subcommittee*. Colorado Springs, CO, 2003.

[13] J. L. Everhart, K. S. Bey, W. A. Wood, and M. A. Pulsonetti. Experimental and computational investigations of cavity flow simulationg debris damage to thermal protection system tiles. In *JANNAF 27th Airbreathing Propulsion Subcommittee*, 2003.

[14] K. L. Bibb and R. K. Prabhu. Computational aerodynamics of shuttle orbiter damage scenarios in support of the Columbia accident investigation. In *37th Thermophysics Conference*, number AIAA Paper 2004-2279. Portland, OR, 2004.

[15] T. J. Horvath. Experimental aerothermodynamics in support of the Columbia accident investigation. In *42nd AIAA Aerospace Science Meeting and Exhibit*, number AIAA Paper 2004-1387. Reno, Nevada, 2004.

[16] G. J. Brauckmann and W. I. Scallion. Experimental hypersonic aerodynamic characteristics of the space shuttles orbiter for a range of damage scenarios. In *37th AIAA Themophysics Conference*, number AIAA Paper 2004-2280. Portland, Oregon, 2004.

[17] Anon. Columbia accident ivestigation report. Technical report, August, 2003.

[18] C. H. Campbell, B. Anderson, G. Bourland, S. Bouslog, A. Cassady, T. J. Horvath, S. A. Berry, P. A. Gnoffo, W. A. Wood, J. J. Reuther, D. M. Driver, D. C. Chao, and J. Hyatt. Orbiter return to flight entry aeroheating. In *9th AIAA/ASME Joint Thermophysics and Heat Transfer Conference*, number AIAA Paper 2006-2917. San Francisco, California, 2006.

[19] J. M. A. Longo, K Hannemann, and V. Hannemann. The challenge of modeling high speed flows. In *Proceedings of the Federation of European Simulation Societies - EUROSIM 2007*. Lujbiana, Slovenien, 2007.

[20] G.A. Bird. *Molecular gas dynamics and the direct simulation of gas flows*. Clarendon, Oxford, 1994.

[21] S. Chapman and T.G. Cowling. *The mathematical theory of non-uniform gases: an Account of the kinetic theory of viscosity, thermal conduction and diffusion in gases*. Cambridge University Press, 1991.

[22] I. D. Boyd, G. Chen, and G. V. Candler. Predicting failure of the continuum fluid equations in transitional hypersonic flows. *Physics of Fluids*, 7(1):210–219, 1995.

[23] W. Wang and I. D. Boyd. Predicting continuum breakdown in hypersonic viscous ows. *Physics of Fluids*, 15(1):91–100, 2003.

[24] D. Burnett. The distribution of velocities in a slightly non-uniform gas. In *Proceedings of the London Mathematical Society*, volume 39, pages 385–430, 1935.

[25] D. Burnett. The distribution of molecular velocities and the mean motion in a non-uniform gas. In *Proceedings of the London Mathematical Society*, volume 40, pages 382–435, 1936.

[26] J. C. Tannehill and G. R. Eisler. Numerical computation of the hypersonic leading edge problem using the Burnett equation. *Physics of Fluids*, 19(9):1958–1988, 1976.

[27] K. A. Fiscko and D. R. Chapman. Comparison of Burnett, super-Burnett, and Monte Carlo solutions for hypersonic shock structure. *Rarefied Gas Dynamics: Theoretical and Computational Techniques*, 118:374–395, edited by E. P. Muntz, D. P. Weaver, and D. H. Campbell, 1988.

[28] D. R. Chapman and K. A. Fiscko. Hypersonic shock structure with Burnett terms in the viscous stress and heat flux. In *AIAA Thermophysics, Plasmadynamics and Lasers Conference*, page 13. San Antonio, TX, 1988.

[29] E. Salomons and M. Mareschal. Usefulness of the Burnett description of strong shock waves. *Physical Review Letters*, 69:269–272, 1992.

[30] F. J. Uribe, R. M. Velasco, and L. S. Garcia-Colin. Burnett description of strong shock waves. *Physical Review Letters*, 81:2044–2047, 1998.

[31] X. Zhong, R. W. MacCormack, and D. R. Chapman. Stabilization of the Burnett equations and application to hypersonic flows. *AIAA Journal*, 31(6):1036–1043, 1993.

[32] X. Zhong and G. Furumoto. Solutions of the Burnett equations for axisymmetric hypersonic flow past spherical blunt bodies. In *6th AIAA/ASME Joint Thermophysics and Heat Transfer Conference*. Colorado Springs, CO, 1994.

[33] C. J. Lee. unique determination of solutions to the Burnett equations. *AIAA Journal*, 32(5):985–990, 1994.

[34] X. Zhong and H. Furumoto. Augmented Burnett-equation solutions over axisymmetric blunt bodies in hypersonic flow. *Journal of Spacecraft and Rockets*, 32(4):588–595, 1995.

[35] K. A. Comeaux, D. R. Chapman, and R. W. MacCormack. An analysis of the Burnett equations based on the second law of thermodynamics. In *33rd Aerospace Science Meeting and Exhibit*, volume AIAA 95-0415. Reno, NV, 1995.

[36] R. Chen, R. K. Agarwal, F. G. Cheremisin, and Y. Bondar. A comparative study of Navier-Stokes, Burnett, DSMC, and Boltzmann solutions for hypersonic flow past 2-D bodies. In *45th AIAA Aerospace Science Meeting and Exhibit*, number AIAA-2007-207, 2007.

[37] H. K. Cheng and G. Emanuel. Perspective on hypersonic nonequilibrium flow. *AIAA Journal*, 33(2):385–400, 1995.

[38] R. K. Agarwal and K. Yun. Burnett equations for simulation of transitional flows. *Applied Mechanics Reviews*, 55(3):219–240, 2002.

[39] C. Cercignani. *Rarefied gas dynamics: from basic concepts to actual calculations*. Cambridge University Press, 2000.

[40] D. C. Rapaport. *The Art of Molecular Dynamics Simulation*. Cambridge University Press, New York.

[41] D. Frenkel and B. Smit. *Understanding Molecular Simulation*. Academic Press, 2002.

[42] G. A. Bird. *Molecular gas dynamics*. Oxford Clarendon Press, 1976.

[43] A. Roshko. Some measurements of flow in a rectangular cutout. Technical Report NACA-3488, 1955.

[44] D. R. Chapman. A theoretical analysis of heat transfer in regions of separated flow. Technical Report NACA TN-3792, 1956.

[45] W. O. Carlson. Heat transfer in laminar, separated, and wake flow regions. In *Proc. 1959 Heat Transfer and Fluid Mechanics Institute*, pages 140–144. Stanford University Press, 1959.

[46] H. K. Larson. Heat transfer in separated flows. *Journal of the Aerospace Sciences*, 26 (11):731–738, 1959.

[47] A. F. Charwat, J. N. Ross, F. C. Dewey, and J. A. Hitz. An investigation of separated flows. Part I: The pressure field. *Journal of Aerospace Sciences*, 28(6):457–470, 1961.

[48] A. F. Charwat, F. C. Dewey, J. N. Ross, and J. A. Hitz. An investigation of separated flows. Part II: Flow in the cavity and heat transfer. *Journal of Aerospace Sciences*, 28 (7):513–527, 1961.

[49] J. L. Shideler, G. L. Webb, and C. M. Pittman. Verification tests of durable thermal protection system concepts. *Journal of Spacecraft and Rockets*, 22(6):598–604, 1985.

[50] M. H. Bertran and Wiggs. M. M. Effect of surface distortions on the heat transfer to a wing at hypersonic speeds. *AIAA Journal*, 1(6):1313–1319, 1963.

[51] D. E. Nestler, A. R. Saydah, and W. L. Auxer. Heat transfer to steps and cavities in hypersonic turbulent flow. *AIAA Journal*, 7(7):1368–1370, 1968.

[52] J. W. Hodgson. Heat transfer in separated laminar hypersonic flow. *AIAA Journal*, 8 (12):2291–2293, 1970.

[53] R. A. Brewer, A. R. Saydah, D. E. Nestler, and D. E. Florence. Thermal performance evaluation of RSI panel gaps for space shuttle orbiter. *Journal of Spacecraft and Rockets*, 10(1):23–28, 1973.

[54] I. Weintein, D. E. Avery, and A. J. Chapman. Aerodynamic heating to the gaps and surfaces of simulated reusable-surface-insulation tile array in turbulent flow at Mach 6.6. Technical Report NASA TM-3225, 1975.

[55] A. R. Wieting. Experimental investigation of heat-transfer distributions in deep cavities in hypersonic separated flow. Technical Report NASA TN-5908, 1970.

[56] H. L. Bohon, J. Sawyer, L. R. Hunt, and I. Weintein. Performance of thermal protection systems in a Mach 7 environment. *Journal of Spacecraft and Rockets*, 12(12):744–749, 1975.

[57] J. J. Bertin. Aerodynamic heating for gaps in laminar and transitional boundary layers. In *18th Aerospace Science Meeting*. Pasadena, California, 1980.

[58] D. P. Rizzetta. Numerical simulation of supersonic flow over a three-dimensional cavity. *AIAA Journal*, 26(7):799–807, 1988.

[59] X. Zhang, E. Morishita, and H. Itoh. Experimental and computational investigation of supersonic cavity flows. In *10th AIAA/NAL-NASDA-ISAS International Space Planes and Hypersonic Systems and Technologies Conference*, number AIAA Paper 2001-1755. Hyoto, Japan, 2001.

[60] A. P. Jackson, R. Hiller, and S. Soltani. Experimental and computational study of laminar cavity flows at hypersonic speeds. *Journal of Fluid Mechanics*, 427:329–358, 2001.

[61] F. L. Jr. Wilcox. Experimental measurements of internal store separation characteristics at supersonic speeds. In *Royal Aeronautical Society Conference*, pages 5.1–5.16. Bath, United Kingdom, 1990.

[62] R. L. Jr. Stallings and D. K. Forrest. Separation characteristics of internally carried stores at supersonic speeds. Technical Report NASA TP-2993, 1990.

[63] J. L. Everhart, S. J. Alter, N. R. Merski, W. A. Wood, and R. K. Prabhu. Pressure gradient effects on hypersonic cavity flow heating. In *44th AIAA Aerospace Sciences Meeting and Exhibit*. Reno, Nevada, 2006.

[64] J. L. Brown, M. Tobak, and R. K. Prabhu. Flow topology about an orbiter leading edge cavity at STS-107 reentry conditions. In *37th AIAA Thermophysics Conference*, number AIAA Paper 2004-2285. Portland, Oregon, 2004.

[65] K. A. Boyles, G. J. LeBeau, and M. A. Gallis. DSMC simulations in suppor of the Columbia shuttle orbiter accident investigations. In *37th AIAA Thermophysics Conference*, number AIAA P-2004-2282. Portland, Oregon, 2004.

[66] G. M. Buck and M. A. Pulsonetti. Downstream effects on orbiter leeside flow separation for hypersonic flows. In *35th AIAA Fluid Dynamics Conference and Exhibit*, number AIAA Paper 2005-5138. Toronto, Canada, 2005.

[67] E. P. Fahrenthold and Y. K. Park. Simulation of foam-impact effects on the space shuttle thermal protection system. *Journal of Spacecraft and Rockets*, 42(2):201–207, 2005.

[68] M. A. Pulsonetti and W. A. Wood. Computational aerothermodynamic assessment of space shuttle orbiter tile damage - open cavities. In *38th AIAA Thermophysics Conference*. Toronto, Canada, 2005.

[69] J. L. Everhart. Supersonic/hypersonic laminar heating correlations for rectangular and impact-induced open and closed cavities. *Journal of Spacecraft and Rockets*, 46(3):545–560, 2009.

[70] J. L. Everhart, K. T. Berger, K. S. Bey, N. R. Merski, and W. A. Wood. Cavity heating experiments supporting shuttle Columbia accident investigation. Technical Report NASA TN-2011-214528, 2011.

[71] F. J. Alexander, A. L. Garcia, and B. J. Alder. Cell size dependence of transport coefficients in stochastic particle algorithms. *Physics of Fluids*, 10(6):1540–1542, 1998.

[72] F. J. Alexander, A. L. Garcia, and B. J. Alder. Erratum: Cell size dependence of transport coefficients in stochastic particle algorithms [Phys. Fluids 10, 1540 (1998)]. *Physics of Fluids*, 12(3):731, 2000.

[73] G. A. Bird. Direct simulation of highvorticity gas flows. *Physics of Fluids*, 30(2):1958–1988, 1987.

[74] A. G. Garcia and W. A. Wagner. Time step truncation error in direct simulation Monte Carlo. *Physics of Fluids*, 12(10):2621–2633, 2000.

[75] N. G. Hadjiconstantinou. Analysis of discretization in the direct simulation Monte Carlo. *Physics of Fluids*, 12(10):2634–2638, 2000.

[76] S. Dietrich. An ecient computation of particle movement in 3D DSMC calculations on structured body-tted grids. In *17th International Symposium on Rareed Gas Dynamics*. Aachen, Germany, 1991.

[77] M. Laux. Optimization and parallelization of the dsmc method on unstructured grids. In *32nd AIAA Thermophysics Conference*, number AIAA-97-2512. Atlanta, 1997.

[78] M. Usami and T. Nakayama. Intermolecular collision scheme of DSMC taking molecular locations within a cell into account. In *23rd International Symposium on Rarefied Gas Dynamics*, volume 663, pages 374–381, 2003.

[79] R. G. Wilmoth, A. B. Carlson, and G. J. LeBeau. DSMC grid methodologies for computing low-density, hypersonic flows about reusable launch vehicles. In *31st AIAA Themophysics Conference*, number AIAA-96-1812, 1996.

[80] R. P. Nance, R. G. Wilmoth, and H. A. Hassan. Comparison of grid-definition schemes for Monte Carlo simulations. *Journal of Thermophysics and Heat Transfer*, 11(2), 1997.

[81] F. Stollmeier and M. Grabe. A Voronoi grid and particle tracking algorith for DSMC. In *27th International Symposium on Rarefied Gas Dynamics*, volume 1333, pages 331–336, 2010.

[82] K. A. Koura. Null-collision tecnique in the direct-simulation Monte Carlo method. *Physics of Fluids*, 29:3509–3511, 1986.

[83] K. A. Koura. Improved null-collision technique in the direct simulation Monte Carlo method: application to vibrational relaxation of nitrogen. *Computer and Mathematics with Applications*, 35(1-2):139–154, 1998.

[84] G. A. Bird. Perception of numerical methods in rarefied gasdynamic. *Progress in Astronautics and Aeronautics*, 118:211, 1989.

[85] T. Abe. Generalized scheme of the no-time-counter scheme for the DSMC in rarefied gas flow analysis. *Computer and Fluids*, 2(2-3):253–257, 1993.

[86] W. F. N. Santos. Gas-surface interaction effect on round leading edge aerothermodynamics. *Brazilian Journal of Physics*, 37(2):337–348, 2007.

[87] J.C. Maxwell. On stresses on rarefied gases arising from inequalities of temperature. *Philosophical Transactions of the Royal Society of London*, 170:231–256, 1879. Reprinted in The Scientific Papers of J. C. Maxwell, Dover, New York, 1965.

[88] R. M. Logan and R. E. Stickney. Simple classical model for the scattering of gas atoms from a solid surface. *Journal fo Chemical Physics*, 33(1):195–201, 1966.

[89] R. M. Logan, J. C. Keck, and R. E. Stickney. Simple classical model for the scattering of gas atoms from a solid surface: additional analysis and comparisons. In *5th Symposium on Rarefied Gas Dynamics*, volume 1, 1966.

[90] J. J. Hinchen and W. M. Foley. Scattering of molecular beams by metallic surfaces. In *Fifth International Symposium on Rarefied Gas Dynamics*, 1966.

[91] C. Cercignani and M. Lampis. Kinetic models for gas-surface interactions. *Transport Theory and Statistical Physics*, 1(2):101–114, 1971.

[92] C. Cercignani and A. Frezzotti. Numerical simulations of supersonic rarefied gas glows past a flat plate: effects of the gas-surface interaction model on the flowfield. *Progress in Aeronautics and Astronautics*, 118:552–566, 1989.

[93] R. G. Lord. Application of the cercignani-lampis scattering kernel to the direct simulation Monte C calculations. In *17th International Symposium on Rarefied Gas Dynamics*, pages 1427–1433, 1990.

[94] R. G. Lord. Some extensions of the cercignani-lampis gas-surface interaction model. *Physics of Fluids A: Fluid Dynamics*, 3(4):706–710, 1991.

[95] R. G. Lord. Some further extensions of the cercignani-lampis gas-surface interaction model. *Physics of Fluids*, 7(5):1159–1161, 1995.

[96] C. White. *Benchmarking, development and applications of an open source DSMC solver*. PhD thesis, University of Strathclyde, Glasgow, Scotland, 2013.

[97] G. A. Bird. Monte-Carlo simulation in an engineering context. In *12th International Symposium on Rarefied Gas Dynamics*, pages 239–255. Charlottesville, VA, 1981.

[98] K. Koura and H. Matsumoto. Variable soft sphere molecular model for inversepowerlaw or Lennard Jones potential. *Physics of Fluids*, 3(10):2459–2465, 1991.

[99] K. Koura and H. Matsumoto. Variable soft sphere molecular model for air species. *Physics of Fluids*, 4(5):1083–1085, 1992.

[100] H. A. Hassan and D. B. Hash. A generalized hardsphere model for monte carlo simulation. *Physics of Fluids*, 3(3):738–744, 1993.

[101] D. B. Hash, H. A. Hassan, and J. N. Moss. Direct simulation of diatomic gases using the generalized hard sphere model. *Journal of Thermophysics and Heat Transfer*, 8(4):758, 1994.

[102] J. A. Kunc, D. B. Hash, and H. A. Hassan. The GHS interaction model for strong attractive potentials. *Physics of Fluids*, 7(5):1173–1175, 1995.

[103] D. Baganoff and J. McDonald. A collision selection rule for a particle simulation method suited to vector computers. *Physics of Fluids A: Fluid Dynamics*, 2(7):1989–1993, 1990.

[104] C. Borgnakke and P. S. Larsen. Statistical collision model for Monte Carlo simulation of polyatomic gas mixture. *Journal of Computational Physics*, 18(4):405–420, 1975.

[105] I. D. Boyd. Analysis of rotational nonequilibrium in standing shock waves of nitrogen. *AIAA Journal*, 28:1997–1999, 1990.

[106] I. D. Boyd. Rotational-tranlational energy transfer in rarefied nonequilibrium flows. *Physics of Fluids A - Fluid Dynamics*, 2(3):447–452, 1990.

[107] I. D. Boyd. Rotational and vibrational nonequilibrium effects in rarefied hypersonic flow. *Journal of Thermophysics and Heat Transfer*, 4(4):478–484, 1990.

[108] F. E. Lumpkin III, B. L. Haas, and I. D. Boyd. Resolution of differences between collision number definitions in particle and continuum simulations. *Physics of Fluids A: Fluid Dynamics*, 3(9):2282–2284, 1991.

[109] B. L. Haas, J. D. McDonald, and L. Dagum. Models of thermal relaxation mechanics for particle simulations. *Journal of Computational Physics*, 107(2):348–358, 1993.

[110] F. Bergmann and I. D. Boyd. New discrete vibrational energy model for the direct simulation Monte Carlo method. *Progress in Aerospace Science*, 158:174–183, 1994.

[111] G. A. Bird. A comparison of collision energy-based and temperature-based procedures in DSMC. In *26th International Symposium on Rarified Gas Dynamics*, volume 1084, pages 245–250. Kyoto, Japan, 2008.

[112] G. Zuppardi, L. Morsa, and F. Romano. Influence of chemical models on the computation of thermo-fluid-dynamic parameters in hypersonic, rarefied flows. *Proc. IMechE Part G: Journal Aerospace Engineering*, 224:637–646, 2010.

[113] G. A. Bird. Sophisticated DSMC. Notes prepared for a short course at the DSMC07 meeting, Santa Fe, 30th September, 2007.

[114] T. J. Scanlon, C. White, M. K. Borg, R. C. Palharini, E. Farbar, I. D. Boyd, J. M. Reese, and R. E. Brown. Open source DSMC chemistry modelling for hypersonic flows (submitted). *International Journal of Heat and Fluid Flow*, 1:1–70, 2014.

[115] C. Rebick and R. D. Levine. Collision induced dissociation: A statistical theory. *Journal of Chemical Physics*, 58(9):3942–3952, 1973.

[116] K. A. Koura. A set of model cross sections for the Monte Carlo simulation of rarefied real gases: atom-diatom collisions. *Physics of Fluids*, 6:3473–3486, 1994.

[117] I. D. Boyd. A threshold line dissociation model for the direct simulation Monte Carlo method. *Physics of Fluids*, 8:1293–1300, 1996.

[118] M. A. Gallis. Maximum entropy analysis of chemical reaction energy dependence. *Journal of Thermophysics and Heat Transfer*, 10:217–223, 1996.

[119] G. A. Bird. Simulation of multi-dimensional and chemically reacting flows (past space shuttle orbiter). In *11th International Symposium on Rarefied Gas Dynamics*, pages 365–388, 1979.

[120] I. D. Boyd. Assessment of chemical nonequilibrium in rarefied hypersonic flow. In *28th Aerospace Sciences Meeting*, number AIAA Paper 90-0145, 1990.

[121] I. D. Boyd. Analysis of vibrational-dissociation-recombination processes behind strong shock waves of nitrogen. *Physics of Fluids A: Fluid Dynamics*, 4:178–185, 1992.

[122] B. L. Hass and I. D. Boyd. Models for direct Monte Carlo simulation of coupled vibrational-dissociation. *Physics of Fluids A: Fluid Dynamics*, 5:478–489, 1993.

[123] M. A. Gallis, R. B. Bond, and J.R. Torczynski. A kinetic-theory approach for computing chemical-reaction rates in upper-atmosphere hypersonic flows. *Journal of Chemical Physics*, 138(124311), 2009.

[124] G. A. Bird. Chemical reactions in DSMC. In *27th Symposium on Rarefied Gas Dynamics*. Pacific Grove, CA, 2010.

[125] G. A. Bird. The quantum-kinetic chemistry model. In *27th International Symposium on Rarefied Gas Dynamics*. Pacific Grove, CA, 2010.

[126] G. A Bird. The Q-K model for gas phase chemical reaction rates. *Physics of Fluids*, 23 (106101), 2011.

[127] I. Wysong, S. Gimelshein, N. Gimelshein, W. McKeon, and F. Esposito. Reaction cross sections for two direct simulation Monte Carlo models: accuracy and sensitivity analysis. *Physics of Fluids*, 24(042002), 2012.

[128] B. L. Hass and J. D. McDonald. Validation of the chemistry models employed in a particle simulation method. *Journal of Thermophysics and Heat Transfer*, 7(1):42–48, 1993.

[129] W. G. Vincent and C. H. Kruger. *Introduction to Physical Gas Dynamics*. Krieger publishing company, Malabar, Florida, 1965.

[130] I. Boyd. Modeling backward chemical rate processes in the direct simulation Monte Carlo method. *Physics of Fluids*, 19(12), 2007.

[131] G. A. Bird. DSMC resources from Graeme A. Bird. URL `http://gab.com.au,2014`.

[132] NIST. National Institute of Standards and Technology database. URL `http://kinetics.nist.gov/kinetics/kineticsearchform.jsp,2014`.

[133] R. N. Gupta, J. M. Yos, R. A. Thompson, and K. Lee. A review of reaction rates and thermodynamic and transport properties for an 11-species air model for chemical and thermal

nonequilibrium calculations to 30000 k. Technical Report NASA-1232, Washington, DC, 1990.

[134] M. H. Bortner. A review of rate constants of selected reactions of interest in re-entry flow fields in the atmosphere. Technical Report NBS TN-484, U.S. Department of Commerce, 1969.

[135] T. J. Scanlon, E. Roohi, C. White, M. Darbandi, and J. M. Reese. An open source, parallel, DSMC code for rarefied gas flows in arbitrary geometries. *Computer and Fluids*, 39:2078–2089, 2010.

[136] OpenFOAM website. URL `http://www.openfoam.com/`.

[137] N. G. Hadjiconstantinou, A. L. Garcia, M. Z. Bazant, and G. He. Statistical error in particle simulations of hydrodynamic phenomena. *Journal of Computational Physics*, 187(1):274–297, 2003.

[138] E. M. Murman and S. S. Ababanel. *Progress and supercomputing in computational fluid dynamics*, volume 6. Proceedings of U.S.-Israel Workshop, Progress in Scientific Computing, 1985.

[139] P. J. Roache. Need for control of numerical accuracy. *Journal of Spacecraft and Rockets*, 27(AIAA Paper 89-1689):98–102, 1989.

[140] G. Sheng, M. S. Elzas, T. I. Oren, and Cronhjort. Model validation: a systemic and systematic approach. *Reliability Engineering ans System Safety*, 42:247–259, 1993.

[141] P. J. Roache. Verification of codes and calc. *AIAA Journal*, 36(5):696–702, 1998.

[142] P. J. Roache. *Verification and validation in computational science and engineering*. Hermosa Publishers, Albuquerquen, NM, 1998.

[143] American Institute of Aeronautics and Astronautics (AIAA). *Guide for the verification and validation of computational fluid dynamics simulations.* Reston, VA, AIAA-G-077-1998, 1998.

[144] W. L. Oberkampf and T. G. Trucano. Verification and validation in computational fluid dynamics. *Progress in Aerospace Science*, 38(SAND2002-0529):209–272, 2002.

[145] W. L. Oberkampf, T. G. Trucano, and C. H. Hirsch. Verification, validation, and predictive capabilities in computational engineering, and physics. Technical Report 2003-3769, Sandia National Laboratories, 2003.

[146] W. L. Oberkampf and M. F. Barone. Measures of agreement between computation and experiment: validation metrics. *Journal of Computational Physics*, 217:5–36, 2006.

[147] J. C. Lengrand, J. Allegre, A. Chpoun, and M. Raffin. Rarefied hypersonic flow over a sharp flat plate: numerical and experimental results. In B. D. Shzgal and D. P. Weaver, editors, *18th International Symposium on Rarefied Gas Dynamics*, volume 160, pages 276–284. AIAA, Washington, DC, 1992.

[148] M. A. Rieffel. A method for estimating the computational resquirement of DSMC simulations. *Journal of Computational Physics*, 149:95–113, 1999.

[149] G. A. Bird. Definition of mean free path for real gases. *Physics of Fluids*, 26:3222–3223, 1983.

[150] K. A. Koura. A sensitive test for accuracy in evaluation of molecular collision number in the direct-simulation Monte Carlo. *Physics of Fluids*, A2(7):706–710, 1990.

[151] H. Kaburaki and M. Yokokawa. Computer simulation of two-dimensional continuum flows by the direct simulation Monte Carlo method. *Molecular Simulation*, 12(3-6):441–444, 1994.

[152] C. Shu, X. H. Mao, and Y. T. Chew. Particle number per cell and scaling factor effect on accuracy of dsmc simulation of micro flows. *International Journal of Numerical Methods for Heat and Fluid Flow*, 15(8):827–841, 2005.

[153] Z. Sun, Z. Tang, Y. He, and W. Tao. Proper cell dimension and number of particles per cell for DSMC. *Computer and Fluids*, 50:1–9, 2011.

[154] S. Stefanov and C. Cercignani. Monte Carlo simulation of the Taylor-couette flow of a rarefied gas. *Journal of Fluid Mechanics*, 256:199–213, 1993.

[155] E. S. Piekos and K. S. Breuer. Numerical modeling of micromechanical devices using the direct simulation Monte Carlo method. *Journal of Fluids Engineering*, 118(3):464–469, 1996.

[156] W. Huang and D. Bogy. Three-dimensional direct simulation Monte Carlo method for slider air bearings. *Physics of Fluids*, 9(6):1764–1769, 1997.

[157] F. J. Axelander and A. G. Garcia. The direct simulation Monte Carlo method. *Computer in Physics*, 11(6):588–593, 1997.

[158] D. W. Machowski, D. H. Papadopoulos, and D. E. Rosner. Comparison of Burnett and DSMC predictions of pressure distribution and normal stress in one-dimensional, strong nonisothermal gases. *Physics of Fluids*, 11(8):2108–2116, 1999.

[159] M. Fallavollita, D. Baganoff, and J. McDonald. Reduction of simulation cost and error for particle simulation of rarefied flows. *Journal of Computational Physics*, 109(1):30–36, 1993.

[160] C. Mavriplis, J. C. Ahn, and R. Goulard. Heat transfer and flowfield in short microchannels using direct simulation Monte Carlo. *Journal of Thermophysics and Heat Transfer*, 11(4):489–496, 1997.

[161] G. Chen and I. D. Boyd. Statistical error analysis for the direct simulation Monte Carlo technique. *Journal of Computational Physics*, 126(2):434–448, 1996.

[162] Anon. Hypersonic experimental and computational capability, improvement and validation. Technical Report AGARD-AR-319, Vol. 1 and 2, 1996.

[163] J. Allegre, M. Raffin, A. Chpoun, and L. Gottesdiener. Rarefied hypersonic flow over a flat plate with truncated leading edge. In B. D. Shizgal and D. P. Weaver, editors, *18th International Symposium on Rarefied Gas Dynamics*, volume 160, pages 285–295. AIAA, Washington, DC, 1992.

[164] N. Tsuboi, H. Yamaguchi, and Y. Matsumoto. Direct simulation Monte Carlo method on rarefied hypersonic flow around flat plates. *Journal of Spacecraft and Rockets*, (3): 397–405, 2004.

[165] J. Davis and Harvey J. K. Comparison of the direct simulated method with experiment for rarefied flat plate flow. *Progress in Astronautics and Aeronautics*, pages 335–348, 1963.

[166] W. L. Chow. Hypersonic rarefied flow past the sharp leading edge of a flat plate. *AIAA*, 5(6):1549–1557, 1967.

[167] M. Becker, F. Robben, and R. Cattolica. Velocity distribution functions near the leading edge of a flat plate. *AIAA Journal*, 12(9), 1974.

[168] W. L. Hermina. Monte Carlo simulation of rarefied flow along a flat plate. *Journal of Thermophysics and Heat Transfer*, 3:7–12, 1989.

[169] R. P. Nance, R. G. Wilmoth, B. Moon, H. A. Hassan, and J. Saltz. Parallel DSMC solution of three-dimensional flow over a finite flat plate. In *6th AIAA/ASME Joint Thermophysics and Heat Transfer Conference*. Colorado Springs, CO, June 1994.

[170] J. Allegre, D. Bisch, and J. C. Lengrand. Experimental rarefied density flowfield at hypersonic conditions over 70–degree blunted cone. *Journal of Spacecraft and Rockets*, 34(6):714–718, 1997.

[171] J. Allegre, D. Bisch, and J. C. Lengrand. Experimental rarefied aerodynamic forces at hypersonic conditions over 70–degree blunted cone. *Journal of Spacecraft and Rockets*, 34(6):719–723, 1997.

[172] J. Allegre, D. Bisch, and J. C. Lengrand. Experimental rarefied heat transfer at hypersonic conditions over 70–degree blunted cone. *Journal of Spacecraft and Rockets*, 34(6):724–728, 1997.

[173] J. N. Moss, V. K. Dogra, and R. G. Wilmoth. DSMC simulations of Mach 20 nitrogen about 70-degree blunted cone and its wake. Technical Report NASA TM-107762, 1993.

[174] J. N. Moss, R. A. Mitcheltree, V. K. Dogra, and R. G. Wilmoth. Direct simulation Monte Carlo and Navier–Stokes simulations of blunt body wake flows. *AIAA Journal*, AIAA Paper 93-2807, 1993.

[175] J. N. Moss, J. M. Price, V. K. Dogra, and D. B. Hash. Comparisons of DSMC and experimental results for hypersonic external flows. In *30th AIAA Thermophysics Conference*, number AIAA Paper 95-2028, 1995.

[176] R. P. Nance, R. G. Wilmoth, and H. A. Hassan. A comparison of grid-definition schemes for DSMC. *AIAA Journal*, (AIAA Paper 96-0604), 1996.

[177] J. F. Pallegoix. Workshop ESTEC - test case no.6 - rarefied sherically blunted cone. In *4th European High-Velocity Database Workshop*. ESTEC, Noordwiwijk, The Netherlands, Nov. 1994.

[178] V. K. Dogra, J. N. Moss, and J. M. Price. Near wake structure for a generic ASTV configuration. *Journal of Spacecraft and Rockets*, 31(6):953–959, AIAA Paper 93-0271, 1996.

[179] L. A. Gochberg, G. A. Allen, M. A. Gallis, and G. S. Deiwet. Comparisons of computations and experiments for nonequilibrium flow expansions around a blunted cone. *AIAA Journal*, AIAA Paper 96-0231, 1996.

[180] D. B. Hash and H. A. Hassan. DSMC/Navier-Stoques analysis of a transitional flow experiment. *AIAA Journal*, AIAA Paper 96-0231, 1996.

[181] D. B. Hash and H. A. Hassan. Two-dimensional coupling issues of hybrid DSMC/Navier-Stoques solvers. *Journal of Thermophysics and Heat Transfer*, AIAA Paper 97-2507, 1997.

[182] J. K. Harvey and M. A. Gallis. Review of code validation studies in high-speed low-density flows. *Journal of Spacecraft and Rockets*, 37(1), 2000.

[183] P. A. Gnoffo, R. N. Gupta, and J. L. Shinn. Conservation equations and physical models for hypersonic air flows in thermal and chemical nonequilibrium. Technical Report NASA TP-2867, Feb. 1989.

[184] P. A. Gnoffo. An upwind-biased, point-implicit relaxation algorithm for viscous compressible perfect gas flows. Technical Report NASA TP-2953, Feb. 1990.

[185] D. R. Olynick and H. A. Hassan. New two temperature dissociation model for reacting flows. *Journa of Thermophysics and Heat Transfer*, 7(4):687–696, 1993.

[186] D. R. Olynick, J. C. Taylor, and H. A. Hassan. Comparisons between DSMC and the Navier–Stokes equations for reentry flows. *AIAA Journal*, (AIAA Paper 93-2810), 1993.

[187] G. A. Bird. Perception of numerical methods in rarefied gas dynamics. *Progress in Astronautics and Aeronautics*, 118:211–226, 1985.

[188] G. J. LeBeau. A parallel implementation of the Direct Simulation monte carlo method. *Computer Methods in Applied Mechanics and Engineering*, 174:319–337, 1999.

[189] J. N. Moss and J. M. Price. Survey of blunt body flows including wakes at hypersonic low-density conditions. *Journa of Thermophysics and Heat Transfer*, 11(3):321, 1997.

[190] J. K. Harvey and M. A. Gallis. Review of code validation studies in high-speed low-density flow. *Journal of Spacecraft and Rockets*, 1(37), 2000.

[191] M. J. Wright and F. S. Milos. Afterbody aeroheating floght data for planetary probe thermal protection system design. *Journal of Spacecraft and Rockets*, 43(5):929–943, 2006.

[192] G. A. Bird. *The DSMC Method*. ISBN 9781492112907. Version 1.1 edition, 2013.

[193] R. G. Wilmoth, D. B. VanGilder, and J. L. Papp. DSMC simulation of entry vehicle flowfields using a collision-based chemical kinetics approach. *27th International Symposium on Rarefied Gas Dynamics*, 1333:1269–1274, 2011.

[194] J. N. Moss, K. A. Boyles, and F. A. Greene. Orion aerodynamics for hypersonic free molecular to continuum conditions. In *14th AIAA/AHI International Space Planes and Hypersonic Systems and Technologies Conference*. Canberra, Australia, 2006.

[195] M. S. Ivanov, Ye. A. Bondar, G. N. Markelov, S. F. Gimelshein, and J. P. Taran. Study of the shock wave structure about a body entering the martian atmosphere. In *23rd International Symposium on Rarefied Gas Dynamics*. Whistler, British Columbia, Canada, 2002.

[196] W. F. N. Santos. Shock wave shape on power law leading edges. *Shock Waves*, pages 275–280, 2005.

[197] G. A. Bird. A comparison of collision energy-based and temperature-based procedures in DSMC. In *26th Symposium on Rarefied Gas Dynamics*. American Institue of Physics, Kyoto, Japan, 2009.

[198] NOAA/NASA/USAF. U. S. Standard atmosphere. U.S. Government Printing Office, 1976.

[199] M. von Smoluchowski. Üeber wärmeleitung in verdünnten gasen. *Annalen der Physik und Chemie*, 64:101–130, 1898.

[200] M. A. Pulsonetti, R. A. Thompson, and B. J. Alder. Prediction of STS-107 hypervelocity flow fields about the shuttle orbiter with various wing leading edge damage. Technical Report 20040084782, National Aeronautics and Space Administration, 2004.

[201] G. B. Macpherson. *Molecular dynamics simulation in Arbitrary geometries for nanoscale fluid mechanics*. PhD thesis, University of Strathclyde, 2008.

[202] OpenFOAM. http://www.openfoam.org/, 2014. URL `http://www.openfoam.org/`.

Appendix A

Verification process for TPS discontinuities

The simulation procedures adopted in Section 3.1 for hypersonic flow over a flat plate were also applied to the cavities investigated in Chapter 4. Simulations were performed with computational meshes that met the general requirements for the DSMC technique. For the particular of cavity length-to-depth ration is equal to 5, the standard structured mesh was created using a simple cuboid with 430 $\times$ 134 $\times$ 20 cells in $x-$, $y-$, and $z-$ coordinate directions, respectively. Figure A.1 shows a schematic of the computational mesh with a total of 1.15 million cells. The influence of the cell size on the aerodynamic surface quantities is shown in Figs. A.2 to A.4 for coarse, standard, and fine meshes. According to this group of plots, the cell size demonstrated to be insensitive to the range of cell spacing considered indicating that the standard mesh is essentially grid independent.

A similar examination was conducted for the time step size. A reference time step of 3.78 $\times$ 10^{-9} s is chosen; this is significantly smaller than the freestream mean collision time and small enough to ensure particles will spend multiple time steps in a single cell. From Figs. A.5 to A.7, it is noticed no alterations on the aerodynamic surfaces quantities when the time step is reduced or increased by a factor of four.

In addition to the mesh and time step sensitivity analysis, simulations were conducted in order to characterise the impact of the number of particles and samples on the computational results. Considering the standard mesh for L/D = 5 cases, with a total of 12.8 million particles, two new cases were investigated. Using the same mesh, it was employed 6.4 and 25.6 million particles in each simulation, respectively. In similar fashion, three different number of samples were considered in order to determine and minimise the statistical error. According to Figs. A.8

to A.13, a total of 12.8 million particles and 600,000 samples were necessary to fully solve the rarefied hypersonic reacting and non-reacting flows over the cavity.

Table A.1 shows the standard verification parameters for rarefied hypersonic flow over 3D cavities considered in the present study.

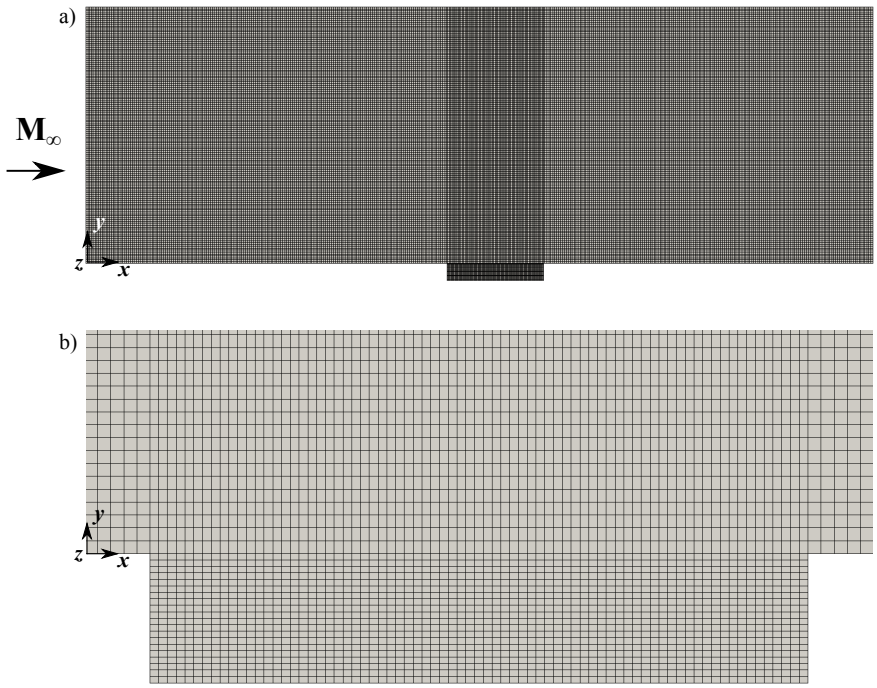

Figure A.1: Schematic of the computational mesh (L/D = 5): a) cavity full domain, and b) inside the cavity.

Table A.1: Standard verification parameters for rarefied hypersonic flow over 3D cavities.

L/D ratio	Number of cells	Time step (s)	Number of Particles	Number of Samples
1	1.05 million	3.78×10^{-9}	11.4 million	600,000
2	1.08 million	3.78×10^{-9}	11.7 million	600,000
3	1.10 million	3.78×10^{-9}	11.9 million	600,000
4	1.13 million	3.78×10^{-9}	12.1 million	600,000
5	1.15 million	3.78×10^{-9}	12.8 million	600,000

Spatial discretisation effects

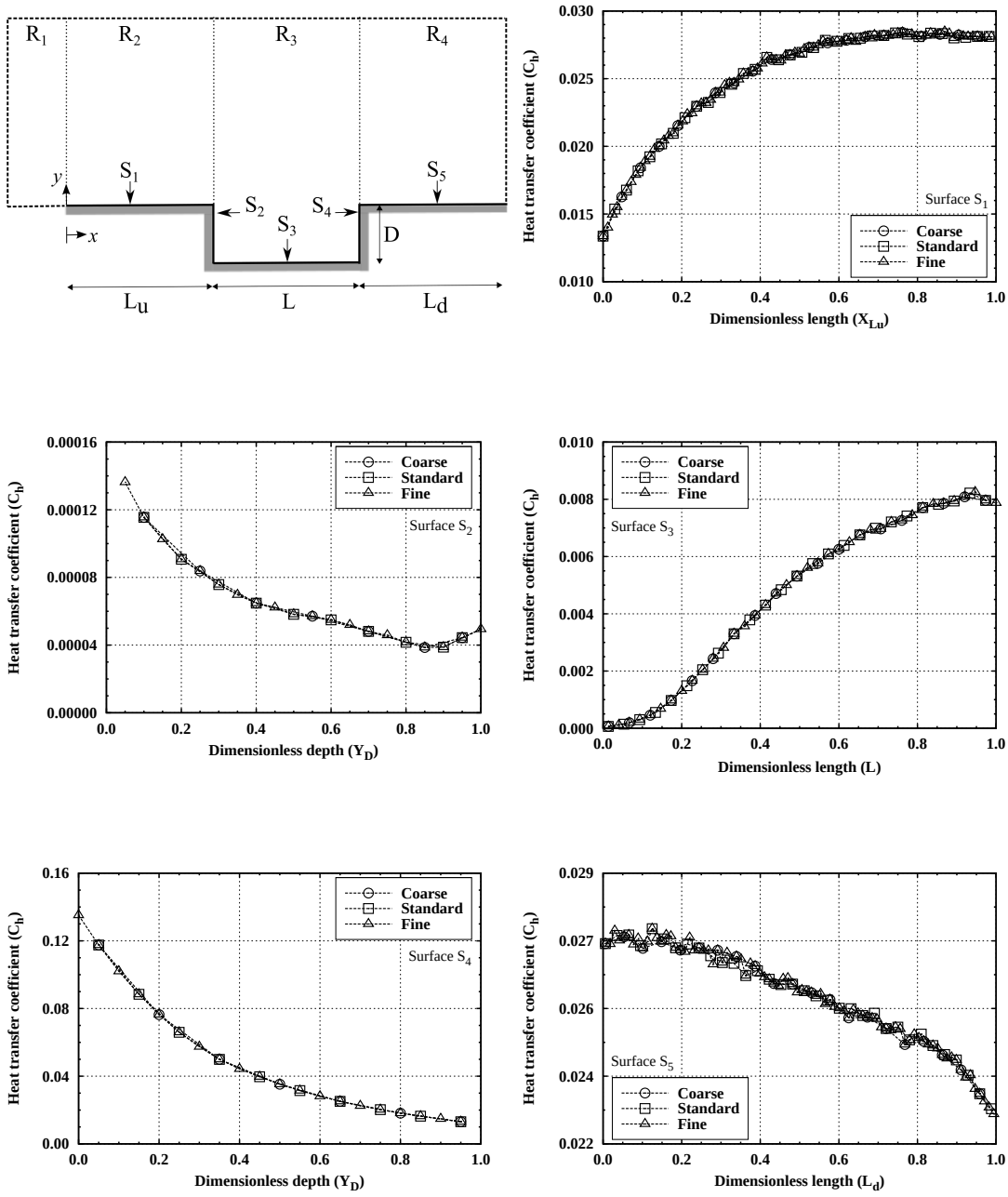

Figure A.2: Influence of cell size on heat transfer coefficient (C_h) along the cavity surfaces.

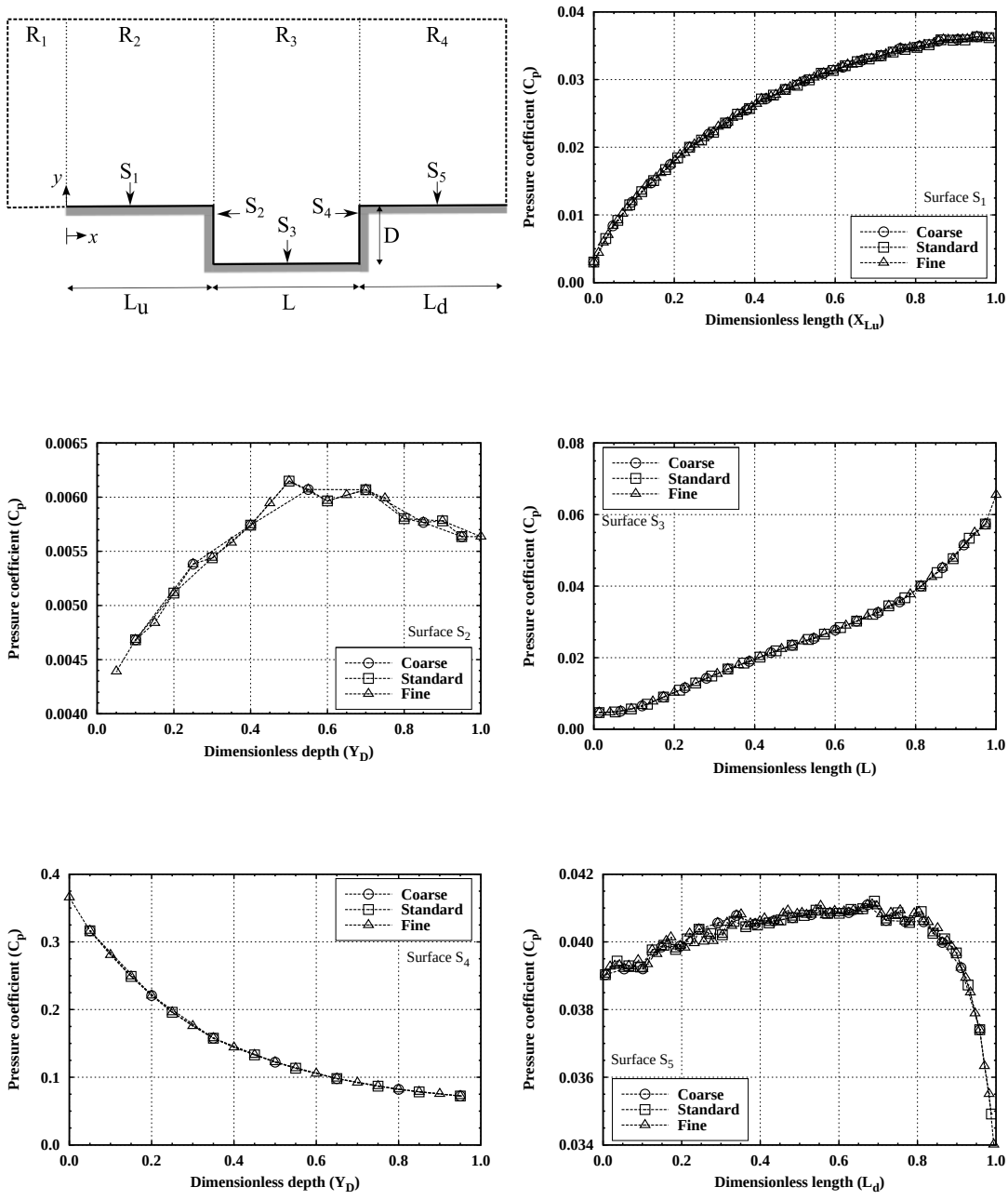

Figure A.3: Influence of cell size on pressure coefficient (C_p) along the cavity surfaces.

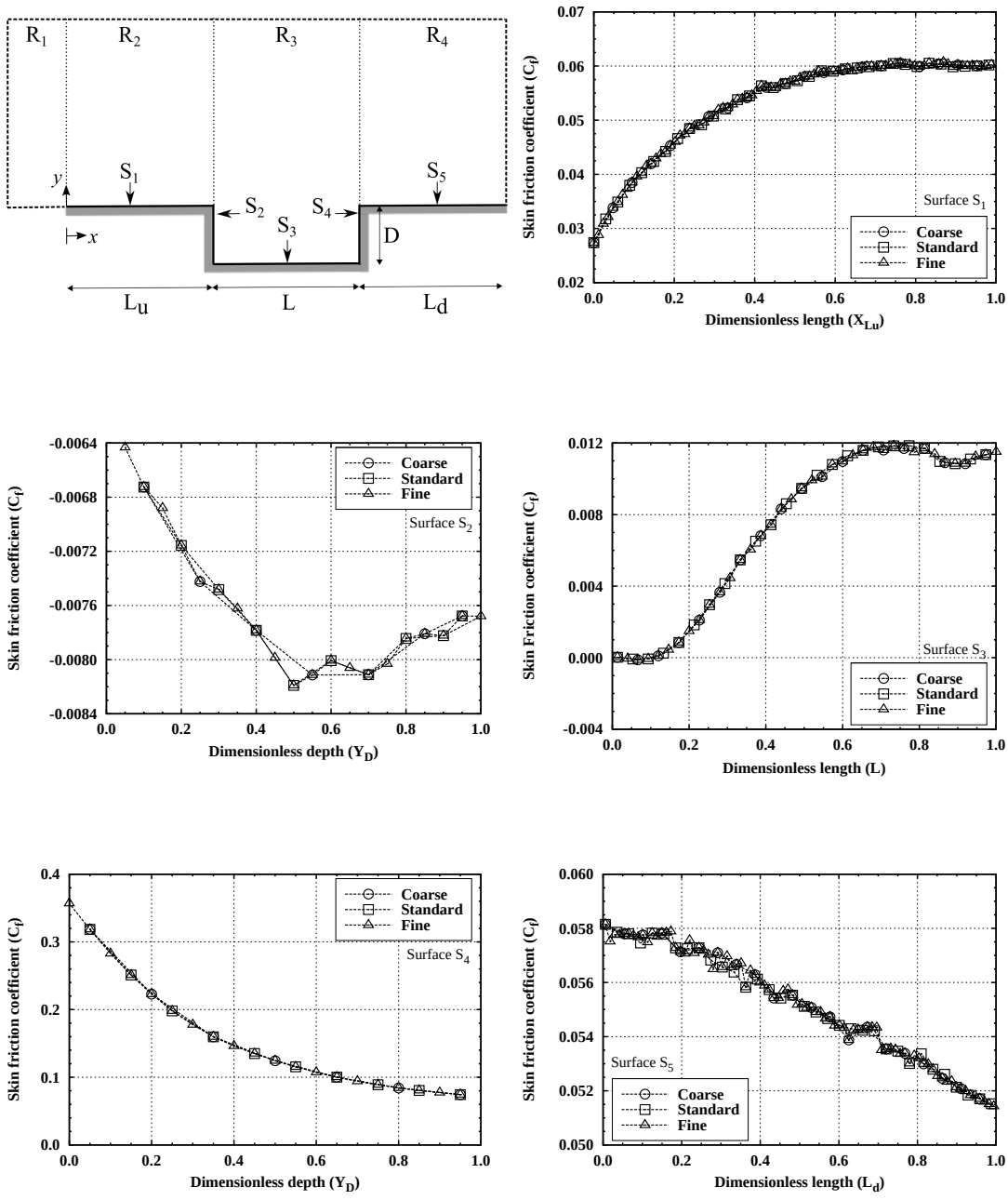

Figure A.4: Influence of cell size on skin friction coefficient (C_f) along the cavity surfaces.

Time discretisation effects

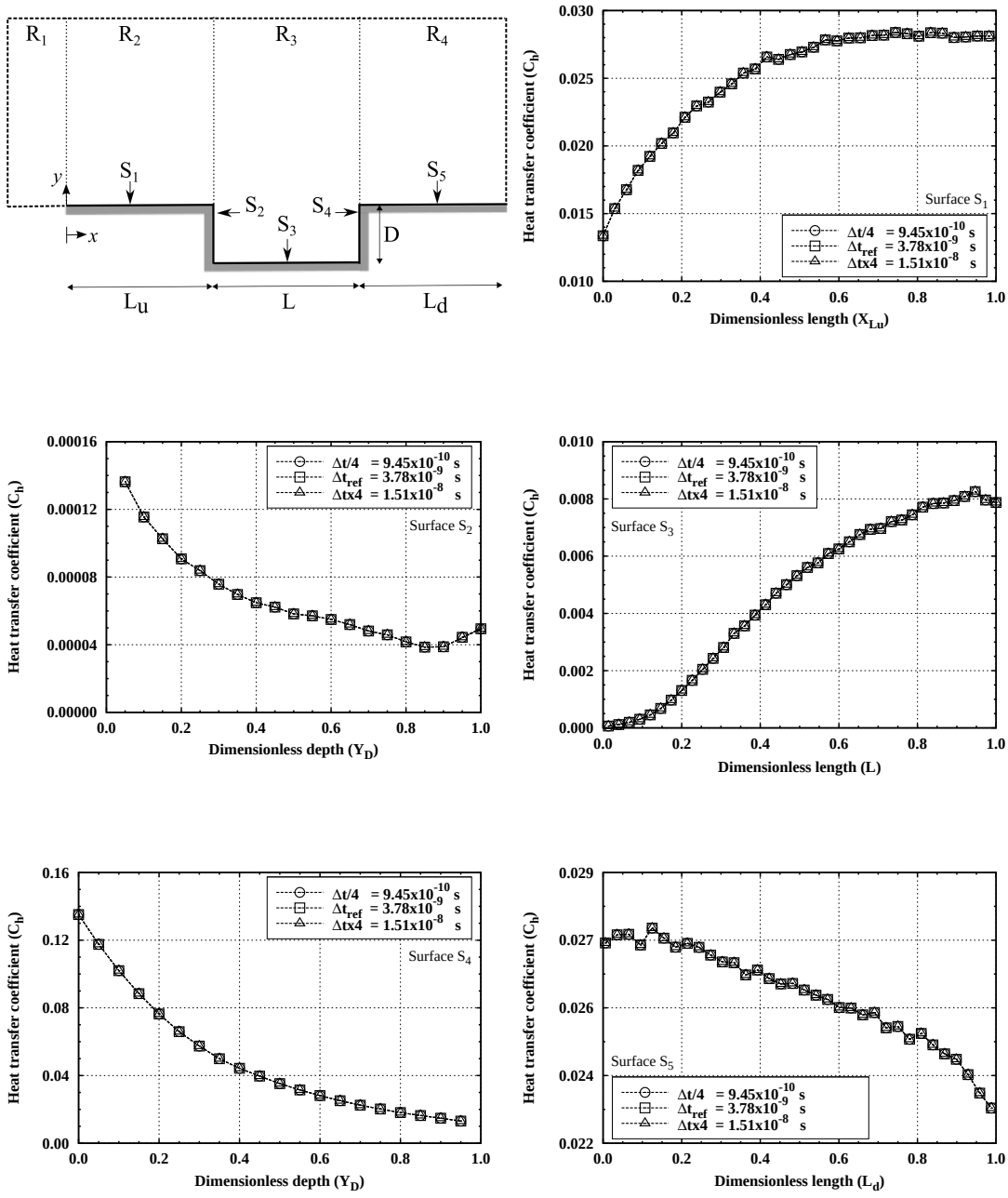

Figure A.5: Influence of time step size on heat transfer coefficient (C_h) along the cavity surfaces.

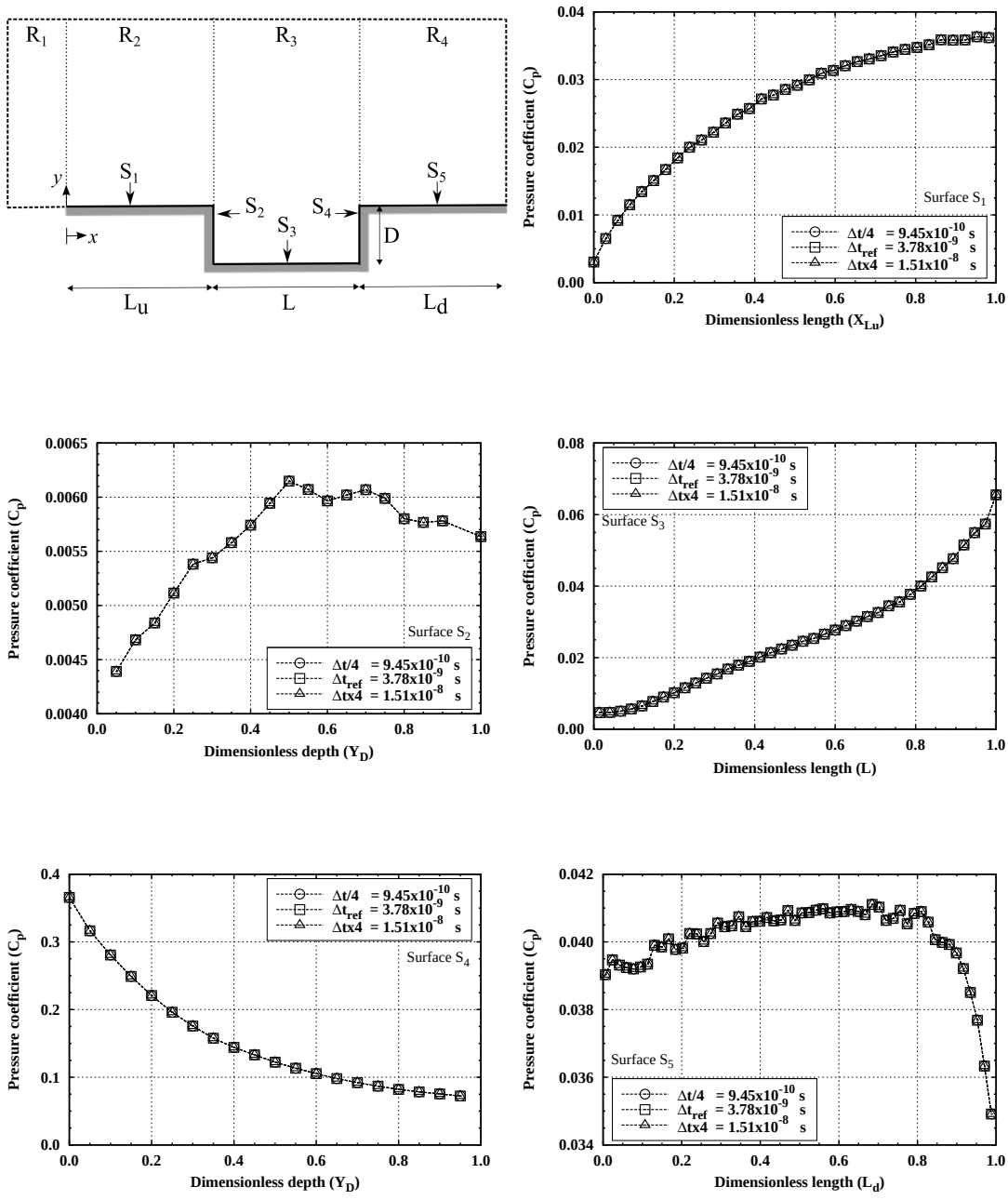

Figure A.6: Influence of time step size on pressure coefficient (C_p) along the cavity surfaces.

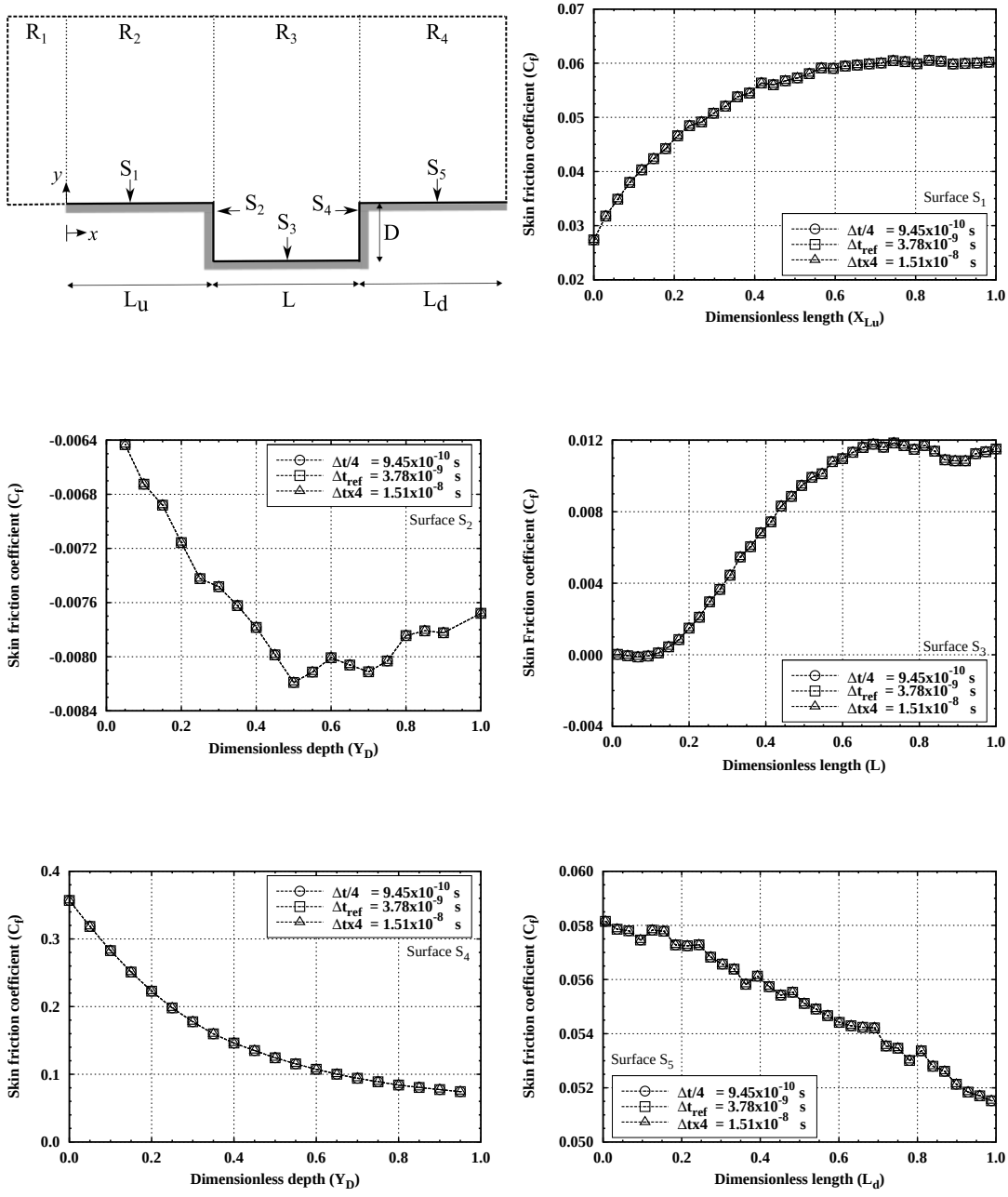

Figure A.7: Influence of time step size on skin friction coefficient (C_f) along the cavity surfaces.

Particle number assessment

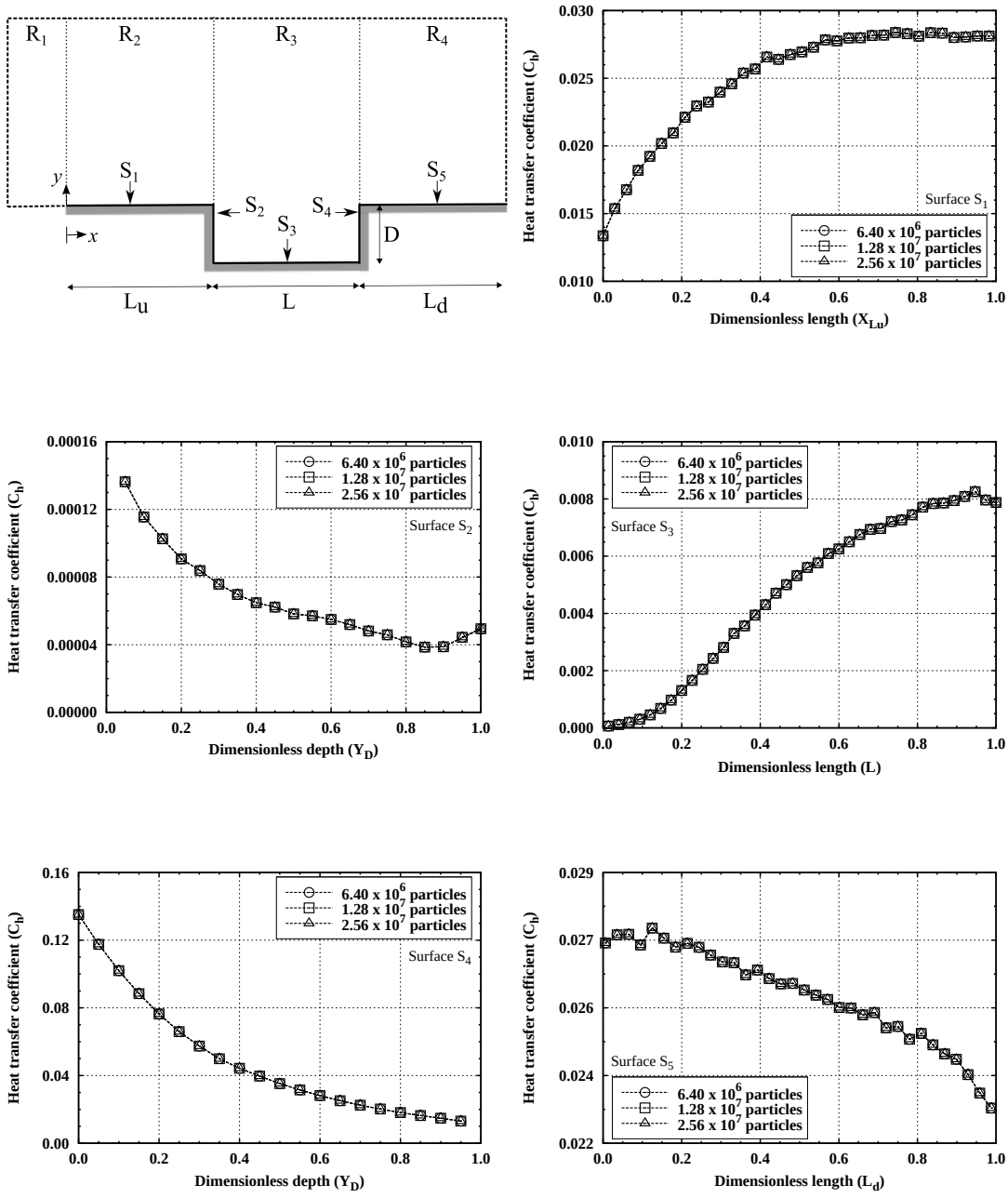

Figure A.8: Influence of number of particles on heat transfer coefficient (C_h) along the cavity surfaces.

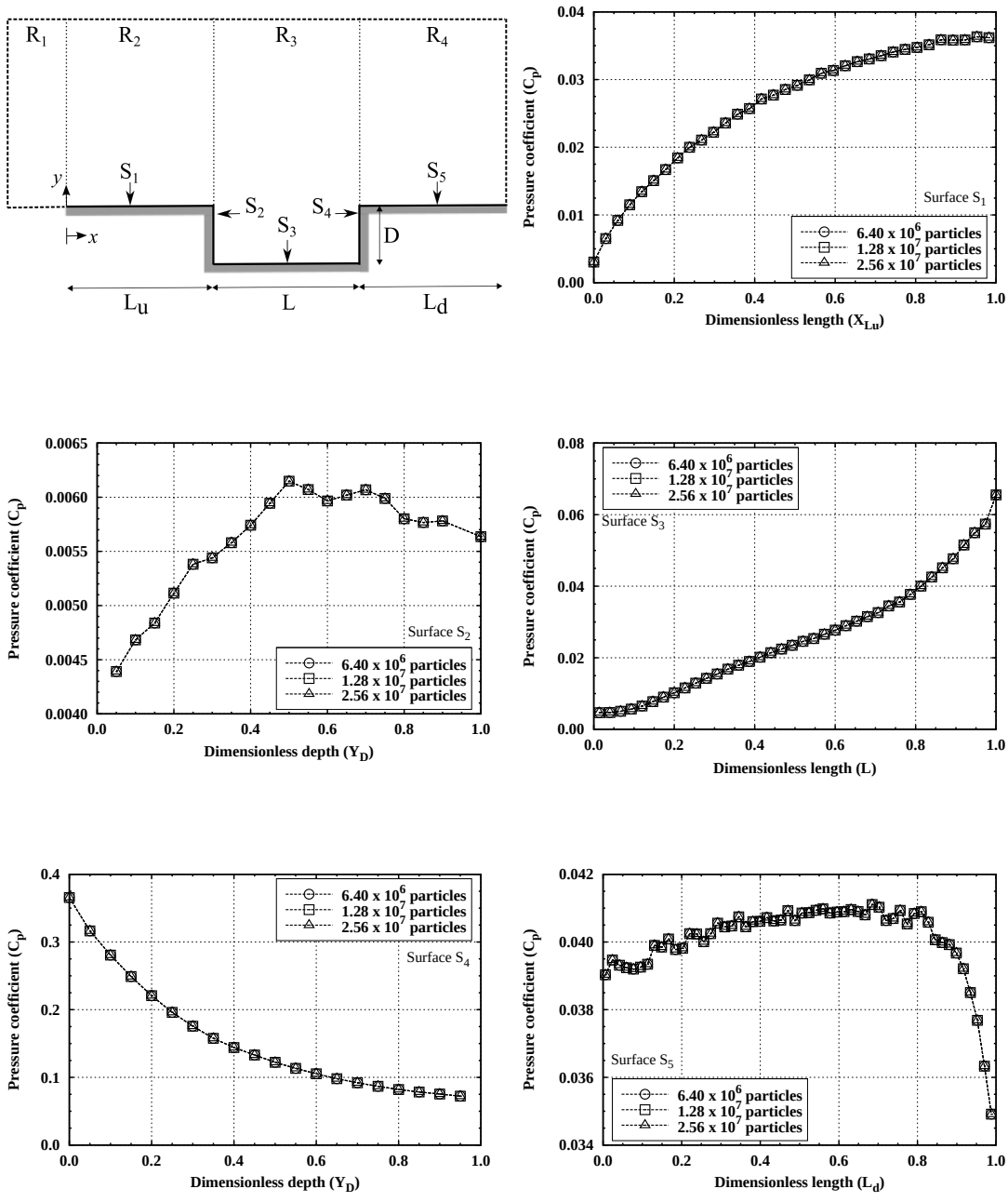

Figure A.9: Influence of number of particles on pressure coefficient (C_p) along the cavity surfaces.

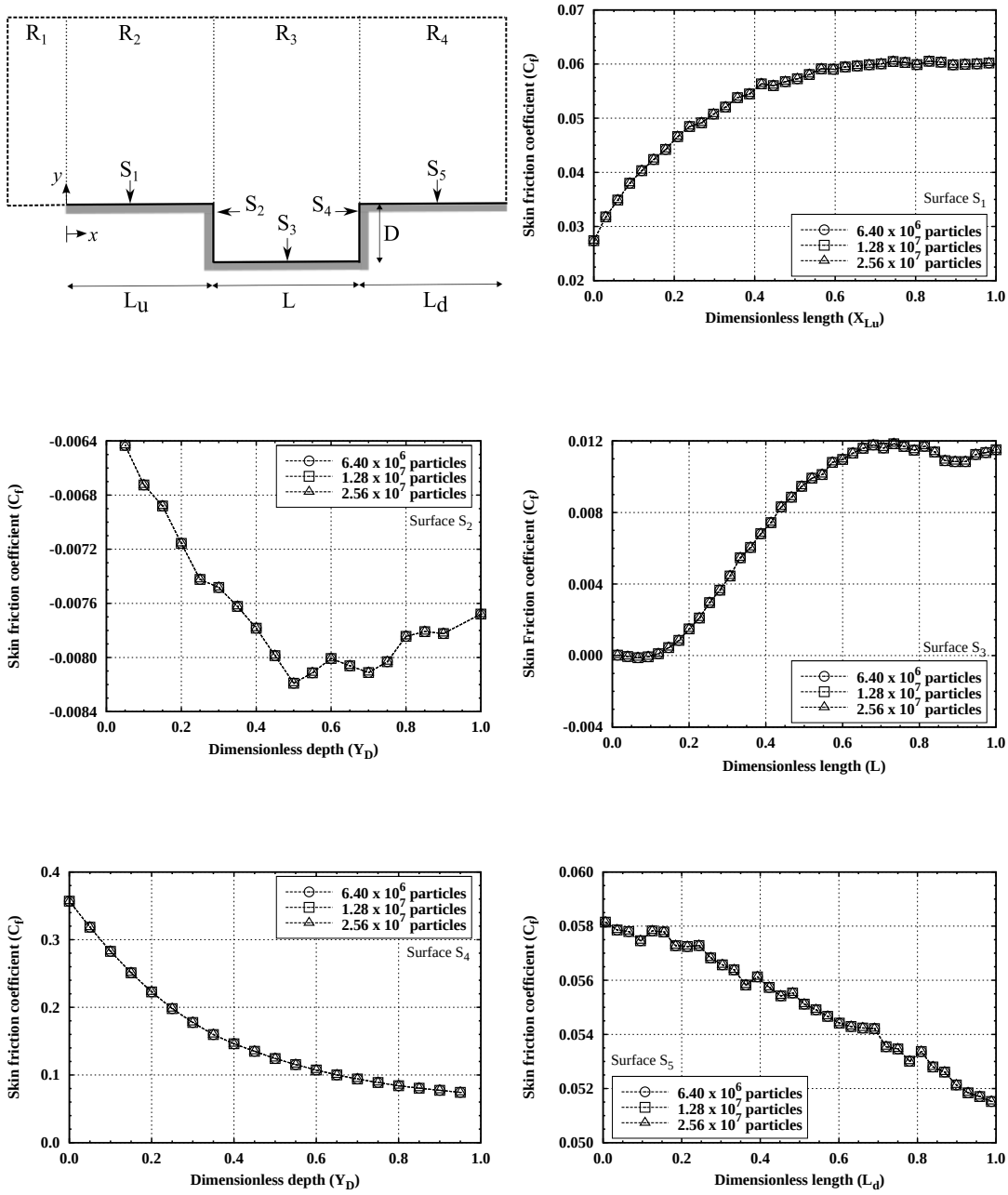

Figure A.10: Influence of number of particles on skin friction coefficient (C_f) along the cavity surfaces.

Sampling effects

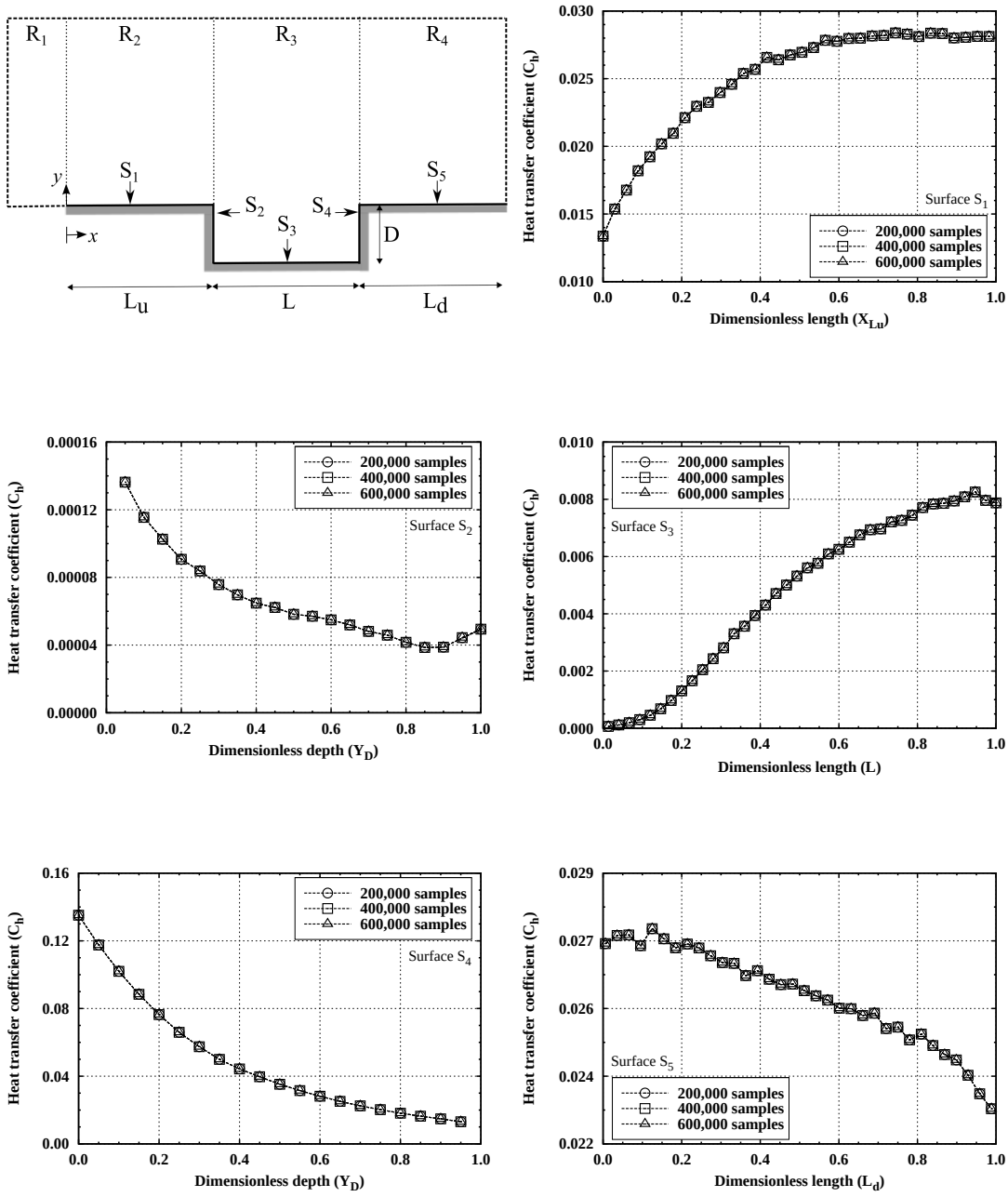

Figure A.11: Influence of number of samples on heat transfer coefficient (C_h) along the cavity surfaces.

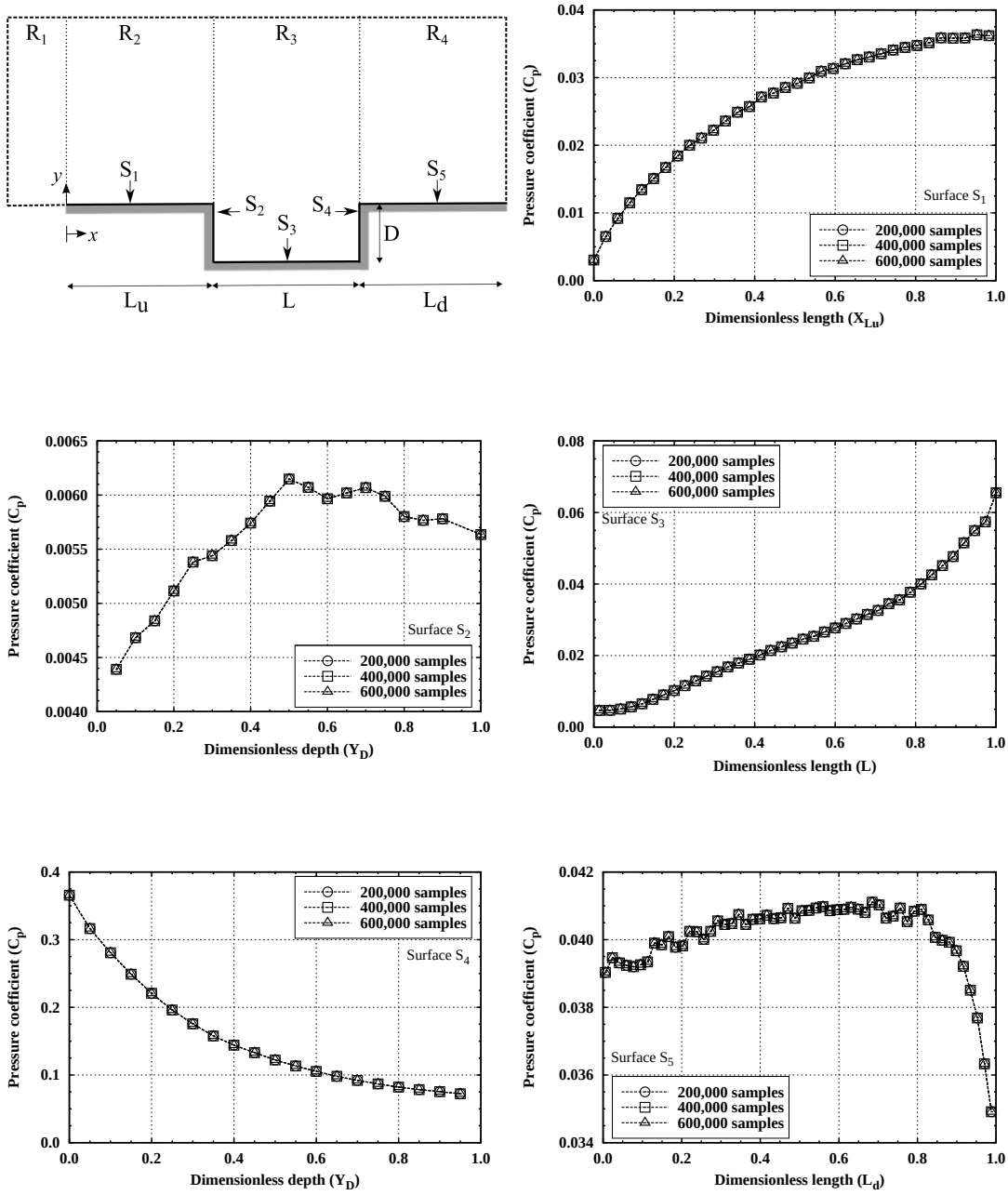

Figure A.12: Influence of number of samples on pressure coefficient (C_p) along the cavity surfaces.

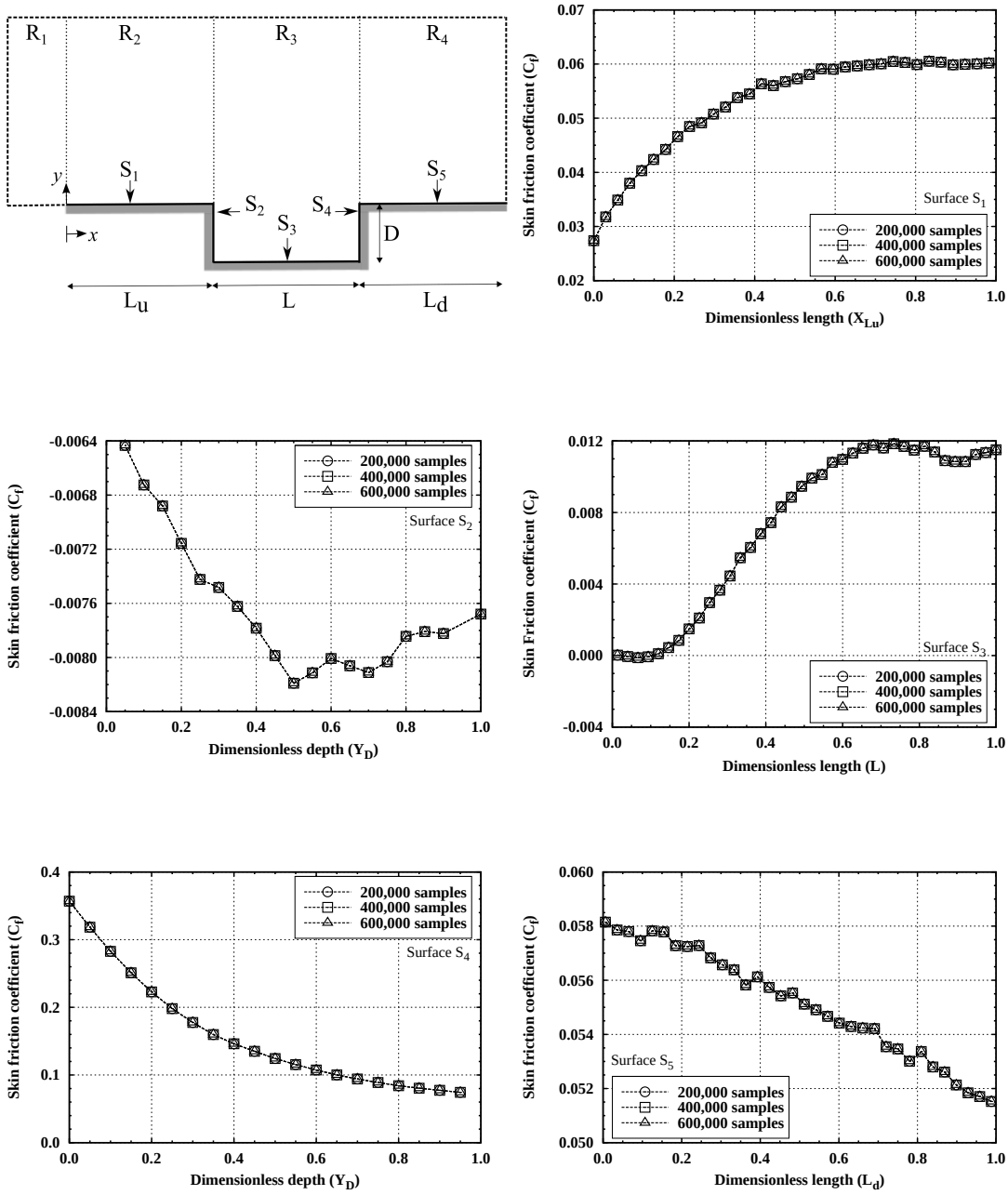

Figure A.13: Influence of number of samples on skin friction coefficient (C_f) along the cavity surfaces.

Appendix B

OpenFOAM tutorial case

Here, we present the main steps required to run a simulation using the *dsmcFoam* hosted at the OpenFOAM C++ Computational Fluid Dynamics toolbox. In the OpenFOAM 2.3.0, four tutorial cases (freeSpacePeriodic, freeSpaceStream, supersonicCorner, and wedge15Ma5) are available in the tutorials folder (path: Tutorials>dicreteMethods >dsmcFoam) for training purposes. However, an additional case was developed in order to introduce the DSMC technique to new users.

In this tutorial case, the Orion Command Module reentry at an altitude of 107 km and 30^o angle of attack [194]. The freestream properties are shown in Table B.1 and are also available in Ref. [198] is considered. The wall temperature is set at 1000 K and diffuse reflection with complete thermal accommodation is the boundary condition applied as wall boundary condition.

Table B.1: Freestream conditions for Orion C.M at 107 km altitude.

Parameter	**Value**	**Unit**
Velocity (V_∞)	6053.4	m/s
Temperature (T_∞)	217.63	K
Number density (n_∞)	3.532×10^{18}	m^{-3}
Density (ρ_∞)	1.610×10^{-7}	kg/m^3
Pressure (p_∞)	0.011×10^{-2}	Pa

The open source DSMC code in OpenFOAM was created as a collaboration between OpenCFD Ltd and the University of Strathclyde as extension to the Molecular Dynamics code developed [201] and it is freely available for download under the GNU general public licence. It is possible to download the OpenFOAM using the Synaptic Package Manager or via terminal

commands according to the OpenFOAM website instructions [202].

Each tutorial cases is composed of three main directories: 1) **constant** - Mesh and specific data for the gas species to be used during the simulation are specified in this directory; 2) **system** - contains all of the information related to boundary and freestream conditions, time step, and sampling; and 3) **0** - this folder is created during the particle initialisation process and comprises all of the information for particles' position, velocity, temperature, number density, pressure, etc.

In order set up and run the tutorial case, the following steps should be executed:

1. Create a run directory (path: Home>OpenFOAM>Run);
2. Copy the tutorial case to the Run directory;
3. Calculate the VHS mean free path [149] according to the freestream conditions;
4. Create a cubic mesh using the *blockMeshDict* at 0 directory and execute it using the command "blockMesh". The cell size must have 1/3 of the mean free path size and the boundary conditions (inlets, outlets, symmetry planes, and walls) must be defined.
5. To check the the cubic mesh, use the command "checkMesh". You should receive information about the number of cells, cells are and volume, orthogonality, and boundaries. In addition, you should visualise the message "Mesh OK"
6. Used a CAD program to generate the Orion geometry and export it to .stl file;
7. Calculate the time step based on the freestream velocity and most probable velocity. Update the *controlDict* for the new time step and choose the data writing interval. In addition, resetOnOutput should be set as "on" to avoid the storage of the simulated data during the transient solution;
8. At *boundariesDict*, specify the Orion wall temperature, gas-surface interaction, inlets and outlets conditions;
9. Define the freestream properties at *dsmcInitialiseDict*;
10. With all the boundaries and freestream conditions defined, open a terminal window and run the command "snappyHexMesh -overwrite". The *snappyHexMesh* utility is used to modify the cubic mesh previously created and 'snaps' it to take on the shape of any CAD geometry and producing a unstructured mesh;
11. Check the snapped mesh using the command "checkMesh" or "checkMesh -allGeometry";
12. In the terminal window, use the command "dsmcInitialise" to introduce particles at the computational domain and initialise the boundaries conditions;

13. To run the case in a single core use the command “dsmcFoam > log &” followed by the command tail -f log in order to visualise the code outputs.

14. To run the case in parallel, first is necessary to determine the number of processors to be used at the “decomposeParDict” and use the command “decomposePar” to decompose the computational domain. Each processors will be used in a specific region of the computational mesh.

15. Use the command “mpirun -n 8 dsmcFoam -parallel > log &” followed by tail -f log to run the tutorial case in parallel. The number 8 corresponds to the number of processors used in the decomposition process in the previous step;

16. During the running interval the transient and steady state may be determined by measuring the kinetic energy and the number of particles into the computational domain. This information is available in the log file and could be read by a gnuplot script in real time;

17. When the kinetic energy and number of particles reached a plateau, switch the resetOnOutput “on” to “off” and the sampling process will take place;

18. Finishing the simulation, use the command “reconstructPar -latestTime” to reconstruct the results for each processor;

19. Use the paraView to post-process the results (command: paraFoam) or any other post-processing programs such as Tecplot.